A NOVEL APPROACH FOR COMBINING BIOMECHANICAL AND MICRO-STRUCTURAL ANALYSES TO ASSESS THE MECHANICAL AND DAMAGE PROPERTIES OF THE ARTERY WALL

by

Michael Raymond Hill

M.S., University of Alabama at Birmingham, 2006

B.S., Mississippi State University, 2004

Submitted to the Graduate Faculty of

the Swanson School of Engineering in partial fulfillment

of the requirements for the degree of

Doctor of Philosophy

University of Pittsburgh

2011

UNIVERSITY OF PITTSBURGH

SWANSON SCHOOL OF ENGINEERING

This dissertation was presented

by

Michael Raymond Hill

It was defended on

November 15, 2011

and approved by

Anne M. Robertson, Ph.D., Associate Professor, Department of Mechanical Engineering and Materials Science

Michael S. Sacks, Ph.D., Professor, Department of Bioengineering

David Vorp, Ph.D., Professor, Department of Bioengineering

Partha Roy, Ph.D., Associate Professor, Department of Bioengineering

William S. Slaugher, Ph.D., Associate Professor, Department of Mechanical Engineering and Materials Science

Dissertation Director: Anne M. Robertson, Ph.D., Associate Professor, Department of Mechanical Engineering and Materials Science

ABSTRACT

A NOVEL APPROACH FOR COMBINING BIOMECHANICAL AND MICRO-STRUCTURAL ANALYSES TO ASSESS THE MECHANICAL AND DAMAGE PROPERTIES OF THE ARTERY WALL

Michael Raymond Hill, PhD

University of Pittsburgh, 2011

Elastin and collagen have been described as the dominant passive load bearing proteins in the artery wall. The highly distensible elastin has been hypothesized to bear most of the load at low pressures, with the less distensible crimped collagen fibers uncoiling and thus becoming available to bear load as the overall tissue stretch is increased. Damage to elastin, a microstructural protein responsible for the elasticity of arteries, has been implicated in the pathogenesis of severe cardiovascular events.

To analyze the structure-function relationship of the artery wall and the acute rupture of elastin, new mechanical testing systems were developed, combining uniaxial mechanical testing with non-destructive multi-photon imaging. By using this system to directly measure the distribution of collagen fiber recruitment stretches in the artery wall, a previous conjecture that collagen fibers begin to be recruited at a finite strain was verified. Collagen fiber recruitment was observed to initiate at a finite strain, under increasing extension along the circumference, corresponding to a sharp increase in the measured mechanical stiffness. To quantify this behavior, a new constitutive model was presented in which fiber recruitment begins at finite strain with subsequent individual fiber recruitment represented by a probability distribution function.

Various isotropic models were fit to experimental data obtained from mechanical testing of isolated arterial elastin. Results suggested that a neo-Hookean model used in pre-

vious studies is suitable. A new structurally-motivated modeling approach was introduced, directly including structural information regarding the distribution of fenestrae in the internal elastic lamina.

Acute elastin rupture in human cerebral arteries was analyzed with the new system. Elastin was modeled as an isotropic material with a scalar damage variable used to represent acute deformation-induced damage. Microscopic images revealed acute rupture of elastin. The internal elastic lamina was torn to reveal medial collagen underneath. These results provided new insights into the micro-structural and mechanical properties of the artery wall.

TABLE OF CONTENTS

LIST OF TABLES

LIST OF FIGURES

1.0 INTRODUCTION

The overall goal of this work is to develop an accurate mechanical model of the artery wall, including micro-structural information and damage. The research is targeted at elucidating the causes and mechanisms behind cardiovascular diseases resulting from damage to a structural protein in the artery wall known as elastin [1, 2, 3, 4, 5, 6]. The clinical relevance of this approach is to increase our understanding of pathological conditions that result from elastin damage, so improved, safe, and effective new treatment modalities may be developed. The objective of the present work, is one step in this process: the analysis of the general structure-function relationship of the artery wall and the response to physical damage to elastin. The development of new methods of measuring the changing structure of the arterial wall under loads up to supra-physiological levels was required to meet the objective.

The field of soft tissue biomechanics offers the means for acquiring a deeper understanding of tissue structure and function. By considering the mechanics at the molecular, cellular, tissue, and organ levels, the relationship between forces, stresses, and strains, and the biological processes such as damage, repair, growth, and remodeling may be better understood [7]. Y. C. Fung [8], who merged the observations of biomedical researchers with the theoretical formulation in nonlinear solid mechanics [9], has been credited with the emergence of interest in soft tissue biomechanics. In this framework, the artery wall has been considered "elastomer-like," and thus its response has been modeled using the formulation of nonlinear elasticity [10, 9]. Many investigators have applied this modeling approach to a vast array of tissues [11, 12, 13, 7, 14, 15, 8].

There is a pressing need for an accurate theoretical and experimental framework in which the mechanical and damage response of the artery wall may be analyzed. Therefore, the central objective of this work is to utilize a soft tissue biomechanics approach to develop an accurate model of the artery wall including damage.

1.1 THE HEALTHY ARTERY WALL

The mechanical integrity of the artery wall is vital to one's health. This integrity is dependent upon the state of the primary load-bearing components of the wall: collagen fibers, elastin, and smooth muscle cells.

The healthy artery wall is divided into three layers (Fig. 1): 1) the tunica intima, including endothelial cells and a thin sheet of elastin defined as the internal elastic lamina (IEL); 2) the tunica media, containing mostly smooth muscle cells, layers of elastin and collagen fibers; and 3) the tunica adventitia, composed mainly of collagen fibers, fibroblasts, and the layer of elastin known as the external elastic lamina (EEL).

The mechanical response of the artery wall has been shown to be nonlinear, with a fairly linear toe region that bends upward at higher strain prior to tissue failure (see, e.g., Fig. 2 and [16, 17]). Based on mechanical experiments, the toe region has been hypothesized as primarily governed elastin, while the upward bend is due to the uncrimping, or recruitment, of medial collagen fibers [16].

Smooth muscle cells (SMCs) are important to the active and passive response of the wall, and their role is considered in some models [18], but in this work, the contribution from SMCs will be ignored. Therefore, the passive mechanical response is assumed to be dominated by the elastin and collagen.

The structure of the cerebral arteries differs from the structure of extracerebral arteries. The internal elastic lamina, the fenestrated layer of elastin lying between the intima and media, is more prominent in cerebral arteries versus extracerebral arteries (Fig. 1) [19]. The media and adventitia of cerebral arteries are thinner than those of extracranial arteries of similar diameter, and therefore, the cerebral arterial wall is thinner [20]. Also, elastin is

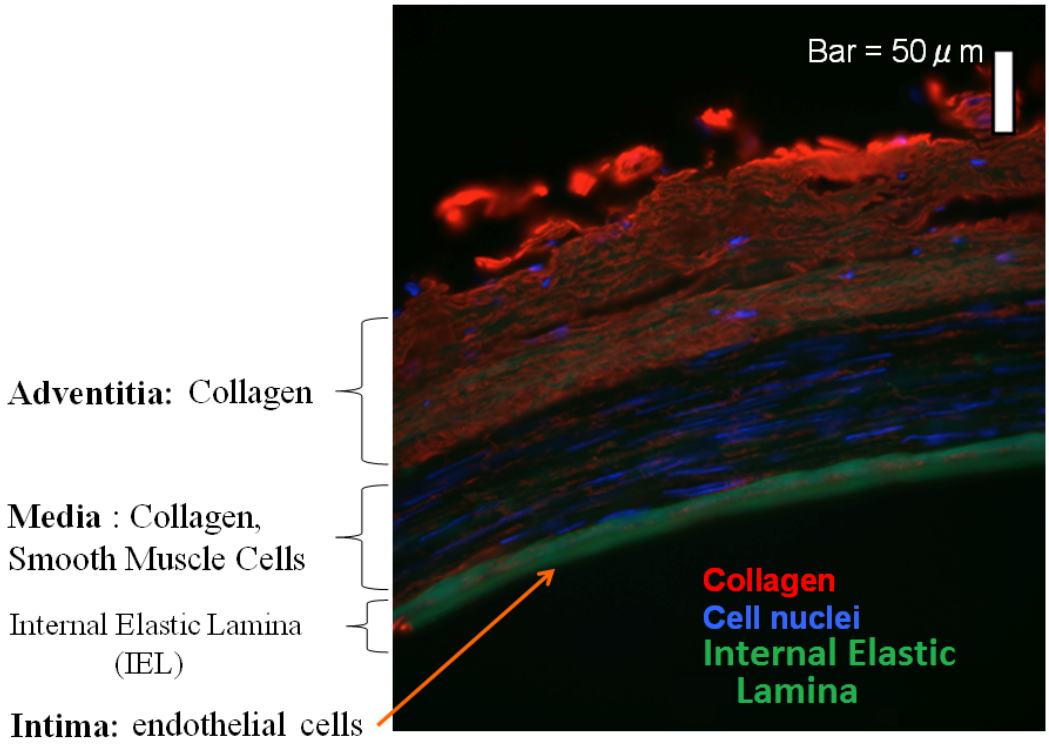

Figure 1: Fluorescence microscopy images of immuno-stained cross sectional preparations of the human left cerebral vertebral artery, fixed at 30% stretch. Bar = 50μm. Histological methods are described in Appendix A

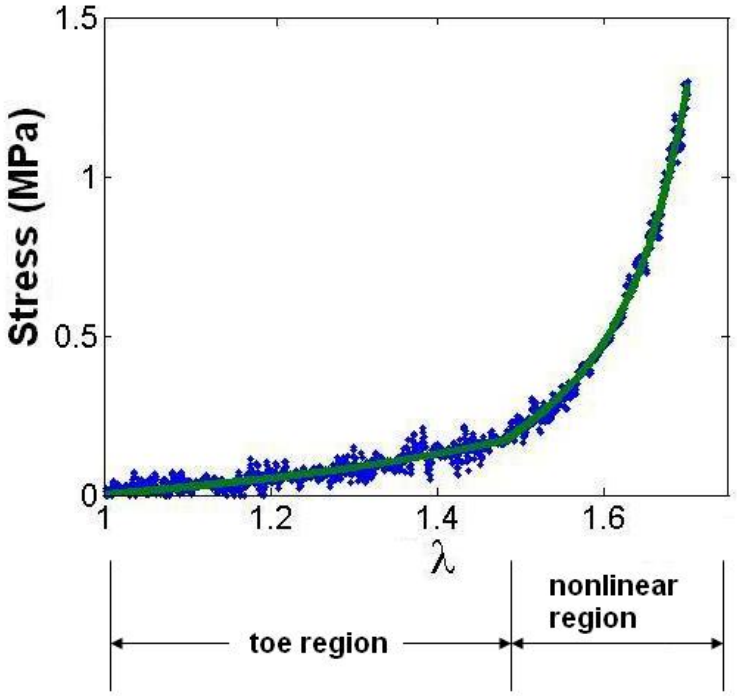

Figure 2: Typical stress-stretch relationship of the artery wall, taken from rabbit carotid arteries under uniaxial extension, depicting the linear toe region at low strain and the nonlinear portion of the response at higher strain

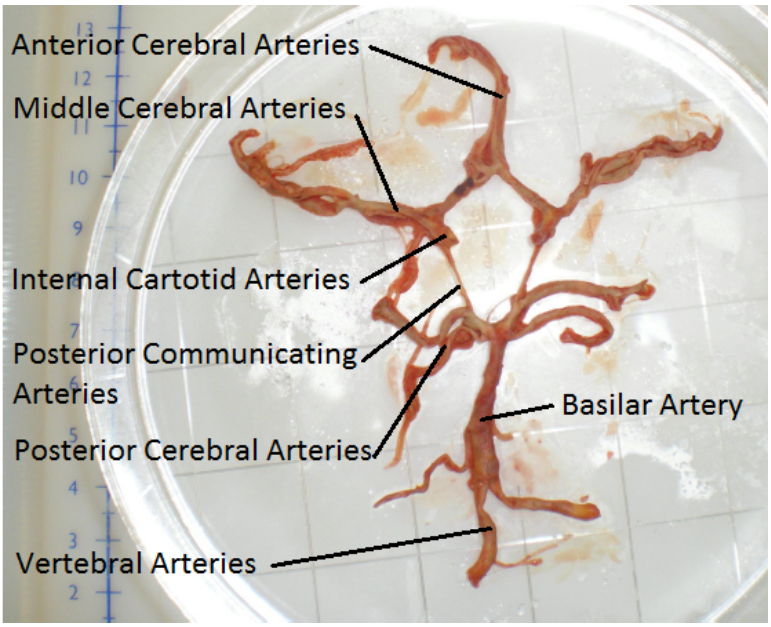

Figure 3: Circle of Willis obtained from a human cadaver at autopsy. Units on the scale are in cm

largely confined to the IEL and the EEL is absent [19]. These differences between cerebral and extra-cerebral arteries may predispose the former to cerebral saccular aneurysms, discussed in the next section.

1.2 CEREBRAL SACCULAR ANEURYSMS

Cerebral saccular aneurysms are abnormal dilatations which usually develop near bifurcations or curved segments of arteries in the Circle of Willis, which is the group of arteries that supply blood to the brain [21] (Fig. 3). The mechanisms underlying intracranial aneurysm formation and rupture remain poorly understood, despite decades of preclinical and clinical research [22, 23, 24, 25, 26, 27].

An estimated 1 to 5% of the population harbors aneurysms [28]. Aneurysms are only identified prior to rupture in 10% of cases, and 12% of individuals who suffer subarachnoid hemorrhage (SAH) from ruptured aneurysm die before they can be treated, while 40-60% die within one month [29].

In cerebral aneurysms, the IEL is severely disrupted or absent [30, 17]. Enlarged fenestrations have been reported at the mouth of saccular aneurysms [31, 32], and from cross sectional histological sections, the IEL and media appear to end abruptly at the entrance to artificially induced aneurysms in rat models [33]. Regions of enlarged fenestrations may stretch more readily than the adjacent areas of normal fenestrations, and these regions could transform into a microinvagination [34]. Therefore, the degradation of elastin and loss of the IEL may be critical to the initiation of cerebral saccular aneurysms.

The specific causes of saccular aneurysm formation remain unknown and are subject to controversy. For example, the arterial layer critical for formation and the factors that damage the wall are subjects of debate [35]. The difference between the arterial wall structure in cerebral arteries and extracranial arteries, described in Section 1.1, may predispose the former to the formation of saccular aneurysms [36] . Regions of enlarged fenestrations, or holes, in the IEL have been observed in apical region of cerebral arterial bifurcations [37]. Therefore, they may be more susceptible to the detrimental effects associated with loss of elastin due to damage [2].

In the next section, approaches to modeling the artery wall are discussed. These approaches are applied in this work to model the structure-function relationship, and damage, of the artery wall.

1.3 MODELS OF THE ARTERY WALL

The response of elastin is nearly always modeled as isotropic (Chapter 5). For isotropic materials, the stress-strain response is independent of the direction of loading (Section 2.2.2). More specifically, the symmetry group of an isotropic material includes all rotations about all possible axes and reflections about any plane. The response of collagen

is nearly always modeled as anisotropic (Chapter 4). This anisotropy is due to crimped, circumferentially-oriented [38, 39] medial collagen fibers that gradually unfurl and begin to bear load under increasing stretch [40, 16, 17]. For anisotropic materials, the material response is dependent upon the direction of loading (Section 2.2.3). For example, in the special case of anisotropy known as orthotropy, there are mutually orthogonal planes of material symmetry. For transversely isotropic materials, there is a single axis of symmetry (see [41, 12, 42, 43], etc. for more details).

For materials that only undergo small deformations, the linearized approximation of nonlinear elasticity can be used [41]. However, for materials that undergo large deformations, such as biological tissues, nonlinear approaches must be taken. Constitutive modeling in nonlinear solid mechanics typically involves the use of a strain energy, or stored energy, function (see Section 2.1.6). In this theory of hyperelasticity, the stress tensor can be written in terms of a single scalar function (see, e.g., [9]).

Phenomenological mechanical models are based on the bulk response of the tissue Fung [44, 45] originally proposed a phenomenological model for arterial mechanics, in which the nonlinear behavior was captured with the strain energy function given as an exponential. In 1987, Humphrey and Yin [46] presented a compromise between the phenomenological and structural models, where the strain energy function was separated into "matrix" and "fiber" terms. Additionally, they applied Rivlin's method [47] to evaluate the specific functional forms of the derivatives of the strain energy function directly from biaxial inflation-extension data, without having to specify a form of the response function *ad hoc* or *a priori* [48]. In their work, the specific functional forms for the media and adventitia were determined independently if separation of the layers was possible. In 1998, Holzapfel and Weizsacker [49] postulated a strain energy function additively decoupled into an isotropic "elastin-dominated" rubber-like response term and an anisotropic "collagen-dominated" fabric-like term. In 1999, Wulandana and Robertson [50] presented a model in which the additive response was used for elastin and collagen, with two different unloaded configurations to account for recruitment of collagen at finite strain. In 2000, Holzapfel [14], modeled the arterial wall as a two-layer (media and adventitia) thick-walled tube and decoupled the strain energy function for each layer. Mixture theo-

ries [51, 52] have been utilized to model the individual growth and mechanical response of four primary individual wall constituents: a fluid/proteoglycan gel matrix, elastin, smooth muscle cells, and collagen [53, 18, 54, 55]. The "elastin-dominated" portion was captured with a neo-Hookean strain energy function, and the collagen-dominated behavior was modeled as a sub-class of "Fung-type" transversely isotropic materials.

Structurally motivated models include aspects of the underlying microstructure to better predict the mechanical behavior. In 1979, Lanir [56] originally formulated a three-dimensional structurally motivated model for flat collagenous tissues in which the tissue's total response is represented as the sum of the responses of its two primary constituents: linearly elastic individual elastin and collagen fibers. He assumed, as described above, that the mechanical behavior is dominated at low strain by elastin and at high strain by collagen; nonlinearity was introduced by nonuniformity of the fibers' undulation. Lanir's model directly included the distribution of both collagen fiber orientation and recruitment [56, 57]. This type of structurally-motivated model has been applied to various biological tissues. For example, small angle light scattering [58] has been coupled with a planar biaxial device for direct analysis of gross fiber angular distribution during mechanical testing on soft tissue [15], with the results directly incorporated into Lanir's model [59]. Also, a structural constitutive model for the anterior cruciate ligament was developed based on Lanir's work [60]

1.3.1 A new approach for modeling the artery wall

Inelastic, isotropic, dual-mechanism constitutive equations were developed to model the response of the artery wall [50, 61], utilizing theories on deformation-induced microstructural changes [62, 63] that account for changing reference configurations. This constitutive equation was extended to include an anisotropic response [64]. The model used the additive de-coupling between the isotropic and anisotropic responses, as described above, to account for elastin and collagen separately. Elastin and collagen were modeled as having separate reference configurations. Previous models have considered the activation stretches of individual collagen fibers to be represented by a probability distribution

function, with some fibers initially becoming engaged at infinitesimal stretch during the onset of loading [65]. The multi-mechanism model treated collagen fibers to be abruptly recruited at a finite tissue strain [61, 64]. Furthermore, isotropic damage to elastin was incorporated in these models by using a scalar damage parameter [2], based on continuum damage mechanics formulations [66]. Thus, these models included parameters to account for collagen fiber recruitment and to account for the loss of elastin. In this work, this multi-mechanism model was extended to include a distribution of collagen fiber orientation and a distribution of collagen fiber recruitment, based on the structurally motivated models of Lanir [56, 57, 67, 68].

Architectural data on the micro-scale must be measured for inclusion in structurally motivated constitutive models. One major hurdle to experimental and microstructural assessment of tissue to obtain parameters for structurally motivated models is the extensive processing that typically must be performed after testing. Therefore, in this work, a new methodology for obtaining combined histological and mechanical data is introduced. The traditional approach to visualizing structural proteins involves aldehyde-based fixation techniques followed by histological staining, which is destructive to the tissue, from a mechanics point of view.

Multi-photon microscopy (MPM) has been utilized to visualize both elastin and collagen in arteries by exploiting auto-fluorescence and second harmonic generation, respectively. MPM techniques are non-destructive, since traditional histological techniques are not necessary, so images may be obtained from a single specimen at various time points and levels of strain. Therefore, a new system for analyzing the structure-function relationship of arteries was developed, combining uniaxial testing (UA) and MPM. This system was used to study collagen fiber orientation & recruitment and elastin structure & damage.

In this work, with a new horizontal system (hUA-MPM), collagen fiber recruitment was quantified from 3D rendered MPM images, and orientation was measured in projected stacks of images (Chapter 4). Results from this device provided evidence that collagen recruitment initiated at a finite stretch, followed by gradual recruitment of the individual fibers. The new constitutive model was successful in capturing this mode

of recruitment. Stress-strain analysis was combined with simultaneous microstructural imaging of collagen recruitment and orientation, providing a new technique by which underlying fiber architecture may be quantified and included in constitutive equations.

To determine the appropriate mathematical model for aterial elastin, analysis was performed on data obtained from experiments performed on isolated elastin, and imaging experiments were performed and on intact cerebral arteries (Chapter 5) . Elastin's mechanical response was analyzed, by collaborators, with uniaxial pin extension on isolated elastin.

Various strain energy functions were fit to experimental data in order to determine an appropriate model for representing the mechanical response. Also, histological analyses by our group and others indicate the cerebral artery wall exhibits a well-defined fenestrated internal layer of elastin (internal elastic lamina). The internal elastic lamina, or large layer of elastin in cerebral arteries, was confirmed to exhibit holes, or fenestrations. A structural modeling approach was developed that includes the effect of these fenestrae, using a scalar measure called the ligament efficiency. Results from these studies are preliminary, but provide the groundwork for developing structurally-motivated models for arterial elastin.

Finally, damage experiments were performed on segments of human cerebral arteries (Chapter 6). As discussed above, damage to elastin in the cerebral arteries may lead to pathologies such as cerebral saccular aneurysm formation. Elastin damage and degradation appear to occur via three basic mechanisms: acute rupture, cyclic fatigue, and biochemical degradation. A recently developed constitutive damage model incorporates the three modes of elastin damage.

One major hurdle to experimental and microstructural assessment of damage to obtain model parameters is the extensive processing that typically must be performed after testing. A new vertical (vUA-MPM) system and protocol allowed elastin damage to be quantified and assessed visually. Damage experiments were conducted on cerebral arteries, and the imaging results revealed cat's eye shaped tears in the internal elastic lamina, which support a previous hypothesis that the elastin is damaged prior to collagen during overextension of the artery wall. A continuum damage mechanics approach was taken

to model this rupture, though the size of the tears in the internal elastic lamina at large loads was on a scale larger than was deemed appropriate for applying the continuum approximation.

1.4 SPECIFIC AIMS

The overall objective of this work is to enhance our knowledge of the relationship between structure and function in the artery wall. Here, the focus is on the passive load bearing components of the wall, elastin and collagen. This objective is broken down into the following three specific aims:

- To develop a new system combining uniaxial mechanical testing and multi-photon microscopy for simultaneous mechanical testing of the artery wall and imaging of collagen and elastin, two primary load-bearing constituents of the artery wall
- To develop a constitutive model for the mechanical response of artery tissue that directly includes measured micro-structural data of collagen and elastin obtained from multi-photon images
- To develop a constitutive model and an experimental system for analyzing the mechanical damage of arteries

Both combined mechanical/histological experiments and damage experiments will provide fundamental knowledge about the nature and behavior of the artery wall.

This thesis is further divided as follows. The mathematical formulation used in nonlinear solid mechanics is described in Chapter 2. This section is intended to highlight the major points relevant to the work in this thesis. To achieve the first specific aim, custom devices are fabricated in order to analyze the structure-function relationship of the artery wall, described in Chapter 3. To achieve the second specific aim, the biomechanical properties of the healthy wall are investigated using the mathematical formulation described in Chapter 2 and the experimental devices described in Chapter 3. To analyze collagen, experiments with the new system are conducted on carotid artery tissue harvested from

new Zealand white rabbits, described in Chapter 4. To analyze elastin, histological images of the internal elastic lamina in human cerebral vessels are used, as well as data from uniaxial ring tests on isolated elastin acquired through collaborators, described in Chapter 5. To achieve the third specific aim, damage experiments are performed on human cerebral artery tissue (Chapter 6). In Chapters 4, 5 and 6, an attempt is made to describe the methods qualitatively, with references made to the appropriate mathematical formulation in Chapter 2. A Conclusion is provided in Chapter 7 to highlight the major contributions from this work, as well as future directions.

2.0 MATHEMATICAL MODELING

The general theory of material behavior relevant to this thesis is described in this section by following the classical work by Truesdell and Noll [9]. Of course, no attempt is made to recreate that treatise in its entirety, only the major points are highlighted, and where possible, the notation is preserved. The requisite mathematical preliminaries may be found in this classic work [9] and in books by other authors to which reference has been made during the writing of this section, e.g., Green, Zerna, and Adkins [42, 43], Chadwick [69], Ogden [70], Spencer [71], Taber [12], and Holzapfel [72], as well as the lecture notes of Robertson [73, 74] and Sacks [75, 76].

This chapter is divided into a section describing the general approach used in nonlinear elasticity (Section 2.1), which is further divided into sections describing kinematics (Section 2.1.1), deformations (Section 2.1.2), forces and stresses (Section 2.1.3), and general thermodynamic processes (Section 2.1.4). Internal constraints are described in Section 2.1.5; these are used to impose conditions such as incompressibility. In this work, the artery wall is treated as a hyperelastic material, which is defined in Section 2.1.6. Furthermore, invariants are described in Section 2.1.7, which are utilized in developing constitutive models. Internal variables are described in Section 2.1.8, which are utilized here to develop damage models of the artery wall.

Following this preliminary section is a description of special cases of the strain energy function used in this work (Section 2.2). An additive decoupling of the strain energy function into isotropic and anisotropic components is given in Section 2.2.1. This split allows the isotropic (elastin) contribution (Section 2.2.2) to be modeled separately from the anisotropic (collagen) contribution (Section 2.2.3). Special cases of the latter are described in subdivisions. An approach to modeling damage is described in Section 2.2.4.

Finally, solutions to specific boundary value problems are given in Section 2.3. The choice of fiber recruitment models (Section 2.3.1) and fiber orientation models (Section 2.3.2) for the anisotropic contribution are given here, followed by the solution of planar biaxial tension (Section 2.3.3), uniaxial tension (Section 2.3.4), and inflation of a thick-walled cylinder (Section 2.3.5), for chosen fiber distribution models.

2.1 GENERAL FORMULATION

In continuum mechanics, the mechanical behavior of materials is modeled on the macroscopic scale, ignoring the discrete nature of matter, so that the material particles are continuously distributed throughout the regions of space, and the atomic structure is not directly considered [71]. The general principles of continuum mechanics (see [9]) are applied here to characterize the mechanical response of materials in the formulation that follows.

2.1.1 Kinematics

A reference configuration $\boldsymbol{\kappa}_0$ of an arbitrary body in space $\mathscr{B}$ at an arbitrary time t is introduced as a means of specifying individual material particles that comprise the body $\mathscr{B}$.

A *motion* of the body is defined as a one-parameter family $\boldsymbol{\chi}_t$ of configurations, with real parameter t = time:

$$\begin{aligned} \mathbf{x} &= \hat{\boldsymbol{\chi}}_t(\mathbf{X}) = \hat{\boldsymbol{\chi}}(\mathbf{X}, t) \\ \mathbf{X} &= \hat{\boldsymbol{\chi}}_t^{-1}(\mathbf{x}) = \hat{\boldsymbol{\chi}}^{-1}(\mathbf{x}, t) \end{aligned} \tag{2.1}$$

with components relative to a three-dimensional rectilinear co-ordinate system given as

$$\begin{aligned} x_k &= \hat{\chi}_k(X_\alpha, t) \\ X_\alpha &= \hat{\chi}_\alpha^{-1}(x_k, t) \end{aligned} \tag{2.2}$$

where κ, α = 1,2,3.

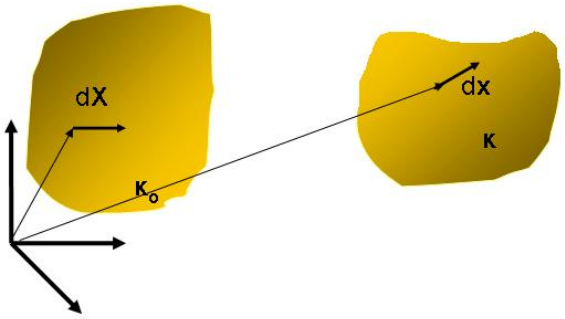

Figure 4: Kinematics of the deformation of an arbitrary body in space

The symbol $\boldsymbol{\chi}$ is used to denote both the motion, and the corresponding deformation, of the body from some original reference configuration $\boldsymbol{\kappa}_0$ to the current configuration $\boldsymbol{\kappa}$ (Fig. 4). The form of $\boldsymbol{\chi} = \hat{\boldsymbol{\chi}}(\mathbf{X}, t)$ depends upon the choice of the reference configuration. Thus, the deformation may be described by Eq. 2.1.

The *velocity* and *acceleration* are defined, with respect to material, or *Lagrangian*, coordinates [41], as the first and second time-derivatives of the motion $\boldsymbol{\chi} = \hat{\boldsymbol{\chi}}(X, t)$, respectively:

$$\mathbf{v} = \dot{\mathbf{x}} = \frac{d}{dt}\hat{\boldsymbol{\chi}}(\mathbf{X}, t) \tag{2.3}$$

$$\mathbf{a} = \ddot{\mathbf{x}} = \dot{\mathbf{v}} = \frac{d^2}{dt^2}\hat{\boldsymbol{\chi}}(\mathbf{X}, t) \tag{2.4}$$

where the single and double overdot denotes the first and second time derivative in a Lagrangian framework, respectively (see [41]).

2.1.2 Description of Material Deformations

The deformation gradient of the motion $\boldsymbol{\chi}$, defined as a second-order tensor field, is given as

$$\mathbf{F} \equiv \nabla \hat{\boldsymbol{\chi}}(\mathbf{X}, t) = \frac{\partial \hat{\boldsymbol{\chi}}(\mathbf{X}, t)}{\partial \mathbf{X}} \tag{2.5}$$

where the Nabla symbol ∇ represents the gradient of the vector $\boldsymbol{\chi}$, with respect to Lagrangian spatial variable $\mathbf{X}$. The determinant of the deformation gradient (Eq. 2.5) is the Jacobian of the transformation defining the deformation, from a reference configuration $\boldsymbol{\kappa}_0$ to the (current) configuration $\boldsymbol{\kappa}$:

$$J \equiv |det\mathbf{F}| \tag{2.6}$$

With the notation that T is the transpose of the tensor and tr is its trace, the time-derivative of the Jacobian is given as (see, e.g., [72])

$$\dot{J} = \dot{\overline{det}\mathbf{F}} = J\mathbf{F}^{-T} : \dot{\mathbf{F}} = Jtr(\mathbf{F}^{-1}\dot{\mathbf{F}}) \tag{2.7}$$

By applying the *polar decomposition theorem*, two unique multiplicative decompositions of $\mathbf{F}$ are given by

$$\begin{aligned} \mathbf{F} &= \mathbf{RU} \\ \mathbf{F} &= \mathbf{VR} \end{aligned} \tag{2.8}$$

where $\mathbf{R}$ is the orthogonal *rotation* tensor ($\mathbf{RR}^T = \mathbf{1}$), and the symmetric, positive-definite tensors $\mathbf{U}$ and $\mathbf{V}$ represent the *right* (or *material*) and *left* (or *spatial*) *stretch tensors* of the deformation, respectively. Applying the basic rules for tensor manipulation (see, e.g., [9, 72]), the following definitions are obtained:

$$\begin{aligned} \mathbf{C} &= \mathbf{U}^2 = \mathbf{F}^T\mathbf{F} \\ \mathbf{B} &= \mathbf{V}^2 = \mathbf{F}\mathbf{F}^T \end{aligned} \tag{2.9}$$

where $\mathbf{C}$ and $\mathbf{B}$ are defined as the *right* and *left Cauchy-Green tensors*, respectively. Note that both are symmetric and positive-definite.

The spatial gradient of the velocity $\mathbf{v}$ (eq. 2.3) is given as

$$\mathbf{L} = \nabla \mathbf{v} = \dot{\mathbf{F}}\mathbf{F}^{-1} \tag{2.10}$$

where the gradient is taken with respect to $\mathbf{x}$. This spatial velocity gradient may be decomposed into

$$\mathbf{L} = \mathbf{D} + \mathbf{W} \tag{2.11}$$

where the stretching tensor $\mathbf{D}$ is the symmetric portion and $\mathbf{W}$ is the anti-symmetric (or skew) portion of $\mathbf{L}$, by following the rules for decomposing second order tensors into their symmetric and antisymmetric components [72].

2.1.3 Forces and Stress

A system of forces for a given body $\mathscr{B}$ in motion (eq. 2.1), may be characterized by:

1. The vector field $\mathbf{b} = \hat{\mathbf{b}}(\mathbf{x}, t)$ per unit mass represents the *external body force* acting on the body $\mathscr{B}$, which is defined for $\mathbf{x}$ in the region occupied by the body at time t.
2. The vector-valued function $\mathbf{t} = \hat{\mathbf{t}}(\mathbf{x}, \mathbf{n})$ representing the *stress vector* at $\mathbf{x}$ acting across an oriented surface element with unit normal $\mathbf{n}$ and is defined for all points $\mathbf{x}$ in the body and for all unit vectors $\mathbf{n}$.

Assuming suitable continuity, the *Cauchy stress tensor field*, $\mathbf{T} = \hat{\mathbf{T}}(\mathbf{x}, t)$, is defined by the *Cauchy Stress Equation* [9] as

$$\mathbf{t} = \mathbf{T}\mathbf{n} \tag{2.12}$$

The Cauchy stress tensor $\mathbf{T} = \hat{\mathbf{T}}(\mathbf{x}, t)$ (eq. 2.12) is determined by the state of a small neighborhood about the particle X, and all conditions in the body $\mathscr{B}$ at time t are determined by the history of the body, i.e., no knowledge of future behavior is necessary to determine all of the natural processes.

2.1.4 Thermodynamic Processes

A brief description of the relevant framework for describing a thermodynamic process is given in this section (see [9] and [77] for more details). Eight functions of position and time are used to describe a thermodynamic process, given by

1. The motion of the body, $\mathbf{x}$, given by eq. 2.1
2. The specific entropy, $\eta = \hat{\eta}(\mathbf{X}, t)$ per unit volume
3. The specific internal energy $\epsilon = \hat{\epsilon}(\mathbf{X}, t)$ per unit mass
4. The symmetric stress tensor $\mathbf{T} = \hat{\mathbf{T}}(\mathbf{X}, t)$, defined in Section 2.1.3
5. The body force $\mathbf{b} = \hat{\mathbf{b}}(\mathbf{X}, t)$ per unit mass, also defined in Section 2.1.3
6. The local temperature $\theta = \hat{\theta}(\mathbf{X}, t) > 0$
7. The heat flux vector $\mathbf{q} = \hat{\mathbf{q}}(\mathbf{X}, t)$
8. The heat supply $r = \hat{r}(\mathbf{X}, t)$ per unit mass

For an elastic material, if the body is homogeneous, an admissible thermodynamic process may be represented by the following four constitutive equations:

$$\epsilon = \hat{\epsilon}(\mathbf{F}, \theta) \tag{2.13}$$

$$\eta = \hat{\eta}(\mathbf{F}, \theta) \tag{2.14}$$

$$\mathbf{T} = \hat{\mathbf{T}}(\mathbf{F}, \theta) \tag{2.15}$$

$$\mathbf{q} = \hat{\mathbf{q}}(\mathbf{F}, \theta) \tag{2.16}$$

where the deformation gradient tensor $\mathbf{F}$ is given by eq. 2.5. Following classic works in this field (see [9]), the constitutive equation is required to obey the principle of material frame indifference.

Ignoring couple stresses, body couples, and other mechanical interactions, these functions represent a *thermodynamic process* if the conservation laws are satisfied for the body $\mathscr{B}$ and each of its parts. Certain balance principles (and inequalities) are applicable to all materials and must be satisfied at all times:

2.1.4.1 The conservation of mass The body $\mathscr{B}$ is assumed to be endowed with a non-negative scalar measure $\mathscr{M}$ defined as the *mass distribution* of the body.

Assuming that $\mathscr{M}$ is absolutely continuous and uniform over the region of space occupied by the body, the *mass density* of the body in the configuration $\boldsymbol{\kappa}$ may be defined as ρ, and similarly for $\boldsymbol{\kappa}_0$ as ρ_0.

The law of conservation of mass requires the mass of a system to be conserved during a process, and therefore identical in all configurations, i.e., no change in net mass in the body, though the volume may change, thus changing the density.

The Jacobian of the deformation gradient (eq. 2.6) relates an infinitesimal element dv of the total volume of the body, $v(\mathscr{B})$, in the current configuration $\boldsymbol{\kappa}$, to an infinitesimal element dV of the volume, $V(\mathscr{B})$, in the reference configuration $\boldsymbol{\kappa}_0$:

$$dv = \hat{J}(\mathbf{X}, t)dV = JdV \tag{2.17}$$

Since mass is conserved, the following continuity equation may be derived from a comparisons of the expressions of the mass in the reference and current configurations, $\boldsymbol{\kappa}_0$ and $\boldsymbol{\kappa}$, respectively [41]:

$$\mathscr{M} = \int_{V(\mathscr{B})} \rho_0 dV = \int_{v(\mathscr{B})} \rho dv \tag{2.18}$$

It follows from eq. 2.18 that the density in the current configuration is related to that in the reference configuration through:

$$\rho = J\rho_0 \tag{2.19}$$

For an isochoric (volume-preserving) process, J is equal to unity and $\rho = \rho_0$.

2.1.4.2 The balance of linear momentum The balance of linear momentum may be written as

$$\int_{\partial V(\mathscr{B})} \mathbf{T}\mathbf{n} ds + \int_{V(\mathscr{B})} \rho \mathbf{b} dV = \int_{V(\mathscr{B})} \rho \ddot{\mathbf{x}} dV \tag{2.20}$$

where $\partial V(\mathscr{B})$ is the surface of $V(\mathscr{B})$, ds the surface area element, and $\mathbf{n}$ the unit normal vector to $\partial V(\mathscr{B})$, in the reference configuration at time t.

Assuming suitable smoothness eq. 2.20 may be given by the local form:

$$\nabla \cdot \mathbf{T} + \rho \mathbf{b} = \rho \ddot{\mathbf{x}} \tag{2.21}$$

where $\nabla \cdot$ is the divergence of a tensor. Note that this equation is also known as *Cauchy's Law of Motion* and may be thought of in terms of Newton's Second Law of Motion.

For zero acceleration and no external forces, eq. 2.21 is given as

$$\nabla \cdot \mathbf{T} = \mathbf{0} \tag{2.22}$$

2.1.4.3 The balance of angular momentum The symmetry of the Cauchy stress tensor $\mathbf{T}$ may be shown from the balance of angular momentum (see [72, 41], and others):

$$\mathbf{T} = \mathbf{T}^T \tag{2.23}$$

2.1.4.4 The balance of energy The balance of energy is an expression of the first law of thermodynamics, which states that the energy can be transformed, but cannot be created nor destroyed:

$$\begin{aligned} \frac{d}{dt} \int_{V(\mathscr{B})} \frac{1}{2} \rho \dot{\mathbf{x}} \cdot \dot{\mathbf{x}} dV + \frac{d}{dt} \int_{V(\mathscr{B})} \rho \epsilon dV = \\ \int_{V(\mathscr{B})} \rho \mathbf{b} \cdot \dot{\mathbf{x}} dV + \int_{\partial V(\mathscr{B})} \mathbf{t} \cdot \dot{\mathbf{x}} ds + \int_{V(\mathscr{B})} \rho r dV - \int_{\partial V(\mathscr{B})} \mathbf{q} \cdot \mathbf{n} ds \end{aligned} \tag{2.24}$$

The first term on the left hand side of eq. 2.24 represents the rate of change in kinetic energy. The second term on the left hand side represents the rate of change in internal

energy. The first and second terms on the right hand side of eq. 2.24 represent the rate of work done by the body and surface forces, respectively. The third term on the right hand side represents the rate of energy entering the system internally. The last term on the right hand side represents the rate of energy entering the system through the surface.

Assuming suitable smoothness and making use of the balance of linear momentum, eq. 2.24 may be given by its local form:

$$tr(\mathbf{TL}) - \nabla \cdot \mathbf{q} - \rho\dot{\epsilon} = -\rho r \tag{2.25}$$

where $\mathbf{L}$ is the velocity gradient given by eq. 2.10. Note that the first term of eq. 2.25 is termed the *stress power*. Since the stress tensor $\mathbf{T} = \mathbf{T}^T$ is symmetric and the trace of a product of a symmetric and a skew tensor is zero, noting eq. 2.11, the stress power may be expressed by [72]

$$tr(\mathbf{TL}) = \mathbf{T} : \mathbf{L} = \mathbf{T} : \mathbf{D} = tr(\mathbf{TD}) \tag{2.26}$$

2.1.4.5 Clausius-Duhem Inequality The Clausius-Duhem inequality is a mathematical expression of the second law of thermodynamics, which states that the entropy, a thermodynamic property that is used to determine the available energy to do useful work, of a system always increases or remains constant. Here, an isothermal condition is considered. The production of entropy Γ in a body $\mathscr{B}$ is given by

$$\Gamma = \frac{d}{dt}\int_{V(\mathscr{B})} \rho\eta dV - \int_{V(\mathscr{B})} \frac{\rho}{\theta} r dV - \int_{\partial V(\mathscr{B})} \frac{-\mathbf{n}\cdot\mathbf{q}}{\theta} ds \tag{2.27}$$

where the first term on the right hand side represents the rate of change in entropy or entropy creation, the second term represents the rate at which entropy is leaving by radiation, and the third term represents the flux of entropy by conduction through the surface. Assuming suitable smoothness conditions, the above can expressed in the local form as

$$\Gamma = \rho\dot{\eta} - \rho\frac{r}{\theta} + \nabla \cdot \frac{\mathbf{q}}{\theta} \tag{2.28}$$

The *Clausius-Duhem inequality* postulate states that for every admissible process in a body,

$$\Gamma \geq 0 \tag{2.29}$$

For this equation to hold for all of $\mathscr{B}$, eq. 2.28 must be non-negative, and combining eq. 2.28 with eq. 2.25 and $\theta > 0$, gives, for the above inequality,

$$\mathbf{T} : \mathbf{D} - \rho\dot{\epsilon} + \rho\theta\dot{\eta} - \frac{1}{\theta}\mathbf{q} \cdot \nabla\theta \geq 0 \tag{2.30}$$

Applying the chain rule to eq. 2.13,

$$\dot{\epsilon} = \left(\frac{\partial \epsilon}{\partial \mathbf{F}}\right)^T : \dot{\mathbf{F}} + \frac{\partial \epsilon}{\partial \theta}\dot{\theta} \tag{2.31}$$

The specific free energy function per unit mass may be defined as

$$\Psi = \epsilon - \theta\eta = \hat{\epsilon}(\mathbf{F}, \theta) - \theta\hat{\eta}(\mathbf{F}, \theta) = \hat{\Psi}(\mathbf{F}, \theta) \tag{2.32}$$

This function is restricted by the normalization condition $\hat{\Psi}(\mathbf{1}) = 0$ and the requirement that $\hat{\Psi}(\mathbf{F}) \geq 0$. Using the chain rule, the time derivative of the strain energy function is given as

$$\dot{\Psi} = \frac{\partial \hat{\Psi}(\mathbf{F})}{\partial(\mathbf{F})} : \dot{\mathbf{F}} \tag{2.33}$$

By combining eqs. 2.31, 2.10, and 2.33, and applying appropriate tensor relations (see [9]), for isothermal conditions, eq. 2.30 becomes

$$\mathbf{T} : \mathbf{D} - \rho\left(\dot{\Psi} + \eta\dot{\theta}\right) - \frac{1}{\theta}\mathbf{q} \cdot \nabla\theta \geq 0 \tag{2.34}$$

Assuming the process is isothermal, the variables η and θ may be ignored. By applying the Coleman-Noll procedure [77] to eq. 2.34 and using eqs. 2.33 and 2.46, the Cauchy stress tensor may be given in indicial notation as

$$T_{ij} = \rho\frac{\partial \Psi}{\partial F_{iA}}F_{jA} \tag{2.35}$$

where i, j, A = 1,2,3.

2.1.5 Internal constraints

A material point in the body is subject to a *simple internal constraint* if the possible motions are restricted to those for which $\tilde{\gamma}(\mathbf{F}) = 0$ for all time, where $\mathbf{F}$ is the deformation gradient tensor. Applying the principle of material frame-indifference (see [9, 69]), the internal constraint may be given as a function the right Cauchy-Green tensor $\mathbf{C}$, defined in eq. 2.9, by

$$\gamma = \hat{\gamma}(\mathbf{C}) = 0 \tag{2.36}$$

Taking the time-derivative of γ gives

$$\dot{\gamma} = tr\left(\frac{\partial \hat{\gamma}(\mathbf{C})}{\partial \mathbf{C}}\dot{\mathbf{C}}\right) = 0 \tag{2.37}$$

The time-derivative of the right Cauchy-Green tensor $\mathbf{C}$ may be expressed in terms of the stretching tensor $\mathbf{D}$ as

$$\dot{\mathbf{C}} = 2\mathbf{F}^T\mathbf{D}\mathbf{F} \tag{2.38}$$

Thus, using the property of the trace operator ($tr(\mathbf{AB}) = tr(\mathbf{BA})$),

$$tr\left(\mathbf{F}\frac{\partial \gamma}{\partial \mathbf{C}}\mathbf{F}^T\mathbf{D}\right) = 0 \tag{2.39}$$

In the purely mechanical theory of constraints, it is assumed that the Cauchy stress tensor $\mathbf{T}$ is determined up to an arbitrary constraint response $\mathbf{N}$ arising from the constraint which does no work. The rate at which stresses do work, per unit volume, is expressed as the stress power (eq. 2.26). Hence, the stress power of $\mathbf{N}$ is equivalent to zero. Therefore, for all symmetric $\mathbf{D}$, it is given as

$$tr(\mathbf{ND}) = 0 \tag{2.40}$$

From the definition of the trace of two second-order tensors (see [9]), $\mathbf{N}$ must be orthogonal to all $\mathbf{D}$ that are orthogonal to $\mathbf{F}(\partial\gamma/\partial\mathbf{C})\mathbf{F}^T$, which may only be the case if $\mathbf{N}$ is a scalar multiple of $\mathbf{F}(\partial\gamma/\partial\mathbf{C})\mathbf{F}^T$:

$$\mathbf{N} = q\mathbf{F}\frac{\partial\gamma}{\partial\mathbf{C}}\mathbf{F}^T \tag{2.41}$$

For multiple internal constraints,

$$\mathbf{N} = \sum_{i=1}^{n} q_i\mathbf{F}\frac{\partial\gamma^i}{\partial\mathbf{C}}\mathbf{F}^T \tag{2.42}$$

Thus, the *extra stress* is given by

$$\mathbf{T}_E = \mathbf{T} + \mathbf{N} \tag{2.43}$$

Special Case: Incompressibility. With a suitably chosen reference configuration, for a motion described as isochoric (volume-preserving), the Jacobian is equal to unity, J=$det\mathbf{C}$=1. A corresponding internal constraint (see [9, 69]) for incompressible materials may then be defined as

$$det\mathbf{C} - 1 = 0 \tag{2.44}$$

Using the rule for differentiating a determinant and the property of the inverse of a second-order tensor (see [72]), the extra stress in eq. 2.43 becomes

$$\mathbf{T}_E = \mathbf{T} + p\mathbf{1} \tag{2.45}$$

where p has replaced q in eq. 2.41 as an indeterminate Lagrange multiplier.

2.1.6 Hyperelastic materials

For a hyperelastic material (see [9, 72]), in a purely mechanical theory, it is assumed that the stress power (eq. 2.26) can be written in terms of a scalar function called the strain energy density or the stored energy per unit mass Σ:

$$\mathbf{T} : \mathbf{D} = \rho\dot{\Sigma} \tag{2.46}$$

For an isothermal process, the strain energy function Σ is equivalent to the free energy Ψ in eq. 2.35.

The strain energy function must be objective, so following the principle of material frame-indifference (see [9]), and using the right Cauchy-Green tensor $\mathbf{C}$ (eq. 2.9), Σ may be given as

$$\Sigma = \tilde{\Sigma}(\mathbf{C}) \tag{2.47}$$

Thus, the gradient of the free energy function may be written as

$$\left(\frac{\partial\hat{\Sigma}(\mathbf{F})}{\partial\mathbf{F}}\right)^T = 2\frac{\partial\tilde{\Sigma}(\mathbf{C})}{\partial\mathbf{C}}\mathbf{F}^T \tag{2.48}$$

The strain-energy function can be given per unit volume in the reference configuration $\boldsymbol{\kappa}_0$ as

$$W = \hat{W}(\mathbf{C}) = \rho\tilde{\Sigma}(\mathbf{C}) \tag{2.49}$$

so the Cauchy stress tensor (eq. 2.35) becomes

$$\mathbf{T} = 2\mathbf{F}\frac{\partial\hat{W}(\mathbf{C})}{\partial\mathbf{C}}\mathbf{F}^T \tag{2.50}$$

An alternative stress measure is the first Piola-Kirchoff stress tensor, which may be related to the Cauchy stress tensor above (see [9]) by

$$\mathbf{P} = J\mathbf{T}\mathbf{F}^{-T} \tag{2.51}$$

where J is given by eq. 2.6 and eq. 2.19.

This stress measure **P** is similar to "engineering" stress [41], and represents the state of stress in relation to the reference configuration $\boldsymbol{\kappa}_0$. Assuming incompressibility (eq. 2.45), eq. 2.50 may be rewritten as

$$\mathbf{T} = -p\mathbf{1} + 2\mathbf{F}\frac{\partial \hat{W}(\mathbf{C})}{\partial \mathbf{C}}\mathbf{F}^T \tag{2.52}$$

2.1.7 Invariants

A scalar-valued tensor function f of symmetric second order tensor variables $\mathbf{A}_\tau$ is isotropic if

$$f = \hat{f}\left(\mathbf{A}_1, ..., \mathbf{A}_l\right) = \hat{f}\left(\mathbf{Q}\mathbf{A}_1\mathbf{Q}^T, ..., \mathbf{Q}\mathbf{A}_l\mathbf{Q}^T\right) \tag{2.53}$$

for all orthogonal **Q** and all $\mathbf{A}_\tau$ in the domain of the definition of f. The scalar-valued isotropic tensor function f is called an orthogonal simultaneous invariant of the tensor-valued variables $\mathbf{A}_\tau$.

For the case of one variable, the principle invariants of a second-order tensor variable **A**, given as $I_k = \hat{I}_k(\mathbf{A})$, $k = 1, 2, ..., n$, are defined as the coefficients of the polynomial in ζ [9]:

$$det(\zeta\mathbf{1} + \mathbf{A}) = \zeta^n + \hat{I}_1(\mathbf{A})\zeta^{n-1} + ... + \hat{I}_{n-1}(\mathbf{A})\zeta + \hat{I}_n(\mathbf{A}) \tag{2.54}$$

In particular:

$$\hat{I}_1(\mathbf{A}) = tr\mathbf{A} \tag{2.55}$$

$$\hat{I}_2(\mathbf{A}) = \frac{1}{2}\left[(tr\mathbf{A})^2 - tr(\mathbf{A}^2)\right] \tag{2.56}$$

$$\hat{I}_n(\mathbf{A}) = \frac{1}{6}\left[tr(\mathbf{A})^3 - 3tr(\mathbf{A})tr(\mathbf{A}^2) + 2tr(\mathbf{A}^3)\right] = det(\mathbf{A}) \tag{2.57}$$

Other invariants of $\mathbf{A}$, which are not independent of the principal invariants, are defined as the *moments* of $\mathbf{A}$:

$$\bar{I}_n(\mathbf{A}) = tr(\mathbf{A}^n) \tag{2.58}$$

Following the description in [78] and [9], the scalar-valued tensor function f is given as a simultaneous invariant of the τ symmetric tensors $\mathbf{A}_1, ..., \mathbf{A}_\tau$. If the proper numbers of $\mathbf{A}_1$ are distinct and the off-diagonal elements of $\mathbf{A}_2$ are non-zero if an orthonormal basis is used relative to which $\mathbf{A}_1$ corresponds to a diagonal matrix, the equation

$$f = \hat{f}\,(\mathbf{A}_1, ..., \mathbf{A}_l) \tag{2.59}$$

(or, equivalently, eq. 2.53) can be expressed as a single-valued function of the 6τ-2 invariants:

$$\begin{array}{cccccc}
tr(\mathbf{A}_1) & tr(\mathbf{A}_1^2) & tr(\mathbf{A}_1^3) & tr(\mathbf{A}_2) & tr(\mathbf{A}_2^2) & tr(\mathbf{A}_2^3) \\
tr(\mathbf{A}_1\mathbf{A}_2) & tr(\mathbf{A}_1\mathbf{A}_2^2) & tr(\mathbf{A}_1^2\mathbf{A}_2) & tr(\mathbf{A}_1^2\mathbf{A}_2^2) & & \\
tr(\mathbf{A}_l) & tr(\mathbf{A}_1\mathbf{A}_l) & tr(\mathbf{A}_1^2\mathbf{A}_l) & & & \\
tr(\mathbf{A}_2\mathbf{A}_l) & tr(\mathbf{A}_1\mathbf{A}_2\mathbf{A}_l) & tr(\mathbf{A}_1^2\mathbf{A}_2\mathbf{A}_l) & & &
\end{array}$$

where l = 3,4,5...

For an arbitrary vector $\mathbf{a}_j$, introducing the tensor product $\mathbf{A}_j = \mathbf{a}_j \otimes \mathbf{a}_j$ (j=2,...,n), and using the identities $tr(\mathbf{a} \otimes \mathbf{a}) = \mathbf{a} \cdot \mathbf{a}$ and $tr(\mathbf{A}, \mathbf{b} \otimes \mathbf{c}) = \mathbf{b} \cdot \mathbf{A}\mathbf{c}$ the above may be given as

$$f = \hat{f}\,(\mathbf{A}_1, \mathbf{a}_2 \otimes \mathbf{a}_2, ..., \mathbf{a}_l \otimes \mathbf{a}_l) \tag{2.60}$$

with invariants

$$\begin{array}{cccccc}
\hat{I}_1(\mathbf{A}_1) & \hat{I}_2(\mathbf{A}_1) & \hat{I}_3(\mathbf{A}_1) & \mathbf{a}_2 \cdot \mathbf{a}_2 & (\mathbf{a}_2 \cdot \mathbf{a}_2)^2 & (\mathbf{a}_2 \cdot \mathbf{a}_2)^3 \\
\mathbf{a}_2 \cdot \mathbf{A}_1\mathbf{a}_2 & (\mathbf{a}_2 \cdot \mathbf{a}_2)(\mathbf{a}_2 \cdot \mathbf{A}_1\mathbf{a}_2) & \mathbf{a}_2 \cdot \mathbf{A}_1^2\mathbf{a}_2 & (\mathbf{a}_2 \cdot \mathbf{a}_2)(\mathbf{a}_2 \cdot \mathbf{A}_1^2\mathbf{a}_2) & & \\
\mathbf{a}_l \cdot \mathbf{a}_l & \mathbf{a}_l \cdot \mathbf{A}_1\mathbf{a}_l & \mathbf{a}_l \cdot \mathbf{A}_1^2\mathbf{a}_l & & & \\
(\mathbf{a}_2 \cdot \mathbf{a}_l)^2 & (\mathbf{a}_2 \cdot \mathbf{a}_l)(\mathbf{a}_2 \cdot \mathbf{A}_1\mathbf{a}_l) & (\mathbf{a}_2 \cdot \mathbf{a}_l)(\mathbf{a}_2 \cdot \mathbf{A}_1^2\mathbf{a}_l) & & &
\end{array}$$

where the first three invariants of eq. 2.59 are given above in the terms of the definitions of the principle invariants in eqs. 2.55, 2.56, and 2.57, with $n = 3$, respectively. If the vector $\mathbf{a}_j$ is given as a unit vector $\mathbf{i}_j$, the above becomes

$$f = \hat{f}\left(\mathbf{A}_1, \mathbf{i}_2 \otimes \mathbf{i}_2, ..., \mathbf{i}_l \otimes \mathbf{i}_l\right) \tag{2.61}$$

with invariants defined as

$$\begin{array}{lll} \hat{I}_1(\mathbf{A}_1) & \hat{I}_2(\mathbf{A}_1) & \hat{I}_3(\mathbf{A}_1) \\ \mathbf{i}_2 \cdot \mathbf{A}_1 \mathbf{i}_2 & \mathbf{i}_2 \cdot \mathbf{A}_1^2 \mathbf{i}_2 & \\ \mathbf{i}_l \cdot \mathbf{A}_1 \mathbf{i}_l & \mathbf{i}_l \cdot \mathbf{A}_1^2 \mathbf{i}_l & \\ (\mathbf{i}_2 \cdot \mathbf{i}_l)^2 & (\mathbf{i}_2 \cdot \mathbf{A}_1 \mathbf{i}_l) & (\mathbf{i}_2 \cdot \mathbf{A}_1^2 \mathbf{i}_l) \end{array}$$

Using the property $\mathbf{a} \cdot \mathbf{B}^T \mathbf{b} = \mathbf{b} \cdot \mathbf{B}\mathbf{a}$, for arbitrary vectors $\mathbf{a}$ and $\mathbf{b}$ and an arbitrary second-order tensor $\mathbf{B}$, and noting the symmetry of $\mathbf{A}_1$, the above invariants may be given in the alternate forms:

$$\hat{I}_1(\mathbf{A}_1) = tr\mathbf{A}_1 \tag{2.62}$$

$$\hat{I}_2(\mathbf{A}_1) = \frac{1}{2}\left[(tr\mathbf{A}_1)^2 - tr(\mathbf{A}_1^2)\right] \tag{2.63}$$

$$\hat{I}_3(\mathbf{A}_) = \frac{1}{6}\left[tr(\mathbf{A}_1)^3 - 3tr(\mathbf{A}_1)tr(\mathbf{A}_1^2) + 2tr(\mathbf{A}_1^3)\right] = det(\mathbf{A}_1) \tag{2.64}$$

$$\hat{I}_4(\mathbf{A}_1, \mathbf{i}_2) = \mathbf{i}_2 \cdot \mathbf{A}_1 \mathbf{i}_2 \tag{2.65}$$

$$\hat{I}_5(\mathbf{A}_1, \mathbf{i}_2) = \mathbf{i}_2 \cdot \mathbf{A}_1^2 \mathbf{i}_2 \tag{2.66}$$

$$\hat{I}_4(\mathbf{A}_1, \mathbf{i}_l) = \mathbf{i}_l \cdot \mathbf{A}_1 \mathbf{i}_l \tag{2.67}$$

$$\hat{I}_5(\mathbf{A}_1, \mathbf{i}_l) = \mathbf{i}_l \cdot \mathbf{A}_1^2 \mathbf{i}_l \tag{2.68}$$

$$\hat{I}_6(\mathbf{i}_2, \mathbf{i}_l) = \mathbf{i}_2 \cdot \mathbf{i}_l \tag{2.69}$$

$$\hat{I}_7(\mathbf{A}_1, \mathbf{i}_2, \mathbf{i}_l) = \frac{1}{2}\left[(\mathbf{i}_2 \cdot \mathbf{A}_1 \mathbf{i}_l) + (\mathbf{i}_l \cdot \mathbf{A}_1 \mathbf{i}_2)\right] \tag{2.70}$$

2.1.8 Internal variables

In certain classes of materials, the internal processes are dissipative. Thus, internal variables, given here for example by the second order tensors $\boldsymbol{\xi}_\alpha$, $\alpha = 1, 2, ..., m$, are introduced [72]. In this case, the strain-energy function (eq. 2.32) may given as a function of the deformation gradient tensor and these internal variables:

$$\Psi \equiv \hat{\Psi}(\mathbf{F}, \boldsymbol{\xi}_1, \boldsymbol{\xi}_2, ..., \boldsymbol{\xi}_m) \tag{2.71}$$

By using the chain rule, the time derivative of the free energy is determined:

$$\dot{\Psi} = \frac{\partial \hat{\Psi}(\mathbf{F}, \boldsymbol{\xi}_\alpha)}{\partial(\mathbf{F})} : \dot{\mathbf{F}} + \sum_{\alpha=1}^{m} \frac{\partial \hat{\Psi}(\mathbf{F}, \boldsymbol{\xi}_\alpha)}{\partial \boldsymbol{\xi}_\alpha} : \dot{\boldsymbol{\xi}}_\alpha \tag{2.72}$$

In a similar manner as was used above to derive eq. 2.34 in Section 2.1.4.5, using eq. 2.72, the Clausius-Duhem inequality may be re-written as

$$\left(\mathbf{T} - \rho \frac{\partial \hat{\Psi}(\mathbf{F}, \boldsymbol{\xi}_\alpha)}{\partial \mathbf{F}} \mathbf{F}^T \right) : \mathbf{L} - \rho \sum_{\alpha=1}^{m} \frac{\partial \hat{\Psi}(\mathbf{F}, \boldsymbol{\xi}_\alpha)}{\partial \boldsymbol{\xi}_\alpha} : \dot{\boldsymbol{\xi}}_\alpha \geq 0 \tag{2.73}$$

Again, using the Coleman-Noll procedure (see [77] and [72]), the Cauchy stress tensor may be given as

$$\mathbf{T} = \rho \frac{\partial \hat{\Psi}(\mathbf{F}, \boldsymbol{\xi}_\alpha)}{\partial(\mathbf{F})} \mathbf{F}^T \tag{2.74}$$

and the second term in eq. 2.73 is given by

$$\rho \sum_{\alpha=1}^{m} \frac{\partial \hat{\Psi}(\mathbf{F}, \boldsymbol{\xi}_\alpha)}{\partial \boldsymbol{\xi}_\alpha} : \dot{\boldsymbol{\xi}}_\alpha \geq 0 \tag{2.75}$$

which represents the dissipation during a thermodynamic process. Note that Ψ may be expressed per unit volume, as W, by using eq. 2.49.

2.2 SPECIAL CASES OF THE STRAIN ENERGY FUNCTION

A de-coupled form of W will be presented in the following chapters, and in subsequent chapters, the limitations will be discussed for isotropic and anisotropic (aeolotropic) materials, as well as for alternate expressions for the strain energy function that include additional scalar, vector, and tensor variables.

2.2.1 The De-Coupled Strain Energy Function

Without a loss in generality, the mechanical response of the tissue may be modeled by using an additive split, first introduced by [49], of the strain energy function into isotropic and anisotropic terms:

$$W = W_{iso} + W_{aniso} \tag{2.76}$$

Inserting eq. 2.76 into the Cauchy stress response for a perfectly elastic (ignoring viscoelasticity), homogeneous, incompressible material (eq. 2.52):

$$\mathbf{T} = -p\mathbf{1} + 2\mathbf{F}\frac{\partial W_{iso}}{\partial \mathbf{C}}\mathbf{F}^T + 2\mathbf{F}\frac{\partial W_{aniso}}{\partial \mathbf{C}}\mathbf{F}^T = -p\mathbf{1} + \mathbf{T}_{iso} + \mathbf{T}_{aniso} \tag{2.77}$$

by making use of eq. 2.49.

2.2.2 Isotropic hyperelastic materials

Consider an arbitrary point $\mathbf{X}$ in reference configuration. A rotation and translation of the reference configuration $\boldsymbol{\kappa}_0$ may be prescribed. Assume this body is translated by a vector $\mathbf{c}$ and rotated by an orthogonal tensor $\mathbf{Q}$ in the reference configuration $\boldsymbol{\kappa}_0$, according to

$$\mathbf{X}^* = \mathbf{c} + \mathbf{Q}\mathbf{X} \tag{2.78}$$

which describes a motion from configuration $\boldsymbol{\kappa}_0$ to $\boldsymbol{\kappa}_0^*$.

Now, a different motion $\mathbf{x} = \tilde{\boldsymbol{\chi}}^*(\mathbf{X}^*, t)$ moves a body in $\boldsymbol{\kappa}_0^*$ to the current configuration $\boldsymbol{\kappa}$, such that $\mathbf{x} = \hat{\boldsymbol{\chi}}(\mathbf{X}, t) = \tilde{\boldsymbol{\chi}}^*(\mathbf{X}^*, t)$. The deformation gradient tensor for this motion is given as

$$\mathbf{F} = \frac{\partial \hat{\boldsymbol{\chi}}(\mathbf{X}, t)}{\partial \mathbf{X}} = \frac{\partial \tilde{\boldsymbol{\chi}}^*(\mathbf{X}^*, t)}{\partial \mathbf{X}^*}\mathbf{Q} = \mathbf{F}^*\mathbf{Q} \tag{2.79}$$

so $\mathbf{C} = \mathbf{C}^* = \mathbf{Q}\mathbf{C}\mathbf{Q}^T$. A material is defined as isotropic relative to a reference configuration $\boldsymbol{\kappa}_0$ if the strain energy functions $\hat{W}_{iso}(\mathbf{C})$ and $\tilde{W}_{iso}(\mathbf{C}^*)$ are equivalent for all orthogonal tensors $\mathbf{Q}$:

$$W_{iso} = \bar{W}_{iso}(\mathbf{C}) = \tilde{\bar{W}}_{iso}(\mathbf{Q}\mathbf{C}\mathbf{Q}^T) \tag{2.80}$$

As defined in Section 2.1.7, the principle invariants of a second-order tensor variable $\mathbf{C}$, or $\mathbf{B}$, in three dimensions (n=3), are given, as in eq. 2.55, eq. 2.56, and eq. 2.64, respectively, as

$$I_{\mathbf{C}} = tr\mathbf{C} = I_{\mathbf{B}} = tr\mathbf{B} \tag{2.81}$$

$$II_{\mathbf{C}} = \frac{1}{2}\left[(tr\mathbf{C})^2 - tr(\mathbf{C}^2)\right] = II_{\mathbf{B}} = \frac{1}{2}\left[(tr\mathbf{B})^2 - tr(\mathbf{B}^2)\right] \tag{2.82}$$

$$III_{\mathbf{C}} = det(\mathbf{C}) = III_{\mathbf{B}} = det(\mathbf{B}) \tag{2.83}$$

The isotropic strain energy function W_{iso} is defined as a scalar-valued tensor function, which may be expressed as a set of three independent invariants of $\mathbf{C}$:

$$W_{iso} = \bar{W}_{iso}(\mathbf{C}) = W_{iso}(I_{\mathbf{C}}, II_{\mathbf{C}}, III_{\mathbf{C}}) \tag{2.84}$$

or as a function of the three independent invariants of $\mathbf{B}$:

$$W_{iso} = \bar{W}_{iso}(I_{\mathbf{B}}, II_{\mathbf{B}}, III_{\mathbf{B}}) \tag{2.85}$$

noting that the three invariants of the right and left Cauchy-Green tensors are identical.

Assuming W_{iso} has continuous derviatives with respect to the invariants of $\mathbf{C}$, by means of the chain rule,

$$\frac{\partial \bar{W}_{iso}(\mathbf{C})}{\partial \mathbf{C}} = \frac{\partial \bar{W}_{iso}(\mathbf{C})}{\partial I_{\mathbf{C}}}\frac{\partial I_{\mathbf{C}}}{\partial \mathbf{C}} + \frac{\partial \bar{W}_{iso}(\mathbf{C})}{\partial II_{\mathbf{C}}}\frac{\partial II_{\mathbf{C}}}{\partial \mathbf{C}} + \frac{\partial \bar{W}_{iso}(\mathbf{C})}{\partial III_{\mathbf{C}}}\frac{\partial III_{\mathbf{C}}}{\partial \mathbf{C}} \tag{2.86}$$

The derivatives of these invariants are given by (see [9, 72]):

$$\frac{\partial I_{\mathbf{C}}}{\partial \mathbf{C}} = \frac{\partial I_{\mathbf{B}}}{\partial \mathbf{B}} = \mathbf{1} \tag{2.87}$$

$$\frac{\partial II_{\mathbf{C}}}{\partial \mathbf{C}} = I_{\mathbf{C}}\mathbf{1} - \mathbf{C}^T = \frac{\partial II_{\mathbf{B}}}{\partial \mathbf{B}} = I_{\mathbf{B}}\mathbf{1} - \mathbf{B}^T \tag{2.88}$$

$$\frac{\partial III_{\mathbf{C}}}{\partial \mathbf{C}} = III_{\mathbf{C}}\mathbf{C}^{-T} = \frac{\partial III_{\mathbf{B}}}{\partial \mathbf{B}} = III_{\mathbf{B}}\mathbf{B}^{-T} \tag{2.89}$$

Inserting eq. 2.86, 2.87, 2.88, and 2.89 into eq. 2.77 gives

$$\mathbf{T}_{iso} = 2\left(\frac{\partial W_{iso}}{\partial I_{\mathbf{B}}} + I_{\mathbf{B}}\frac{\partial W_{iso}}{\partial II_{\mathbf{B}}}\right)\mathbf{B} - 2\frac{\partial W_{iso}}{\partial II_{\mathbf{B}}}\mathbf{B}^2 \tag{2.90}$$

From the Cayley-Hamilton theorem (see [72]), any tensor satisfies its own characteristic equation:

$$\mathbf{B}^3 - I_{\mathbf{B}}\mathbf{B}^2 + II_{\mathbf{B}}\mathbf{B} - III_{\mathbf{B}}\mathbf{1} = \mathbf{0} \tag{2.91}$$

Multiplying the above by $\mathbf{B}^{-1}$ and inserting into eq. 2.90, noting eq. 2.77, gives

$$\mathbf{T}_{iso} = 2\frac{\partial W_{iso}}{\partial I_{\mathbf{B}}}\mathbf{B} - 2\frac{\partial W_{iso}}{\partial II_{\mathbf{B}}}\mathbf{B}^{-1} \tag{2.92}$$

2.2.2.1 Functional forms of the strain energy function A large number of functional forms of the strain energy function have been considered for isotropic materials, and new models are being continuously developed. For example, for isotropic materials with a mechanical response that is typically linear (even for large deformations), the multi-parameter model of Rivlin and Saunders may be applied, or special cases of this model,

the two parameter Mooney-Rivlin and the single parameter neo-Hookean models, may be utilized to capture the behavior. The isotropic strain energy functions W_{iso} used in this work are of three different general forms: Exponential, Mooney-Rivlin, and Ogden.

An Exponential strain energy function (SEF) [79] is given by

$$W_{iso} = \frac{a}{b}\left[e^{\beta b(I_{\mathbf{B}}-3)^{\beta}} - 1\right] \tag{2.93}$$

A special case of the exponential function is formulated by setting $b \equiv 1$ and $\beta \equiv 1$:

$$W_{iso} = a\left[e^{(I_{\mathbf{B}}-3)} - 1\right] \tag{2.94}$$

The Mooney-Rivlin SEF [9] is given as:

$$W_{iso} = \frac{1}{2}\mu\left[\left(\frac{1}{2}+\beta\right)(I_{\mathbf{B}}-3) + \left(\frac{1}{2}-\beta\right)(II_{\mathbf{B}}-3)\right] \tag{2.95}$$

where $\mu > 0$ and $\beta \in [-\frac{1}{2}, \frac{1}{2}]$, and the neo-Hookean SEF, a special case ($\beta = \frac{1}{2}$) of the Mooney-Rivlin, is given as

$$W_{iso} = \frac{\mu}{2}(I_{\mathbf{B}}-3) \tag{2.96}$$

Note that equation (eq. 2.95) is a special case of that considered by Rivlin and Saunders [47],

$$W_{iso} = \sum_{i=0}^{n}\sum_{j=0}^{m} C_{ij}(I_1-3)^i(I_2-3)^j \tag{2.97}$$

where $C_{00} \equiv 0$, $C_{11} \equiv 0$, $n \equiv 1$, $m \equiv 1$, $C_{10} \equiv \frac{1}{2}\mu(\frac{1}{2}+\beta)$ and $C_{01} \equiv \frac{1}{2}\mu(\frac{1}{2}-\beta)$. Clearly, eq. 2.96 is obtained by setting $\beta \equiv \frac{1}{2}$.

Additionally, in 2004, Zulliger et al. [80], proposed a slight modification of the neo-Hookean strain energy function:

$$W_{iso} = \frac{\mu}{2}(I_{\mathbf{B}} - 3)^n \tag{2.98}$$

where n = 1.50. Note that if $n = 1.00$, the neo-Hookean form is recovered. Also, Watton et al., 2009, compared n values of 1.25 and 1.75 with the previous two cases [81]. Furthermore, n may be used as a parameter obtained by a least-squares fit.

Ogden [82][83][70] postulated the strain energy as a function of principal stretches $\lambda_a, a = 1, 2, 3$ (see [72]):

$$W_{iso} = \hat{W}_{iso}(\lambda_1, \lambda_2, \lambda_3) = \sum_{p=1}^{N} \frac{\mu_p}{\alpha_p}(\lambda_1^{\alpha_p} + \lambda_2^{\alpha_p} + \lambda_3^{\alpha_p} - 3) \tag{2.99}$$

Assuming incompressiblity, $J = \lambda_1\lambda_2\lambda_3 \equiv 1$, and axisymmetric deformation, $\lambda_2 = \lambda_3$, with $N \equiv 1$ gives

$$W_{iso} = \frac{\mu_1}{\alpha_1}(\lambda_1^{\alpha_1} + 2\lambda_1^{-\frac{\alpha_1}{2}} - 3) \tag{2.100}$$

2.2.3 Anisotropic materials

The fibrous architecture of the material considered here gives rise to the anisotropic mechanism. A single fiber is considered in a representative volume element (RVE) at an arbitrary material point in the body. Unit direction vectors may be assigned to each fiber, and the orientations of these directions are distributed in three-dimensional space. Here, the direction of a fiber in configuration $\boldsymbol{\kappa}_0$ is denoted with a unit vector $\mathbf{m}_0 = \hat{\mathbf{m}}_0(\mathbf{X})$, defined at point $\mathbf{X}$ in the reference configuration.

In this section, the general case for materials with multiple fiber families will be presented (Section 2.2.3.1), followed by a description of distributed fiber models (Section 2.2.3.2), which are then specialized to the case of conic splay (Section 2.2.3.3), in which

the fiber orientation distribution is independent of a given Euler angle, fan splay (Section 2.2.3.4), in which the fiber orientation dispersion is confined to a single plane, and transverse isotropy (Section 2.2.3.5), in which a single preferred fiber orientation is given.

Finally, fiber recruitment models are described in Section 2.2.3.6. Here, the forms of a fiber distribution function are given, allowing the direct inclusion of various amounts of measured fiber structural data.

2.2.3.1 Materials with Multiple Fiber Families For the case in which multiple fiber families are given, the anisotropic strain energy function (eq. 2.76) may again be given as a function of the invariants in Section 2.1.7, but now, for eq. 2.61, with those listed in eq.2.62- 2.70, and again, $\mathbf{A}_1$ is replaced with the left Cauchy-Green tensor $\mathbf{C}$ and $\mathbf{i}_l$ by $\mathbf{m}_0^{(j)}$:

$$W_{aniso} = \hat{W}_{aniso}\left(\mathbf{C}, \mathbf{m}_0^{(j)} \otimes \mathbf{m}_0^{(j)}\right) \tag{2.101}$$

or by

$$W_{aniso} = \hat{W}_{aniso}\left(IV^{(j)}, V^{(j)}, IV^{(j)}, VII^{(j)}\right) \tag{2.102}$$

where $j = 1, 2, ..., N$ is the fiber family, and $IV^{(j)}$ - $VII^{(j)}$ are given by [72, 84]:

$$IV^{(j)} = \hat{IV}(\mathbf{C}, \mathbf{m}_0^{(j)}) = \hat{I}_4(\mathbf{C}, \mathbf{m}_0^{(j)}) = \mathbf{C} : \mathbf{m}_0^{(j)} \otimes \mathbf{m}_0^{(j)} = \mathbf{m}_0^{(j)} \cdot \mathbf{C}\mathbf{m}_0^{(j)} \tag{2.103}$$

$$V^{(j)} = \hat{V}(\mathbf{C}, \mathbf{m}_0^{(j)}) = \hat{I}_5(\mathbf{C}, \mathbf{m}_0^{(j)}) = \mathbf{m}_0^{(j)} \cdot \mathbf{C}^2\mathbf{m}_0^{(j)} \tag{2.104}$$

$$VI^{(j)} = \hat{VI}(\mathbf{m}_0^{(j-1)}, \mathbf{m}_0^{(j)}) = \hat{I}_6(\mathbf{m}_0^{(j-1)}, \mathbf{m}_0^{(j)}) = \left(\mathbf{m}_0^{(j-1)} \cdot \mathbf{m}_0^{(j)}\right)^2 \tag{2.105}$$

$$VII^{(j)} = \hat{I}_7(\mathbf{C}, \mathbf{m}_0^{(j-1)}, \mathbf{m}_0^{(j)}) = \frac{1}{2}\left[(\mathbf{m}_0^{(j-1)} \cdot \mathbf{C}\mathbf{m}_0^{(j)}) + (\mathbf{m}_0^{(j)} \cdot \mathbf{C}\mathbf{m}_0^{(j-1)})\right] \tag{2.106}$$

Note that when $j = 1$, VI and VII are undefined, and for the case of $N = 1$, the case of transverse isotropy (see Section 2.2.3.5) is obtained.

It is common to define the strain energy function above as only a function of the fourth invariant, $IV^{(j)}$, so that

$$W_{aniso} = \hat{W}_{aniso}\left(IV^{(j)}\right) = \hat{W}_{aniso}\left(IV^{(1)}, IV^{(2)}, ..., IV^{(N)}\right) \tag{2.107}$$

2.2.3.2 Distributed Fiber Models Rather than considering the materials to have individual fiber orientations that must be accounted for by functional forms that include a finite number (N) of invariants $IV^{(j)}$, the anisotropic material may be assumed to consist of continuously distributed fibers (see [85, 67]). In this case, an *orientation distribution function*, $\tilde{\rho}(\mathbf{m}_0)$, is introduced [56], which characterizes the three-dimensional dispersion of fiber angles over the unit sphere, for a given family of fibers in the reference configuration, $\boldsymbol{\kappa}_0$.

Therefore, the anisotropic portion of the de-coupled strain energy function given in eq. 2.107 may be replaced by

$$W_{aniso} = \hat{W}_{aniso}\left(IV^{(j)}\right) = \hat{W}_f\left(\lambda_f^2\right) = W_f \tag{2.108}$$

where λ_f^2 is the stretch of the tissue in the direction of a given fiber ensemble, defined as

$$\lambda_f^2 = \tilde{IV}(\mathbf{C}, \tilde{\rho}(\mathbf{m}_0)) \tag{2.109}$$

If an arbitrary material point in the body is identified by a vector $\mathbf{0}$, defined relative to global orthonormal base vectors $(\mathbf{E}_1, \mathbf{E}_2, \mathbf{E}_3)$, an arbitrary fiber direction for material point $\mathbf{0}$ can then be represented with respect to Euler angles ϕ and θ, defined relative to local rectilinear co-ordinates with unit base vectors $(\mathbf{e}_1, \mathbf{e}_2, \mathbf{e}_3)$ (Fig. 5),

$$\mathbf{m}_0 = \hat{\mathbf{m}}_0(\theta, \phi) = \cos(\theta)\mathbf{e}_1 + \sin(\theta)\cos(\phi)\mathbf{e}_2 + \sin(\theta)\sin(\phi)\mathbf{e}_3. \tag{2.110}$$

The inclination angle θ is measured from the zenith angle defined by $\mathbf{e}_1$, and the azimuthal angle ϕ is measured from a fixed reference direction $\mathbf{e}_2$ orthogonal to the zenith in the $\mathbf{e}_2 \otimes \mathbf{e}_3$ plane (see [85, 67]).

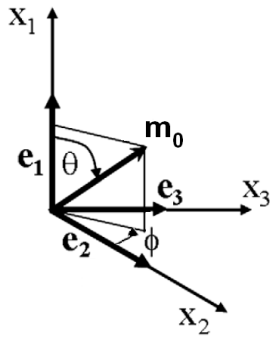

Figure 5: The unit vector $\mathbf{m}_0$ which represents the generic fiber orientation in the reference configuration in terms of the polar angles relative to rectangular Cartesian co-ordinates

The orientation can be defined as a function of $\mathbf{m}_0$ or Euler angles ϕ, θ with $\theta \in [0, \pi]$ and $\phi \in [0, 2\pi]$ (Fig. 5), so the probability density function may then be given by $\rho = \tilde{\rho}(\mathbf{m}_0) = \hat{\rho}(\theta, \phi)$.

$$\lambda_f^2 = I\tilde{V}(\mathbf{C}, (\theta, \phi)) = \begin{bmatrix} \cos(\theta) \\ \sin(\theta)\cos(\phi) \\ \sin(\theta)\sin(\phi) \end{bmatrix} \cdot \begin{bmatrix} C_{11} & C_{12} & C_{13} \\ C_{21} & C_{22} & C_{23} \\ C_{31} & C_{32} & C_{33} \end{bmatrix} \begin{bmatrix} \cos(\theta) \\ \sin(\theta)\cos(\phi) \\ \sin(\theta)\sin(\phi) \end{bmatrix}$$

Using the normalization condition,

$$1 = \frac{1}{4\pi} \int_0^{2\pi} \int_{-\pi/2}^{\pi/2} \hat{\rho}(\theta, \phi)\ \cos\theta \, d\theta \, d\phi \tag{2.111}$$

and defining $w_f = \hat{w}_f(\lambda_f^2)$ as the fiber strain energy function, representing the response of a fiber ensemble, the fiber strain energy function W_f (eq. 2.108) may be written as

$$W_f = \frac{1}{4\pi} \int_0^{2\pi} \int_{-\pi/2}^{\pi/2} \hat{w}_f(\lambda_f^2)\hat{\rho}(\theta, \phi)\ \cos\theta \, d\theta \, d\phi \tag{2.112}$$

Therefore, the anisotropic component of the Cauchy stress tensor (eq. 2.77) becomes

$$\mathbf{T}_{aniso} = 2\mathbf{F}\frac{\partial W_f}{\partial \mathbf{C}}\mathbf{F}^T \tag{2.113}$$

2.2.3.3 Conic Splay Assuming conic splay [85, 86] the fiber stretch is equivalent in any direction when θ is held constant and the generic unit vector for each fiber, $\mathbf{m}_0$, is rotated about ϕ (Fig. 6, left). Thus, the orientation distribution function $\hat{\rho}(\theta, \phi)$ is assumed independent of ϕ, and now given by $\bar{\rho}(\theta)$, so the normalization condition (eq. 2.111) is re-written as

$$1 = \frac{1}{2} \int_{-\pi/2}^{\pi/2} \bar{\rho}(\theta) \, \cos\theta \, d\theta \tag{2.114}$$

and eq. 2.112 becomes

$$W_f = \frac{1}{2} \int_{-\pi/2}^{\pi/2} \hat{w}_f(\lambda_f^2) \bar{\rho}(\theta) \cos\theta \, d\theta \tag{2.115}$$

2.2.3.4 Fan Splay Materials may be idealized as exhibiting a planar, or fan, splay of distributions confined to a single plane [87, 86].

To model the fibers as dispersed only in the plane of $\mathbf{e}_1 \otimes \mathbf{e}_2$, the angle ϕ, measured from the axis along $\mathbf{e}_2$ is set to zero, $\phi = 0$ (Fig. 6, right). Therefore, eq. 2.110 becomes

$$\mathbf{m}_{0,2D} = \hat{\mathbf{m}}_{0,2D}(\theta, \phi = 0) = \cos(\theta)\mathbf{e}_1 + \sin(\theta)\mathbf{e}_2 \tag{2.116}$$

The orientation distribution function is then given in two-dimensions, ρ=$\hat{\rho}_{2D}(\theta) = \rho_{2D}$, and for definiteness, a normalization condition in 2D, similar to that given for 3D in eq. 2.111, is introduced:

$$1 = \frac{1}{\pi} \int_{-\pi/2}^{\pi/2} \hat{\rho}_{2D}(\theta) \, d\theta. \tag{2.117}$$

and eq. 2.112 becomes

$$W_f = \frac{1}{\pi} \int_{-\pi/2}^{\pi/2} \hat{w}_f(\lambda_f^2) \hat{\rho}_{2D}(\theta) \, d\theta \tag{2.118}$$

2.2.3.5 Transversely Isotropic Materials When a material is reinforced by a single family of fibers with a single preferred orientation, it is considered transversely isotropic with respect to this preferred direction, where typically, the stiffness in this direction is much

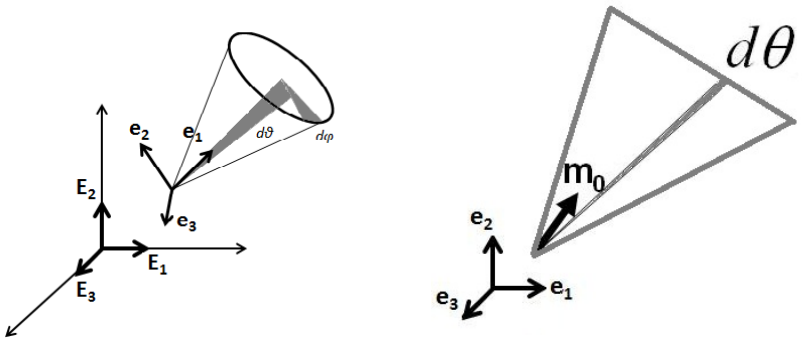

Figure 6: Schematics representing conic (left) and planar "fan" splay (right) fiber dispersion

greater than in those orthogonal to the fibers [72]. The anisotropic strain energy function (eq. 2.76) may thus be given as a function of the invariants in Section 2.1.7, for eq. 2.61 listed in eq.2.62- 2.66, with $l = 2$, and $\mathbf{A}_1$ replaced with the left Cauchy-Green tensor $\mathbf{C}$ and $\mathbf{i}_2$ by $\mathbf{m}_0$:

$$W_{aniso} = \hat{W}_{aniso}\left(\mathbf{C}, \mathbf{m}_0 \otimes \mathbf{m}_0\right) = \hat{W}_{aniso}\left(I\hat{V}(\mathbf{C}, \mathbf{m}_0), \hat{V}(\mathbf{C}, \mathbf{m}_0)\right) \tag{2.119}$$

where and IV and V by

$$I\hat{V}(\mathbf{C}, \mathbf{m}_0) = \hat{I}_4(\mathbf{C}, \mathbf{m}_0) = \mathbf{m}_0 \cdot \mathbf{C}\mathbf{m}_0 \tag{2.120}$$

$$\hat{V}(\mathbf{C}, \mathbf{m}_0) = \hat{I}_5(\mathbf{C}, \mathbf{m}_0) = \mathbf{m}_0 \cdot \mathbf{C}^2\mathbf{m}_0 \tag{2.121}$$

2.2.3.6 Fiber Recruitment In a given representative volume element (RVE), fibers display a distribution of waviness or "crimp" so that they are recruited over a range of stretch values. As in [56], the fibers are assumed to be undulated and thus bear no load until they are straightened.

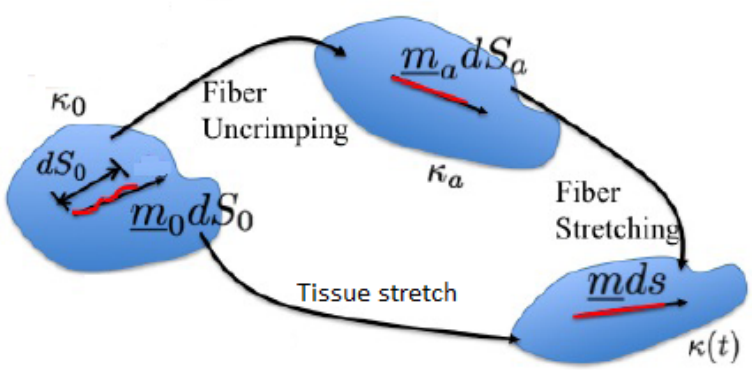

Figure 7: Schematic of reference configurations and notation used for fiber recruitment kinematics.

Kinematics of fiber recruitment A body in its original configuration denoted $\boldsymbol{\kappa}_0$ may be deformed into the current configuration $\boldsymbol{\kappa}$. To model fiber recruitment, utilizing a multi-mechanism constitutive equation, developed to model the recruitment of collagen fibers [61, 2, 64], an intermediate configuration $\boldsymbol{\kappa}_a$ is introduced (Fig. 7). The mapping from it to the original configuration represented by the deformation gradient tensor $\mathbf{F}_{ao}$ and from the current to this intermediate configuration by $\mathbf{F}_{ca}$. Relationships between the tensors were given by standard techniques, and the right Cauchy stress tensors computed by $\mathbf{C}_{co} = \mathbf{F}_{co}^T \mathbf{F}_{co}$, $\mathbf{C}_{ao} = \mathbf{F}_{ao}^T \mathbf{F}_{ao}$, and $\mathbf{C}_{ca} = \mathbf{F}_{ca}^T \mathbf{F}_{ca}$.

Utilizing the multi-mechanism approach, the configuration in which a fiber is recruited to bear load (become activated) is denoted as $\boldsymbol{\kappa}_a$ and a unit vector $\mathbf{m}_a$ denotes its direction in $\boldsymbol{\kappa}_a$. The current configuration is denoted as $\boldsymbol{\kappa}$ and a unit vector $\mathbf{m}$ denotes the direction of a fiber in $\boldsymbol{\kappa}$. Under an affine transformation, an infinitesimal material element $\mathbf{m}\, ds$ in the current configuration $\boldsymbol{\kappa}$ may be mapped back to a material element $\mathbf{m}_0\, dS_0$ in the reference configuration $\boldsymbol{\kappa}_0$, where $\mathbf{m}_0$ is also a unit vector, and these may be mapped to the intermediate configuration represented by an infinitesimal material element $\mathbf{m}_a\, dS_a$. These material elements are related through

$$\mathbf{m}\, ds = \mathbf{F}_{ca}\mathbf{m}_a\, dS_a = \mathbf{F}_{co}\, \mathbf{m}_0\, dS_0 = (\mathbf{F}_{ca}\mathbf{F}_{ao})\, \mathbf{m}_0\, dS_0 \tag{2.122}$$

Defining $\lambda_f = ds/dS_0$ and the "true" fiber stretch $\lambda_t = ds/dS_a$, it then follows that

$$\lambda_t = \frac{\lambda_f}{\lambda_a} \tag{2.123}$$

where λ_f can be obtained through eq. 2.109 and eq. 2.103, and the activation stretch is defined as λ_a. The distribution of λ_a for an arbitrary RVE is treated as a material property of the fiber reinforced material and may be measured directly. The approach for modeling the distribution of the recruitment stretch is described in the next section.

Distribution of fiber recruitment The strain energy function of a single fiber when straight, $\hat{w}_f^*(\lambda_t^2)$, is given as a function of the "true" stretch λ_t, which is related to the overall tissue stretch in this fiber direction, λ_f, by Eq. 2.123 [67]. Following Lanir, the recruitment distribution of an entire fiber ensemble is modeled with a recruitment probability distribution function (PDF) [67], which is represented here as $\hat{d}_1(\lambda_a)$. This function is defined so that over the range of stretch between λ_a and $\lambda_a + d\lambda_a$, the fraction of all the fibers in the given ensemble that become straight at a given tissue stretch in the fiber ensemble direction are represented by $\hat{d}_1(\lambda_a)d\lambda_a$. Therefore, the strain energy potential of the whole fiber ensemble is given by the sum of strain energy potentials of the individual fibers $\hat{d}_1(\lambda_a)\hat{w}_f^*(\lambda_t)d\lambda_a$, as

$$w_f = \hat{w}_f(\lambda_f^2) = \int_1^{\lambda_f} \hat{d}_1(\lambda_a)\hat{w}_f^*\left(\frac{\lambda_f^2}{\lambda_a^2}\right) d\lambda_a. \tag{2.124}$$

2.2.4 Modeling Damage

To model isotropic damage, the approach using internal variable is taken (See Section 2.1.8). This damage is assumed to be a result of the loss of the "isotropic" portion of the strain energy. For an incompressible, homogeneous, hyperelastic solid, the isotropic strain-energy function per unit volume may be defined as a function of the deformation gradient tensor and the internal (scalar) variable d_0 which represents the scalar isotropic damage parameter. Using eq. 2.48, eq. 2.49, and eq. 2.71, the first term, W_{iso}, on the right-hand side of eq. 2.76 becomes

$$W_{iso} = \hat{W}_{iso}(\mathbf{C}, d_0) \tag{2.125}$$

where the single internal variable $\boldsymbol{\xi}_\alpha$ (α = 1) is given by the scalar damage parameter d_0, so the dissipation (eq. 2.75) is given by

$$\frac{\partial \hat{W}_{iso}(\mathbf{C}, d_0)}{\partial d_0} \dot{d}_0 \geq 0 \tag{2.126}$$

A particular form of the strain energy function may be given by

$$\hat{W}_{iso}(\mathbf{C}, d_0) = (1 - d_0)\hat{W}_0(\mathbf{C}) \tag{2.127}$$

where $\hat{W}_0(\mathbf{C})$ is defined as the effective (isotropic) strain energy function.

By restricting this formulation to the isotropic case, the objectivity requirements (frame-indifference) [9] must be met: $\hat{W}_0(\mathbf{Q}\mathbf{C}\mathbf{Q}^T) = \hat{W}_0(\mathbf{C})$, where $\mathbf{Q}$ is an arbitrary orthogonal tensor. As in [66], the thermodynamic force which drives the damage evolution may be defined as $f = \partial \hat{W}_{iso}(\mathbf{C}, d_0)/\partial d_0 = \hat{W}_0(\mathbf{C})$, so eq. 2.126 reduces to

$$f \dot{d}_0 \geq 0 \tag{2.128}$$

The time derivative of the thermodynamic damage evolution force may be computed directly as

$$\dot{f} = \dot{W}_{iso} = \frac{\partial \hat{W}_{iso}(\mathbf{C}, d_0)}{\partial \mathbf{C}} : \dot{\mathbf{C}} = \frac{1}{2} J \mathbf{F}^{-1} \mathbf{T}_{iso} \mathbf{F}^{-T} : (\dot{\mathbf{F}}^T \mathbf{F} + \mathbf{F}^T \dot{\mathbf{F}}) \tag{2.129}$$

or

$$\dot{f} = J \mathbf{T}_{iso} : \mathbf{D} \tag{2.130}$$

by using the relevant tensor properties [72] and applying incompressibility ($J = 1$).

Here we only consider a Mullins-type *discontinuous* damage evolution, assumed to occur only within the first cycle of a strain-controlled loading process, with no damage contribution from additional strain cycles below a maximum effective strain energy. The scalar isotropic damage function is thus expressed as

$$d_0 = \hat{d}_0 \left(\alpha(t) \right)$$

where $d_0 : \Re_+ \rightarrow \Re_+$ is a monotonically increasing smooth function with properties $\hat{d}_0(0) = 0$ and $\hat{d}_0(\infty) \in [0, 1]$, considered as a shape function which relates the damage variable d_0 to the new variable α which describes the discontinuous damage:

$$\alpha = \hat{\alpha}(t) = max_{s \in [0,t]} \sqrt{2 W_0} \tag{2.131}$$

where α is defined as the maximum thermodynamic "force" or the maximum effective isotropic strain energy which has been achieved in the history interval [0,t].

The evolution of equation (2.131) is given by

$$\dot{\alpha} = \begin{cases} \dot{f} = \mathbf{T}_{iso} : \mathbf{D} & if \quad f - \alpha = 0 \ \ \& \ \ \dot{f} > 0 \\ 0 \qquad otherwise \end{cases}$$

Since only quasi-static loading is prescribed, all time and velocity affects are ignored, assuming that damage occurs after the tissue has been extended to a critical level of effective strain energy. From previous work [2], the form of the scalar isotropic damage function d_0 may be given as

$$\hat{d}_0(\alpha) = 1 - \frac{1 - e^{c(\frac{\alpha_f - \alpha}{\alpha_s})}}{1 - e^{c(\frac{\alpha_f}{\alpha_s} - 1)}} \tag{2.132}$$

where α_f is the final effective isotropic strain energy at total loss of the isotropic response, α_s is the starting effective isotropic strain energy at which the isotropic response initially becomes damaged, and a is a fitting parameter.

2.3 SOLUTION OF ISOTHERMAL BOUNDARY VALUE PROBLEMS

In this section, isothermal theories for the quasi-static deformation of hyperelastic materials were applied to solve boundary value problems, including planar biaxial tension, uniaxial tension, and inflation of a thick-walled cylinder. Under the isothermal assumption, the mechanical equations were de-coupled from the thermal equations in eq. 2.46. Therefore the balance of energy (Section 2.1.4.4) and the entropy relation (Section 2.1.4.5) led to eq. 2.46. The specific forms of the strain energy function per unit volume were given for W in this equation (using eq. 2.49). The boundary value problems were solved by applying the

1. **Kinematic relations**, described in Section 2.1.1, are given for each of the boundary value problems given below.
2. **Stress relations**, given in Section 2.1.3, are defined for the constitutive equation used in each case.
3. **The conservation of mass** (Section 2.1.4.1) may be utilized to obtain a relation for the volume and density changes during a deformation. For incompressible materials, J is equal to unity, and the Cauchy stress tensor is given by eq. 2.52.

4. **The balance of linear momentum** (Section 2.1.4.2) gives rise to the equations of motion. For no body forces and zero acceleration, with the Cauchy stress tensor for an incompressible material given by eq. 2.45, the balance of linear momentum (eq. 2.22) is given by

$$\nabla \cdot \mathbf{T} = -\nabla p + \nabla \cdot \mathbf{T}_E = 0 \tag{2.133}$$

5. **The balance of angular momentum** (Section 2.1.4.3) may be used to show the symmetry of the Cauchy stress tensor. It may easily be shown that the Cauchy stress tensor is symmetric (eq. 2.23).

6. **Boundary conditions** imposed upon the boundary surface of a body are given for each case.

The constitutive stress stretch relationship for a homogeneous hyperelastic material may be given by eq. 2.50, where here the strain energy function is given with the isotropic and anisotropic portions additively de-coupled (eq. 2.76). Thus, the additive Cauchy stress tensor is given by $\mathbf{T} = \mathbf{T}_{iso} + \mathbf{T}_{aniso}$, with the isotropic portion given by eq. 2.92 and the anisotropic portion given by eq. 2.113, in Cartesian co-ordinates, assuming incompressibility (eq.2.45) the Cauchy stress tensor (eq. 2.52) is given in indicial notation as

$$T_{ij} = -p\delta_{ij} + 2F_{iA}\left(\frac{\partial W_{iso} + W_{aniso}}{\partial C_{AB}}\right)F_{jB} \tag{2.134}$$

Below, the fiber recruitment models (Section 2.3.1) and the fiber orientation models (Section 2.3.2) are given in explicit forms, followed by descriptions of the special cases of planar biaxial (Section 2.3.3) and uniaxial (Section 2.3.4) tension, and the cylindrical inflation (Section 2.3.5), of a homogeneous, incompressible, hyperelastic material.

2.3.1 Fiber Recruitment Models

For the functional form of W_{aniso} given by eq. 2.112, the derivative $\partial W_f/\partial \mathbf{C}$ in eq.2.113 is determined, using the Leibniz rule, to be

$$\frac{\partial W_f}{\partial \mathbf{C}} = \frac{1}{4\pi}\int_0^{2\pi}\int_{-\pi/2}^{\pi/2} \frac{\partial \hat{w}_f(\lambda_f^2)}{\partial \lambda_f^2}\frac{\partial \lambda_f^2}{\partial \mathbf{C}}\rho(\theta,\phi)\,\cos\theta d\theta\, d\phi \tag{2.135}$$

where

$$\frac{\partial \lambda_f^2}{\partial \mathbf{C}} = \mathbf{m}_0 \otimes \mathbf{m}_0 \tag{2.136}$$

was utilized, with the vector product given by

$$\mathbf{m}_0 \otimes \mathbf{m}_0 = \begin{bmatrix} \cos^2(\theta) & \sin(\theta)\cos(\theta)\cos(\phi) & \sin(\theta)\cos(\theta)\sin(\phi) \\ \sin(\theta)\cos(\theta)\cos(\phi) & \sin^2(\theta)\cos^2(\theta) & \sin^2(\theta)\sin(\phi)\cos(\phi) \\ \sin(\theta)\cos(\theta)\sin(\phi) & \sin^2(\theta)\sin(\phi)\cos(\phi) & \sin^2(\theta)\sin^2(\phi) \end{bmatrix} \tag{2.137}$$

2.3.1.1 Distributed fiber recruitment stretches If the strain energy potential of the whole fiber ensemble is given by eq. 2.124, by applying the Leibniz rule and the chain rule, and noting eq. 2.123, its derivative with respect to λ_f^2 in eq. 2.135 is given by

$$\frac{\partial \hat{w}_f(\lambda_f^2)}{\partial \lambda_f^2} = \int_1^{\lambda_f} \hat{d}_1(\lambda_a)\frac{1}{\lambda_a^2}\frac{\partial \hat{w}_f^*(\lambda_t^2)}{\partial \lambda_t^2}\,dx. \tag{2.138}$$

2.3.1.2 Single fiber recruitment stretch For the case in which fiber recruitment occurs abruptly, with no distribution of activation stretches, the strain energy of the fiber ensemble is equivalent to eq. 4.1 where d_1 is given by eq. 4.2, so the derivative of w_f by λ_f^2 given in eq. 2.135 is given by

$$\frac{\partial \hat{w}_f(\lambda_f^2)}{\partial \lambda_f^2} = \hat{d}_1(\lambda_a)\frac{1}{\lambda_a^2}\frac{\partial \hat{w}_f^*(\lambda_t^2)}{\partial \lambda_t^2} \tag{2.139}$$

2.3.2 Fiber Orientation Models

The particular functions used in the constitutive equations to represent fiber orientation distribution modeled as conic splay, fan splay, transversely isotropic, and isotropic are given in the sections that follow.

2.3.2.1 Conic Splay Assuming the fibers are distributed evenly as ϕ is rotated (Section 2.2.3.3), eq. 2.135 is given as

$$\frac{\partial W_{aniso}}{\partial \lambda_i^2} = \frac{1}{2} \int_{-\pi/2}^{\pi/2} \frac{\partial \hat{w}_f(\lambda_f^2)}{\partial \lambda_i^2} \hat{\rho}(\theta) \cos\theta \, d\theta \tag{2.140}$$

2.3.2.2 Fan Splay For materials that exhibit a dispersion of fiber orientations confined to a single plane, $\mathbf{e}_1 \otimes \mathbf{e}_2$ (see Section 2.2.3.4), using eq. 2.118, eq. 2.135 becomes

$$\frac{\partial W_{aniso}}{\partial \lambda_i^2} = \frac{1}{\pi} \int_{-\pi/2}^{\pi/2} \frac{\partial \hat{w}_f(\lambda_f^2)}{\partial \lambda_i^2} \hat{\rho}_{2D}(\theta) \, d\theta \tag{2.141}$$

2.3.2.3 Transverse isotropy In the limiting case in which the orientation distribution is given in a single direction, here given as $\mathbf{e}_1$, the orientation distribution function may be given as $\rho = 2\delta(\theta - 0)$, where δ is the dirac delta function, so the strain energy function in eq. 2.112 may be given so that eq. 2.119, as a function of IV only, is recovered.

2.3.2.4 Isotropy For isotropic materials (Section 2.2.2), the anisotropic portion of the strain energy function is neglected. In this case, the symmetry group includes all rotations about all possible axes and reflections about any plane.

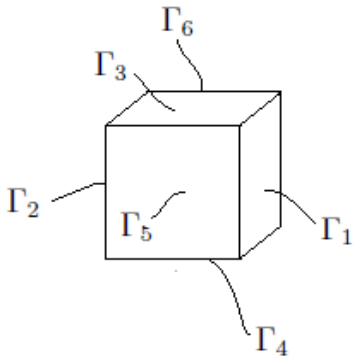

Figure 8: Surfaces of a unit cube

2.3.3 Planar Biaxial Tension

For the case in which a rectangular slab (Fig. 8) is stretched by λ_1 in the $\mathbf{e}_1$ direction and λ_2 in the $\mathbf{e}_2$ (Fig. 9), the **Boundary Conditions** are given by

- Γ_1, with $\mathbf{n} = \mathbf{e}_1$: $\mathbf{t} = \mathrm{T}_1\mathbf{e}_1$, so $T_{11} = T_1$, $T_{12} = 0$, and $T_{13} = 0$
- Γ_2, with $\mathbf{n} = -\mathbf{e}_1$: $\mathbf{t} = -\mathrm{T}_1(-\mathbf{e}_1)$, so $T_{11} = T_1$, $T_{12} = 0$, and $T_{13} = 0$, similar to above
- Γ_3, with $\mathbf{n} = \mathbf{e}_2$: $\mathbf{t} = \mathrm{T}_2\mathbf{e}_2$, so $T_{21} = 0$, $T_{22} = T_2$, and $T_{23} = 0$
- Γ_4, with $\mathbf{n} = -\mathbf{e}_2$: $\mathbf{t} = -\mathrm{T}_2(-\mathbf{e}_2)$, so $T_{21} = 0$, $T_{22} = T_2$, and $T_{23} = 0$, similar to above
- Γ_5, with $\mathbf{n} = \mathbf{e}_3$: $\mathbf{t} = \mathbf{0}$, so $T_{31} = 0$, $T_{32} = 0$, and $T_{33} = 0$
- Γ_6, with $\mathbf{n} = -\mathbf{e}_3$: $\mathbf{t} = \mathbf{0}$, so $T_{31} = 0$, $T_{32} = 0$, and $T_{33} = 0$, similar to above

where T_1 and T_2 are prescribed.

The deformation is considered in which a unit cube of homogeneous hyperelastic material in the reference configuration $\boldsymbol{\kappa}_0$ with sides parallel to the X_1, X_2, and X_3 axes, is deformed into a cube of dimensions $(\lambda_1, \lambda_2, \lambda_3)$ parallel to the X_1, X_2, and X_3 axes, respectively.

The co-ordinates of the strained body in the current configuration $\boldsymbol{\kappa}$ may be referred to a fixed Cartesian set of axes, x_i which coincide with the axes $X_I = (X_1, X_2, X_3)$ (i, I = 1,2,3).

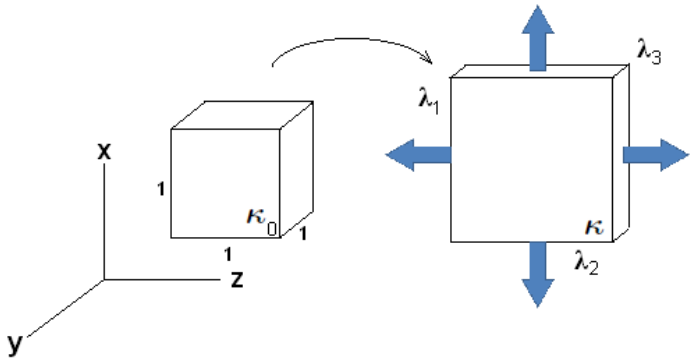

Figure 9: Deformation of a unit cube during biaxial extension

Therefore, these co-ordinates are represented by

$x_1 = \lambda_1 X_1 \qquad x_2 = \lambda_2 X_2 \qquad x_3 = \lambda_3 X_3$

where λ_1, λ_2, and λ_3 are constants. The kinematic relations are derived from the deformation above; in this case, the deformation gradient tensor (eq. 2.5) becomes, after applying the incompressibility condition, $\lambda_1\lambda_2\lambda_3 = 1$,

$$\mathbf{F} = \frac{\partial x_i}{\partial X_j} = \begin{bmatrix} \lambda_1 & 0 & 0 \\ 0 & \lambda_2 & 0 \\ 0 & 0 & \frac{1}{\lambda_1\lambda_2} \end{bmatrix}$$

so the left and right Cauchy-Green tensors (eq. 2.9) may be given, respectively, as

$$\mathbf{B} = \mathbf{F}\mathbf{F}^T = \mathbf{C} = \mathbf{F}^T\mathbf{F} = \begin{bmatrix} \lambda_1^2 & 0 & 0 \\ 0 & \lambda_2^2 & 0 \\ 0 & 0 & \frac{1}{\lambda_1^2\lambda_2^2} \end{bmatrix}$$

Conic Splay Applying these boundary conditions to a material with anisotropy described as conic splay gives, for the non-zero components of eq. 2.134:

$$T_1 = 2\left(\lambda_1^2 - \frac{1}{\lambda_1\lambda_2}\right)\frac{\partial W_{iso}}{\partial I_{\mathbf{B}}} + \left(\lambda_1\lambda_2 - \frac{1}{\lambda_1^2}\right)\frac{\partial W_{iso}}{\partial II_{\mathbf{B}}} + \frac{1}{2}\int_{-\pi/2}^{\pi/2}\frac{\partial \hat{w}_f(\lambda_f^2)}{\partial \lambda_f^2}\hat{\rho}(\theta)\left(\lambda_1^2\cos^3\theta - \frac{1}{\lambda_1\lambda_2}\sin^2\theta\cos\theta\right)d\theta \tag{2.142}$$

$$T_2 = 2\left(\lambda_2^2 - \frac{1}{\lambda_1\lambda_2}\right)\frac{\partial W_{iso}}{\partial I_{\mathbf{B}}} + \left(\lambda_1\lambda_2 - \frac{1}{\lambda_2^2}\right)\frac{\partial W_{iso}}{\partial II_{\mathbf{B}}} + \frac{1}{2}\int_{-\pi/2}^{\pi/2}\frac{\partial \hat{w}_f(\lambda_f^2)}{\partial \lambda_f^2}\hat{\rho}(\theta)\left(\lambda_2^2 - \frac{1}{\lambda_1\lambda_2}\right)\sin^2\theta\cos\theta\, d\theta \tag{2.143}$$

Note that the off-diagonal components are equal to zero because ρ is independent of ϕ.

Fan Splay Applying these boundary conditions to a material with anisotropy described as planar, or fan, splay gives, for the non-zero components of eq. 2.134:

$$T_1 = 2\left(\lambda_1^2 - \frac{1}{\lambda_1\lambda_2}\right)\frac{\partial W_{iso}}{\partial I_{\mathbf{B}}} + \left(\lambda_1\lambda_2 - \frac{1}{\lambda_1^2}\right)\frac{\partial W_{iso}}{\partial II_{\mathbf{B}}} + \lambda_1^2\frac{1}{\pi}\int_{-\pi/2}^{\pi/2}\frac{\partial \hat{w}_f(\lambda_f^2)}{\partial \lambda_f^2}\hat{\rho}_{2D}(\theta)\cos^2\theta\, d\theta \tag{2.144}$$

$$T_2 = 2\left(\lambda_2^2 - \frac{1}{\lambda_1\lambda_2}\right)\frac{\partial W_{iso}}{\partial I_{\mathbf{B}}} + \left(\lambda_1\lambda_2 - \frac{1}{\lambda_2^2}\right)\frac{\partial W_{iso}}{\partial II_{\mathbf{B}}} + \lambda_2^2\frac{1}{\pi}\int_{-\pi/2}^{\pi/2}\frac{\partial \hat{w}_f(\lambda_f^2)}{\partial \lambda_f^2}\hat{\rho}_{2D}(\theta)\sin^2\theta\, d\theta \tag{2.145}$$

The shear terms T_{12} and T_{21} can only be neglected if the distribution function ρ_{2D} is symmetric about the co-ordinate axis along $\mathbf{e}_1$ (see [88]). In this work, averaging is used to force this (measured) function to be symmetric so that the shear terms vanish.

Transverse Isotropy Applying these boundary conditions to a transversely isotropic material, the non-zero components of eq. 2.134 become:

$$T_1 = 2\left(\lambda_1^2 - \frac{1}{\lambda_1\lambda_2}\right)\frac{\partial W_{iso}}{\partial I_{\mathbf{B}}} + \left(\lambda_1\lambda_2 - \frac{1}{\lambda_1^2}\right)\frac{\partial W_{iso}}{\partial II_{\mathbf{B}}} + \frac{\partial w_f(\lambda_f^2)}{\partial \lambda_f^2}\lambda_1^2 \tag{2.146}$$

$$T_2 = 2\left(\lambda_2^2 - \frac{1}{\lambda_1\lambda_2}\right)\frac{\partial W_{iso}}{\partial I_{\mathbf{B}}} + \left(\lambda_1\lambda_2 - \frac{1}{\lambda_2^2}\right)\frac{\partial W_{iso}}{\partial II_{\mathbf{B}}} \tag{2.147}$$

Isotropy Applying these boundary conditions to a transversely isotropic material, the non-zero components of eq. 2.134 become:

$$T_1 = 2\left(\lambda_1^2 - \frac{1}{\lambda_1\lambda_2}\right)\frac{\partial W_{iso}}{\partial I_{\mathbf{B}}} + \left(\lambda_1\lambda_2 - \frac{1}{\lambda_1^2}\right)\frac{\partial W_{iso}}{\partial II_{\mathbf{B}}} \tag{2.148}$$

$$T_2 = 2\left(\lambda_2^2 - \frac{1}{\lambda_1\lambda_2}\right)\frac{\partial W_{iso}}{\partial I_{\mathbf{B}}} + \left(\lambda_1\lambda_2 - \frac{1}{\lambda_2^2}\right)\frac{\partial W_{iso}}{\partial II_{\mathbf{B}}} \tag{2.149}$$

2.3.4 Uniaxial Tension

For the case in which a rectangular slab (Fig. 8) is stretched by λ_1 in the $\mathbf{e}_1$ direction only (Fig. 10), the **Boundary Conditions** are given by

- Γ_1, with $\mathbf{n} = \mathbf{e}_1$: $\mathbf{t}$ = T$_1\mathbf{e}_1$, so $T_{11} = T_1$, $T_{12} = 0$, and $T_{13} = 0$
- Γ_2, with $\mathbf{n} = -\mathbf{e}_1$: $\mathbf{t}$ = -T$_1$(-$\mathbf{e}_1$), so $T_{11} = T_1$, $T_{12} = 0$, and $T_{13} = 0$, similar to above
- Γ_3, with $\mathbf{n} = \mathbf{e}_2$: $\mathbf{t} = \mathbf{0}$, so $T_{21} = 0$, $T_{22} = 0$, and $T_{23} = 0$
- Γ_4, with $\mathbf{n} = -\mathbf{e}_2$: $\mathbf{t} = \mathbf{0}$, so $T_{21} = 0$, $T_{22} = 0$, and $T_{23} = 0$, similar to above
- Γ_5, with $\mathbf{n} = \mathbf{e}_3$: $\mathbf{t} = \mathbf{0}$, so $T_{31} = 0$, $T_{32} = 0$, and $T_{33} = 0$
- Γ_6, with $\mathbf{n} = -\mathbf{e}_3$: $\mathbf{t} = \mathbf{0}$, so $T_{31} = 0$, $T_{32} = 0$, and $T_{33} = 0$, similar to above

where T_1 is prescribed.

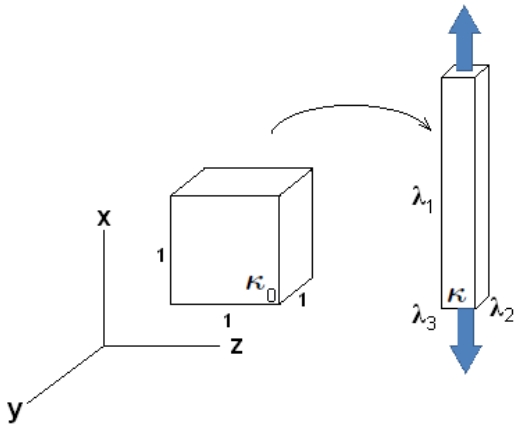

Figure 10: Deformation of a unit cube during uniaxial extension

Conic Splay Noting that $\lambda_2 \equiv \lambda_3$ to satisfy the boundary conditions (BCs) $T_{22} = 0$ and $T_{33} = 0$, the non-zero components of eq. 2.134 become

$$T_1 = 2\left(\lambda_1^2 - \frac{1}{\lambda_1}\right)\frac{\partial W_{iso}}{\partial I_{\mathbf{B}}} + \left(\lambda_1 - \frac{1}{\lambda_1^2}\right)\frac{\partial W_{iso}}{\partial II_{\mathbf{B}}} + \frac{1}{2}\int_{-\pi/2}^{\pi/2} \frac{\partial \hat{w}_f(\lambda_f^2)}{\partial \lambda_f^2}\hat{\rho}(\theta)\left(\lambda_1^2\cos^2\theta - \frac{1}{\sqrt{\lambda_1}}\sin^2\theta\right)\cos\theta\, d\theta \tag{2.150}$$

Fan Splay Applying these boundary conditions to a material with anisotropy described as planar, or fan, splay gives, with symmetric ρ_{2D} for the non-zero components of eq. 2.134:

$$T_1 = 2\left(\lambda_1^2 - \frac{1}{\lambda_1^2\lambda_2^2}\right)\frac{\partial W_{iso}}{\partial I_{\mathbf{B}}} + \left(\lambda_1^2\lambda_2^2 - \frac{1}{\lambda_1^2}\right)\frac{\partial W_{iso}}{\partial II_{\mathbf{B}}} + \frac{1}{\pi}\int_{-\pi/2}^{\pi/2} \frac{\partial \hat{w}_f(\lambda_f^2)}{\partial \lambda_f^2}\hat{\rho}_{2D}(\theta)\cos^2\theta\, d\theta\lambda_1^2 \tag{2.151}$$

where

$$\lambda_2^2 = \sqrt{\frac{2\left(\frac{1}{\lambda_1^2}\right)\frac{\partial W_{iso}}{\partial I_{\mathbf{B}}} + \frac{\partial W_{iso}}{\partial II_{\mathbf{B}}}}{2\frac{\partial W_{iso}}{\partial I_{\mathbf{B}}} + \lambda_1^2\frac{\partial W_{iso}}{\partial II_{\mathbf{B}}} + \frac{1}{\pi}\int_{-\pi/2}^{\pi/2}\frac{\partial \hat{w}_f(\lambda_f^2)}{\partial \lambda_f^2}\hat{\rho}_{2D}(\theta)\sin^2\theta\, d\theta}} \tag{2.152}$$

Transverse Isotropy Applying these boundary conditions to a transversely isotropic material, the non-zero components of eq. 2.134 become:

$$T_1 = 2\left(\lambda_1^2 - \frac{1}{\lambda_1}\right)\frac{\partial W_{iso}}{\partial I_{\mathbf{B}}} + \left(\lambda_1 - \frac{1}{\lambda_1^2}\right)\frac{\partial W_{iso}}{\partial II_{\mathbf{B}}} + \frac{\partial w_f(\lambda_f^2)}{\partial \lambda_f^2}\lambda_1^2 \tag{2.153}$$

Isotropy Applying these boundary conditions to an isotropic material, the non-zero components of eq. 2.134 become:

$$\begin{aligned} T_1 &= 2\left(\lambda_1^2 - \frac{1}{\lambda_1}\right)\frac{\partial W_{iso}}{\partial I_{\mathbf{B}}} + \left(\lambda_1 - \frac{1}{\lambda_1^2}\right)\frac{\partial W_{iso}}{\partial II_{\mathbf{B}}} \\ &= 2\left(\lambda_1^2 - \frac{1}{\lambda_1}\right)\left(\frac{\partial W_{iso}}{\partial I_{\mathbf{B}}} + \frac{1}{\lambda_1}\frac{\partial W_{iso}}{\partial II_{\mathbf{B}}}\right) \end{aligned} \tag{2.154}$$

which also may be given by

$$T_1 = \lambda_1 \frac{\partial W_{iso}}{\partial \lambda_1} \tag{2.155}$$

The above may be shown by

$$\begin{aligned} T_1 &= \lambda_1 \tfrac{\partial W_{iso}}{\partial \lambda_1} = \lambda_1 \left[\tfrac{\partial I_{\mathbf{B}}}{\partial \lambda_1}\tfrac{\partial W_{iso}}{\partial I_{\mathbf{B}}} + \tfrac{\partial II_{\mathbf{B}}}{\partial \lambda_1}\tfrac{\partial W_{iso}}{\partial II_{\mathbf{B}}}\right] \\ &= \lambda_1 \left[\left(2\lambda_1 - \tfrac{2}{\lambda_1^2}\right)\tfrac{\partial W_{iso}}{\partial I_{\mathbf{B}}} + \left(2 - \tfrac{2}{\lambda_1^3}\right)\tfrac{\partial W_{iso}}{\partial II_{\mathbf{B}}}\right] \\ &= 2\lambda_1 \left[\left(\lambda_1 - \tfrac{1}{\lambda_1^2}\right)\tfrac{\partial W_{iso}}{\partial I_{\mathbf{B}}} + \tfrac{1}{\lambda_1}\left(\lambda_1 - \tfrac{1}{\lambda_1^2}\right)\tfrac{\partial W_{iso}}{\partial II_{\mathbf{B}}}\right] \\ &= 2(\lambda_1^2 - \tfrac{1}{\lambda_1})(\tfrac{\partial W_{iso}}{\partial I_{\mathbf{B}}} + \tfrac{1}{\lambda_1}\tfrac{\partial W_{iso}}{\partial II_{\mathbf{B}}}) \end{aligned}$$

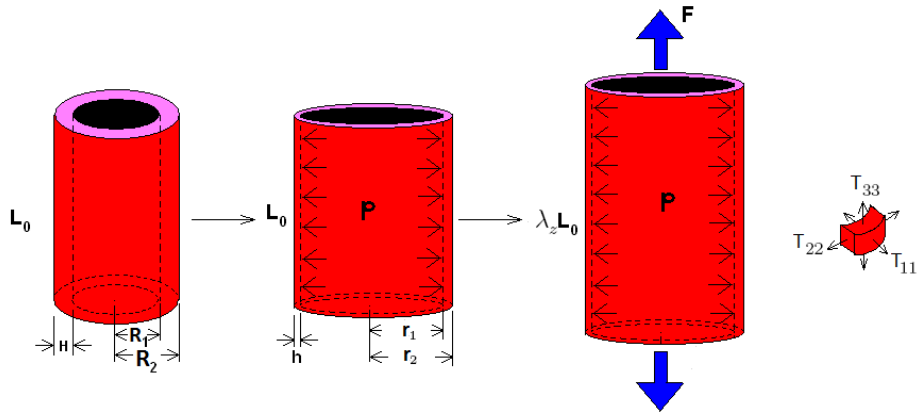

Figure 11: Biaxial inflation/extension of a thick-walled cylinder

2.3.5 Inflation of a Thick-Walled Cylinder with Fan Splay

Consider a circular cylindrical tube which in the unstrained state is of length L_0 and has internal and external radii R_1 and R_2, respectively. Assume the tube is strained by a uniform inflation in which its external and internal radii change to r_1 and r_2, respectively, and a uniform simple extension of extension ratio λ_z, parallel to the tube, is applied (Fig. 11). The inner surface of the cylinder is denoted by Γ_1, and the outer surface by Γ_2. The surfaces of the ends of the cylinder are denoted by Γ_3 and Γ_4. For this deformation, the **Boundary Conditions** are given by

- Γ_1, with $\mathbf{n} = -\mathbf{e}_r$: $\mathbf{t}$ = P$_1$(-$\mathbf{e}_r$), so T_{rr} = -P_1, $T_{r\theta}$ = 0, and T_{rz} = 0, at R_1
- Γ_2, with $\mathbf{n} = \mathbf{e}_r$: $\mathbf{t}$ = -P$_2\mathbf{e}_r$, so T_{rr} = -P_2, $T_{r\theta}$ = 0, and T_{rz} = 0, at R_2
- Γ_3, with $\mathbf{n} = \mathbf{e}_z$: $\mathbf{t}$ = T$_1\mathbf{e}_z$, so T_{zr} = 0, $T_{z\theta}$ = 0, and $T_{zz} = T_1$
- Γ_4, with $\mathbf{n} = -\mathbf{e}_z$: $\mathbf{t}$ = -T$_1$(-$\mathbf{e}_z$), so T_{zr} = 0, $T_{z\theta}$ = 0, and $T_{zz} = T_1$, similar to above

The body in the reference configuration $\boldsymbol{\kappa}_0$ in the unstrained state, with fixed polar cylindrical axes, is defined and related to Cartesian co-ordinate axes (X_1, X_2, X_3) by

$R = \sqrt{X_1^2 + X_2^2}, \qquad \Theta = \tan^{-1}\left(\frac{X_2}{X_1}\right), \qquad Z = X_3$

and

$X_1 = R\cos\Theta, \qquad X_2 = R\sin\Theta, \qquad X_3 = Z$

Thus, for the body in the reference configuration, the cylindrical co-ordinates are given by

$$R \in [R_1, R_2] \tag{2.156}$$

$$\Theta \in [0, 2\pi] \tag{2.157}$$

$$Z \in [0, L] \tag{2.158}$$

Assume the body in the unstrained reference configuration $\boldsymbol{\kappa}_0$ is deformed to a strained configuration $\boldsymbol{\kappa}$, which is referred to a fixed set of polar cylindrical co-ordinates (ρ, θ, z), so that

$x_1 = \hat{r}(R)\cos\theta, \qquad x_2 = \hat{r}(R)\sin\theta, \qquad x_3 = z$

Thus, for the body in the deformed configuration, the cylindrical co-ordinates are given by

$$r \in [r_1, r_2] \tag{2.159}$$

$$\theta \in [0, 2\pi] \tag{2.160}$$

$$z \in [0, l] \tag{2.161}$$

The kinematic relations are derived from the deformation above. In this case, the deformation gradient tensor (eq. 2.5) becomes

$$\mathbf{F} = \frac{\partial x_i}{\partial X_j} = \begin{bmatrix} \frac{\partial \hat{r} R}{\partial r} & 0 & 0 \\ 0 & \frac{\hat{r}(R)}{R} & 0 \\ 0 & 0 & \frac{l}{L} \end{bmatrix} = \begin{bmatrix} \lambda_r & 0 & 0 \\ 0 & \lambda_\theta & 0 \\ 0 & 0 & \lambda_z \end{bmatrix}$$

so the left and right Cauchy-Green tensors (eq. 2.9) may be given, respectively, as

$$\mathbf{B} = \mathbf{F}\mathbf{F}^T = \mathbf{C} = \mathbf{F}^T\mathbf{F} = \begin{bmatrix} \lambda_r^2 & 0 & 0 \\ 0 & \lambda_\theta^2 & 0 \\ 0 & 0 & \lambda_z^2 \end{bmatrix}$$

Again, the constitutive stress stretch relationship for a homogeneous hyperelastic material may be given by eq. 2.50, where here the strain energy function is given with the isotropic and anisotropic portions additively de-coupled (eq. 2.76).

For an incompressible material, (eq. 2.19) is equal to unity, and the constitutive mechanical relation (eq. 2.50) is give by eq. 2.52.

For no body forces and zero acceleration, the components of the balance of linear momentum (eq. 2.133) is given by

$$\mathbf{e}_r : -\frac{\partial p}{\partial r} + \frac{\partial T_{E,rr}}{\partial r} + \frac{1}{r}\frac{\partial T_{E,r\theta}}{\partial \theta} + \frac{\partial T_{E,rz}}{\partial z} + \frac{T_{E,rr} - T_{E,\theta\theta}}{r} = 0 \tag{2.162}$$

$$\mathbf{e}_\theta : -\frac{1}{r}\frac{\partial p}{\partial \theta} + \frac{\partial T_{E,r\theta}}{\partial r} + \frac{1}{r}\frac{\partial T_{E,\theta\theta}}{\partial \theta} + \frac{\partial T_{E,\theta z}}{\partial z} + \frac{T_{E,\theta r} - T_{E,r\theta}}{r} = 0 \tag{2.163}$$

$$\mathbf{e}_z : -\frac{\partial p}{\partial z} + \frac{\partial T_{E,zr}}{\partial r} + \frac{1}{r}\frac{\partial T_{E,z\theta}}{\partial \theta} + \frac{\partial T_{E,zz}}{\partial z} + \frac{T_{E,zr}}{r} = 0 \tag{2.164}$$

Since the off-diagonal components vanish, and the Cauchy stress tensor is a function of r alone (independent of θ and z), the above may be given in the reduced form:

$$\mathbf{e}_r : -\frac{\partial p}{\partial r} + \frac{\partial T_{E,rr}}{\partial r} + \frac{T_{E,rr} - T_{E,\theta\theta}}{r} = 0 \tag{2.165}$$

$$\mathbf{e}_\theta : -\frac{1}{r}\frac{\partial p}{\partial \theta} = 0 \tag{2.166}$$

$$\mathbf{e}_z : -\frac{\partial p}{\partial z} = 0 \tag{2.167}$$

so $p = \hat{p}(r)$ at most. With eq. 2.45, eq. 2.165 becomes

$$T_{rr} - T_{rr}|_{r_1} = \int_{r_1}^{r} \frac{T_{\theta\theta} - T_{rr}}{r} dr \tag{2.168}$$

Applying the boundary conditions at $\mathbf{\Gamma}_1$ and $\mathbf{\Gamma}_2$, eq. 2.168 leads to

$$\Delta P = P_1 - P_2 = \int_{r_1}^{r_2} \frac{T_{\theta\theta} - T_{rr}}{r} dr \tag{2.169}$$

Again, as in the above formulation for uniform extensions, using the strain energy function given in eq. 2.76, the additive Cauchy stress tensor is given by $\mathbf{T} = \mathbf{T}_{iso} + \mathbf{T}_{aniso}$, with the isotropic portion given by eq. 2.92 and the anisotropic portion given by eq. 2.113, in polar cylindrical co-ordinates, assuming incompressibility (eq.2.45) the Cauchy stress tensor (eq. 2.52) is given by eq. 2.134 with $i, j, A, B = (r, \theta, z)$.

Fan Splay For materials that exhibit a dispersion of fiber orientations confined to a single plane, $\mathbf{e}_z \otimes \mathbf{e}_\theta$ (see Section 2.2.3.4), using eq. 2.118, the derivative of the anisotropic portion of the strain energy function by the stretch λ_i is given by 2.141 with $i = (r, \theta, z)$.

Therefore, the non-zero components of 2.134 become

$$T_{zz} = -p + 2\frac{\partial W_{iso}}{\partial I_{\mathbf{B}}}\lambda_z^2 - \frac{\partial W_{iso}}{\partial II_{\mathbf{B}}}\frac{1}{\lambda_z^2} + \lambda_z^2\frac{1}{\pi}\int_{-\pi/2}^{\pi/2}\frac{\partial \hat{w}_f(\lambda_f^2)}{\partial \lambda_f^2}\hat{\rho}_{2D}(\theta)\cos^2\theta\, d\theta \tag{2.170}$$

$$T_{\theta\theta} = -p + 2\frac{\partial W_{iso}}{\partial I_{\mathbf{B}}}\lambda_\theta^2 - \frac{\partial W_{iso}}{\partial II_{\mathbf{B}}}\frac{1}{\lambda_\theta^2} + \lambda_\theta^2\frac{1}{\pi}\int_{-\pi/2}^{\pi/2}\frac{\partial \hat{w}_f(\lambda_f^2)}{\partial \lambda_f^2}\hat{\rho}_{2D}(\theta)\sin^2\theta\, d\theta \tag{2.171}$$

$$T_{rr} = -p + 2\frac{\partial W_{iso}}{\partial I_{\mathbf{B}}}\lambda_r^2 - \frac{\partial W_{iso}}{\partial II_{\mathbf{B}}}\frac{1}{\lambda_r^2} \tag{2.172}$$

By utilizing the incompressibility condition, $\lambda_r\lambda_\theta\lambda_z = 1$, eq. 2.169 may be given as

$$\Delta P = \int_{r_1}^{r_2}\frac{1}{r}\left[2\frac{\partial W_{iso}}{\partial I_{\mathbf{B}}}\left(\lambda_\theta^2 - \frac{1}{\lambda_\theta^2\lambda_z^2}\right) - \frac{\partial W_{iso}}{\partial II_{\mathbf{B}}}\left(\frac{1}{\lambda_\theta^2} + \lambda_\theta^2\lambda_z^2\right) + f_{aniso}\right]dr \tag{2.173}$$

where

$$f_{aniso} = \lambda_\theta^2\frac{1}{\pi}\int_{-\pi/2}^{\pi/2}\frac{\partial \hat{w}_f(\lambda_f^2)}{\partial \lambda_f^2}\hat{\rho}_{2D}(\theta)\sin^2\theta\, d\theta \tag{2.174}$$

3.0 COMBINED MECHANICAL TESTING AND IMAGING

To achieve the first specific aim listed in the Introduction (Section 1.4), new systems were developed to analyze the mechanical response of the artery wall, combined with microstructural analysis. Custom devices were fabricated for performing uniaxial (UA) mechanical experiments on the artery vessel wall with simultaneous multi-photon microscopy (MPM) imaging of two primary load-bearing constituents, collagen fibers and elastin, without typical destructive techniques of aldehyde-based fixation, microtome sectioning, and histological staining (examples of these methods are given in Appendix A).

A background on this technique is presented in Section 3.1. The multi-photon microscope system is described in Section 3.2. The uniaxial testing device development is outlined in Section 3.3. Finally, nonlinear regression is outlined in Section 3.4, which is used to fit the theoretical models described in Chapter 2 to the experimental data obtained with these devices.

3.1 BACKGROUND

Both elastin [89, 90] and collagen [38, 39] have been visualized in fixed tissues under various applied extensions. For example, small angle light scattering (SALS) has been utilized to determine the gross fiber orientation [58] of tissue. This technique has been coupled with a planar biaxial device for direct structural analysis during mechanical testing [15].

One of the limitations of the SALS techniques was the restriction to gross fiber analysis: individual types of structural proteins, namely elastin and collagen, could not be distinguished. Further, only data from a single plane of fibers was obtained with this method, rather than a three-dimensional rendering of the fibers, unless the tissue was sectioned [91].

Based on the need to conduct mechanical experiments with simultaneous structural analysis, a system and protocol were developed for combining soft tissue mechanical testing with multi-photon imaging for visualizing elastin and collagen structure. The current work builds on earlier work in which MPM analysis was used to analyze the tissue structure [92, 93]. In their work, artery tissue was inflated and imaged under a multi-photon microscope. The mechanical stress-strain response was reported, and images of elastin and collagen were obtained, but no quantitative measures were taken from the acquired images. While in those studies, MPM was combined with mechanical testing, here the fiber microstructure is quantified for direct inclusion into a structurally motivated mathematical model.

This combined device was constructed in a horizontal fashion (hUA-MPM) with the testing device mounted directly underneath the MPM objective lens, so the lens could be lowered for vessel imaging during mechanical experimentation (Section 3.3.1). A vertical device (vUA-MPM) was fashioned similarly to the horizontal device, though this device enabled non-destructive imaging of loaded tissue in a two-stage process (Section 3.3.2). In particular, a custom bridge piece allowed the tissue to be removed under strain for imaging.

3.2 MULTI-PHOTON MICROSCOPY

In this work, non-destructive multi-photon microscopy (MPM) imaging of collagen and elastin is performed on artery segments under applied strain. Arterial collagen can be imaged without staining or fixation due to its nonsymmetrical triple helix arrangement, utilizing second harmonic generation (SHG). SHG takes place when the electric field from

exciting light deforms a non-symmetrical molecule, creating an oscillating field at twice the frequency, the second harmonic [94]. Arterial elastin can be imaged due to its intrinsic fluorescence under two-photon excited autofluorescence (TPEA), likely from the lysine-residue-linked pyridolamine groups that form covalent cross links between the chains [95].

An Olympus FV1000 (Olympus, Tokyo Japan) multi-photon microscope equipped with a Spectra-Physics DeepSee Mai Tai Ti-Sapphire laser (Newport, Mountain View, CA) was used for all experiments. The SHG and TPEA signals were all collected using backscattered epi-detectors. These provided images of collagen and elastin, respectively. The detectors were non-descanned. An excitiation wavelength of 870nm and 1.12NA 25x MPE water immersion objective was used for all samples. The SHG signal was collected using a 400nm emission filter with a +/- 50 spectral bin. The autofluorescence signal was collected using a 525 nm emission filter with a +/- 12nm spectral bin. All filters were provided by Chroma (Brattleboro VT). The dwell time was 10 microseconds/pixel at a scan pixel count of 1024X1024. Resolution of 0.12μm was achieved with this system.

Planar stacks of images, each measuring 1024x1024 pixels, of the media were initially taken near the adventitia, and subsequent image stacks were taken in 0.5μm intervals moving upward to the intima. Imaris software (Bitplane, Switzerland) was utilized to process the images. Image stacks were superimposed to form 2D projections for evaluation of collagen fiber orientation. Volumetric (3D) reconstructions were formed from these same stacks for analysis of collagen recruitment.

3.3 COMBINED UNIAXIAL TESTING WITH MULTI-PHOTON MICROSCOPY

Two uniaxial mechanical testing devices were constructed to operate in conjunction with a multi-photon microscope for coincident stress-strain analysis and laser scanning imaging of collagen and elastin. The uniaxial tensile testing devices were developed by following guidelines established in the ASM Handbook [96] and in ASTM Standards for tensile testing of rubbers [97]. Here, tensile testing involves placing a prepared specimen to

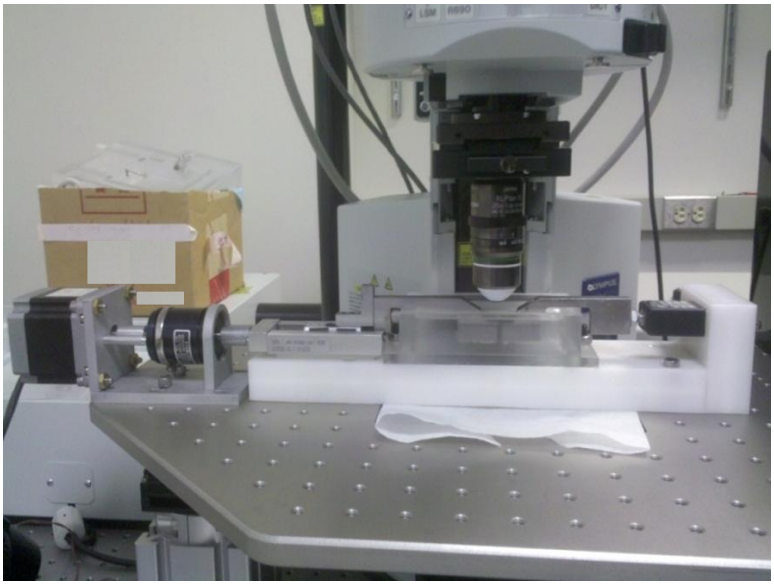

Figure 12: Horizontal uniaxial mechanical testing device (hUA-MPM) mounted on the stage of the multi-photon microscope

gradually increasing (static) uniaxial load (stress). Opposite ends of a prepared specimen are gripped and pulled, which results in elongation of the specimen in the direction of applied load. The specimen is subjected to an increasing load, while the elongation and force are continuously recorded [97]. Each system consisted of a load cell and a linear motor for acquiring force and applying strain. One system (Fig. 12) was constructed to test the tissue short-term in a horizontal fashion mounted directly underneath the MPM objective lens. The physical components of this system are described in Section 3.3.1. The other (Fig. 13) was built to test tissue vertically with a removable clamping mechanism so that long term tissue testing (such as for fatigue experiments) can be conducted and specimens can be periodically removed under strain for MPM imaging. The physical components of this system are described in Section 3.3.2. The principles of operation of the uniaxial systems are described in Section 3.3.3

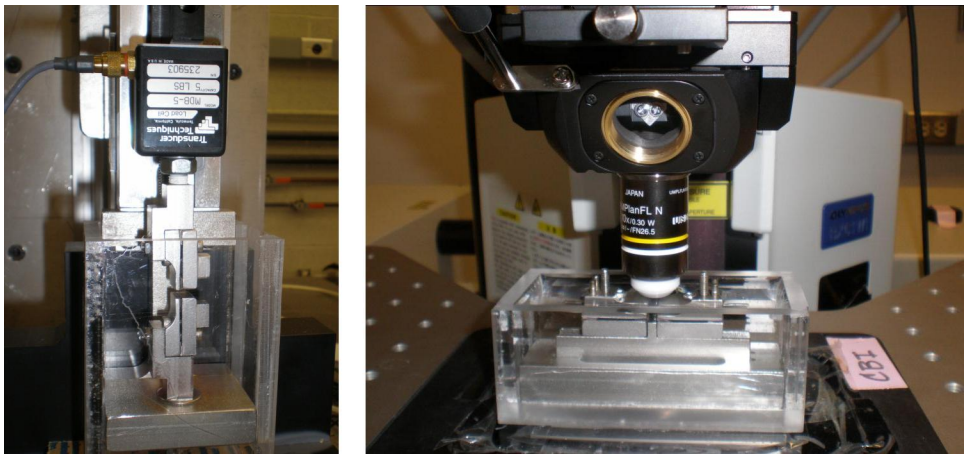

Figure 13: Left: Vertical uniaxial mechanical testing device (vUA-MPM). Right: Bridge piece containing clamps and specimen underneath the lens of the multi-photon microscope

3.3.1 Horizontal Uniaxial Mechanical Device

To analyze the constitutive stress-strain properties of arteries, a device for performing uniaxial extension experiments on horizontally-oriented vessel segments was developed. To construct the hUA-MPM device, physical components were drafted as part files and assembled in SolidWorks (Dassault Systemes SolidWorks Corp, Concord, MA) (Fig. 14). A clamping mechanism was created from stereolithography (Fig. 15) from the SolidWorks part files to check for usability and any design flaws, and then final parts were cut from 303 stainless steel (McMaster Carr) via water-jet cutting techniques (Kutz Fabrication, Pittsburgh, PA). Clamps were lined with fine sandpaper to grip the tissue without slipping.

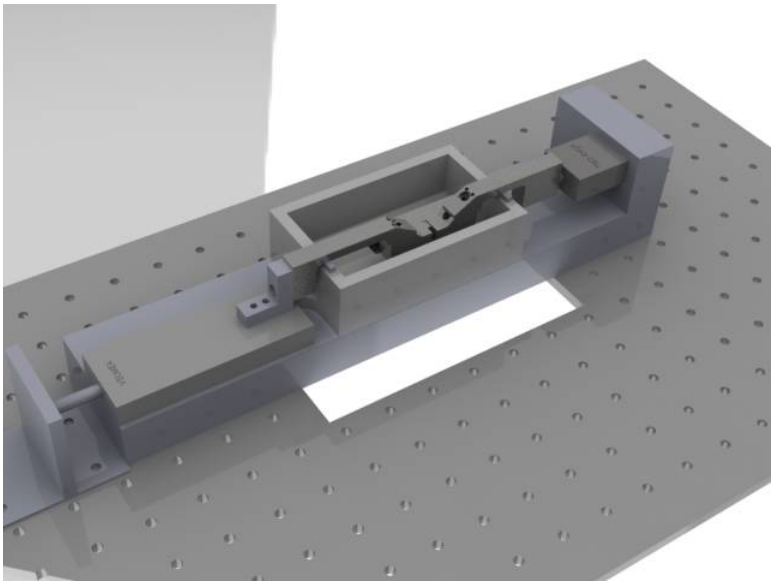

Figure 14: SolidWorks assembly of the horizontal uniaxial mechanical testing device mounted on an optical stage

Figure 15: Stereolithography model of the clamping system used in the uniaxial testing device

3.3.2 Vertical Uniaxial Mechanical Device

Motivated by the desire to perform long term damage tests on artery segments, a vertical system was developed with the capability to remove the sample under strain and transport it to the microscope facility for MPM imaging (Fig. 13). Furthermore, this setup allowed convenient camera placement for optical strain measurement.

Hardware and software similar to that used for the hUA-MPM device were used for system control and data acquisition in the vUA-MPM. Clamp design remained consistent between devices. Displacement was measured both by recording clamp distance traveled and by optically tracking four markers on the surface of the vessel [98, 99] (See Appendix C).

3.3.3 Principles of Operation

Components of the hUA-MPM are outlined in the SolidWorks image in Fig. 16 and Table 1. Main components were conserved between the horizontal and vertical systems.

For motion control, an HT23-396 stepper motor driven by a PDO 2035 stepper motor driver (Applied Motion Products, Watsonville, CA) was connected to a linear slide (Velmex, Inc.), used for vessel extension (Figs. 16 and 17). Commands to the motor were provided, through a connection to an electronic interface (Fig. 18), with a National Instruments (NI; Austin, TX) UMI 7764 motion controller connected to a NI PCI 7340 motion board (4MHz maximum stepper output pulse rate) on the computer. On this end, one clamp was mounted for vessel extension (Fig. 16).

For data acquisition (DAQ), a MDB-5 5-lb. capacity load cell (Transducer Techniques, Temecula, CA) was connected to the opposite clamp for load measurement (Fig. 16), and output from the load cell was acquired through a NI SCB-68 NI connector block plugged into a NI PCI 6014 data acquisition card (200kS/s sampling rate) (Figs. 17 and 18).

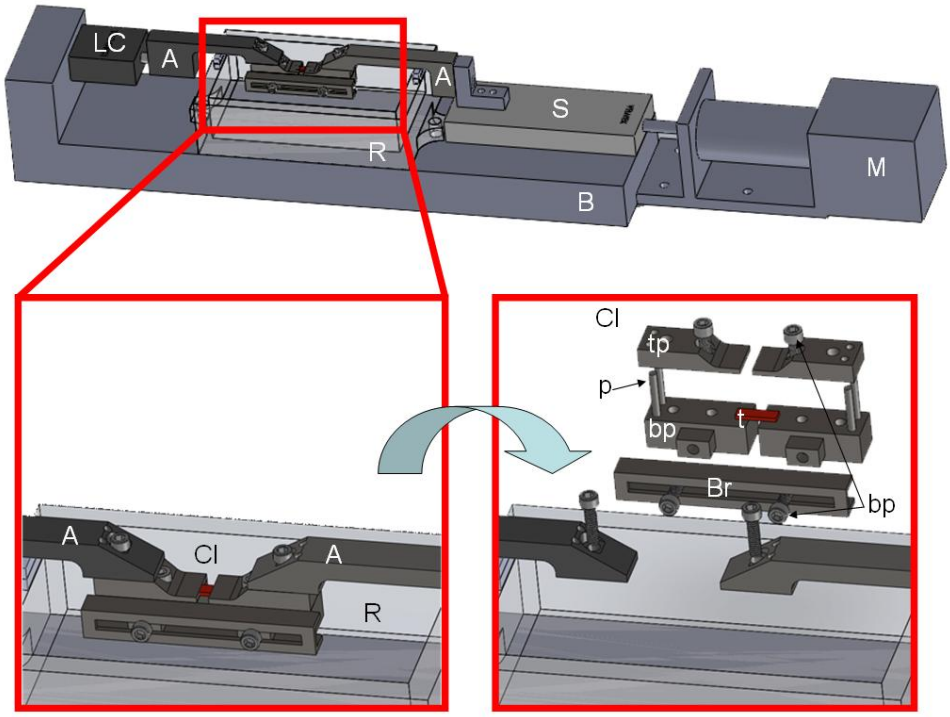

Figure 16: SolidWorks rendering of the physical components of the hUA-MPM testing system, with exploded views depicting the manner in which the specimen is clamped in the assembly and mounted onto the device. Parts are defined in the table above (NS = not shown).

Table 1: Parts and materials used in the uniaxial testing device. NS = not shown

Physical		**Motion**	
A	303 stainless steel (SS) arm	M	Stepper Motor (Appl. Mot. HT23-96)
B	Delrin base	NS	Step Motor Driver (Appl. Mot. PDO 2035)
bp	303 SS bottom clamping piece	S	Linear Slide (Velmex)
Br	303 SS bridge piece	NS	Controller (NI UMI 7764)
bt	size 4-40 thread SS bolts	NS	Motion Board (NI PCI 6340)
Cl	303 SS clamping mechanism	**DAQ**	
p	3/32-inch SS pins	LC	MDB-5 5-lb load cell
R	acrylic reservoir for tissue immersion	NS	Connector block (NI SCB 68)
t	tissue sample	NS	DAQ board (NI PCI 6014)
tp	303 SS top clamping piece		

To control the uniaxial system, custom LabVIEW Virtual Instrument (VI) software loaded onto a Dell Dimension desktop (Dell Inc., Round Rock, TX) was utilized for step motor control and data acquisition. Both applied force and clamp position were recorded at approximately 100ms intervals during loop cycles in the main VI. These were used for stress and stretch calculation.

A Sony XC-ST50 Monochrome CCD camera with a 0.50x telecentric lens, connected to a NI PCI 1407 image acquisition board on a Dell desktop equipped with NI Vision Assistant software for image analysis was used to acquire images. NI Vision VIs were integrated into custom LabVIEW software for simultaneous data acquisition and imaging.

Testing specimens are described in Section 3.3.3.1 Calibration of the load cell is described in Section 3.3.3.2. Verification of the displacement/strain measurement is given in Section 3.3.3.3. The National Instruments LabVIEW (Austin, TX) software used to control the device described in the Appendix B.

3.3.3.1 Testing Specimens The artery wall tissue is manually cut into rectangular, flat, dumbbell-shaped specimens (Fig. 19) [97]. Total working distance of the system is 27mm. Thus, only specimens whose total stretched length is greater than or equal to this distance may be tested in the devices. The minimum specimen length that may be clamped in the

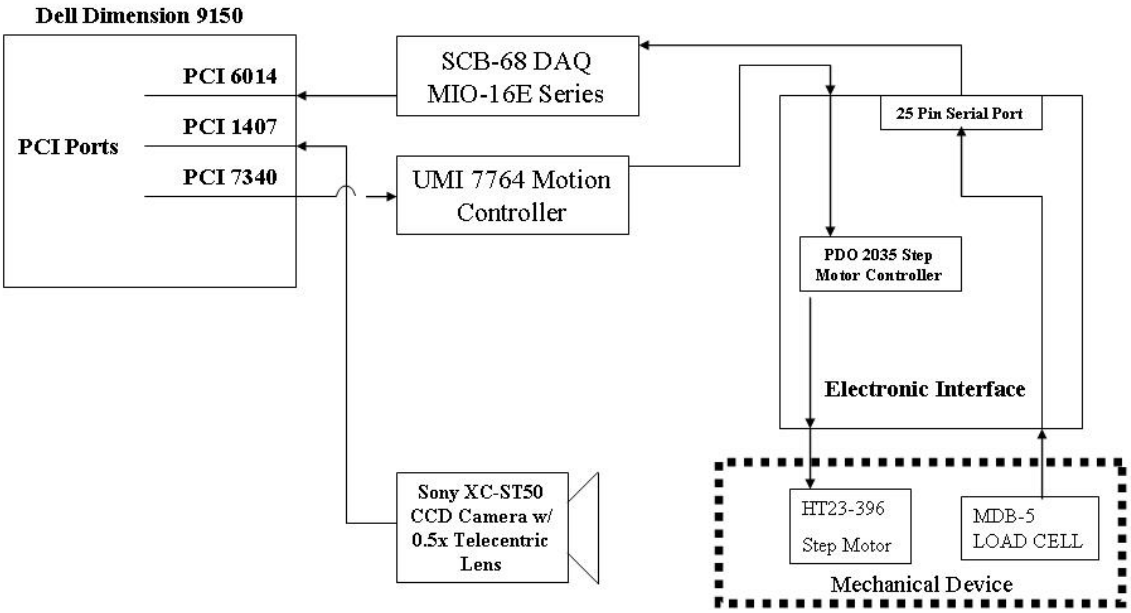

Figure 17: Controls for the unaxial tensile testing machines

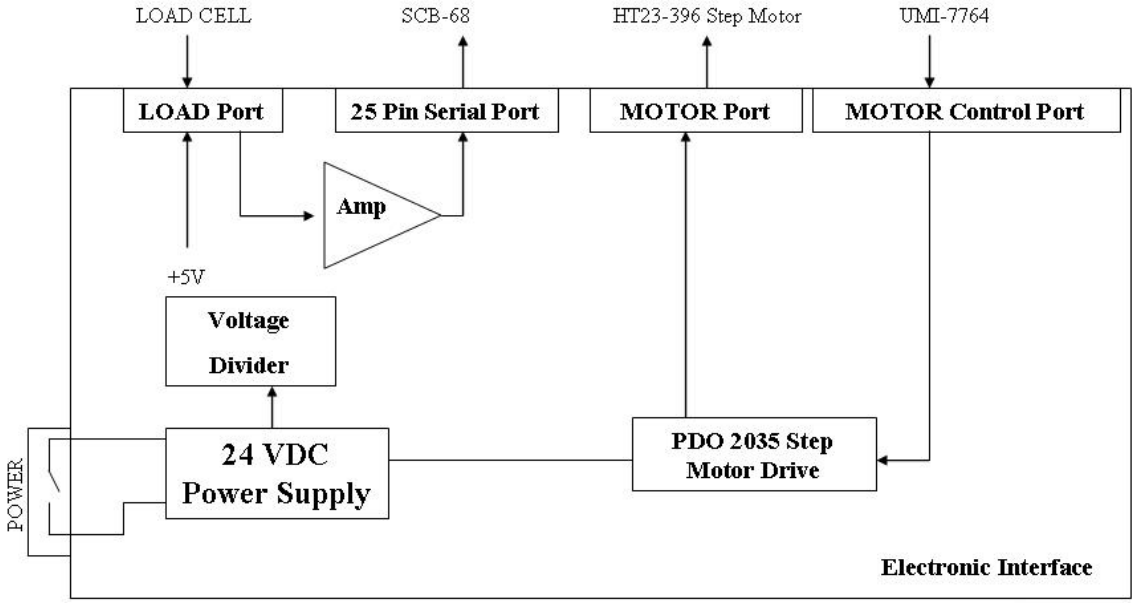

Figure 18: Electronic interface for the unaxial tensile testing machines

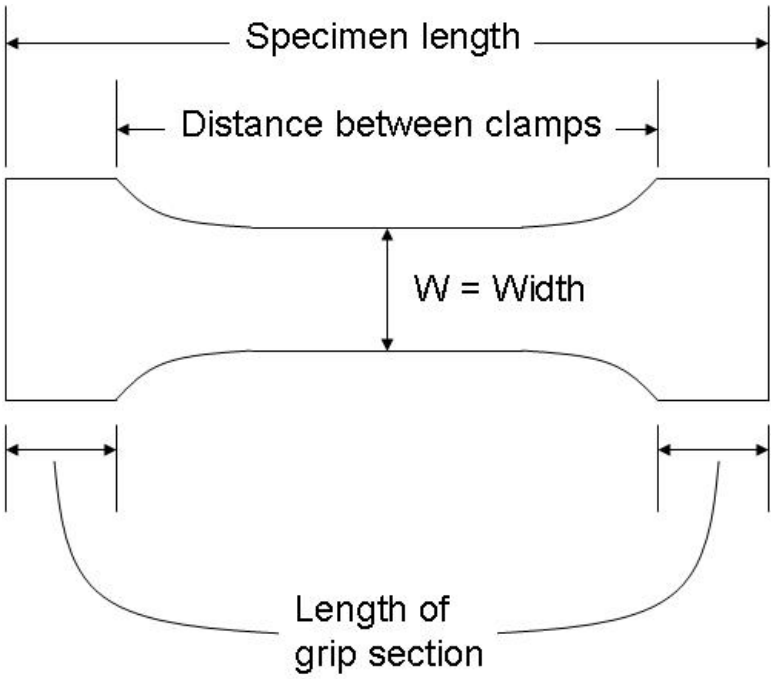

Figure 19: Dumbbell-shaped tension test specimen

device is 3 mm. Maximum allowable specimen width is 9 mm. No specimens above 1 cm in thickness may be tested in these devices. Note that thickness is limited in maximum by slip (larger samples may slip more readily) and in minimum by the load cell resolution. Force is recorded with the load cell. Since first Piola stress is defined as force divided by cross sectional area in the reference configuration, a sample with decreasing thickness (and width) will have lower stress resolution.

3.3.3.2 Force Verification The load cell was factory calibrated in compression and confirmed in tension with hanging weights (Fig. 20) following the ASTM standard [100], assuming a linear relation between force and output voltage. Non-linearity was 0.01% full scale (FS); non-repeatability was -0.03%FS; and hysteresis was 0.02%FS.

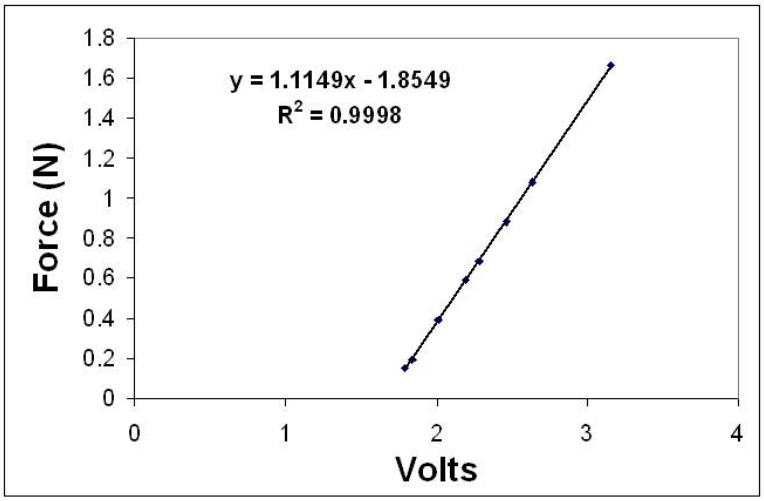

Figure 20: Example calibration curve of load cell using hanging standard weights

3.3.3.3 Displacement Verification To verify our displacement and strain measurements were accurate [96, 101], a sample of rubber was tested in the vertical device (vUA-MPM). In this work, we used clamp displacement for strain measurements. Strain calculations from clamp displacement were compared to strain measurements from optical methods optical methods with an example rubber segment (Fig. 21). The segment was cut into a flat dumbbell shape, as in Fig. 19. Overall specimen length was 5.9 mm. Distance between the clamps was L_0 = 4.6 mm. Width of the specimen was w = 6.2 mm. Four markers were placed on the surface of the strip of latex with permanent ink. Images were taken periodically throughout the test. Optical strain measurement was performed by methods given in Appendix C (Fig. 22). The specimen was clamped into the vUA-MPM device, and tested to 50 % of L_0. Similar results were obtained with optical methods and by using clamp displacement (Fig. 23), thus supporting clamp displacement as a suitable measure of strain in our applications.

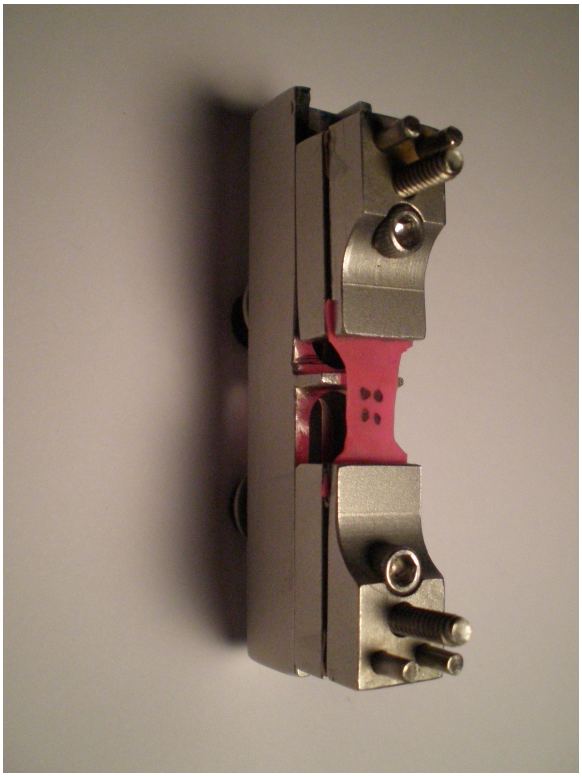

Figure 21: Rubber specimen with four ink markers on the surface, mounted on bridge piece of the vUA-MPM device, used to confirm strain measurements from clamp displacement with optical methods, by tracking markers with methods given in Appendix C

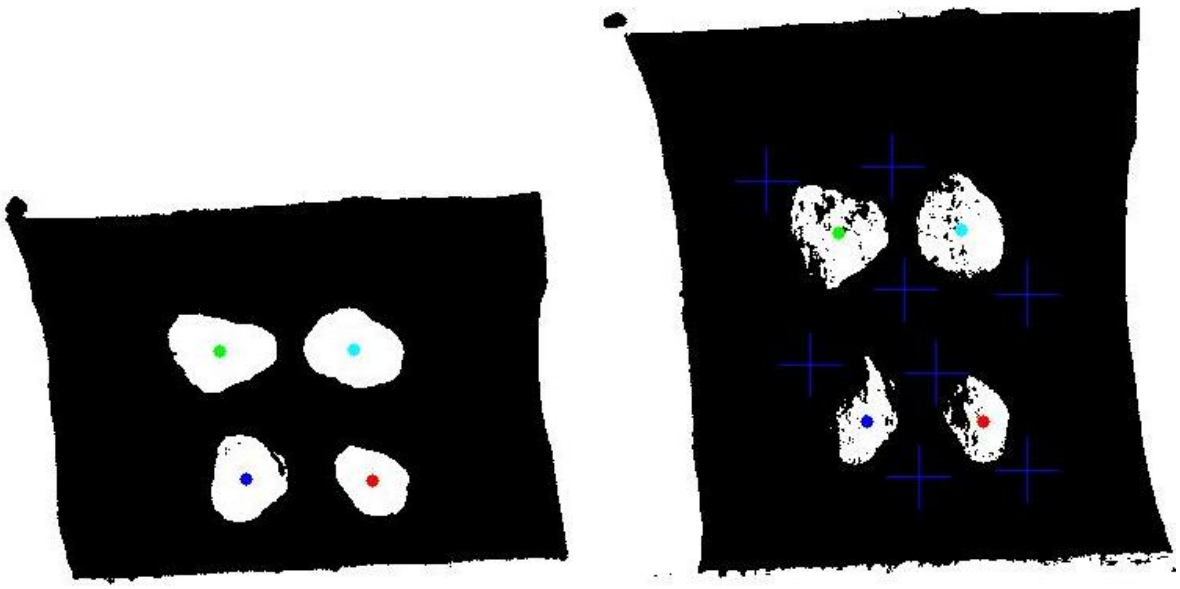

Figure 22: Left: Centroids (colored dots) of the four markers on the image following thresholding. Right: Marker tracking at highest strain. Blue crosses indicate the outlines of the selected regions for analyzing the four individual markers, illustrating the method used for tracking the markers. Colored dots are marker centroids

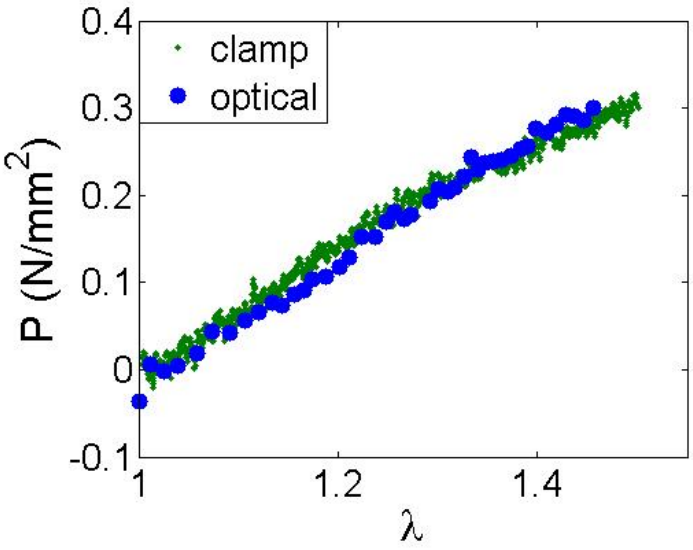

Figure 23: Optical Strain Measurement results plotted with Clamp Displacement Results from a rubber specimen

3.4 NON-LINEAR REGRESSION

Nonlinear least-squares regression analysis was accomplished with MATLAB, utilizing a modified Levenberg-Marquardt [102, 103] algorithm (*lsqcurvefit.m*) to generate a sequence of approximations to a minimum point. R^2 values were computed by

$$R^2 = 1 - \frac{\sum \left(\sigma^{data} - \sigma^{theor}\right)^2}{\sum \left(\sigma^{data} - \overline{\sigma}^{data}\right)^2} \tag{3.1}$$

where σ^{data} are the measured values from experimental data, σ^{theor} are the values computed from the theoretical model, and $\overline{\sigma}^{data}$ are the average of experimental data points.

4.0 A THEORETICAL AND NON-DESTRUCTIVE EXPERIMENTAL APPROACH FOR DIRECT INCLUSION OF MEASURED COLLAGEN ORIENTATION AND RECRUITMENT INTO MECHANICAL MODELS OF THE ARTERY WALL

The objective of this chapter was to develop a constitutive model for the mechanical response of artery tissue that directly includes measured micro-structural data of collagen obtained from multi-photon images. Therefore, this chapter addressed Specific Aim 2 (Section 1.4).

To achieve these objectives, carotid arteries were evaluated in the hUA-MPM system under increasing load. From this analysis, **direct histological evidence that fiber recruitment initiates at finite stretch** was obtained. While this response has previously been described *qualitatively*, until now it has not commonly been used in *quantitative* models of the artery wall.

Therefore, a major contribution of this work was **the development of a new model combining abrupt and distributed fiber recruitment**, which represents collagen fiber recruitment as initiating at a finite strain, with subsequent gradual fiber recruitment represented by a probability distribution function.

Furthermore, **histological results confirmed the collagen fiber orientation distribution to be distributed primarily over a single plane**, defined by the axial direction of blood flow and the circumferential direction. Thus, **a special case of the orientation distribution function termed "planar splay" was utilized to represent the collagen orientation**.

4.1 BACKGROUND

In general, collagen types I, III, IV, V, and VI have been identified in the artery wall, with type I mostly identified in the adventitia with some present in the media, type III distributed throughout the wall with a large concentration in the adventitia, type IV throughout the media, and type V and VI mostly confined to the adventitia [104]. However, the location and distribution of these collagen types varies in different arteries as well as with age and disease.

Medial collagen fibers have been assumed to dominate the passive mechanical response under physiological conditions [105]. From analysis of fixed artery tissue under various applied extensions [38, 39], the medial collagen fibers are considered to be aligned along the circumference in the media (Fig. 24). These fibers have been shown to exhibit a distribution primarily in the plane defined by circumferential and axial direction, termed planar splay [87, 86].

While adventitial collagen may play a critical role in the response during physiological pressures, it has been considered to serve primarily as a protective sheath to prevent rupture during hyperinflation, so the focus of this work was on the media, leaving the adventitia for future study (see the discussion in Section 4.4).

In 1957, Roach and Burton [16] provided indirect evidence that elastic fibers are primarily responsible for resisting deformation at low pressures, while at higher pressures collagen is the predominant load bearing constituent. They showed that the slope of the elastic response curve at high pressures was not significantly altered after elastin was digested using trypsin, but the slope was significantly altered at low pressures. The initial radius of the artery increased after removal of elastin. Thus, they claimed that elastic fibers are mainly responsible for tension at low pressures and have a minor role at higher pressures.

In contrast, using formic acid degradation of collagen, they showed that the slope of the elastic response curve was significantly reduced at high pressures, and that the initial radius of the artery decreased after collagen removal. They concluded that "at low pressures, only the elastic fibers have reached their unstretched length, but as the

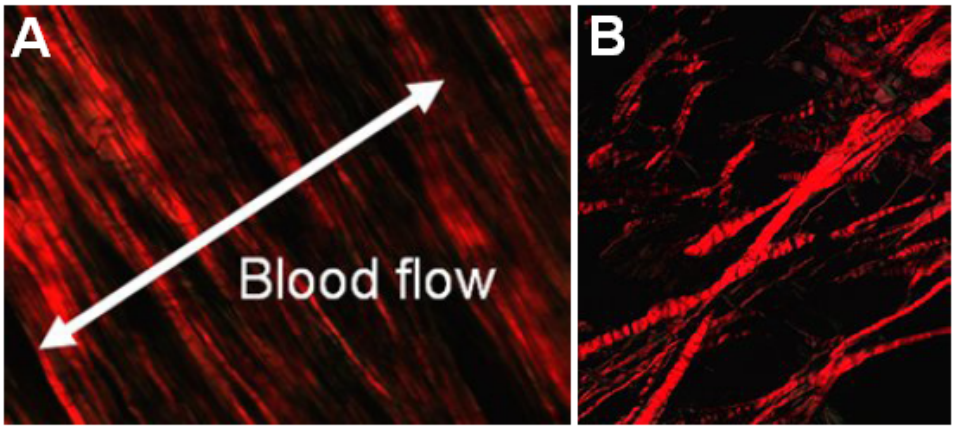

Figure 24: Picrosirius red-stained tangential section of an artery wall, revealing collagen fiber orientation, through birefringence visualized under polarized light, in the media (A) and the adventitia (B). Note medial collagen fibers are oriented primarily perpendicular to the blood flow direction. Histological methods are described in the Appendix A

pressure is increased, more and more of the collagenous fibers of the 'fibrous jacket' reach their unstretched length" [16]. Thus, the passive mechanical response of the artery wall has been assumed to be dominated by an isotropic "elastin-dominated" contribution of the extracellular matrix at low pressures, while the crimped circumferentially-oriented medial collagen fibers gradually unfurl and begin load bearing under increasing pressure [40, 16, 17].

Modeling approaches have been taken, assuming the recruitment of these fibers begins (i) at infinitesimal strain with abrupt recruitment, (ii) at finite strain with abrupt recruitment, (iii) at infinitesimal strain with gradual recruitment of all fibers, and, in this work, (iv) at finite strain followed by gradual recruitment.

Traditionally, fiber recruitment has been modeled as beginning at infinitesimal strain with abrupt recruitment (i), e.g., Model A in Table 2 [14]. Based on results from previous damage testing [17], an abrupt collagen recruitment model (e.g., Models B and C in Table 2), which considers the activation or recruitment of collagen fibers to begin at a finite strain (ii), was developed for arteries [50, 61, 64].

Previous approaches have considered the collagen contribution as been modeled as beginning at infinitesimal strain (iii), with the gradual fiber recruitment described using a probability distribution function (PDF) (e.g., Model D in Table 2). For example, the measured biaxial mechanical response and distribution of fiber orientation from small angle light scattering of heart valve tissue [58, 15] has been directly incorporated into a structurally motivated constitutive model [59], with the parameters of the gradual recruitment PDF obtained from a least-squares fit. Additionally, using a staining protocol with confocal microscopy, collagen fiber recruitment has been has been quantified in rabbit carotid arteries and modeled with a similar gradual PDF beginning at infinitesimal strain [65].

In the current work, the new hUA-MPM system, which combines uniaxial stress-strain analysis with microscopic imaging, was used to evaluate the mechanical and microstructural recruitment of medial collagen fibers in the common carotid artery of New Zealand white rabbits.

Collagen recruitment and fiber orientation were directly assessed from studies of circumferentially loaded tissue samples. Distribution of fiber tortuosity was evaluated from three-dimensional volumetric renderings of the artery wall. Fibers were defined as recruited when this tortuosity decreased below a critical level. The collagen fiber orientation was calculated using a method that involves the standard Sobel-kernel filter [106, 107, 108] that has previously been used to determine the distribution of fiber angle in tissue-engineered scaffolds [109].

Based on experimental results obtained with this device, a new structurally motivated strain energy function for the artery wall (Model E in Table 2) is developed (iv), strongly motivated by the theoretical work of Lanir [56, 57] and the experimental work of Sacks [15]. In contrast to previous models (A, B, C, and D), in this model, fiber recruitment begins at finite strain with gradual recruitment stretches modeled using a PDF. The measured structural and mechanical data taken with the hUA-MPM system are directly incorporated into this constitutive model. For comparison, the data are also used to assess the other constitutive models with different levels of measured structural content. The utility of each model is discussed.

4.2 METHODS

Arterial wall tissue was modeled as a homogeneous, incompressible, multi-mechanism [61, 64] hyperelastic material (Section 2.1.6). The passive anisotropic mechanical response of arteries was assumed to be dominated by collagen fibers, with the other constituents, primarily elastin, contributing to the passive response as an isotropic ground matrix. Thus, the strain energy function was given with an additive decoupling of the isotropic and anisotropic responses (eq. 2.76) [49]. A neo-Hookean model was used for the isotropic response, based on previous work (see Sections 5.1 and 5.4). Five functional forms were chosen for the anisotropic portion of the strain energy function. The fiber orientation distribution analysis is described in Section 4.2.1, and quantification of fiber recruitment is described in Section 4.2.2. The testing protocol is described in Section 4.2.3.

4.2.1 Collagen Fiber Orientation

Based on observations of the orientation of collagen in the artery wall (See Section 4.1), the passive anisotropic response of the artery wall was assumed to be dominated by medial collagen fibers whose orientation were confined to a single plane, described previously as fan splay (Section 2.2.3.4) [87, 86] (Fig. 6). Thus, the recruitment distribution, as well as fiber properties, were independent of ϕ in Fig. 5 .

Stacks of MPM images of the collagen fibers taken with the MPM were superimposed with Imaris software (Section 3.2) and imported into MATLAB, in which a custom program was used to determine fiber distribution (Section 4.2.1.1 below) to determine the orientation distribution function $\hat{\rho}_{2D}(\theta)$.

4.2.1.1 Orientation Analysis Collagen fiber orientation methods were determined using a method [106, 107, 108] that has previously been used to determine the distribution of fiber angle in tissue-engineered scaffolds [109]. Superimposed image stacks of collagen were imported to MATLAB, in which a custom program was written to obtain collagen

alignment, based on previous methods [109, 107, 108]. This method utilizes a variation of the Sobel operator to obtain pixel intensity gradient. Specific details of the method were given in previous publications [109, 107, 108], and have been highlighted here. A histogram of dominant local orientations was computed from an edge detection algorithm, with custom software developed in MATLAB. Edge detection was performed by convolving two masks of a selected size s, one horizontal and the other vertical, with the image at each pixel, to give gradient measures Gx and Gy, respectively. The vector containing the sum of the squares of the convolved horizontal and vertical gradient measures was used as a weighting function ($G = Gx^2 + Gy^2$), while the direction at each pixel was computed as the inverse tangent of the gradient measures ($\tan^{-1}$Gx/Gy). The histogram for direction vector calculation as constructed by defining a subregion with a given size and computing the direction associated with the highest weighted value in the subregion.

A weighted accumulator function (see [107] & [109] for specific details) was implemented over this subregion, and the summed gradient-weighted contribution of each pixel was determined for each angle on the domain $[-90\,^\circ, 90\,^\circ]$ at $1\,^\circ$ increments. The dominant orientation was identified as the maximum accumulator bin value within a sub-region, and values representing each bin were accumulated in a histogram to define the collagen fiber orientation distribution. The direction at $90\,^\circ$ ($\mathbf{e}_2$), or $-90\,^\circ$,was defined as the North-South direction along the vessel axis, while $0\,^\circ$ ($\mathbf{e}_1$) was defined as the West-East direction along the circumference. The fiber distribution data were normalized to satisfy eq. 2.117 using the trapezoid rule.

Three points were selected and averaged for background intensity, and grayscale values falling below this level were disregarded. The MPM image stacks were imported into MATLAB and superimposed, giving a 2D projection from the 3D stacks. Vertical and horizontal mask sizes were 7x7 pixels (s = 3). Subregion size for direction vector calculation was 4x4 pixels.

For all specimens, the collagen orientation probability distribution function $\hat{\rho}_{2D}(\theta)$ was evaluated at maximum stretch to avoid artifacts from crimped fibers. A "pull-back" operation (Eq. 2.122) was performed to obtain the fiber distribution in the appropriate reference configuration.

4.2.2 Collagen Fiber Recruitment

Five anisotropic models (Section 2.2.3) were considered (Table 2). In Models A and B, the fibers were assumed to be oriented circumferentially, with no orientation distribution (θ set to 0), and recruitment occurred abruptly at finite strain. All the fibers were assumed to have the same "activation" stretch λ_a, so the strain energy of the fiber ensemble was given as

$$w_f = \hat{w}_f(\lambda_f^2) = \hat{d}_1(\lambda_f^2)\hat{w}_f^*(\lambda_t^2) \tag{4.1}$$

where, as in [64], the activation criterion was given as

$$\hat{d}_1(\lambda_f^2) = \begin{cases} 1 & \lambda_f^2 \geq \lambda_a^2 \\ 0 & \lambda_f^2 < \lambda_a^2 \end{cases} \tag{4.2}$$

Model A considered the fibers to be recruited at infinitesimal strain, while Models B and C considered all fibers to be recruited at a given finite strain. In all of these three models, an exponential response function was used to represent the anisotropic behavior in the nonlinear regime. The recruitment function d_1 for B and C was given as a unit step function.

Models D and E treated the response of each recruited fiber as exhibiting simple dependence on the true stretch modeled as neo-Hookean, with the distribution of activation lengths represented by a probability distribution function (PDF). In Model D, fiber recruitment was assumed to occur at infinitesimal strain. Model E was a combination of abrupt and distributed models, in that no collagen activation occurred until finite strain, and afterwards the recruitment of fibers was modeled as gradual, using a probability distribution function.

The recruitment functions were depicted graphically (Table 2), by using illustrative plots for each of the functions (as in Fig. 4 of [80]) and by using the disconnecting hook model of Wiederhelm, in which the isotropic matrix was represented as a single spring engaging with the tissue, and collagen fibers were represented a number of springs that engage at various levels of tissue extension (see [110] and [111]).

Table 2: Five forms of the anisotropic strain energy function considered for collagen

	Model A	**Model B**	**Model C**	**Model D**	**Model E**
			Fiber strain energy		
w_f^*	$\frac{\eta}{\gamma}\left[e^{\gamma(\lambda_t^2-1)}-1\right]$	$\frac{\eta}{\gamma}\left[e^{\gamma(\lambda_t^2-1)}-1\right]$	$\frac{\eta}{\gamma}\left[e^{\gamma(\lambda_t^2-1)}-1\right]$	$\frac{\eta}{2}\left(\lambda_t^2-1\right)$	$\frac{\eta}{2}\left(\lambda_t^2-1\right)$
			Fiber recruitment		
	Abrupt at $\lambda=1$	Abrupt at $\lambda>1$	Abrupt at $\lambda>1$	Gradual at $\lambda=1$	Gradual at $\lambda>1$
d_1	1	$\begin{cases} 1 & \lambda_a \geq \lambda_{a1} \\ 0 & \lambda_a < \lambda_{a1} \end{cases}$	$\begin{cases} 1 & \lambda_a \geq \lambda_{a1} \\ 0 & \lambda_a < \lambda_{a1} \end{cases}$	$\begin{cases} \Gamma_{PDF} & \lambda_a \geq 1 \\ 0 & \lambda_a < 1 \end{cases}$	$\begin{cases} \Gamma_{PDF} & \lambda_a \geq \lambda_{a1} \\ 0 & \lambda_a < \lambda_{a1} \end{cases}$
	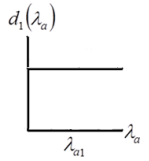	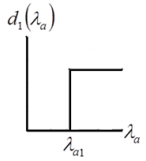	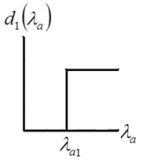	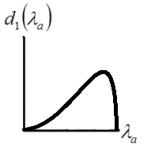	
	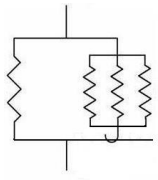	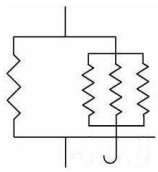	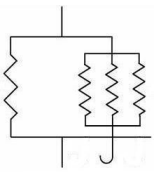	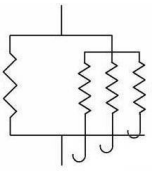	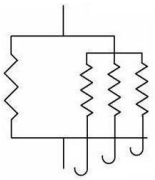
			Fiber orientation		
ρ_{2D}	$\pi\delta[\theta]$	$\pi\delta[\theta]$	general	general	general

The condition that collagen fibers should not bear load under compression was directly imposed through the distribution function, though it can also be imposed using a Heaviside function [11]. As in [59], the form of $\hat{d}_1(\lambda_a)$ was given as a Gamma probability distribution function (Γ_{pdf}):

$$\hat{d}_1(\bar{\lambda}_a) = (\bar{\lambda}_a - \lambda_{a1})^{\alpha-1}\, e^{-\frac{(\bar{\lambda}_a - \lambda_{a1})}{\beta}} \frac{1}{\beta^{\alpha}\Gamma(\alpha)} \qquad \lambda_a \geq \lambda_{a1}, \quad \alpha, \beta > 0, \tag{4.3}$$

where α was the shape parameter, β was the scale parameter, $\alpha\beta$ the mean, $\alpha\beta^2$ the variance, and $\Gamma()$ the Gamma function.

The non-zero location parameter λ_a was introduced to model initiation of collagen recruitment at finite values of strain, as described above. The variable $\bar{\lambda}_a$ was normalized to the interval $\in$[0,1] using $\bar{\lambda}_a$ = (λ_a-λ_{a1})/(max(λ_a)-λ_{a1}), where λ_a was the recruitment stretch at which individual fibers begin to bear load, and λ_{a1} was the tissue strain at which fibers first begin to bear load. The value λ_{a1} was determined from the tortuosity results. It was chosen as the stretch at which the fibers had first become recruited: the stretch at which a single fiber was observed to exhibit tortuosity above the critical value of 1.02.

Recruitment was quantified through the thickness of the vessel wall, by performing the tortuosity analysis on the 3D MPM stacks in Imaris. Tortuosity was defined as the arc-chord ratio, $\tau = s/l$, the ratio of the length along the curve (the arc length, s) to the chord length, l. Fiber arc length was measured in 3D reconstructed images by using the Filament function in Imaris (Bitplane, Switzerland), a fast marching algorithm that is a generalization of the 2D method described in [112]. The chord length was determined as the best fit line to the fiber trace. Note that it was important to use the best fit line, so that the chord length is not dependent upon the choice of the end points. Further, an advantage of using the 3D renderings was that longer fibers may be traced than with 2D methods, since portions of fibers that travel out of the plane, or that overlap, may be included. As the chord length increased, the tortuosity approximation improved [113].

It was important to quantify only the *crimp* of the collagen fibers, not larger scale undulations. It was clear from the images that this crimp period was on the order of a few microns. Some fibers were found to display large tortuosity with periods on the

order of tens of microns. Upon further investigation using stains for cell nuclei, it was determined that these large periods were associated with fibers passing around smooth muscle cells (Fig 25). With our method of determining the arc-chord ratio, curvature with periods on the order well above the crimp period gave significant results. Thus, fibers were manually selected by the operator, omitting those with curvatures exhibiting long periods that have been associated with smooth muscle cell nuclei. Only fibers which did not exhibit this large curvature were included.

The stretch at which each image was taken was blinded to the operator to reduce bias. Tortuosity was determined for at least 20 fibers per image. Images were taken at 6 different stretch values per specimen. Fibers were defined as recruited when the tortuosity decreased below a $\tau_{critical}$ of 1.02. Percentage of recruited fibers at a given stretch were computed and placed into bins. The parameters α and β in Eq. 4.3 were obtained by fitting the corresponding cumulative Gamma distribution function to the data using the Levenberg-Marquardt nonlinear least squares method (Section 3.4).

4.2.3 Testing Protocol

Tissue testing and microstructural analysis were performed on fresh artery segments, with the methods for combining stress-strain analysis and histological analysis from the hUA-MPM outlined in Fig. 26.

Samples (n = 8) of left and right rabbit carotid arteries were obtained from New Zealand white rabbits, sacrificed for other studies that did not interfere with the carotid arteries or the circulation. A sample of artery tissue was removed from its source, opened longitudinally, manually cut into a "dumbbell" shape, so the long axis of the bone was oriented along the circumference of the vessel. Thickness (H) and width (W) were measured 5x times with calipers and averaged.

The tissue strips were loaded in the hUA-MPM (Section 3.3.1) system with the intimal side facing the MPM lens, and oriented for extension in the circumferential direction. The tissue was subjected to uniaxial extension with a triangular displacement curve, at 19μm per second.

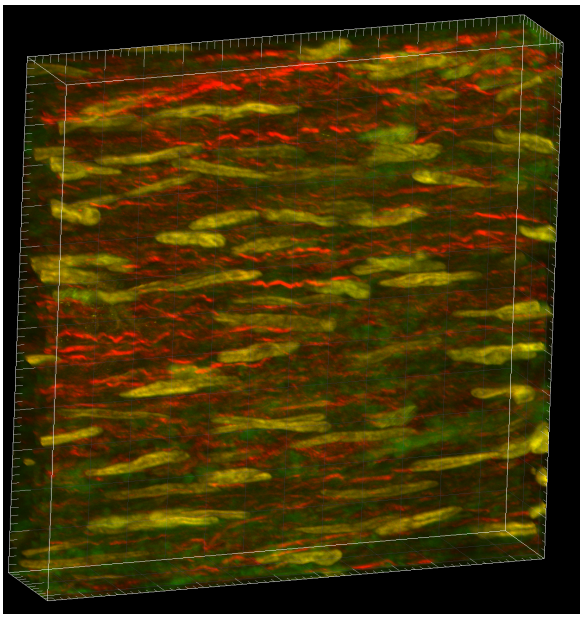

Figure 25: 3D rendering of the rabbit carotid artery wall, stained for nuclei with Hoechst staining (yellow). Collagen and elastin are shown in red and green, respectively. Scale ticks are 2μm

Force and displacement were recorded from the last cycle, post pre-conditioning of at least 5 cycles. The average of 100 voltage data points taken from the load cell per acquisition were converted to force by multiplying a calibration factor in a subroutine, or "sub-VI" in LabVIEW. Force data was filtered post-testing with *filter.m* in MATLAB (The MathWorks, Inc.), a direct form II transposed implementation of the standard difference equation, to reduce noise from system vibration. Displacement of the clamps was used for strain measurement. Official L_0 was determined after testing by performing linear regression of the toe region of the stress-position plot. First Piola (engineering) stress P_{11} (eq. 2.51) was computed by dividing force by the original cross sectional area, with area calculated as specimen width (A) multiplied by wall thickness (H), both measured with calipers. First Piola Stress was converted to Cauchy stress (per unit area of the deformed configuration) by standard techniques (eq. 2.51) [9], assuming volume was preserved in the deformation.

Testing/imaging was performed in 0.9%w/v saline. The tissue was tested until 1.0±0.2N of maximum force was recorded after preconditioning. Following uniaxial testing, the tissue was extended and held at 6 levels of (increasing) stretch, and the MPM was lowered for imaging (Fig. 12)

4.2.4 Stiffness constants

Since uniaxial testing was performed with the fiber orientation distribution modeled as planar splay, the solution of the boundary value problem given in Section 2.3.4 was used. Stress-stretch data from uniaxial testing were fit to the equation using a nonlinear regression analysis (Section 3.4)

Once d_1 and $\hat{\rho}_{2D}(\theta)$ were determined from the imaging data, the remaining material constants μ and η for Models D and E were obtained from a nonlinear least-squares regression analysis of the stress-stretch data and a numerical solution for uniaxial stretch for the material models defined in eqs. 2.151, 2.141, 2.118, 2.138 & 2.96 and in Table 2. Material constants (μ, η, γ) for Models A, B, and C were obtained by a least squares fit, and by including measured values λ_{a1} for Model B and λ_{a1} and $\hat{\rho}_{2D}(\theta)$ for Model C.

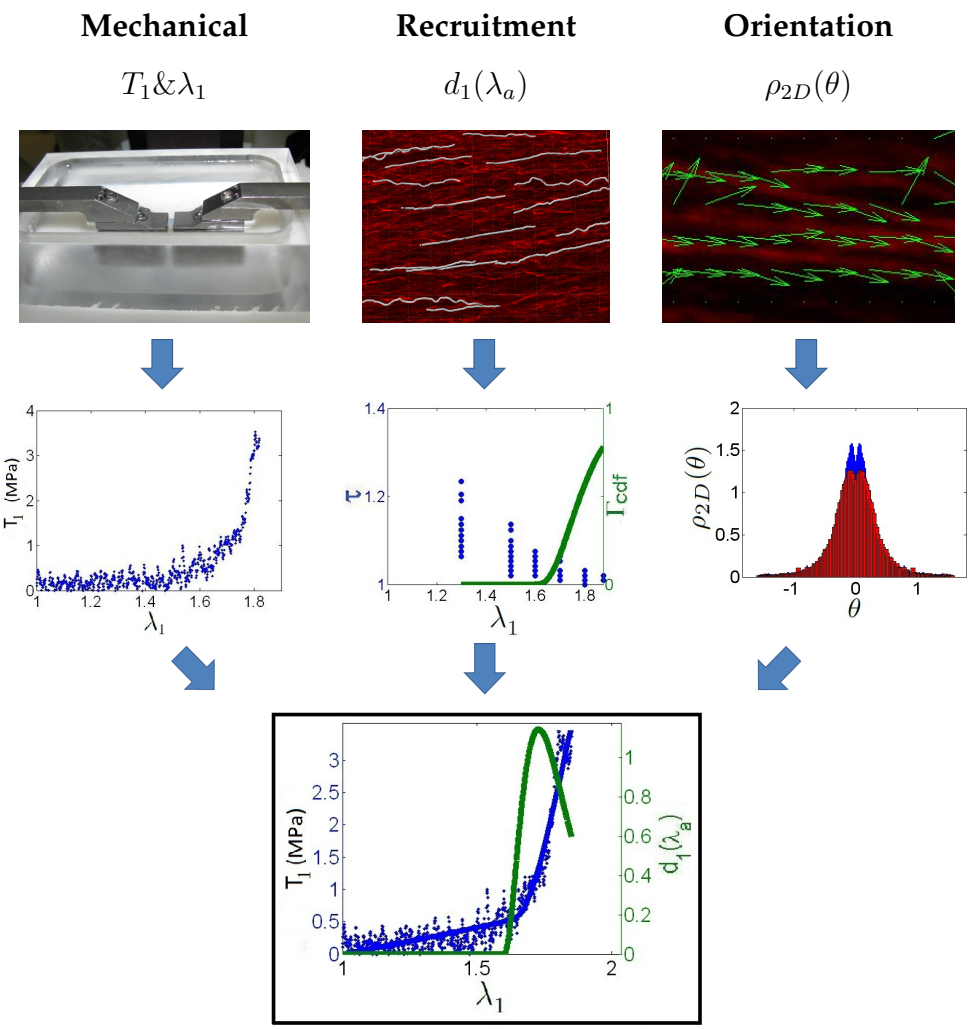

Figure 26: Illustration of the methodology used to determine model parameters. Top row, left to right: specimen of carotid artery between the clamps of the hUA-MPM device; illustration of collagen recruitment analysis; depiction of collagen orientation analysis. Middle row, left to right: raw stress-stretch results from testing; tortuosity data and the Gamma cumulative distribution function plotted against stretch; orientation distribution histogram. Bottom: final results from hUA-MPM testing of a rabbit carotid artery. Raw (blue dots) and fitted (blue line) stress-stretch data from uniaxial tension tests in the circumferential direction are plotted along with the recruitment probability distribution function (green line).

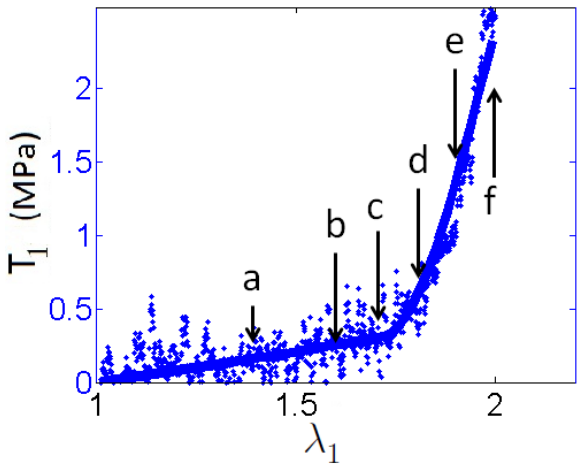

Figure 27: Raw (blue dots) and fitted (blue line) data from uniaxial extension of a rabbit carotid artery, plotted alongside the recruitment function (green line) (associated MPM images given in Fig. 28)

4.3 RESULTS

Mechanical data (Fig. 27) and fiber tracings for fiber crimp were obtained with associated 2D projected MPM images (Fig. 28), at increasing stretch, for one illustrative example (Sample 01). In this case, n=1,037 data points were obtained in the loading cycle, with full extension timed at 1 minute 43 seconds from the unloaded configuration. A clear toe region was identified in the stress-strain response of the carotid artery (Fig. 27). The curve began to bend upward as more and more collagen fibers became uncrimped to bear load. Crimped fibers were observed at low circumferential stretch, and fiber tortuosity greatly diminished at the largest stretch. In this example, the most dramatic increase in fiber recruitment apparently occurred in a strain region of about 20%, between $\lambda_1 = 1.70$ and $\lambda_1 = 1.90$ (Fig. 28). The collagen uncrimping process seemed to have initiated by Fig. 28(c) with increasing straightening up through Fig. 28(d-f). The process was quantified through the tortuosity, (Fig. 26 *second row, middle column*), and this observation was confirmed by the quantitative assessment of tortuosity, with $\lambda_{a1} = 1.7$ (see Sample 01 in Table 3).

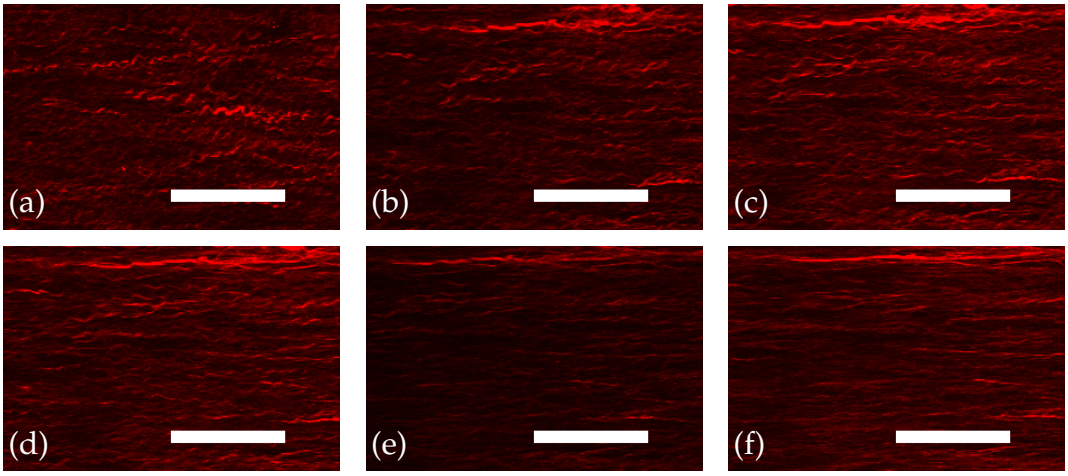

Figure 28: Multi-photon images (MetaMorph) of collagen at stretches of (a) 1.40, (b) 1.60, (c) 1.70, (d) 1.80, (e) 1.90, and (f) 2.00, corresponding to Fig. 27. Bars = 50μm

The model fit the data from each specimen quite well (Table 3 and Fig. 29), with R^2 values close to unity. Here, the geometry of the sample was defined by the original circumference of the vessel (C), the initial clamp-to-clamp distance (L_0), the width of the specimen in the center of the dumbbell-shape (w), and the thickness (H). Parameters were given with 95% confidence interval, and average values were reported in the final column.

4.3.1 Fiber Recruitment

Based on measurements of fibers traced in 3D reconstructed volumes (Figs. 28, 30, and 31), collagen recruitment was found to initiate at finite tissue stretch using a predefined critical tortuosity ($\tau_{critical}$) of 1.02. These stretch values were well above the unloaded value of 1.0, supporting the choice of the new model (E) as most accurately describing the response. Furthermore, with this model, the non-zero portion of the recruitment distribution function d_1 corresponded to the nonlinear portion of the stress-strain curve (Fig. 29). Raw tortuosity data and the fitted cumulative recruitment function revealed that the number of fibers recruited at maximum stretch varied between the specimens (Fig. 31).

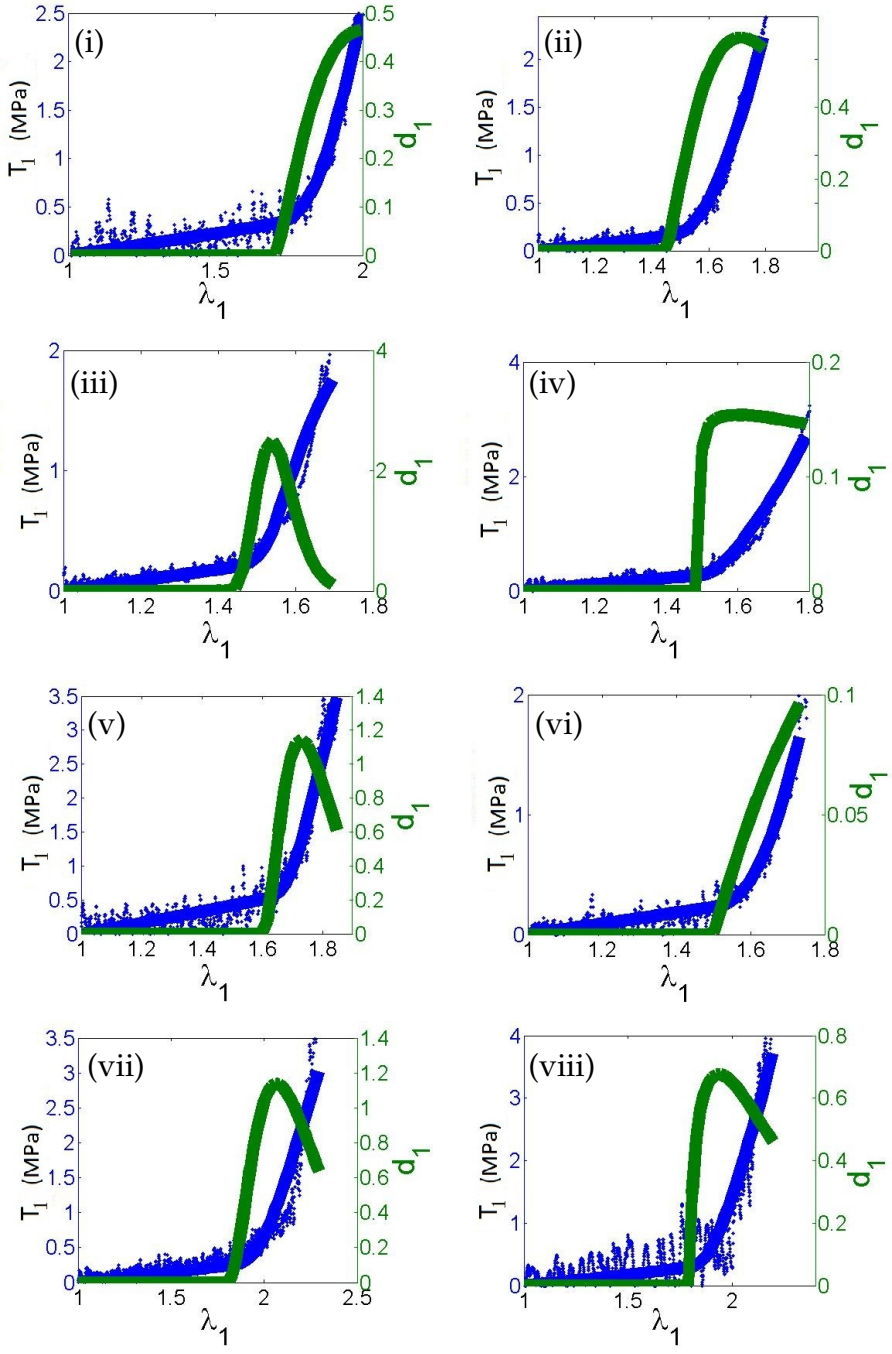

Figure 29: Raw mechanical data from the uniaxial device (blue dots), with fitted response (blue line) and fiber recruitment distribution function d_1 of model E. Specimens 01-08 are labeled with Roman numerals.

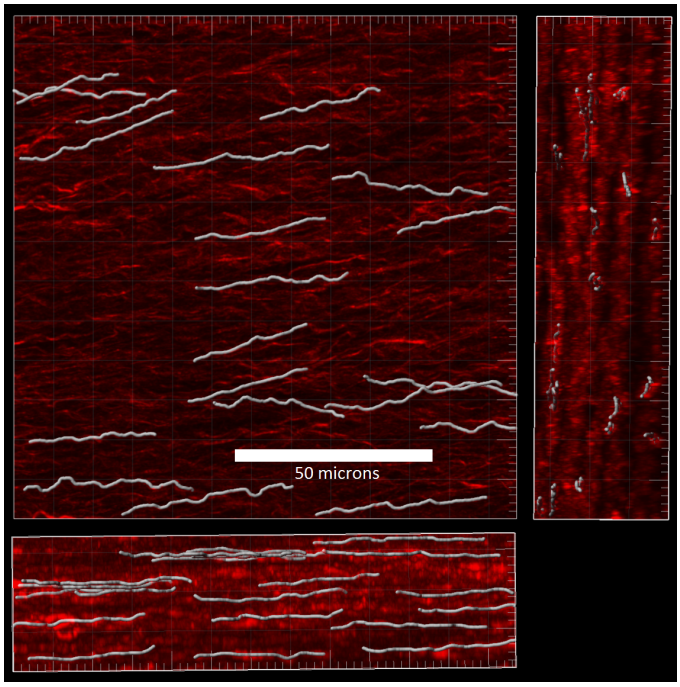

Figure 30: 3D rendering of multiphoton image stacks, revealing collagen fibers with superimposed arc lengths. Bar = 50μm

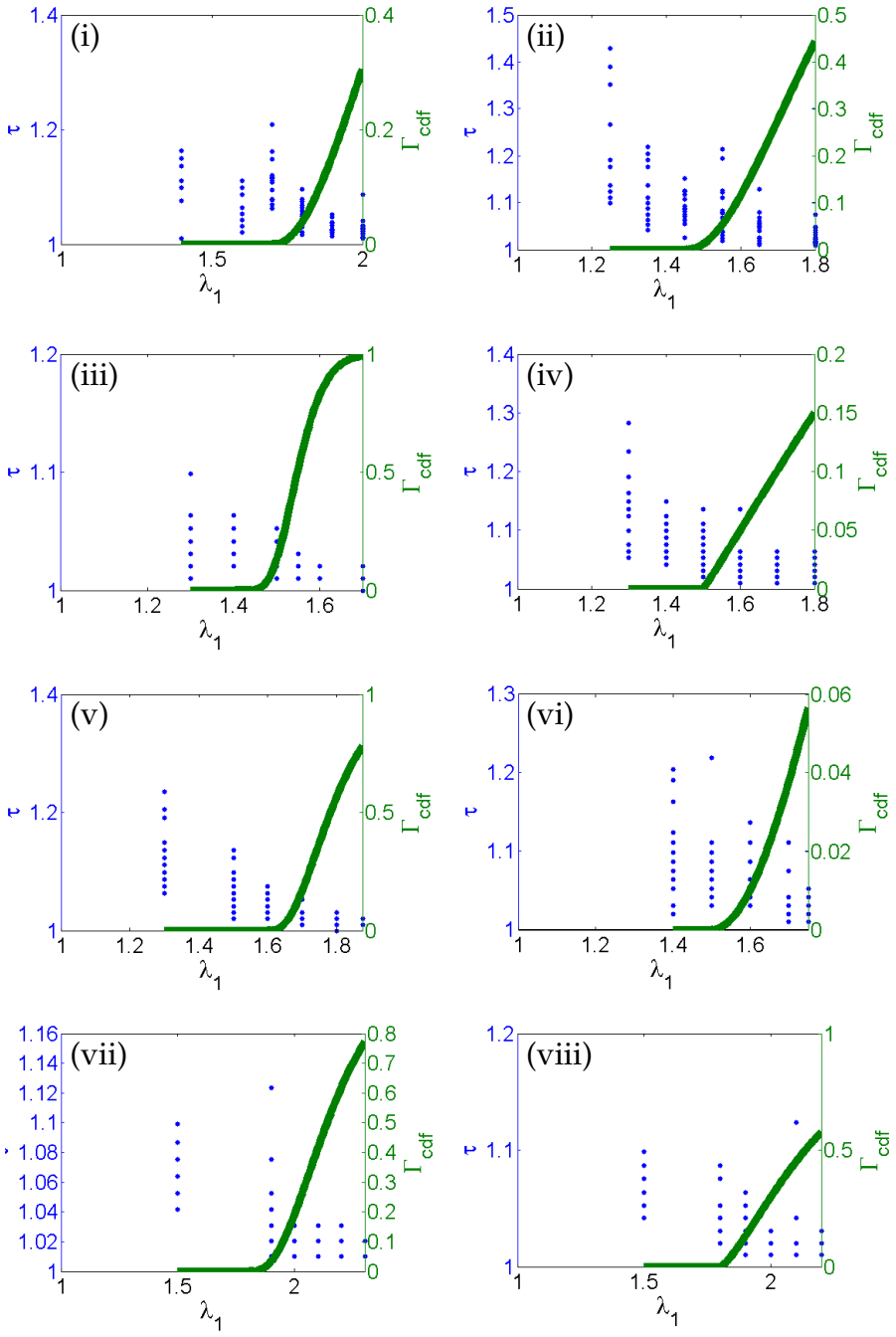

Figure 31: Individual recruitment data (blue dots) with fitted cumulative recruitment distribution function (green line) for each sample. Specimens 01-08 are labeled with Roman numerals.

4.3.2 Fiber Orientation

The 2D superimposed stacks revealed the spatial distribution of fibers in the $\mathbf{e}_1 \otimes \mathbf{e}_2$ plane (Fig. 30, upper left). This image was rotated by 90° about the $\mathbf{e}_2$ axis to reveal the fiber distribution along the blood flow direction, in the $\mathbf{e}_2 \otimes \mathbf{e}_3$ plane (Fig. 30, right), and it was rotated by 90° about the $\mathbf{e}_1$ axis to reveal the fiber orientation distribution in the $\mathbf{e}_1 \otimes \mathbf{e}_3$ plane (Fig. 30, bottom).

Fiber tracings were made on 3D stacks, making it possible to assess the planarity of the fibers (Fig. 30). The angle between the fiber and $\mathbf{e}_1$ was evaluated for a projection of the fiber on the $\mathbf{e}_1 \otimes \mathbf{e}_2$ and $\mathbf{e}_1 \otimes \mathbf{e}_3$ planes at activation stretch. The results for all fiber traces at the activation stretch were depicted in Fig. 32. The average angles for the these two projections were found to be $9.25^o \pm 2.4^o$ and $1.6^o \pm 0.74^o$, respectively. Hence, results from the orientation analysis confirmed that medial collagen fibers were predominantly oriented about the circumferential direction, with some distribution within the $\mathbf{e}_1 \otimes \mathbf{e}_2$ plane, described as fan splay.

4.4 DISCUSSION

The nonlinear mechanical response of the artery wall has been previously conjectured to be due to the uncrimping of collagen fibers, represented by an upward bend in the stress-strain curve [16]. This uncrimping behavior has been captured phenomenologically with exponential strain energy functions [8], and structurally-motivated approaches have introduced distribution functions that may be utilized to directly include quantified microstructural information regarding collagen activation into the constitutive response [56, 57, 67, 68].

Here, the response was modeled using a strain energy function, additively decoupled into the "collagen-dominated" anisotropic portion and the "elastin-dominated" isotropic portion. In the former, five constitutive models were considered, with increasing levels of measured microstructural data included (Table 2). High R^2 values were obtained for

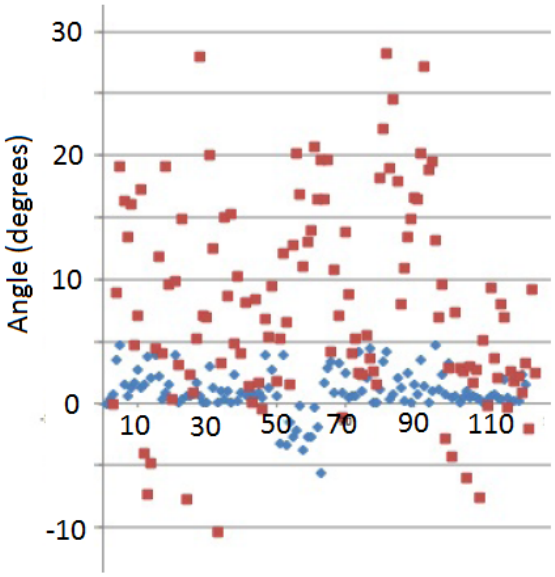

Figure 32: Distribution of magnitude of angle between fiber and $\mathbf{e}_1$ axis for (a) projection on $\mathbf{e}_1 \otimes \mathbf{e}_2$ plane (red) and (b) projection on $\mathbf{e}_1 \otimes \mathbf{e}_3$ plane (blue).

each of the models, indicating that each may suitable capture the nonlinear response of the artery (Table 3), though not necessarily capturing the underlying microstructural behavior.

When limited microstructural information is available, the more phenomenological models (A, B & C) may be utilized. However, to gain further insights into the mechanism behind the mechanical response of the vessel wall, more structurally-motivated models are necessary (D & E). Each model has its advantages and disadvantages with respect to number of parameters and degree of structural data included, and these are discussed in more detail below. Further, the pros and cons of each model are summarized in Table 4.

Using a predefined critical tortuosity of 1.02 (See Appendix D), collagen recruitment was found to initiate at finite strain. Recruitment initiation stretch was based on measurements of 3D reconstructed fibers. These values were well above the unloaded stretch value of 1.0, supporting the choice of the new model (E) as most accurately describing the microstructural response.

Table 3: Geometric measurements, distribution function parameters, and material constants ($\pm$ 95% confidence interval) determined by the least-squares fit to the stress-stretch data from uniaxial testing of rabbit carotid arteries, with averages of parameters. C = vessel circumference, L_0 = specimen initial length, w = specimen width, H = thickness

Sample	01	02	03	04	05	06	07	08	AVG
Geometry									
C (mm)	4.3	4.2	4.0	4.2	4.0	4.3	4.5	4.2	4.2
L_0 (mm)	2.0	2.0	2.0	2.0	2.0	2.0	2.0	2.0	2.0
w (mm)	4.4	3.6	5.0	3.9	3.8	4.3	4.3	3.7	4.1
H (μm)	112	134	124	116	96	154	102	102	118
Model A									
λ_{a1}	1.00	1.00	1.00	1.00	1.00	1.00	1.00	1.00	1.00
μ (kPa)	110±43	14±80	120±40	170±60	98±150	110±42	130±19	130±73	110
η (MPa)	5.7±8.1	87±72	15±12	28±25	65±99	7.5±10	0.24±0.26	4.4±8.7	27
γ	2.6±0.57	2.2±0.47	3.8±0.52	3.0±0.50	2.3±0.78	3.7±0.80	2.7±0.29	2.3±0.62	2.8
R^2	0.9977	0.9989	0.9994	0.9991	0.9965	0.9988	0.9990	0.9949	
Model B									
λ_{a1}	1.70	1.45	1.40	1.50	1.60	1.50	1.80	1.80	1.59
μ (kPa)	120±31	96±38	150±27	220±32	220±69	130±26	87±33	110±63	140
η (GPa)	5.5±13	0.13±0.081	0.49±0.26	2.0±1.6	3.1±8.7	5.4±8.6	6.5±9.8	6.2±18	9.8
γ	19±6.7	15±2.9	23±2.9	21±3.2	18±8.6	24±5.8	20±4.3	18±7.6	20
R^2	0.9974	0.9990	0.9994	0.9993	0.9965	0.9989	0.9972	0.9940	
Model C									
λ_{a1}	1.70	1.45	1.40	1.50	1.60	1.50	1.80	1.80 1.59	
μ (kPa)	140±28	100±35	160±25	230±27	230±66	140±26	140±17	160±52	160
η (MPa)	3.4±1.6	2.6±0.8	1.3±0.4	4.5±1.1	11±5.8	3.1±1.4	0.36±0.16	3.4±2.3	3.7
γ	6.0±2.2	3.8±1.1	6.8±1.0	4.8±1.1	2.7±3.2	6.3±2.4	8.7±0.97	6.4±2.4	5.7
R^2	0.9977	0.9990	0.9994	0.9995	0.9966	0.9988	0.9990	0.9950	
Model D									
λ_{a1}	1.00	1.00	1.00	1.00	1.00	1.00	1.00	1.00	1.00
α	32 ± 39	16 ± 3.3	130 ± 74	8.3 ± 5.3	62 ± 40	14 ± 36	40 ± 46	24 ± 41	41
β ($x10^{-3}$)	34 ± 45	65 ± 14	6.0 ± 3.4	180 ± 150	14 ± 9.0	110 ± 360	22 ± 26	41 ± 74	59
R^2	0.9287	0.9977	0.9944	0.9755	0.9886	0.8718	0.9403	0.8585	
μ (kPa)	130±24	83±28	140±40	110±52	230±55	120±24	77±38	75±62	120
η (MPa)	22±2.1	15±1.0	4.2±0.45	54±5.2	12±1.3	120±11	6.3±0.79	17±2.5	31
R^2	0.9977	0.9991	0.9978	0.9982	0.9969	0.9988	0.9947	0.9930	
Model E									
λ_{a1}	1.70	1.45	1.40	1.50	1.60	1.50	1.80	1.80	1.59
α	2.5 ± 3.0	2.4 ± 0.22	9.4 ± 5.3	1.1 ±0.018	3.3 ± 1.3	2.0 ± 3.8	3.5 ± 3.5	1.5 ± 2.3	3.2
β ($x10^{-2}$)	67 ± 120	54± 6.5	5.4 ± 3.1	530 ± 23	22 ± 9.2	250 ± 1000	22 ± 24	74 ± 160	130
R^2	0.9198	0.9996	0.9942	1.0000	0.9957	0.9012	0.9568	0.8809	
μ (kPa)	140±24	110±28	140±47	180±44	260±53	140±23	90±40	110±60	150
η (MPa)	84±8.0	37±2.6	11±1.4	150±14	47±5.5	390±36	20±2.8	46±7.0	98
R^2	0.9976	0.9990	0.9972	0.9984	0.9969	0.9987	0.9939	0.9927	

Table 4: Pros and cons of each anisotropic model for collagen considered

Model	Pros	Cons
Model A	• No fiber quantification necessary	• Collagen recruitment not directly modeled • 3 fitted material parameters (μ, η, γ) • Orientation idealized with single vector, no distribution • Some collagen fibers exceed ultimate strain under physiological conditions
Model B	• λ_{a1} is the only parameter to quantify • Includes collagen recruitment - modeled as abrupt	• Collagen recruitment is only abrupt, not gradual • 3 fitted material parameters (μ, η, γ) • Orientation idealized with single vector, no distribution
Model C	• λ_{a1} is the only parameter to quantify • Collagen fiber orientation included • Includes collagen recruitment - modeled as abrupt	• Collagen recruitment is only abrupt, not gradual • 3 fitted material parameters (μ, η, γ)
Model D	• Includes structural information - both fiber recruitment and orientation • 2 fitted material parameters (μ, η)	• Fiber quantification necessary • Some collagen fibers exceed ultimate strain under physiological conditions
Model E	• Includes structural information • 2 fitted material parameters (μ, η) • Includes structural information - both fiber recruitment and orientation • Most accurately represents underlying physical mechanism	• Fiber quantification necessary

During uniaxial circumferential extension, collagen fibers were observed to initiate uncrimping over a very narrow range (Fig. 28). This range corresponded to a period of increasing slope on the stress-stretch curve (Fig. 27). Thus, the previous conjecture [16] that the mechanical response of arteries is dominated by anisotropic collagen fibers that become recruited at finite strain was validated by this study. This result supports earlier work using models with abrupt recruitment at finite strain when recruitment data is not available (e.g., [61, 64, 2]).

Typically, in a purely phenomenological approach, models with at least two material parameters, such as exponential functions, are needed to capture the highly nonlinear collagen contribution. Thus, at least three parameters are needed for the combined response of elastin and collagen. These higher order equations are utilized for the models A, B, and C. In the original simplified model (A), no histological measurements are included. The fiber orientation is assumed to be directed entirely in the circumferential direction, and the nonlinear stiffening behavior is modeled with an exponential function beginning at infinitesimal strain. Model B is an extension of A, and the only measurable parameter necessary to capture the response is the activation stretch, λ_{a1}, but in both cases, three parameters must be determined numerically (μ for elastin; η and γ for collagen). Model C is similar to B, except the measured orientation data were included. Quantification of the distribution of fiber orientation from histological data is necessary in Model C.

Only two fitted material parameters (μ for elastin; η for collagen) are necessary for the models D and E, with the single neo-Hookean parameter η representing the response of a recruited collagen fiber. In both cases, the orientation distribution and the fiber recruitment distribution must be directly measured. In model D, a distribution function is used to model the gradual recruitment of collagen beginning at infinitesimal strain. In model E, a similar distribution function is used with recruitment beginning at a finite strain, and knowledge of the activation stretch λ_{a1} is necessary. This new theoretical model (E) advances these earlier models (A, B, C, and D) by including a distribution of collagen recruitment stretches d_1 beginning at the activation stretch, λ_{a1}. It is chosen as most accurately representing the tissue response, since no fibers appeared to be recruited at stretches below the critical activation stretch (Figs. 27 & 28). Further, the neo-Hookean

strain energy function is used in this approach, which may be more representative of the response of recruited collagen fibers, which have been shown to exhibit a linear response, with respect to strain, when isolated from the tissue [16].

Finally, an ultimate strain of 50% has been determined previously for isolated collagen [40]. If collagen recruitment were to begin at infinitesimal strain, some collagen fibers would reach their ultimate strain at tissue stretch values above λ=1.5. No clear evidence of collagen fiber failure was observed in the multi-photon images. Therefore, Models A and D were rejected (Table 4) on the basis that, for the range of strain considered in these experiments, collagen failure would have occurred had collagen recruitment begun at infinitesimal strain (See Fig. 29). The good fit of the data and the evidence of initiation of recruitment at finite strain support the use of models previously introduced with abrupt recruitment [61, 64] in cases where collagen recruitment data is not available.

In this work, both the orientation of the fibers and the distribution of recruitment stretch were measured from multi-photon images of collagen. Collagen fiber crimp and orientation were successful quantified for direct inclusion in structural models. Since staining and fixation were not used, collagen orientation and recruitment measurements could be made at multiple stretch values for the same sample. Although other methods may be used to measure and include the fiber orientation distribution in the mechanical response, the method presented here offers the ability to distinguish collagen fibers from other tissue structures. Further, the current methodology provides data at slices through the thickness enabling 3D reconstruction of the tissue structure.

There are some limitations to the study. Biaxial inflation/extension is more clinically relevant than uniaxial loading considering here. However, the cylindrical configuration would make collagen fiber analysis more difficult. The fiber recruitment stretch is reported in terms of the tissue stretch along the circumference rather than the angle-dependent fiber stretch. For this case presented here, medial collagen fibers are tightly clustered about the circumferential direction, so this method is deemed acceptable. Dumbbell shaped specimens were used to diminish some of the end effects from using grip displacement rather than local strain measurements. Further, the fiber recruitment stretch is reported in terms of the tissue stretch along the circumference rather than the angle-

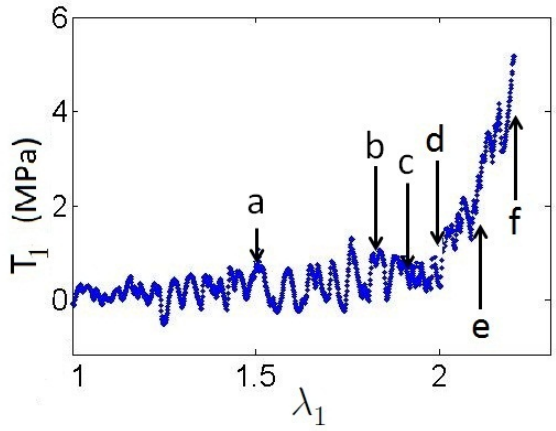

Figure 33: Raw stress-stretch data from uniaxial extension of a rabbit carotid artery (Sample 08 in Table 3, associated MPM images given in Fig. 34)

dependent fiber stretch. Medial collagen fibers are tightly clustered about the circumferential direction, so this method is deemed acceptable. Furthermore, coupling between the isotropic and anisotropic components, residual stresses, and time-dependent effects are not considered in this work.

Methods are currently being developed to automate tortuosity analysis so more fibers can be considered. In the future, layer thickness measurements and volumetric concentrations of wall components will be measured and included in the structurally motivated models.

Finally, as mentioned briefly above (Section 4.1), adventitial collagen has been considered to serve as sheath to protect the artery from damage due to hyperinflation. Its role in the mechanical response was neglected in this study. Preliminary work has been conducted by our group to analyze the role of the adventitia, similar to the approach here taken for the media. Using rabbit carotid arteries, the adventitia was imaged at 6 different increasing values of stretch with the hUA-MPM. Adventitial collagen fibers appeared to be crimped, and thus not recruited until after the transition region in the stress-stretch curve. (Figs. 33 and 34). Future work should involve further quantitative analysis.

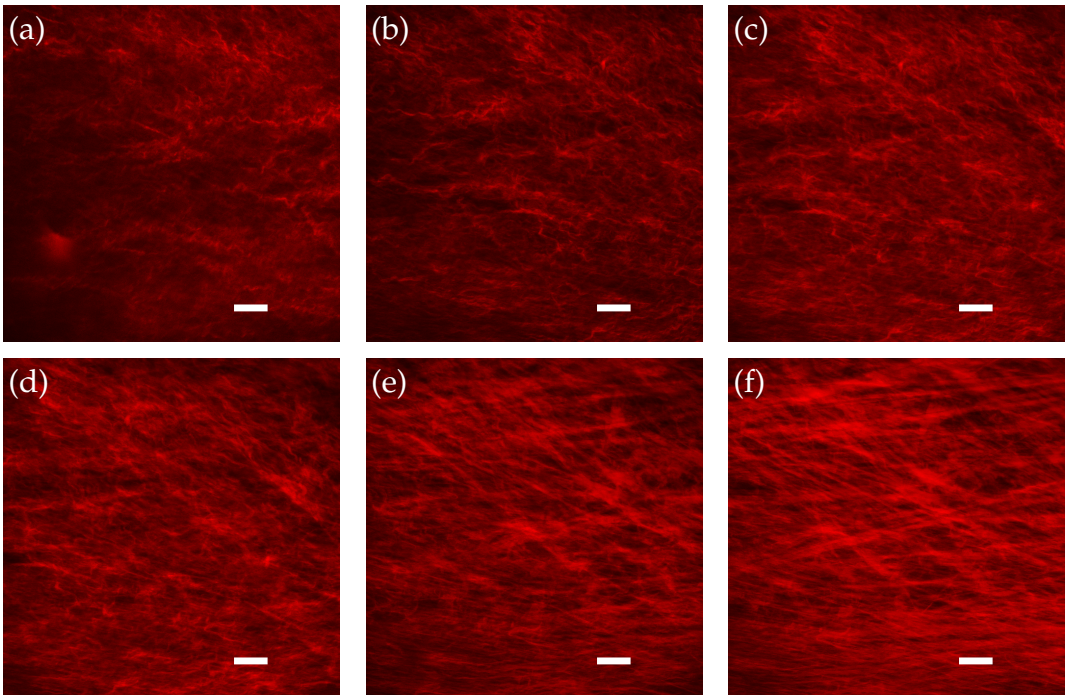

Figure 34: Multi-photon images of the adventitia of a rabbit carotid artery at various stretches: (a) 1.50, (b) 1.80, (c) 1.90, (d) 2.00, (e) 2.10, and (f) 2.20, corresponding to Fig. 33. Bars = 50μm

5.0 EVALUATION OF SUITABLE MODELS FOR THE MECHANICAL RESPONSE OF ARTERIAL ELASTIN

The objective of this chapter was to investigate the structure-function relationship of arterial elastin by using mechanical data acquired from isolated arterial elastin and images of the internal elastic lamina of cerebral arteries. Therefore, this chapter addressed Specific Aim 2 (Section 1.4). Mechanical ring testing was utilized to analyze the mechanical response of elastin isolated from the artery wall. In this work, **various isotropic strain energy function were fit to this data**, and the utility of each choice is described, based on the fit to this data and from comparison to previous reports. However, further analysis on the structure-function relationship of arterial elastin is warranted. Additionally, a parameter known as ligament efficiency is utilized to *quantitatively* capture the distribution of the fenestrations, or holes, in the internal elastic lamina of arteries. Here, **a novel approach of including ligament efficiency in constitutive models to describe the internal elastic lamina** in arteries is presented. This parameter may be very useful in analyzing the artery wall under healthy and pathological conditions, since fenestration size has been correlated with conditions such as hypertension, in animal studies [89, 90]. Further, it is a means of including additional structural information for the elastin mechanism.

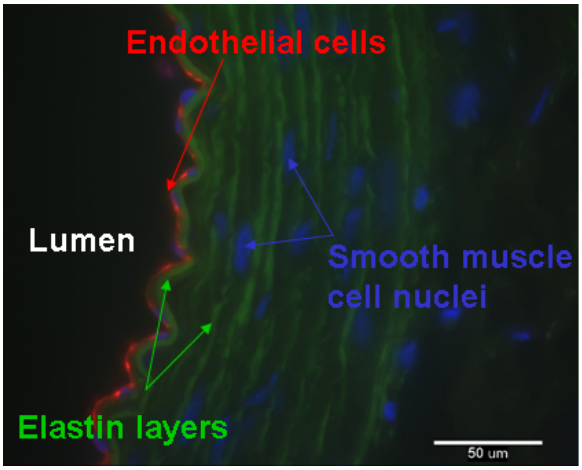

Figure 35: Cross sectional image of a rabbit carotid artery segment, taken with fluorescence microscope. Elastin layers are shown in green due to autofluorescence. Red indicates endothelial cells lining the lumen. Histological methods are given in Appendix A

5.1 BACKGROUND

Elastin is the protein hypothesized to give elastic recoil to arteries and other soft tissues of the body. As discussed in the Introduction (Chapter 1), degeneration and malformation of elastin is indicated in many arterial diseases.

Elastogenesis is a complex process by which pro-elastin is secreted by smooth muscle cells onto a microfibrillar scaffold [114, 115] to form elastin. In the artery wall, the elastin primarily exists in the form of layered sheets (Fig 35), e.g., the internal elastic lamina. Elastin is an insoluble polymer composed of several tropoelastin molecules covalently bound to each other by cross links. It is considered extremely stable, so that, after development is complete (i.e., by the second decade of human life) it degrades and regenerates so slowly that it can be thought to last the lifetime of the organism [114, 116, 117].

Elastin has been isolated by various techniques, and autoclaving has been described as the best method, though other techniques have been considered. In 1942, Hass (see

[118, 119, 120]) isolated elastin from human aortas with formic acid and, by performing uniaxial extension tests on ring segments, showed elastic purified tissue was linear up to the yield point. From this data, Burton [40] reported an ultimate stress of 1.0MPa and a Young's modulus of 0.3MPa for isolated elastin. However, formic acid has been shown to degrade the elastin (see [121] and references therein). By analyzing the tangential modulus of purified elastin compared to native tissue, in 1994, Lillie [121] showed that autoclaving does not affect the mechanical behavior of elastin (uniaxial ring extension tests) [122]. Furthermore, in 2007, Gundiah, Ratcliffe, and Pruitt [123] compared two common elastin purification methods, one involving autoclaving [122] and the other hot alkaline treatment [124], and favored the former for mechanical analysis. In this study, autoclaving methods were used to extract elastin from porcine aortas.

In 1977, Dorrington and McCrum [125] performed uniaxial tests at controlled temperature to 35% strain (to prevent rupture) on aortic elastin, purified by autoclaving followed by fat removal with ethanol/ether rinses and extraction of glycoprotein in sodium hydroxide solution. Likely because the force-length relationships of isolated aortic elastin [125] were linear, neo-Hookean models (Section 2.2.2.1) have been commonly chosen (e.g., [14, 81, 126, 127, 128, 18, 55, 129, 123]) to represent the elastin-dominated isotropic response. In the present work, isolated elastin was tested in a ring testing device. The resulting mechanical data were fit to various isotropic strain energy functions to determine the most appropriate representation for the mechanical response.

Furthermore, histological analysis by our group has revealed the elastin in cerebral arteries to be confined to the inner layer, or internal elastic lamina (IEL) (Fig. 36), consistent with the earlier reports discussed above. Fenestrations, or holes, of various diameter have been observed throughout the IEL (Fig. 36).

Campbell and Roach took a novel approach to modeling a fenestrated sheet. They used a scalar parameter, termed ligament efficiency (LE), or the ratio of solid band of material to centre-to-centre spacing between holes, to characterize the spatial distribution of fenestrations [130, 131]. Furthermore, they developed an equation for ligament efficiency applied to a uniform array of fenestrations and generalized for a nonuniform array of fenestrations. They performed uniaxial tension experiments on latex replicas. One set

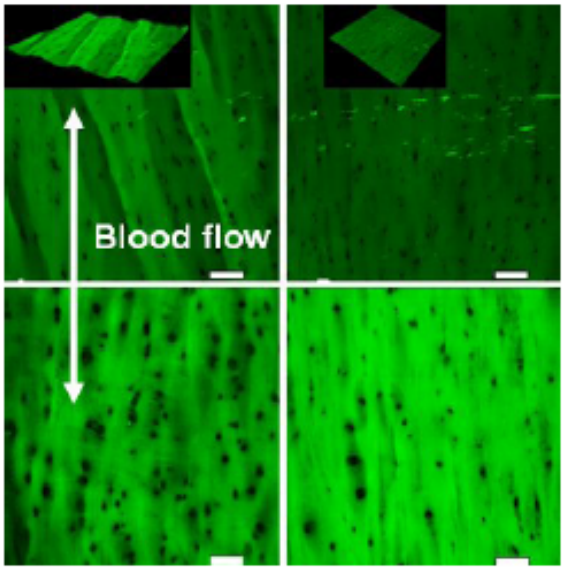

Figure 36: En face confocal microscope images revealing the autofluorescent internal elastic lamina of a human anterior cerebral artery (ACA) fixed in paraformaldehyde under zero (top left) and 30% (top right) strain, (bottom left) a posterior cerebral artery (PCA), and (bottom right) a middle cerebral artery (MCA), both fixed at 30% strain. Note differences in fenestration size and distribution between the PCA, MCA, and ACA. Bars = 50μm. Histological methods are described in the Appendix

exhibited hole patterns taken from scanning electron microscopy images of the internal elastic lamina. The other set consisted of a uniform array of holes, created to give similar ligament efficiency values to the replicas. Comparable results were obtained from the replicas and the corresponding uniform arrangement [34].

The internal elastic lamina is a large layer of elastin located between the intima and media of the artery wall. For the cerebral arteries, most of the arterial elastin lies within this layer. Here, we introduce a new approach to modeling the IEL, whereby the distribution and size of the fenestrae are introduced as a scalar internal variable (Section 2.1.8). Ligament efficiency is quantified in an image of the internal elastic lamina in human cerebral arteries.

5.2 METHODS

Elastin was analyzed from ring tests performed on isolated elastin, and different isotropic models were fit to the data (Section 5.2.1). The suitability of utilizing ligament efficiency as a material parameter was investigated using previous data taken from experiments on rubber, and quantification of LE on a histological image of the internal elastic lamina was presented (Section 5.2.2).

5.2.1 Uniaxial Testing of Isolated Elastin

Raw data (Engineering Stress (eq. 2.51) versus stretch) from uniaxial ring testing of isolated elastin from 2 (porcine) aortas were obtained via a personal communication with Dr. Margot Lillie. Several isotropic strain energy functions, given in Section 2.2.2.1, were fit to the data.

Collaborators (Dr. M. Lillie's group) performed the elastin isolation and mechanical testing experiments and provided our group with the raw mechanical data. Elastic tissue was isolated from porcine thoracic aortas and tested in a uniaxial ring extension device (Fig 37).

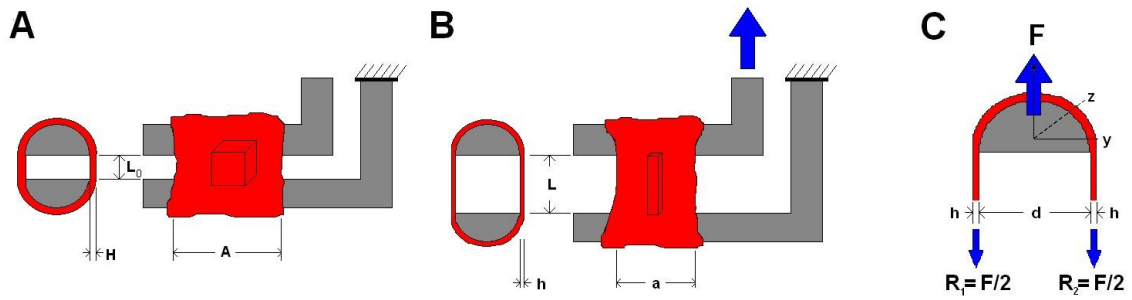

Figure 37: Uniaxial pin extension device. A: Artery ring segment mounted on uniaxial extension device prior to stretching; B: Specimen under uniaxial stretch; C: Free body diagram of setup.

Thoracic aortas were dissected from two approximately 100-kg pigs (5-6 month old) obtained from an abattoir, transported in iced phosphate buffered saline (PBS) and then frozen in PBS at $-20°C$ until experimentation. Aortas were thawed then cleaned of loosely adhering tissue. Tissue more than 40 mm distal to the first intercostal artery was excluded. The elastic tissue was isolated by 8 hours of autoclaving [121] and then stored in a sterile environment until used.

Straight segments of the two purified aortas without branches were sliced into 22 and 17 rings, respectively, of approximately 100mg average dry weight each. The position of the proximal edge of each ring was measured with digital calipers. Location 0mm was taken as the proximal edge of the ring immediately distal to the first intercostal branch, while rings proximal to the first branch were given negative values increasing in absolute magnitude towards the heart.

Quasi-static uniaxial extension tests were performed as described previously [132]. Briefly, the purified aortic rings were placed between two steel bars of a uniaxial pin extension device (Fig. 37) and immersed in distilled water maintained at $37 \pm 0.5°C$. Uniaxial tension was applied with an Instron 5500R tensile testing machine at a crosshead rate of 20mm/min. Specimens were preconditioned by performing two cycles to between 40% and 75% extension. Force (F) and extension were measured on the third cycle.

Lagrangian (engineering) stress was computed by dividing force by twice the original cross sectional area (2AH) (Fig. 37):

$$P = \frac{F}{2AH} \tag{5.1}$$

Area was calculated as ring width (A) multiplied by wall thickness (H), which was measured with calipers and from submerged weight of the ring. The original midwall length, L_0, was determined by linear regression to the stress-length data between the stresses of 50 and 100kPa and regressing to zero load. Stretch ratio $\lambda_1 = L/L0$, was determined from midwall circumferential length, L. First Piola Stress was converted to Cauchy stress by standard techniques (eq. 2.51) [9]. The Cauchy stress versus stretch from the raw data were used to determine the coefficients of the exponential (eq. 2.93), Mooney-Rivlin (eq. 2.95), modified neo-Hookean (eq. 2.98), and Ogden-type (eq. 2.100) strain energy functions by the least-squared fitting method (Section 3.4).

Furthermore, based on the work of Zulliger et al., 2004 [80], Watton, Ventikos, and Holzapfel, 2009 [81] compared different choices of the exponent n for the modified neo-Hookean strain energy function given in eq. 2.98 with reported experimental uniaxial data from isolated arterial elastin [132, 133].

With eq. 2.155, the tangent modulus E_{tan} was computed by (See [81])

$$E_{tan} = \frac{\Delta T_1}{\Delta \epsilon_1} = \frac{\partial \lambda_1}{\partial \epsilon_1}\frac{\partial T_1}{\partial \lambda_1} = \frac{1}{\lambda_1}\frac{\partial}{\partial \lambda_1}\left[\lambda_1 \frac{\partial W_{iso}}{\partial \lambda_1}\right] \tag{5.2}$$

where ϵ_1 was the traditional Green's strain given by $\epsilon_1 = 0.5 * (\lambda_1^2 - 1)$.

Following the method of Watton et al. [81], the coefficient μ of the neo-Hookean strain energy function (eq. 2.98) was determined so that the tangent modulus E_{tan} was equal to 1.12 MPa when the stretch λ = 1.2, consistent with experiments of [133]. The tangent modulus was plotted along with the previously reported corrected [134] and erroneous [133] data, the former being published as a correction of the latter.

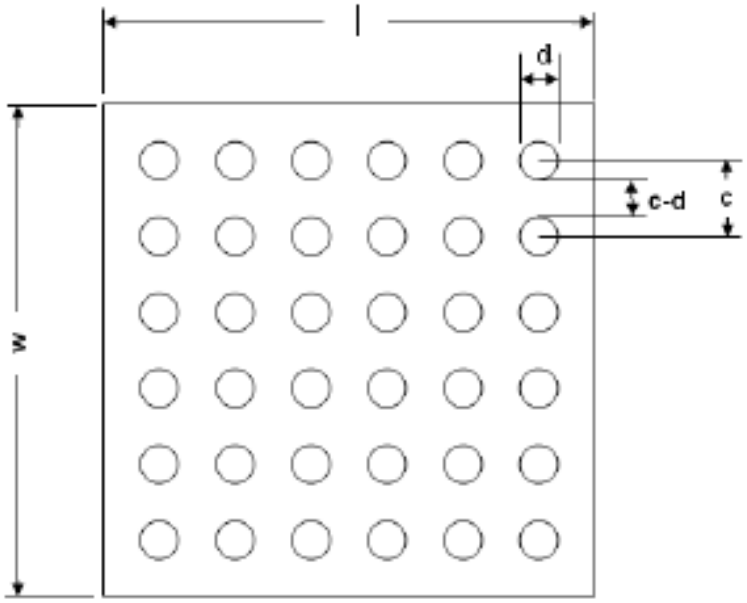

Figure 38: Demonstration of the measurement of LE parameters for a uniform 6x6 array of holes

5.2.2 Ligament Efficiency

Ligament efficiency, a means by which the fenestration properties may be quantified, is utilized to model the internal elastic lamina (IEL) as an isotropic sheet with fenestrations.

Ligament efficiency is included in the constitutive model as a structural parameter. The scalar internal variable (see Section 2.1.8) Φ_{LE}, given as a function of ligament efficiency, is introduced into the response function, similar to the approach used for damage (Section 2.2.4). For any arbitrary distribution of fenestrations, ligament efficiency is calculated as

$$\Phi_{LE} = 1 - \frac{\sum_{i=1}^{n} d_i}{\sqrt{wln}} \tag{5.3}$$

where i is the individual fenestration, d_i is the diameter of the individual fenestration, n is the total number of fenestrations, and w and l are the width and length of the region of interest, respectively.

For the case of a uniform array of holes, eq. 5.3 above reduces to

$$\Phi_{LE} = LE = 1 - \frac{d}{c} \tag{5.4}$$

with the measures depicted in Fig. 38. In eq. 5.4, for the uniform case, d is the diameter of the holes, c is the center-to-center distance for all of the holes, and w is the length of one side of the area of interest.

With this approach, the (isotropic) strain energy function depends on the right Cauchy-Green tensor $\mathbf{C}$ and this variable:

$$W_{iso} = \hat{W}_{iso}(\mathbf{C}, \Phi_{LE}) \tag{5.5}$$

5.2.2.1 Uniaxial tests on rubber Since data are not currently available for mechanical testing of isolated elastin with histological images of the fenestrations, experiments on rubber performed previously [130, 131, 34] were utilized to establish a methodology to investigate ligament efficiency as a viable mechanical parameter.

In this previous work, described in [130], scanning electron images of the internal elastic lamina were used as stencils to create replica strips of fenestrated rubber sheets with similar patterns of holes. Ligament efficiency was calculated from the distribution of fenestrations of these replicas by using eq. 5.3.

Latex strips with a uniform array of holes were created to similar ligament efficiency as the replicas, computed by eq. 5.4 for uniform fenestrations. When tested in uniaxial tension, the fenestrated rubber sheets with uniform holes gave identical results to the replicas.

Further, the authors reported the mechanical data from a tensile test on a solid piece of latex rubber, along with the response of a similar piece of latex with a uniform 6x6 array of perforated holes, with reported ligament efficiency of 0.71.

Since rubber is considered here, a Mooney-Rivlin (MR) type strain energy function (SEF) was chosen to fit the solid latex piece. This MR form fit the raw uniaxial data from latex rubber better than other isotropic SEFs.

Including ligament efficiency as an internal variable (eq. 5.5), in this case, as a multiplicative coefficient into a Mooney-Rivlin type strain energy function (eq. 2.95) for an elastic, homogenous, isotropic material, gives the function

$$\hat{W}_{iso}(\mathbf{C}, \Phi_{LE}) = \Phi_{LE} * \left[\frac{1}{2}\mu \left[\left(\frac{1}{2} + \beta\right)(I_{\mathbf{C}} - 3) + \left(\frac{1}{2} - \beta\right)(II_{\mathbf{C}} - 3)\right]\right] \tag{5.6}$$

where Φ_{LE} is given by eq. 5.4. This equation was fit to the data using a nonlinear regression analysis (Section 3.4).

5.2.2.2 Ligament efficiency analysis of the internal elastic lamina A segment of human middle cerebral artery was fixed under 30% strain in para-formaldehyde and placed under a confocal microscope (See Appendix A). Stacks of images were taken though the thickness of the IEL and superimposed (Fig 36, bottom right), and LE was determined by a custom MATLAB program with eq. 5.3 [130].

Briefly, an image threshold was applied to produce a black and white image, with the fenestrations represented by white pixels. The MATLAB function *bwtraceboundary.m* was then applied to trace the boundary of the (n total) individual fenestrations (i) in the region of interest (Fig. 39). The length of the boundary was used as the circumference of a circle, from which the diameter, d_i of each fenestration was computed. The length (l) and width (w) were determined by the row and column of pixels that defined the region of interest. These values were input into eq. 5.3 to compute LE.

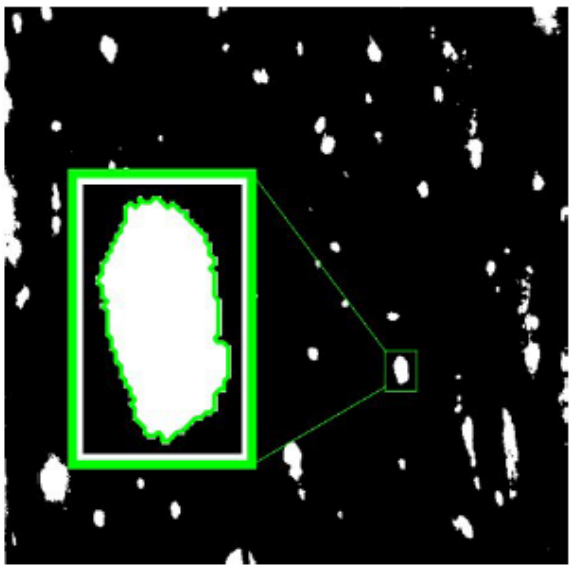

Figure 39: Ligament Efficiency method. Middle Cerebral Artery IEL after applying threshold. Inset: Trace of the boundary of a fenestration obtained in MATLAB.

5.3 RESULTS

Results from mechanical analysis of isolated elastin (Section 5.3.1) and from ligament efficiency analysis (Section 5.3.2) are presented below.

5.3.1 Uniaxial Testing of Isolated Elastin

The stress-stretch response of each the isolated elastin segments followed a very similar path, especially in the low load/extension region (Fig. 40). The Ogden-type strain energy function (eq. 2.100) gave the highest R^2 value when fit to the data, followed by the exponential (eq. 2.93), the modified neo-Hookean (eq. 2.98) with $n = 1.18$ obtained via least-squares fitting, and then by the single-parameter neo-Hookean strain energy functions with n = 1.25, 1.00, 1.50, and 1.75, in respective order (Table 5, Fig 41). Note that results from fitting to the Mooney-Rivlin model (eq. 2.95) were identical to results from the neo-Hookean model: the Mooney-Rivlin model reduced to the neo-Hookean model.

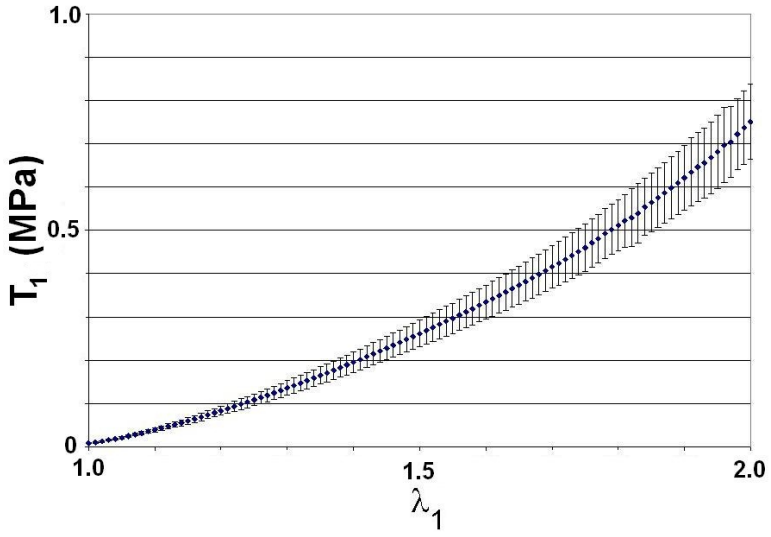

Figure 40: Stress-stretch response of isolated elastin segments from two porcine aortas (n = 39). Bars represent one standard deviation

The tangent modulus from eq. 5.2 was plotted, along the corrected and erroneous data (Figure 42)[1], for the modified neo-Hookean SEFs, eq. 2.98, with n=1.00 (μ = 217.2 kPa), n=1.25 (μ = 207.6 kPa), n=1.50 (μ = 229.8 kPa), and n = 1.75 (μ = 277.7 kPa).

5.3.2 Ligament Efficiency

The stress-stretch data were taken from reference [130], for the "solid" latex strip (Fig. 43, blue dots) and for the "fenestrated" latex strip with a 6x6 pattern of holes (Fig. 43, green dots). The "solid" data was fit to eq. 5.6 with LE = 1 (no fenestrations) to give coefficients μ = 770 kPa and β = -0.31, with R^2 = 0.9987 (Fig. 43, blue line). Substituting the reported ligament efficiency for the fenestrated latex (LE = 0.71), with these material parameters, into eq. 5.6 gave a response very similar to that observed experimentally (Fig. 43, green lines).

[1]Data were originally published in 2007 [133], and the authors noted an error with the reported data in a corrigendum published in 2009 [134], including the corrected data

Table 5: Parameters from least-squared fit of various strain energy functions (SEF) to data, $\pm$ 95% confidence interval

SEF	Parameters	SEF	Parameters
Exponential (eq. 2.93)	R^2 = 0.9997 β = 0.50 b = 0.38$\pm$0.01 $a\ (kPa)$ = 150$\pm$1	Mooney-Rivlin (eq. 2.95)	R^2 = 0.9741 β =0.50$\pm$0.27 $\mu\ (kPa)$ = 190$\pm$22
Ogden (eq. 2.100)	R^2 = 0.9998 α_1 = 3.3$\pm$0.02 $\mu_1\ (kPa)$ = 79$\pm$0.0		

SEF	Parameters		
neo-Hookean (eq. 2.98)	R^2 = 0.9741 n = 1.00 $\mu\ (kPa)$ = 190$\pm$0.00	R^2 = 0.9984 n = 1.18$\pm$0.01 $\mu\ (kPa)$ = 160$\pm$0.00	R^2 = 0.9957 n = 1.25 $\mu\ (kPa)$ = 140$\pm$0.00
	R^2 = 0.9521 n = 1.50 $\mu\ (kPa)$ = 110$\pm$0.00	R^2 = 0.8778 n = 1.75 $\mu\ (kPa)$ = 84$\pm$0.00	

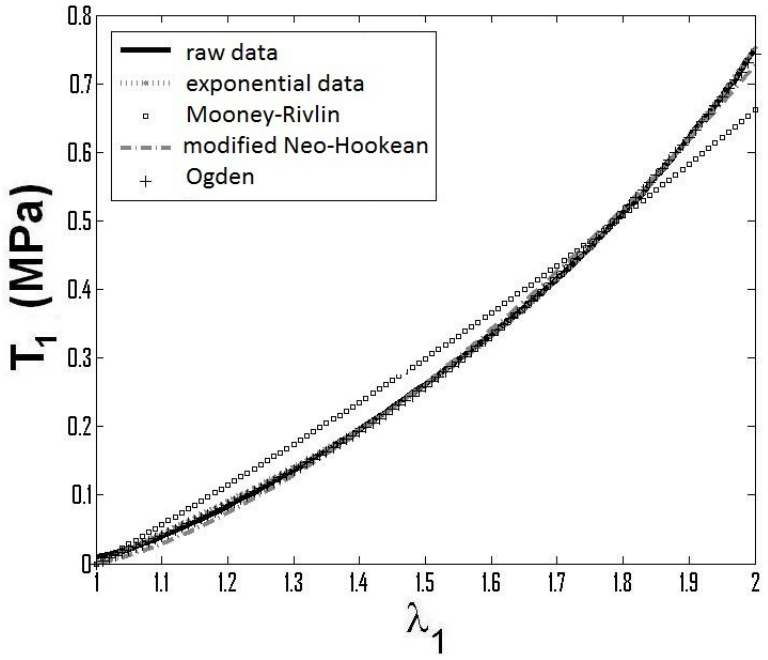

Figure 41: Stress-stretch results for isotropic strain energy functions. Note that both the coefficient and the exponent in the modified neo-Hookean model were fit with the least-squares method.

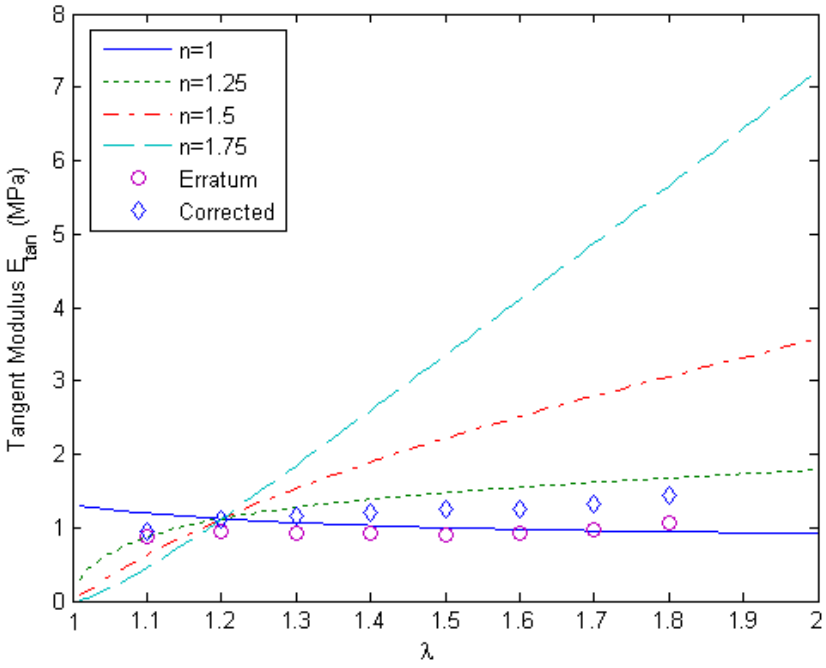

Figure 42: Tangent modulus E_{tan} versus stretch for the modified neo-Hookean strain energy function. Note that this figure is a modification of Figure 2 in [81]. Visual comparison can be made with the erroneous (Erratum) results from [133] and the corrected data from [134]

Note that data were not fit to obtain the green line in Fig. 43. This curve was obtained by using the fitted parameters from the "solid data" and the reported ligament efficiency value.

Ligament efficiency for a middle cerebral artery was computed with the custom program as 0.85 (Fig. 44), falling within the range of reported values given in the literature for cerebral arteries [130].

5.4 DISCUSSION

Chosen isotropic strain energy functions (SEFs) were fit to data from uniaxial ring extension experiments on isolated arterial elastin. The strain energy function given by Ogden [70], the exponential SEF [79], and the modified neo-Hookean SEF [80, 81] with fitting parameter n all gave higher R^2 values when fit to experimental data than did the traditional neo-Hookean SEF, where $n = 1$ (Table 5). However, Watton et al. [81] observed that when subject to pressure-inflation, the traditional neo-Hookean model yielded a stress-flattening pressure-radius curve, consistent with physiological observations [81]. Also, out of four choices considered for the modified neo-Hookean SEF [81], the case with n = 1 gave the best qualitative representation of the experimental "tangent modulus" data (Fig. 42).

As discussed in Section 4.4, regarding collagen, neo-Hookean strain energy functions, with a single material parameter, are commonly used to model a linear response. The other SEFs investigated in this work require two fitting parameters. While they may give a slightly better fit to the experimental data here, there may be advantages to using a single parameter to represent the entire contribution from the arterial elastin. Indeed, this model is used quite frequently [5, 6, 14, 81, 126, 127, 128, 18, 55, 129]. However, more experiments should be performed to elucidate the most appropriate model for arterial elastin. For example, while elastin has been assumed to be an isotropic solid, some results have indicated otherwise. In 1954, Dempsey and Lansing observed birefringence in stretched elastin with a polarizing microscope [135], suggesting arterial elastin is

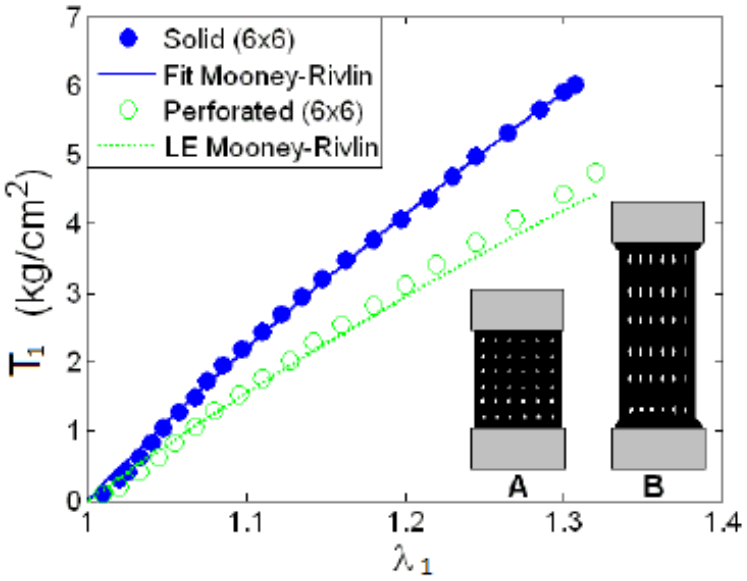

Figure 43: Plot of stress-strain curves from solid and perforated rubber sheets with data taken from Figure 3 in [130]. Raw data are given as circles, and the fit to a Mooney-Rivlin (MR) strain energy function (SEF) is given as a solid blue line, while a MR SEF with ligament efficiency (LE) as a multiplicative coefficient is given as the green line. Inset: representation of fenestrated latex sheet with 6x6 array of punched holes under no (A) and applied (B) strain.

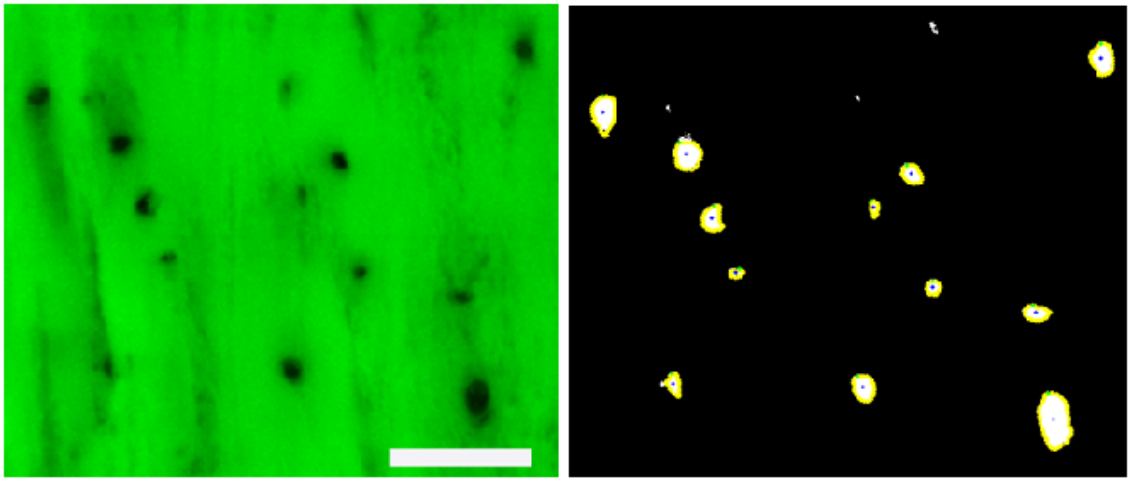

Figure 44: Internal elastic lamina (IEL) of a middle cerebral artery (MCA) before (left) and after (right) applying the ligament efficiency (LE) algorithm in MATLAB. LE was computed as 0.85 for this sample. Bar = 50μm

anisotropic. In 1964, Wolinsky and Glagov [105] noticed, in fixed cross-sections, that in the physiological pressure range, the net of elastin fibrils exhibited an almost circumferential orientation. Furthermore, anisotropic strain energy functions were evaluated for arterial elastin in a recent study by Rezakhaniha et al. [136].

The SEFs assessed in this work were deemed appropriate for capturing the mechanical response, though other methods, such as using ligament efficiency as an internal variable, may be found to be more suitable as our knowledge of the structure and function of arterial elastin increases. Ligament efficiency was evaluated as a possible means for including structural information of the internal elastic lamina, the layer of elastin containing a majority of arterial elastin in cerebral arteries. Here, this approach was used for experimental data obtained from strips of fenestrated latex rubber.

Also, a new method was developed for measuring ligament efficiency from images of the internal elastic lamina of arteries. This method was applied to a segment of a middle cerebral artery. The ligament efficiency of 0.85 was comparable to the literature

on cerebral arteries [130]. Thus, a framework by which ligament efficiency may be used as a structural parameter is presented, though future studies are warranted on intact and isolated elastin to provide accurate models for the mechanical response.

6.0 EXPERIMENTAL ANALYSIS OF DAMAGE IN THE CEREBRAL ARTERY WALL

The objective of this chapter was to develop an experimental approach for analyzing damage to the cerebral artery wall. A new method and protocol for obtaining damage parameters was developed. Therefore, this chapter addressed Specific Aim 3 (Section 1.4). The results from damage experiments on the internal elastic lamina of human cerebral arteries were reported. A mathematical damage model (Section 2.2.4), previously applied to the artery wall [2], was fit to data obtained from experiments with a new experimental device (vUA-MPM, Section 3.3.2). Previous studies indicate that elastin rupture results in a stiffer artery with increased diameter, since after elastin fails, collagen takes over as the primary load-bearing constituent. To the author's knowledge, results from these experiments are **the first to provide microscopic confirmation of deformation induced elastin rupture in cerebral arteries**

6.1 BACKGROUND

Elastin may be damaged by acute rupture from overexpansion of arteries by stent deployment techniques; it may be naturally frayed, fragmented, and calcified over time; or it may be destroyed by cellular actions, such as the release of matrix metalloproteinases (MMPs) in response to biochemical or biomechanical changes. After puberty, functional elastin likely does not regenerate after it has been damaged (See Section 5.1). The inability of the cell to reactivate the many genes in the proper ratios and sequences required for normal fiber assembly [137] may prevent its repair, perhaps resulting in the loss of

elasticity with increasing age. Therefore, the detrimental effects of damage, acute rupture, or tearing from abrupt loading, cyclic fatigue due to the repeated loading from pulsatile blood pressure, and/or biochemical degradation due to enzymes released from cells likely will not be repaired and thus may lead to pathological conditions such as failures in balloon angioplasty [138], dissection aneurysms [139], arteriosclerosis [140, 141, 142, 143, 144], and cerebral saccular aneurysms [145, 146, 34, 147, 148, 149, 150, 151, 115, 152, 17, 1]. As discussed in the Introduction (Section 1.2), elastin damage has been implicated in cerebral saccular aneurysm formation. Also, cerebral artery wall damage may occur due to over distension of the arterial wall during the deployment of balloons during angioplasty [138], which is also commonly used in cerebral arteries in the case of atherosclerosis.

In 1972, Scott et al. [17] performed mechanical experiments on cerebral artery tissue and provided evidence of a loss in the toe region of the stress-strain response curve, following repeated inflation to 200 mmHg. They hypothesized that this change in mechanical behavior was due to damage of elastin. This mechanical damage to arterial elastin has been conjectured to be responsible for the observed increase in unloaded radius of cerebral arteries that had been subjected to supra-physiological loading [17]. These studies provided groundwork for the development of a structurally-motivated continuum damage mechanics (CDM) model of artery tissue [2].

Furthermore, histological examination of the internal layer of elastin in common carotid arteries subjected to longitudinal uniaxial failure tests have shown the presence of mechanically induced tears [153]. Tests have been performed on "dumbbell" shaped specimens from the human aorta to evaluate ultimate stress and extension ratio at failure during circumferential and axial loading [154], though neither a continuum damage framework nor histological techniques were employed.

In this study, a continuum damage mechanics model was utilized for quantifying damage in the artery wall. Mechanical damage testing was performed with the vUA-MPM system on human cerebral artery segments obtained at autopsy. Data from these experiments were fit to the damage model. With the vUA-MPM system, biomechanical measurements of damage may be correlated with the underlying tissue microstructure to better understand the degenerative processes.

6.2 METHODS

The vessel wall was modeled as a homogeneous, incompressible, multi-mechanism, transversely isotropic hyperelastic solid, with preferred fiber orientation in the circumferential direction. A decoupled strain energy function was used to model the elastin and collagen contributions separately (eq. 2.76). For uniaxial extension, the stress-stretch response for a transversely isotropic material was given by eq. 2.153. A single recruitment model was used (Section 2.3.1.2), so the anisotropic term in this equation was given by eqs. 2.139, 4.1, and 4.2, where $\lambda_f = \lambda_1$, or, equivalently, by model B in Table 2. The form of the fiber strain energy function was given by the exponential form:

$$\hat{w}_f^*(\lambda_t^2) = \frac{\eta}{\gamma}\left[e^{\gamma(\lambda_t^2-1)} - 1\right] \tag{6.1}$$

Isotropic damage was modeled with a single scalar damage parameter (Section 2.2.4) [64] by using eq. 2.127, where $\hat{W}_0(\mathbf{C})$, the effective (isotropic) strain energy function, was given by the exponential type (eq. 2.93), with $\beta = 1$.

6.2.1 Testing protocol

Segments of the basilar artery from two cerebral arteries (Fig. 3) were taken from human cadavers at autopsy, frozen in a $-80\,^{\circ}C$ freezer, and then thawed prior to testing. Five adjacent segments were taken from the basilar artery of the circle labeled CW09-011, with Sample 01 taken near the circle and Sample 05 taken near the vertebral arteries (Fig. 3). Several segments were taken from CW09-012, though only one sample (04) taken near center of the basilar artery was successfully tested.

Damage experiments were performed on these six circumferential segments from two basilar arteries mounted in the vertical vUA-MPM system (Section 3.3.2). All testing and imaging were performed in 0.9%w/v saline. Each sample of artery tissue was removed from its source, opened longitudinally, manually cut into a "dumbbell" shape, and then placed between the clamps, which were held at a separated distance by a custom bridge piece. The clamping mechanism, including the segment of artery, was then placed onto

the arms of the device, for extension. The bridge piece was removed, and then the clamps were separated until a pre-set significant load was observed. Stretch was applied in the circumferential direction.

Testing was performed at a rate of approximately 19μm per second to a specified position based on choice of strain, $L = L_0 * (strain + 1)$. A bridge piece was affixed to the clamps to remove under strain (Fig. 13) for imaging. Specimens were tested and imaged at increasing levels of stretch until total rupture of elastin was confirmed with MPM.

Images of the optical markers were processed in MATLAB to determine L_0, defined as the position just prior to a pre-set significant change in value of strain. While strain was computed from optical methods, clamp separation was taken as official displacement. All curves were plotted to determine the yield point or position at which elastin first became damaged, assigned (L_s). Total elastin rupture was confirmed with the MPM images. The position at which collagen was recruited (L_a) was determined by analyzing marker tracking and clamp displacement on the damage curve.

The last damage curve was assumed to be representative of the collagen-only response (i.e., the isotropic response has been removed by total elastin rupture). This response was defined as the stress-strain curve at which elastin was shown via MPM to totally rupture by completely splitting across the width of the artery. These values were then divided by L_0 to give the appropriate stretch ratios, λ_s and λ_a, respectively.

Curve-fitting was accomplished via a nonlinear regression analysis (Section 3.4). The metric α (eq. 2.131), was computed by substituting in the stretch values to eq. 2.93 for W_0. The value λ_s was used to calculate W_0, and, in turn, to calculate α_s by eq. 2.131, for use in eq. 2.132. The value λ_a was used in eq. 4.2 to specify the stretch at which collagen fibers (abruptly) became recruited.

Parameters η and γ were obtained by fitting the final, "completely damaged," collagen-only curve to eq. 2.153 with the strain energy function given by eq. 4.1, while setting d_0 to unity (thus giving only the anisotropic collagen-dominated response).

To obtain the parameters a and b, the undamaged curve was then fit to eq. 2.153 with strain energy functions given by eqs. 2.127, 2.93, & 4.1, setting d_0 to zero (thus giving both isotropic elastin-dominated and anisotropic collagen-dominated response), with values

of η and γ input from the previous fit. To obtain the damage parameters c and α_f, the damage curves were simultaneously fit to eq. 2.153 with the damage parameter given by eq. 2.132.

6.3 RESULTS

Stress-strain data were obtained from uniaxial experiments with the vertical vUA-MPM device. At high strain, the intima region split perpendicular to the circumferential loading direction and peeled away from the media, as observed from visual inspection and images taken from the CCD camera (Fig. 45, right). Multi-photon imaging revealed damage to the internal elastic lamina as a cat's eye shaped tear (Fig. 45), which pulled back under strain to reveal intact, primarily circumferentially oriented, collagen in the media beneath, indicating elastin was damaged prior to collagen. The data were fit to the model as described in Section 6.2 to obtain material and damage parameters (Fig. 46 and Table 6).

6.4 DISCUSSION

Damage experiments were performed on human cerebral artery tissue, with the results analyzed in the context of continuum damage experiments. An isotropic exponential strain energy function with a scalar damage variable was used to represent the functional loss of elastin due to acute rupture. An exponential model with abrupt collagen fiber recruitment was used to model collagen in this case, since direct histological analysis of the fibers was not possible in this experimental approach (See Chapter 4).

The vUA-MPM system was used to perform acute damage analysis on circumferential strips of human cerebral arteries exposed to loading cycles of increasing strain magnitude. Specimens were tested and imaged at increasing levels of strain until total rupture of elastin was confirmed visually and with MPM. Striking tears in the IEL were

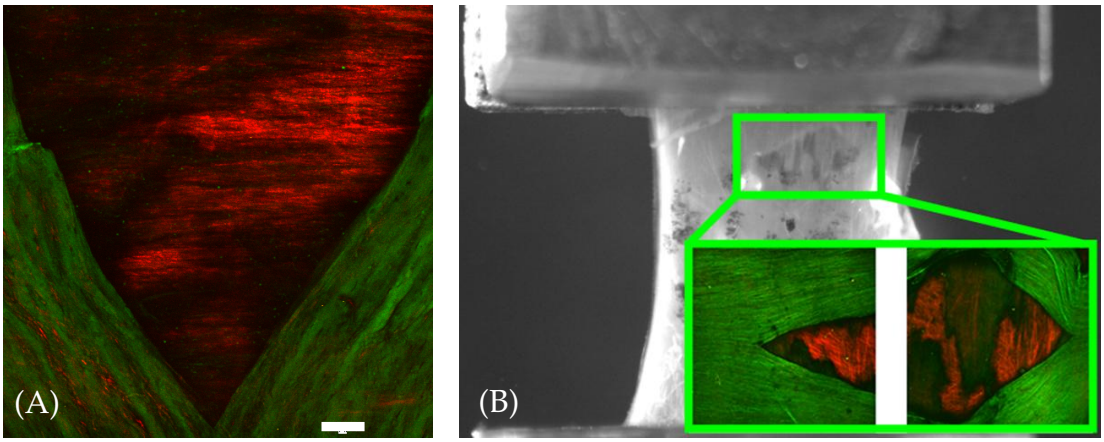

Figure 45: Images of damage results. A: Damaged internal elastic lamina (green) revealing collagen fibers (red) underneath, primarily circumferentially-aligned in the media (Basilar Artery 2, segment 4 in Table 6), bar = 50μm. B: Image of torn elastin depicted on the macro- and micro-scale

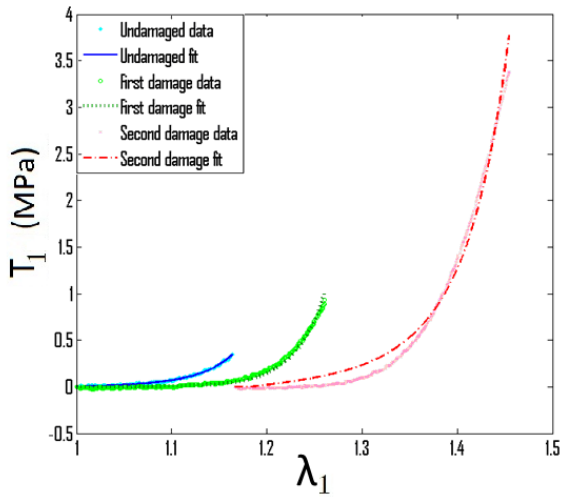

Figure 46: Raw data and fitted damage model (indicated by legend), taken from a cerebral artery (Basilar Artery 1, segment 2 in Table 6)

found, revealing the medial collagen fibers underneath (Fig. 45). However, these tears did sometimes occur away from the middle of the dumbbell-shaped specimens, so we acknowledge that clamp effects may have influenced the results. The data fit the damage constitutive equation well, with R^2 values close to one for each of the six basilar artery specimens tested (Table 6). There was variability in the model parameters between specimens (interspecimen variability).

The types of damage mode observed in the experiment may be similar to failure from acute rupture of arteries from overexpansion of arteries by stent deployment techniques. However, this damage mechanism is on a scale larger than what can be reasonably considered in continuum damage mechanics, which are typically microcracking or some uniform destruction of material. Therefore, the continuum criterion defined in the first sentence of Section 2.1 is not met. It is clear that in these experiments, large cracks were present (Fig. 45), making it difficult to homogenize the artery with such localized damage. Alternative approaches may be considered in the future. At lower loads, the continuum damage model may be appropriate.

The vUA-MPM system and the damage model presented here may be applied to pathological conditions caused by elastin damage from other mechanisms, such as cyclic fatigue, that leads to the stiffening of arteries (arteriosclerosis), or biochemical degradation by matrix metalloproteinases (MMPs), that may lead to aneurysm formation.

As humans advance beyond their age of optimal cardiovascular health, cyclic fatigue of arteries may lead to arteriosclerosis, arterial weakening, and detrimental cardiac changes [142]. For example, the increase in stiffening of the artery wall caused by arteriosclerosis and aging leads to an increase in elastic modulus and thus an increase in pulse wave velocity (PWV) [13]. This increase in PWV causes the reflected wave to return to the heart earlier, thus the favorable "tuning" is lost [155]. A decrease in coronary perfusion may result, which over time may lead to severe cardiovascular events due to ischemia of the myocardium. Elastin damage by fragmenting, fraying, or calcification may be the underlying cause for the increase in artery wall stiffening observed in arteriosclerosis and ageing [155].

In vivo studies suggested that fatigue is responsible for the frayed appearance of the internal elastic lamina in aged arteries [156], and constituent-based structural models have been developed to account for ageing [157, 158]. This distributed frayed appearance suggests a continuum damage approach is suitable for modeling cyclic fatigue. Fractal analysis has been performed on histological sections of elastin lamellae in arteries [159], with results indicating that elastin fatigue occurred due to increased cardiac cycles over the same time period [160]. O'Rourke stated that elastin fatigue is responsible for increasing stiffness in arteries with age and disease [13, 161, 155]. Since there is little direct evidence in the literature linking elastin damage to cyclic loading [162], he pointed to research on mechanical fatigue of rubber [163] to estimate the number of cardiac cycles for fatigue rupture of arteries [161]. Apparently, only a few studies on fatigue have been performed on soft tissues that undergo cyclic loading, such as tendons, e.g., [164, 165]. Even less of this work has been done on arteries, and few attempts to formulate predictive models of damage have been made. One such experiment involved in vitro fatigue experiments performed on isolated elastin, in which several variables, such as initial strain prior to cyclic loading, were altered and the ultimate number of cycles to failure reported [132], although the modes of damage and eventual rupture due to fatigue were not evaluated histologically.

In the future, the vUA-MPM system may be modified for performing other types of damage experiments on arteries, such as cyclic fatigue. This avenue of research may provide the foundation for new experimental treatments for an array of cardiovascular diseases.

Table 6: Damage results from segments taken from two human basilar arteries

Basilar Arteries	CW09-011					CW09-012
	Seg 01	Seg02	Seg 03	Seg 04	Seg 05	Seg 04
Geometry						
w (mm)	3.6	3.2	2.7	4.0	1.5	6.7
H (μ m)	190	190	200	200	140	230
L_0 (mm)	4.0	3.8	3.8	5.6	3.4	4.3
Parameters						
λ_a	1.001	1.182	1.191	1.194	1.246	1.164
λ_s	1.295	1.222	1.344	1.446	1.255	1.320
a (kPa)	79.0	59.0	20.0	3.0	235	20.0
b	19.1	24.3	16.8	14.5	20.7	11.7
η (kPa)	26.0	664	375	200	1630	1170
γ	2.34	7.50	3.80	4.30	6.94	8.45
c	1.86	2.68	3.25	3.03	5.55	1.00
α_f	17.6	28.2	26.1	6.25	93.8	1.30
R^2_{iso}	0.9979	0.9953	0.9970	0.9995	0.9959	0.9995
R^2_{aniso}	0.9959	0.9883	0.9865	0.9862	0.9949	0.9973
R^2_{d1}	0.9633	0.9882	0.9637	0.9708	0.9292	0.9931
R^2_{d2}	0.9552	0.9872	0.2794	0.9861	-0.0780	
R^2_{d3}			0.9834		0.9904	

7.0 CONCLUSION

In this work, a new theoretical and experimental approach was developed for analyzing collagen and elastin in the artery wall. New systems were fabricated for performing uniaxial experiments on biological tissues. Protocols were established for incorporating histological measurements and mechanical data into a mathematical modeling scheme. Based on results from mechanical and microstructural analysis of the artery wall, new structurally-motivated constitutive models were presented for collagen and elastin.

Collagen fibers were shown to exhibit an orientation distribution over a single plane defined by the axial blood flow direction and the circumferential direction. Fiber recruitment was observed to initiate at a finite tissue stretch, followed by gradual individual fiber activation. A new model was developed to accurately model this response. By directly including this recruitment data, the (recruited) collagen contribution could be modeled using a simple Neo-Hookean strain energy function. As a result, only two fitted phenomenological material constants were necessary. Further, this model can capture the increase in unloaded radius when the isotropic mechanism is damaged. Three additional models of the collagen-dominated response were considered that may be of value when some histological measurements are unavailable.

An isotropic neo-Hookean model, which treats the material response as linear in the left Cauchy stretch tensor, was deemed sufficient for modeling arterial elastin at present. This conclusion was based on our results and on previous work. However, new theoretical and experimental approaches are necessary to elucidate the mechanical behavior of elastin. Here, a new modeling scheme involving ligament efficiency was presented as a structurally-motivated approach to modeling the internal elastic lamina, the inner layer of elastin present in the artery wall.

Acute rupture of elastin was observed to occur in the internal elastic lamina of cerebral arteries, prior to any observed collagen breakage. A continuum damage mechanics approach was utilized to represent this damage, though the mechanism was deemed to be on a scale larger than that allowed by the continuum approximation. The application of this approach to model other damage mechanisms was discussed.

Though some technical aspects of the current approach can be refined, this work presents a new theoretical and non-destructive approach for direct inclusion of measured collagen fiber orientation and recruitment in a structurally motivated constitutive model of the artery wall. Collagen recruitment was found to initiate at finite strain in all samples. These results have important implications for vessels in which the low strain mechanism is damaged, such as during balloon angioplasty. Further, loss of elastin may be attributed to aging. By using an abrupt recruitment model [61, 64, 6], the change in radius and loss of the toe region in mechanical experiments [17], attributed to loss of elastin, may be accurately modeled. To the author's knowledge, the multi-mechanism model presented here and elsewhere [6, 61, 64, 2] is the only one available to account for the change in unloaded radius as observed in early studies [17], due to the additional reference configuration introduced for collagen recruitment.

Our work is also important because the methods introduced here provide a means of assessing collagen recruitment during different stages of growth and remodeling. In particular, it has the potential to be used to evaluate collagen deposition stretch. It also presents a method for analyzing elastin structure and damage in the artery wall. Future application of this knowledge may reduce the burden of vascular diseases, such as cerebral aneurysms, on the human population, since new safe and effective treatment technologies may be developed based on increased understanding of this disease progression. For example, the constitutive models presented here may be utilized in finite element models to predict arterial damage from mechanical loading during clinical intervention, as in previous work, e.g., [2, 166].

Further steps should be taken to analyze the role of the adventitia in the mechanical response of the artery wall. Additional experiments should be performed on the artery wall to investigate ligament efficiency as a structural parameter. Finally, fatigue experiments

should be performed on the cerebral artery wall, with the results analyzed in the context of continuum damage mechanics. Histological images of the fatigue-induced damage may determine the suitability of applying the continuum approximation.

APPENDIX A

HISTOLOGICAL TECHNIQUES

All histological methods and analyses were performed at the Center for Biologic Imaging (CBI) at the University of Pittsburgh Medical Center (UPMC). For fixation, segments were placed under strain in a 4% v/v solution of paraformaldehyde (PFA) in phosphate buffered saline (1x PBS) for two hours.

A.1 FIXATION

Various fixation methods have been used for histological preparation. Segments have been fixed in Bouin's fixative (75mL saturated picric acid, 25 mL of 37% formalin, and 5mL glacial acetic acid) or 2, 4, 6, 8, or 37% paraformaldehyde (PFA) in phosphate buffered saline (1x PBS), each for two hours. 4% PFA was chosen as our preferred method to be consistent with previous research.

A.2 SECTIONING

En face preparations were performed to examine the lumen (or adventitial) side of the artery. Arteries were fixed then cut open longitudinally and placed adventitia-side down on a microscope slide in a shallow well, and then the lumen-side was covered with a

cover glass. *Cross sections* were taken of the arteries after fixation by slowly freezing the segments in liquid nitrogen and then slicing with a cryostat (HM 505E, Microm). The segment was oriented so that 6μm-thick cross-sections could be sliced from the segment and then placed on a positively charged microscope slide. Slides were kept at 4°C until removed for staining or analysis. *Tangential* sections were taken with the cryostat in a similar manner as cross-sections, except the vessel segment was oriented so as to slice tangential to the cylinder.

A.3 PICROSIRIUS RED STAINING

Picrosirius red (PSR) was utilized to enhance collagen birefringence under polarized light microscopy.

Transverse or cross sections were taken with the cryostat and the slides were placed in picrosirius red solution - 0.1g Sirius Red (F3BA, Pfaltz and Bauer, Inc.) in 100 mg Picric Acid (1.2% w/v, VWR) - for one hour, then in acidic water (1mL glacial acetic acid in 200mL DI H2O) for 5 minutes, and finally into ethanol until coverslipped.

Samples were coverslipped by placing 2 drops of Permount (SP15-500, Toluene Solution UN1294, Fisher) on a long glass coverslip (Cat No. 12-545-F, Fisher). En face segments were fixed in Bouin's fixative for 2 hours. The segments were soaked in phosphate buffered saline (PBS) at 4°C overnight to remove the fixative, briefly blotted with a paper towel to remove excess PBS, and then frozen slowly in liquid nitrogen.

They were then frozen onto blocks with OTC compound, oriented with the adventitial side facing the block so they could be sectioned transversely from the adventitia to the lumen (tangent to the cylinder). The samples were sectioned into 6 micrometer thick slices with a cryotome, and then mounted on positively charged microscope slides, followed by immersion in picrosirius red for one hour, acidic water (5mL glacial acid acid per 100mL de-ionized water) for five minutes, and finally 100% ethyl alcohol for 5 minutes prior to mounting coverslips.

The slides were coverslipped by placing two small drops of Permount onto the coverslips and placing them on the slides before the ethanol was allowed to dry.

Slides were then examined under a Provis fluorescence microscope with two polarizers oriented 90 degrees from each other so collagen birefringence could be detected.

A.4 IMMUNOHISTOCHEMICAL STAINING

Immunohistochemical staining was performed by the methods outlined in the Center for Biologic Imaging (CBI) protocol. The tangential or cross sections were removed from the refrigerator and a drop of 1x PBS at room temperature was placed on each segment to rehydrate. The samples were then placed in Triton X (10μL Triton X-100 in 10mL 1x PBS) for 15 minutes, followed by 3x washes of 1x PBS and then 5x washes of bovine serum albumin (BSA) solution (0.5% w/v BSA in 1xPBS). Samples were then blocked for 45 minutes in normal donkey serum (NDS) solution (500μL NDS + 500μL 0.5% BSA) or normal goat serum (NGS) solution (50μL NGS + 950|muL BSA). After blocking, samples were washed 5x in 0.5% BSA then placed in primary antibody in 0.5% BSA (vortex and spin down in centrifuge) for 60 minutes Samples were washed 5x in 0.5% BSA then placed in secondary antibody in 0.5% BSA (vortex and spin down in centrifuge) for 60 minutes. Samples were then washed 5x in 0.5% BSA, then 5x in 1x PBS, and then placed in Dapi nuclear stain for 30 seconds, followed by 3x washes with 1x PBS. The slides were then coverslipped (Cat No. 12-545-F, Fisher) in gelvatol mounting solution (recipe by CBI) and placed in 4°C overnight.

A.4.1 Visualization of the internal elastic lamina

Arteries were fixed in 4% PFA for 2 hours on the uniaxial ring tester at a prescribed strain, followed by en face or cross section preparation. Elastin has autofluorescent properties, so a confocal microscope was ultilized, with 488nm wavelength excitation and 500-560nm wavelength detection.

A.4.2 Visualization of collagen fibers

Following fixation, samples were sectioned on a cryotome (6μm thick; cross-sections and transverse sections) and then prepared with picrosirius red staining and immunohistochemistry (only cross-sections). The former was used to enhance birefringent properties utilized for the evaluation of collagen orientation. Collagen III was analyzed by the latter method via guinea pig anti-human collagen III primary antibody (1:1000) with Donkey anti-Guinea Pig (DaGP) Cy3 secondary antibody; Dapi nuclear stain was added to reveal cell nuclei. In both methods, collagen was analyzed on a Provis I fluorescence microscope. Samples stained with PSR were analyzed with brightfield illumination and two polarizers and those stained with Cy3 under the proper laser settings.

APPENDIX B

UNIAXIAL SYSTEM CONTROL WITH LABVIEW

To control the uniaxial mechanical devices described in Chapter 3, custom National Instruments LabVIEW software programs, or virtual instruments (VIs), were created. In the following sections, the main steps for performing a uniaxial test are described (Section B.1), with reference to the front panel of the main VI. Also, the subroutines, or sub-Virtual Instruments (sub-VIs), used to control the motor (Section B.2) and to acquired data from the load cell (Section B.3) are given in the following.

B.1 INSTRUCTIONS FOR PERFORMING A UNIAXIAL TEST

To perform a uniaxial test with the custom systems in our lab, with reference to MAIN.vi (Fig. 47), the following steps must be taken:

1. With no sample loaded and the clamps in place, start MAIN.vi and press the button "Zero-Position" under the heading "ZERO POSITION" to bring the clamps together until a predefined Load is recorded (set with "Zero-Pos Load (N)"). Note that here and in other sections the Velocity is set to 19.257 μm per second. This value may be changed, but it was chosen as optimal for reducing system vibrations.
2. Determine the initial gage length of your specimen, and separate the clamps to this displacement by typing in this value in mm into "Set or Go To Position (mm)" and

pressing "Go To Position," under the heading "HOME." Note: the button "SET HOME" may be used to set the new position as the zero position - it is not essential for performing tests.

3. Remove the clamps from the system, insert the specimen, and reattach clamps to system, using the custom bridge piece.
4. OPTIONAL: If you would like to stretch the tissue until a pre-set significant load is achieved, set this load in "Contact Load (N)" and press "Contact."
5. The testing parameters may be set in the section under the heading, "RUN EXPERIMENT." After setting the specimen to the appropriate gage length, select the maximum strain you would like to stretch the tissue and set this value into "Maximum Strain (%). The default value is 30%. Also, set the "Minimum Position (mm)" if you would like it to differ from the gage length. Note that strain is calculated from the clamp separation at the initialization of the experiment (just prior to pressing "RUN"). Set the total number of loading/unloaded cycles in "Total Loops." Note that this software only allows full loading/unloaded of the specimen to be performed. Press "RUN" to begin the experiment. A command window will ask you to select a file name and location for your output data, which will be saved as a "*.txt" file.

B.2 SUB-VIS FOR CONTROLLING THE STEP MOTOR

The sub-VI for setting up the step motor during the experiments is called by the main VI, "MAIN.vi," to start the motor and extend the arm of the uniaxial device to a pre-set position at a given velocity. Here, the front panel (Fig. 48) and block diagram (Fig. 49) are depicted, with the latter illustrating the conversion of stepper motor steps into extension of the arm of the uniaxial device.

The stepper motor we use is set to half step mode. A single revolution of the motor shaft is achieved by sending 400 steps to the motor. The shaft of the motor is connected to a speed reducer, in which 259.56 revolutions of the motor shaft is converted to one revolution of the speed reducer.

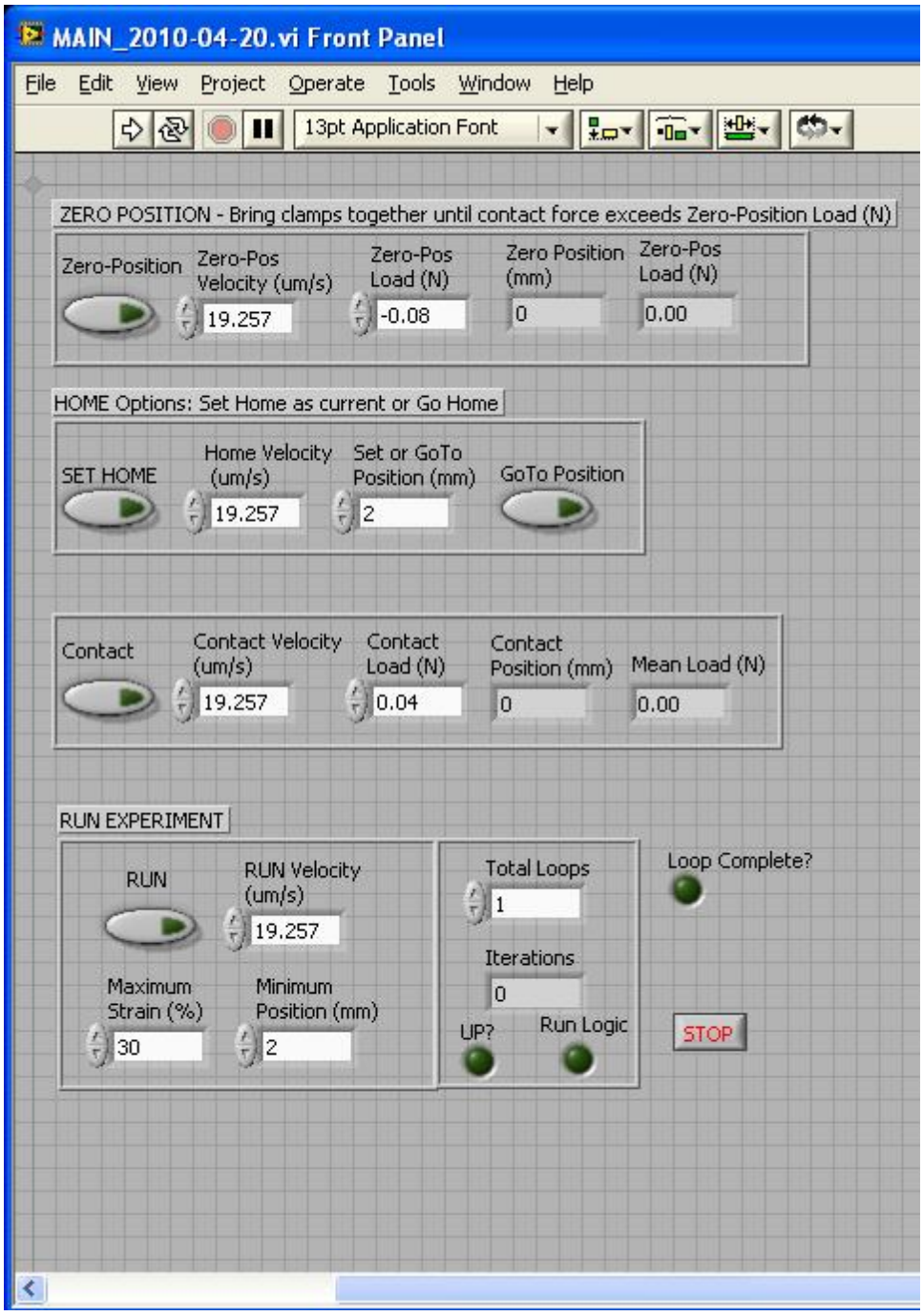

Figure 47: Front Panel of MAIN.vi, the main program for performing uniaxial experiments

For the linear Velmex slide, a single revolution of the worm gear results in an increment of one millimeter. Therefore, 103,850 steps must be sent to the motor to achieve a one millimeter displacement of the specimen.

B.3 SUB-VIS FOR ACQUIRING FORCE MEASUREMENTS

Force is acquired from the load cell attached to the system. The front panel of the sub-VI used to acquire the load signal is depicted in Fig. 50. The block diagram of this sub-VI is depicted in Fig. 51. In the latter, note that the voltage for this transducer is acquired through the Virtual Channel Dev1/ai2 in LabVIEW. The number of data points acquired each time this subroutine is called may be set in "number of samples per Channel" on the front panel. An average of these data points is computed to give the force in voltages. The volts are converted to Newtons using the calibration factor that my be set in the sub-VI "Volts to Load." The force is output as "Mean Load (N)."

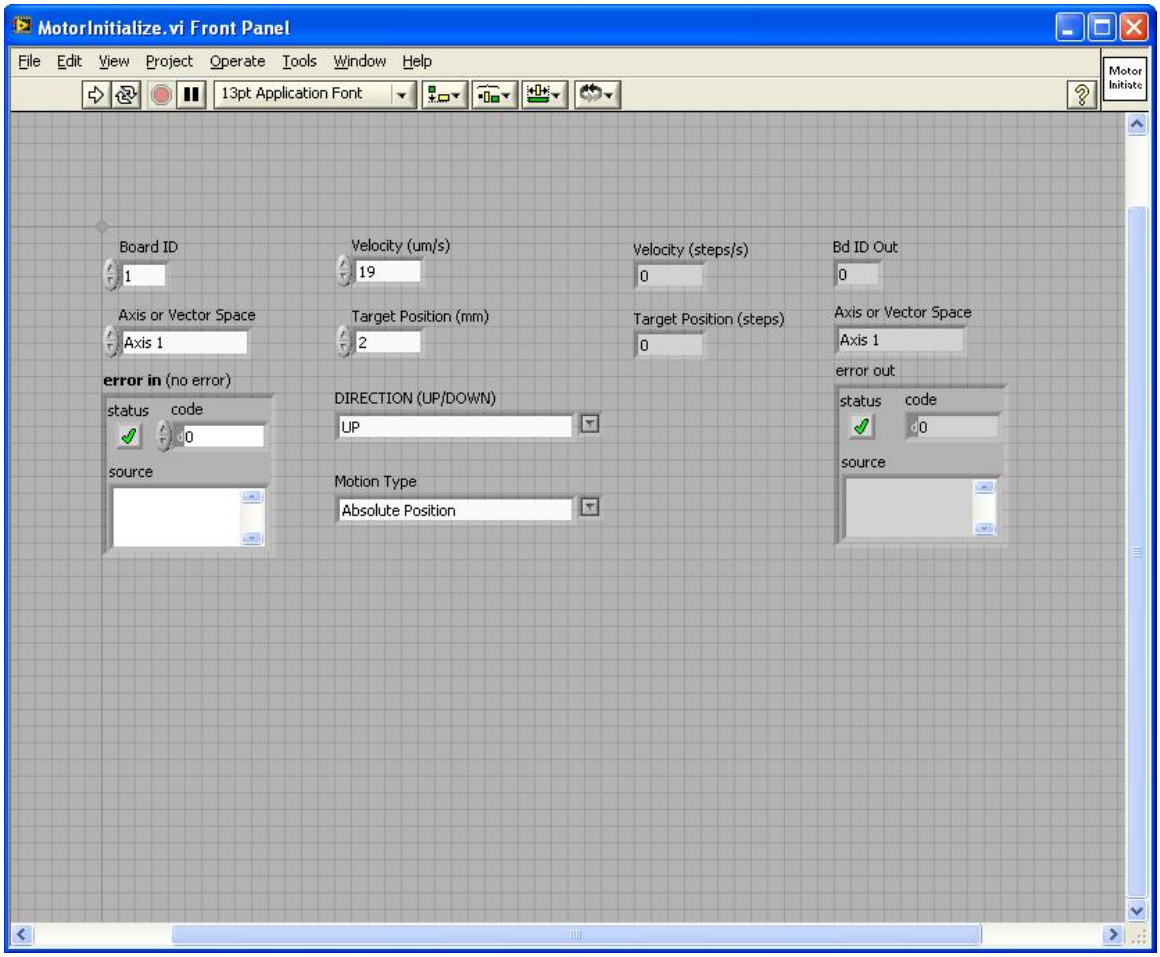

Figure 48: Front Panel of MotorInitialize.vi, a sub-VI, or subroutine, for initializing the motor

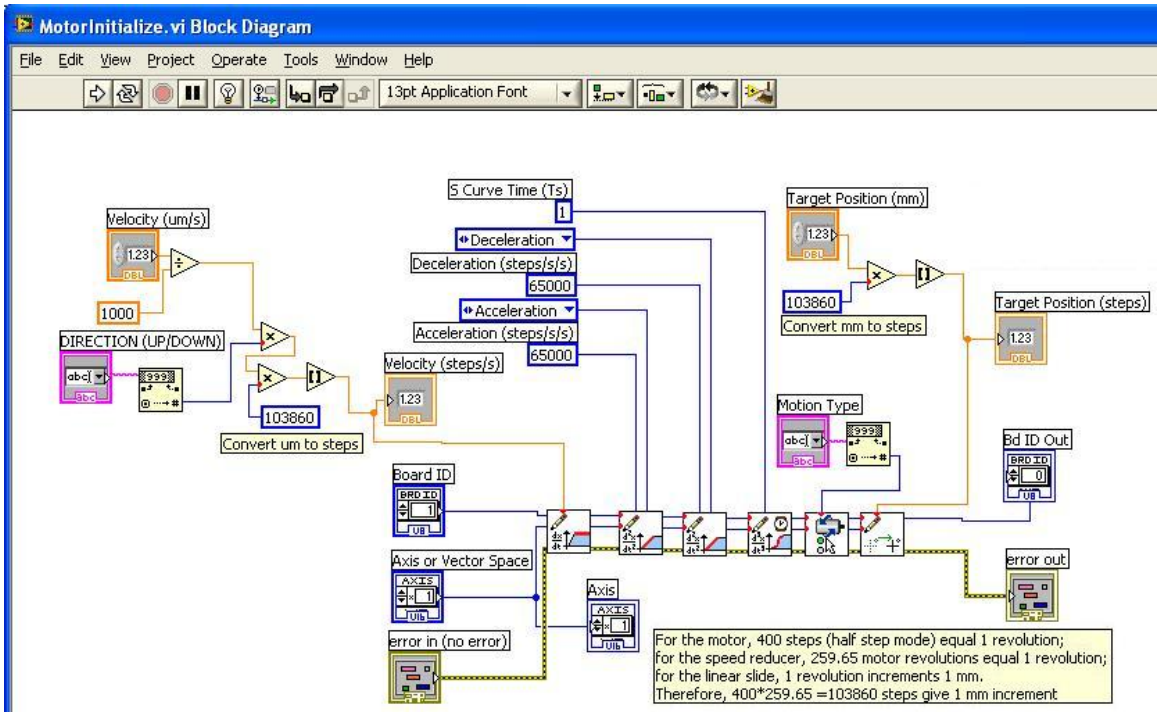

Figure 49: Block Diagram of MotorInitialize.vi, a sub-VI, or subroutine, for initializing the motor

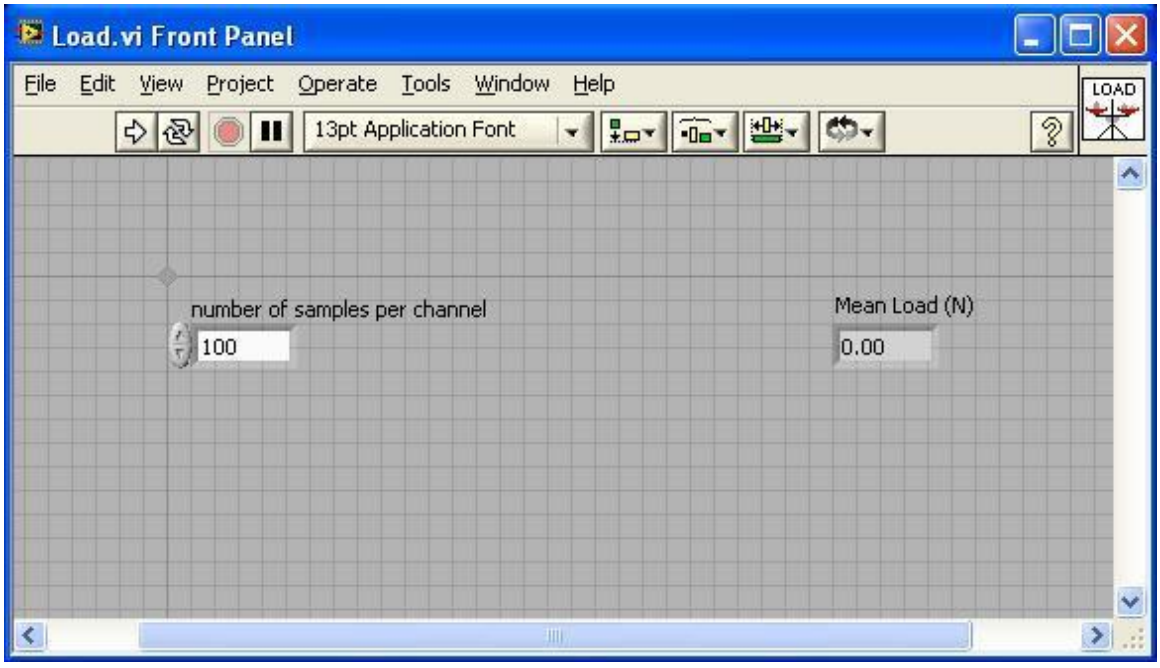

Figure 50: Front Panel of Load.vi, a sub-VI, or subroutine, for acquiring force data

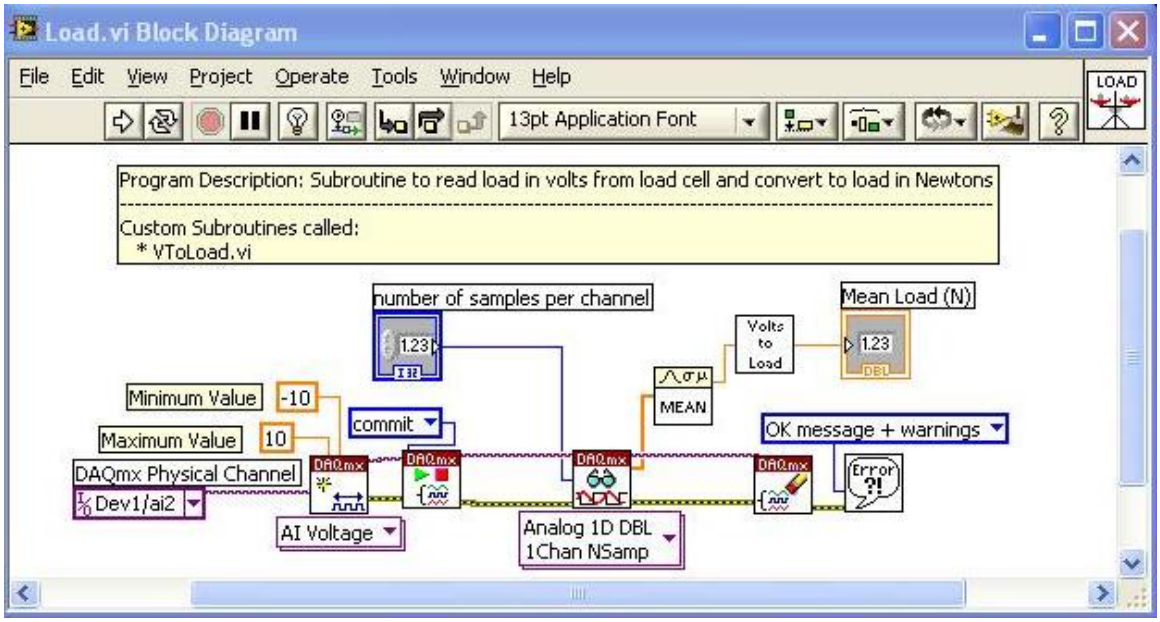

Figure 51: Block diagram of Load.vi, a sub-VI, or subroutine, for acquiring force data

APPENDIX C

OPTICAL STRAIN MEASUREMENT

Optical strain measurements were used to verify clamp displacement measurements used with the systems described in Chapter 3. Clamp displacement was used as official displacement for computing strain due to limitations discussed in Section 3.3.3.3. The instruction manual for the MATLAB graphical user interface (GUI) used to computing strain is given in Section C.1, the theory behind optical strain measurement is described in Section C.2, and the MATLAB source code used to develop this GUI is given in Section C.3.

C.1 SOFTWARE INSTRUCTIONS MANUAL

Main program to calculate Green's strain in Cartesian coordinates from the displacement of the centroids of four surface markers, by utilizing the inverse finite element method.

Instructions for using the software

1. Save all m-files to a single folder
   a. Highlight all files on this disk
   b. Drag them with mouse to an empty folder in MATLAB directory e.g., create the directory: C:\Program Files\MATLAB\R2006a\work\StrainMeasure

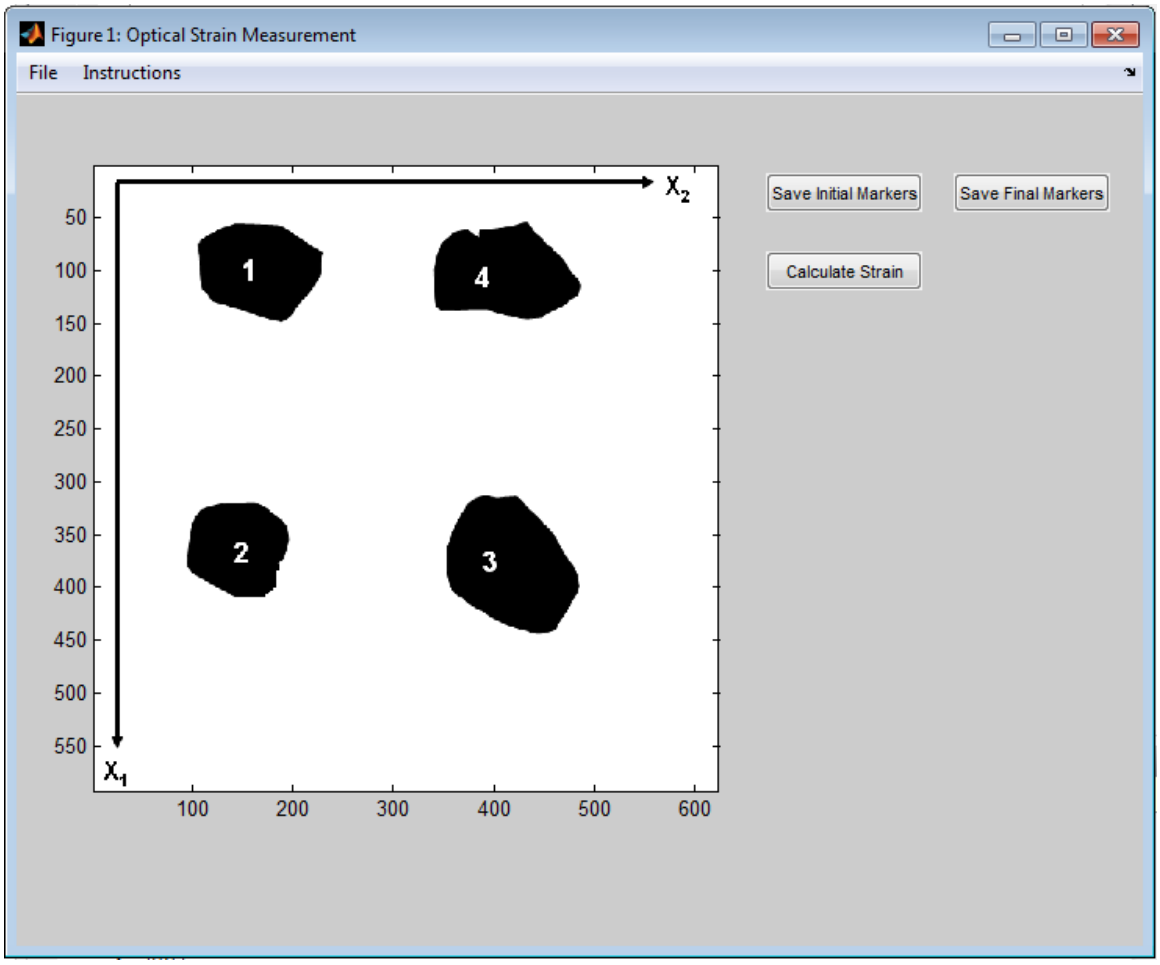

Figure 52: Main MATLAB Graphical User Interface (GUI) for performing optical strain measurement

2. Obtain the images

    a. The user must first obtain two high contrast images of four markers: one in the undeformed (initial) configuration and one in the deformed (final) configuration

    b. These images must be converted to binary

    c. The image file format must be bitmaps

    d. The markers must have highest pixel intensity value (1, 255, or "white") and the background must have the lowest value (0, or "black")

    e. Save the images with any filename and extension *.bmp to your folder (C:\Program Files\MATLAB\R2006a\work\StrainMeasure), for example, Undeformed configuration: initial.bmp; Deformed configuration: final.bmp

3. Run the program

    a. Open MATLAB

    b. Navigate to the folder: C:\Program Files\MATLAB\R2006a\work\StrainMeasure

    c. Type "run maingui" in the Command Window and press "Enter"

    d. A pop-up entitled "Figure 1: Optical Strain Measurement" should appear (Fig. 52) [Note: These instructions may be opened under "Instructions" in the heading]

    e. Please note the numbering of the four markers and the coordinate system [Note: The current image displayed gives the coordinate system and the proper numbering of markers; the user may open the file "display.bmp" for reference]

4. Open and Save the locations of the four markers for each of the 2 images:

    a. Under "File," in the heading, Click "Open Figure"

    b. Select the file containing the undeformed configuration, e.g., "initial.bmp"

    c. Using the "T axis" that appears, with the mouse, locate the upper left bound of the first marker and left-click on it with the mouse (See Fig. 53, (i))

    d. Again, using the "T axis," locate the lower right bound of the first marker and left-click on it with the mouse [See Fig. 53, (ii)]

    e. Continue outlining the other three markers as indicated in Fig. 54 - 56 [Note: When finished outlining the marks, the program will save the locations of the

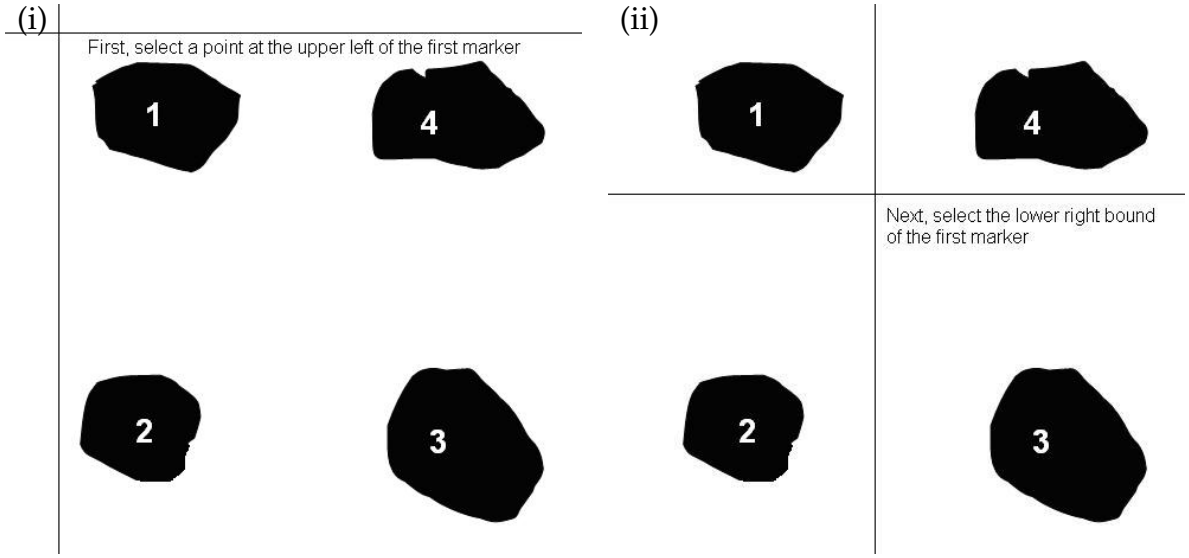

Figure 53: Methods for outlining the first of four markers: (i) Mark the upper left bound of the first marker, then (ii) the lower right bound of the first marker

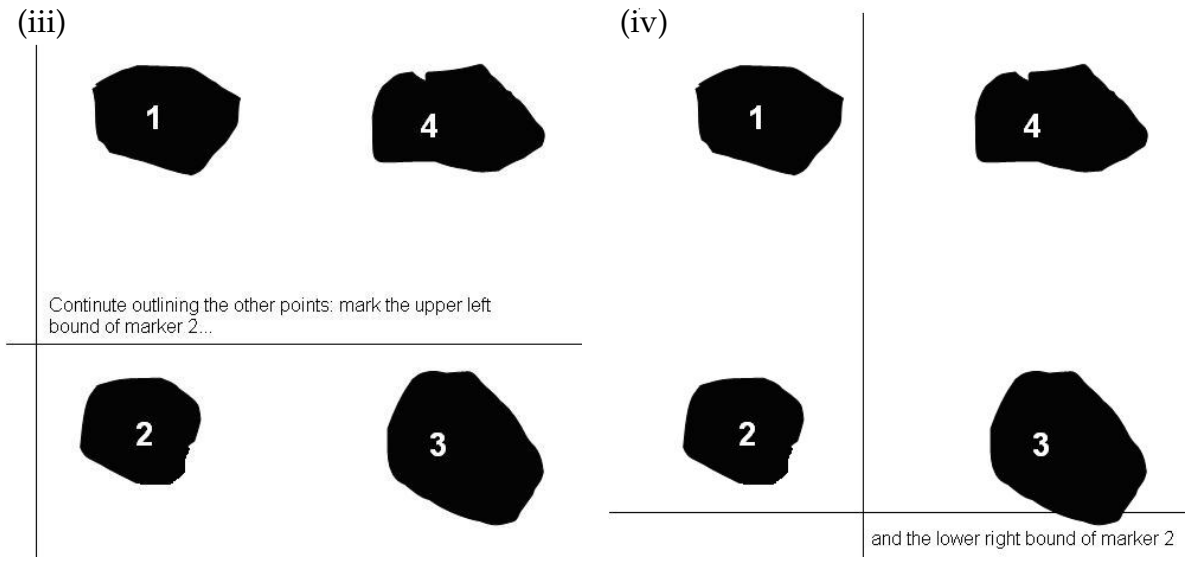

Figure 54: Methods for outlining the second of four markers: (iii) Mark the upper left bound of the second marker, then (iv) the lower right bound of the second marker

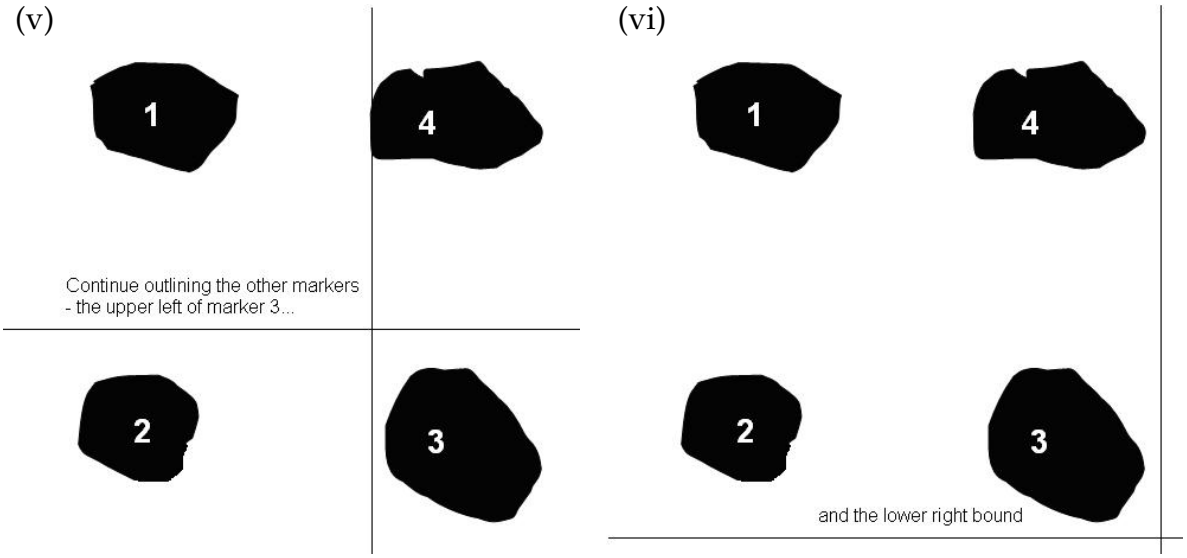

Figure 55: Methods for outlining the third of four markers: (v) Mark the upper left bound of the third marker, then (vi) the lower right bound of the third marker

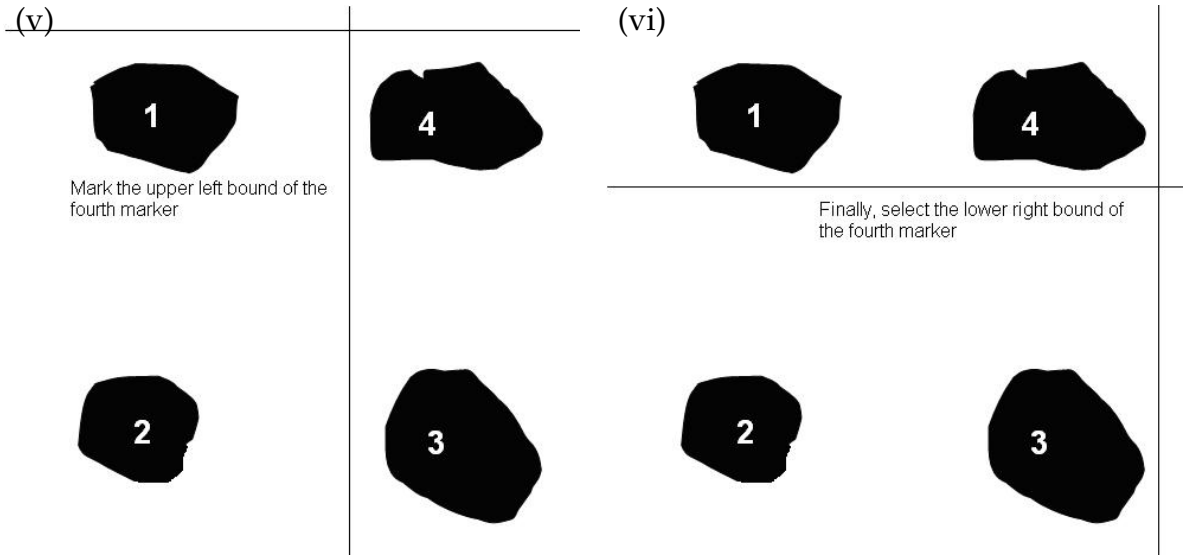

Figure 56: Methods for outlining the fourth of four markers: (vii) Mark the upper left bound of fourth marker, then (viii) the lower right bound of fourth marker

centroids of the markers in a temporary file, "centroids_temp.csv," and the markers saved in a temporary file, "marks_temp.csv." WARNING: Each time a file is opened and the markers are outlined, these files will be overwritten!]

f. After outlining the four markers, click "Save Initial Markers" [Note: If the user is not sure he/she has outlined the markers, the user may open the figure again and repeat. The locations of the centroids are stored in a temporary file that is overwritten each time the user opens the images and outlines the markers - or after 8 left-clicks of the mouse]

g. Repeat steps a through d for the file containing the deformed configuration, e.g., "final. bmp," and click "Save Final Markers" (instead of "Save Initial Markers") [Note: Each time the user clicks either "Save Initial Markers" or "Save Final Markers," he/she is saving the temporary files containing the locations of the centroids (centroids_temp.csv) to "image1_cents.csv" and "image2_cents.csv," respectively. These files may be opened with Microsoft Excel or a similar spreadsheet as delimited text];

h. Click "Calculate Strain." The program calls a subroutine to calculate the Green's strain at each 'node' (centroids of each markers in undeformed configuration) and average interpolated extensional strains at the nodal location (s,t) = (0,0), based on method of Hoffman and Grigg, 1984 [98] (See Section C.2 below).

The program prints to the Command Window:

1. The matrix containing the components of the average Right Cauchy-Green Deformation tensor at nodal location (0,0), or C_avg
2. The matrices containing the components of the Green's Strains at each of the four nodes
3. The matrix containing the components of the average interpolated extensional strains at nodal location (0,0)

C.2 MATHEMATICAL FOUNDATIONS

Strain was measured optically by taking images of four ink markers placed on the tissue. The markers had high contrast with the surrounding tissue, so that the pixel intensities had a large degree of difference and a threshold algorithm could be utilized to distinguish them. Global co-ordinates were taken as the axis of the image (Fig. 57).

The technique is described in detail by Hoffman and Grigg, 1984 [98] and is based on first-order Lagrange interpolation functions (see, for example, [167]). Briefly, a pth-order Lagrange rectangular element has n nodes, with

$$n = (p+1)^2 \tag{C.1}$$

where (p = 0,1,2,...) and the associated polynomial contains the terms from the pth parallelogram or the pth rectangle in Pascal's triangle (Figure 9.5 in [167]). The pth-order Lagrange rectangular element has the pth-degree polynomial

$$r(X_1, X_2) = \sum_{i=1}^{n} a_1 X_1^j X_2^k = \sum_{i=1}^{n} r_i \Psi_i \tag{C.2}$$

where $j, k \leq p$

By taking the tensor product of the X_1-direction (one-dimensional) interpolation functions with the X_2-direction (one-dimensional) interpolation functions, one can obtain the Lagrange interpolation functions associated with rectangular elements (two-dimensional):

$$\begin{bmatrix} \Psi_1 & \Psi_{p+2} & \dots & \Psi_k \\ \Psi_2 & & & \\ \dots & & & \\ \Psi_{p+1} & \Psi_{2p+2} & \dots & \Psi_n \end{bmatrix} = \begin{bmatrix} f_1 \\ f_2 \\ \dots \\ f_{p+1} \end{bmatrix} \begin{bmatrix} g_1 & g_2 & \dots & g_{p+1} \end{bmatrix} \tag{C.3}$$

where $k = (p+1)p+1$, $n = (p+1)^2$ and $f_i(x_1)$ and $g_i(x_2)$ are the pth-order interpolants in X_1 and X_2, respectively.

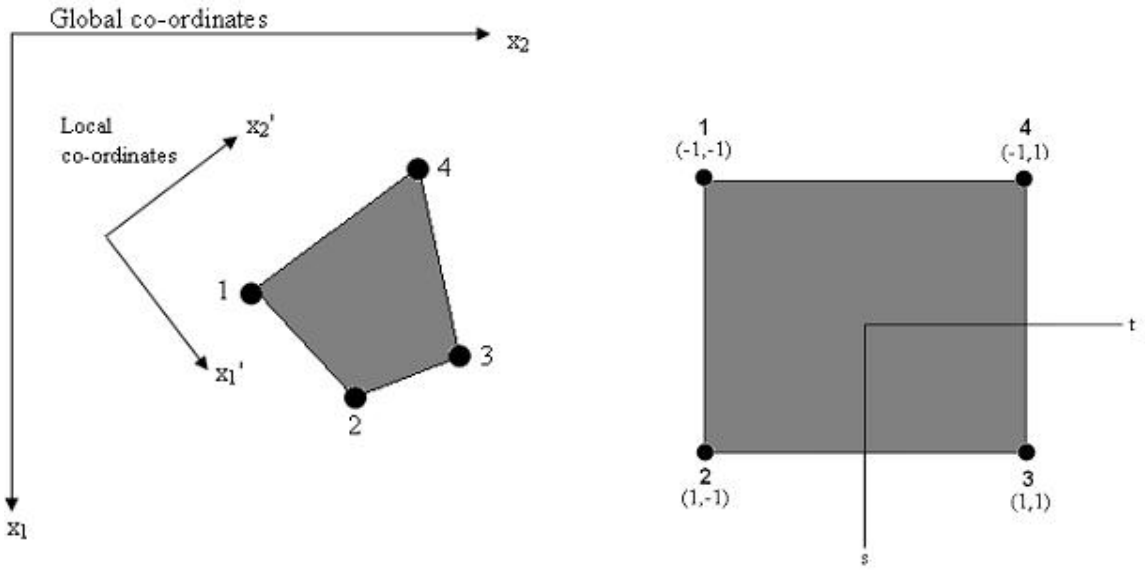

Figure 57: Four node quadrilateral element in different co-ordinate systems, global and local (left), and natural co-ordinates (right). Note that the global co-ordinate axes are placed in line with the image axis used in MATLAB, and the local co-ordinates have origin at the marker on the bone, for example, and although are shown otherwise, in our case are in the same direction as the global co-ordinates.

The interpolation functions in the above can be expressed in terms of natural co-ordinates s and t (Fig. 57),

$$s = \frac{2(X_1 - x) - a}{a} \tag{C.4}$$

and

$$t = \frac{2(X_2 - y) - b}{b} \tag{C.5}$$

where x and y are global co-ordinates of the node 1 in the local X_1' and X_2' co-ordinates, and a and b are the dimensions along the X_1 and X_2 directions, respectively.

In our case, with 4 nodes, p = 1 and n = 4, so the equation above becomes

$$\begin{bmatrix} \Psi_1 & \Psi_4 \\ \Psi_2 & \Psi_3 \end{bmatrix} = \begin{bmatrix} 1 - \frac{X_1}{a} \\ \frac{X_1}{a} \end{bmatrix} \begin{bmatrix} 1 - \frac{X_2}{b} & \frac{X_2}{b} \end{bmatrix} = \begin{bmatrix} \left(1 - \frac{X_1}{a}\right)\left(1 - \frac{X_2}{b}\right) & \left(1 - \frac{X_1}{a}\right)\left(\frac{X_2}{b}\right) \\ \left(\frac{X_1}{a}\right)\left(1 - \frac{X_2}{b}\right) & \left(\frac{X_1}{a}\right)\left(\frac{X_2}{b}\right) \end{bmatrix} \tag{C.6}$$

If we take a co-ordinate system with the origin fixed at node 1 and co-ordinates parallel to the sides of the element, we have x = y = 0 (Fig. 58).

Thus, using eqs. C.4 & C.5 with $x = y = 0$, the interpolation functions in eq. C.6 can be written in terms of natural co-ordinates as

$$\Psi_1 = \frac{1}{4}(1 - s)(1 - t) \tag{C.7}$$

$$\Psi_2 = \frac{1}{4}(1 + s)(1 - t) \tag{C.8}$$

$$\Psi_3 = \frac{1}{4}(1 + s)(1 + t) \tag{C.9}$$

$$\Psi_4 = \frac{1}{4}(1 - s)(1 + t) \tag{C.10}$$

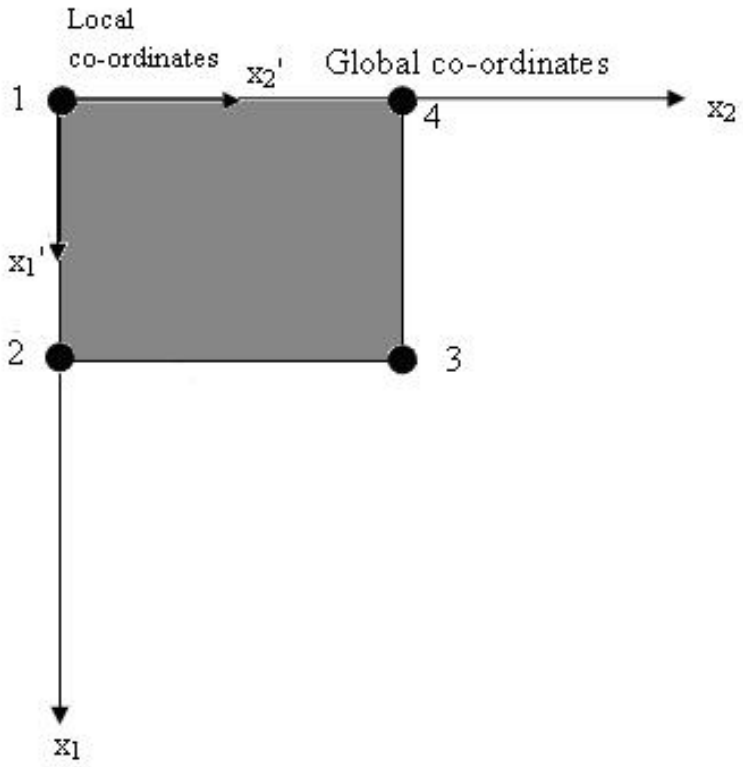

Figure 58: Co-ordinate system with origin fixed at node 1 and the local and global co-ordinates parallel to the sides of the element.

Therefore, the (X_1, X_2) co-ordinates of any point within the four node element can be expressed using the interpolation functions Ψ_i as

$$X_1 = \sum_{i=1}^{4} \Psi_i X_1^i \tag{C.11}$$

$$X_2 = \sum_{i=1}^{4} \Psi_i X_2^i \tag{C.12}$$

where the Ψ_i are given in eqs. C.7 - C.10. These equations define the mapping of the element from the X_1, X_2 plane to the s, t plane.

Similarly, the components of displacement u = (u, v) of any point X = (X_1, X_2) within the element can be given in terms of the nodal displacements (u_i, v_i) by the relations

$$u = \sum_{i=1}^{4} \Psi_i u_i \tag{C.13}$$

$$v = \sum_{i=1}^{4} \Psi_i v_i \tag{C.14}$$

Therefore, the same interpolation functions that are used to define the geometry can be used to describe the displacement field (element is isoparametric). By parameterizing the geometry as such, we may use four markers at any arbitrary location, so long as their (local) co-ordinates do not cross during deformation.

Below is a discussion of how we compute strain.

The Green-Lagrange strain tensor is given by

$$\mathbf{E} = \frac{1}{2}\left(\mathbf{F}^T\mathbf{F} - \mathbf{1}\right) \tag{C.15}$$

where **F** is the deformation gradient in Lagrangian form and **1** is the identity tensor.

The components of the tensor **E** in 2D Cartesian co-ordinates, given in matrix form by

$$\mathbf{E} = \begin{bmatrix} E_{11} & E_{12} \\ E_{21} & E_{22} \end{bmatrix} \tag{C.16}$$

are found by the equations given in [98], which is used frequently in finite element analysis. The derivation of these equations is shown below.

Let **X** be the direction vector from the origin to a point in space, and let **x** be a direction vector from the origin to that same point in space at some later time after deformation has occurred. The displacement is given as **u** = **x** - **X**, or in component form in 2D Cartesian space,

$$\begin{bmatrix} u \\ v \end{bmatrix} = \begin{bmatrix} x_1 \\ x_2 \end{bmatrix} - \begin{bmatrix} X_1 \\ X_2 \end{bmatrix} \tag{C.17}$$

The deformation gradient, **F**, is given as

$$\mathbf{F} = \nabla \mathbf{x} \tag{C.18}$$

or in 2D Cartesian co-ordinates,

$$\begin{bmatrix} F_{11} & F_{12} \\ F_{21} & F_{22} \end{bmatrix} = \begin{bmatrix} \frac{\partial u}{\partial X_1} + 1 & \frac{\partial v}{\partial X_1} \\ \frac{\partial u}{\partial X_2} & \frac{\partial v}{\partial X_2} + 1 \end{bmatrix} \tag{C.19}$$

The (symmetric) Green-Lagrange strain tensor is given by eqs. C.15 & C.16, which is computed, by using the above, to give

$$\begin{bmatrix} E_{11} & E_{12} \\ E_{21} & E_{22} \end{bmatrix} \tag{C.20}$$

with components

$$E_{11} = \frac{\partial u}{\partial X_1} + \frac{1}{2}\left[\left(\frac{\partial u}{\partial X_1}\right)^2 + \left(\frac{\partial v}{\partial X_1}\right)^2\right] \tag{C.21}$$

$$E_{22} = \frac{\partial v}{\partial X_2} + \frac{1}{2}\left[\left(\frac{\partial v}{\partial X_2}\right)^2 + \left(\frac{\partial u}{\partial X_2}\right)^2\right] \tag{C.22}$$

$$E_{12} = E_{21} = \frac{1}{2}\left[\frac{\partial u}{\partial X_2} + \frac{\partial v}{\partial X_1} + \left(\frac{\partial u}{\partial X_1}\right)\left(\frac{\partial u}{\partial X_2}\right) + \left(\frac{\partial v}{\partial X_1}\right)\left(\frac{\partial v}{\partial X_2}\right)\right] \tag{C.23}$$

Thus, the strain is given in 2D by the above equations, with E_{11} and E_{22} the components in the X_1 and X_2 directions, respectively, and E_{12} the shear component.

The partial derivatives are computed from the property of the chain rule, described in the appendix of [98]:

$$\begin{bmatrix} \frac{\partial u}{\partial X_1} \\ \frac{\partial u}{\partial X_2} \end{bmatrix} = \frac{1}{|J|} \begin{bmatrix} \frac{\partial X_2}{\partial t} & -\frac{\partial X_2}{\partial s} \\ -\frac{\partial X_1}{\partial t} & -\frac{\partial X_1}{\partial s} \end{bmatrix} = \begin{bmatrix} \frac{\partial u}{\partial s} \\ \frac{\partial u}{\partial t} \end{bmatrix} \tag{C.24}$$

$$\begin{bmatrix} \frac{\partial v}{\partial X_1} \\ \frac{\partial v}{\partial X_2} \end{bmatrix} = \frac{1}{|J|} \begin{bmatrix} \frac{\partial X_2}{\partial t} & -\frac{\partial X_2}{\partial s} \\ -\frac{\partial X_1}{\partial t} & -\frac{\partial X_1}{\partial s} \end{bmatrix} = \begin{bmatrix} \frac{\partial v}{\partial s} \\ \frac{\partial v}{\partial t} \end{bmatrix} \tag{C.25}$$

where $|J| = \frac{\partial X_1}{\partial s}\frac{\partial X_2}{\partial t} - \frac{\partial X_1}{\partial t}\frac{\partial X_2}{\partial s}$.

The displacements (u, v) of each node are computed from the position vector components of each node in the undeformed (X_1, X_2) and deformed (x_1, x_2) configuration, (u, v) = (x_1, x_2) - (X_1, X_2). These position vector components are found by computing the centroid of each one of the four markers in the initial and deformed configuration, or in the first and subsequent images, respectively.

Finally, using polar decomposition (eq. 2.8), we can decouple pure stretch, **U**, from pure rotation, **R**. The deformation gradient can be written in terms of these tensors

Substituting eq. 2.8 into eq. C.15 gives (from properties of tensor multiplication and symmetry of **U**):

$$\mathbf{E} = \frac{1}{2}\left[\mathbf{U}^2 - \mathbf{1}\right] \tag{C.26}$$

Thus, if we find **E** from positions of four markers via the method described above, we can compute **U** from the above equation, **F** from eq. C.19, and then **R** from eq. 2.8. The tensor **U** will give us information about the pure stretch or change in local shape, while the tensor **R** provides information about pure rotation of the set of markers.

C.3 MATLAB CODE FOR OPTICAL STRAIN MEASUREMENT

Below are the MATLAB programs developed for performing optical strain measurement. This code should be used along with the Instruction manual given above.

C.3.1 maingui.m

Below is the main program for running the optical strain measurement graphical user interface (GUI).

```
function maingui
% Program maingui is the main interface for running the optical strain
% measurement software
% ———————————————————
% Custom subroutines used in this program:
% calccentroid
% Strain.m
% ———————————————————
% Initialize and hide the GUI as it is being constructed.
hMainFigure = figure('Visible','off','Position',[360,400,720,550],...
    'MenuBar','none');
% Define the file menu at the top of the gui
hFileMenu = uimenu(... % File menu
    'Parent',hMainFigure,...
    'HandleVisibility','callback', ...
    'Label','File');
% Define the three options in the file menu
hOpenMenuitem = uimenu(... % Open menu item
    'Parent',hFileMenu,...
    'Label','Open Figure',...
    'HandleVisibility','callback', ...
```

```
    'Callback', @hOpenMenuitemCallback);
hPrintMenuitem = uimenu(... % Print menu item
    'Parent',hFileMenu,...
    'Label','Print',...
    'HandleVisibility','callback', ...
    'Callback', @hPrintMenuitemCallback);
% Define the Instruction menu at the top of the gui
hInstMenu = uimenu(... % Instruction menu
    'Parent',hMainFigure,...
    'HandleVisibility','callback', ...
    'Label','Instructions');
% Define the one option in the Instructions menu
hInstructions = uimenu(... % Open menu item
    'Parent',hInstMenu,...
    'Label','Open Instructions',...
    'HandleVisibility','callback', ...
    'Callback', @hOpenInstructionsCallback);
% Construct the components: the three buttons and the display.
himg1 = uicontrol('Style','pushbutton',... %'Save Initial Markers' button
    'String','Save Initial Markers','Position',[480,470,100,25],...
    'Callback',@img1Callback);
himg2 = uicontrol('Style','pushbutton',... %'Save Final Markers' button
    'String','Save Final Markers','Position',[600,470,100,25],...
    'Callback',@img2Callback);
hcalcstrrain = uicontrol('Style','pushbutton',... %'Calculate Strain' button
    'String','Calculate Strain','Position',[480,420,100,25],...
    'Callback',@calcCallback);
% Generate an arbitrary axes graphis object
ha = axes('Units','pixels','Position',[50,100,400,400]);
% Initialize the GUI.
```

```
% Change units to normalized so components resize automatically.
set([hMainFigure],'Units','normalized');
% Display a figure in the axes.
img1 = imread('display.bmp');
image(img1);
% Assign the GUI a name to appear in the window title.
set(hMainFigure,'Name','Optical Strain Measurement')
% Move the GUI to the center of the screen.
movegui(hMainFigure,'center')
%Make the GUI visible
set(hMainFigure,'Visible','on')
% Push button callbacks. Each callback plots current data in
% specified plot type.
function img1Callback(source,eventdata) % Callback for 'Save Initial Markers' button
    % Save file for original position
    marks=csvread('markstemp.csv');
    csvwrite('image1marks.csv',marks);
    cents=csvread('centroidstemp.csv');
    csvwrite('image1cents.csv',cents);
    image1=imread('img.bmp','bmp');
    imwrite(image1,'image1.bmp')
end
function img2Callback(source,eventdata) % Callback for 'Save Final Markers' button
    % Save file for final position
    marks=csvread('markstemp.csv');
    csvwrite('image2marks.csv',marks);
    cents=csvread('centroidstemp.csv');
    csvwrite('image2cents.csv',cents);
    image2=imread('img.bmp','bmp');
    imwrite(image2,'image2.bmp');
```

```
end
function calcCallback(source,eventdata) % Callback for 'Calculate Strain'
    % Obtain file for original position
    centsimg1=csvread('image1cents.csv');
    centsimg2=csvread('image2cents.csv');
    Cx1img1=centsimg1(:,1);
    Cx2img1=centsimg1(:,2);
    Cx1img2=centsimg2(:,1);
    Cx2img2=centsimg2(:,2);
    % Calculate horizontal and vertical displacement
    x = Cx1img1;
    y = Cx2img1;
    u = Cx1img2 - Cx1img1;
    v = Cx2img2 - Cx2img1;
    % Calculate Green's Strain
    [E1,E2,E3,E4,Eavg] = Strain(x,y,u,v,4);
    % Display Strain values for each 'node,' or centroid of each marker
    disp('E of first marker is ')
    disp(E1)
    disp('E of second marker is ')
    disp(E2)
    disp('E of third marker is ')
    disp(E3)
    disp('E of fourth marker is ')
    disp(E4)
    disp('The average, i.e., at (s,t)=(0,0), interpolated extensional strains are')
    disp(Eavg)
    % Show the original and final location of centroids or 'nodes'
    image1=imread('image1.bmp','bmp');
    imshow(image1)
```

```
    hold on;
    plot(Cx2img1(1),Cx1img1(1),'b.');
    plot(Cx2img1(2),Cx1img1(2),'g.');
    plot(Cx2img1(3),Cx1img1(3),'r.');
    plot(Cx2img1(4),Cx1img1(4),'c.');
    plot(Cx2img2(1),Cx1img2(1),'bx');
    plot(Cx2img2(2),Cx1img2(2),'gx');
    plot(Cx2img2(3),Cx1img2(3),'rx');
    plot(Cx2img2(4),Cx1img2(4),'cx');
    % Write the data to file
    csvwrite('E1.csv',E1);
    csvwrite('E2.csv',E2);
    csvwrite('E3.csv',E3);
    csvwrite('E4.csv',E4);
    csvwrite('Eavg.csv',Eavg);
end
% Callbacks for the File Menu and 3 options:
% Option 1: Open Figure
function [marks]=hOpenMenuitemCallback(hObject, eventdata)
% Callback function run when the Open menu item is selected
    imgfile = uigetfile('*.bmp', 'Select file for original position');
    img = imread(imgfile);
    imwrite (img, 'img.bmp');
    image(img)
    image(img); axis image
    % Use ginput to select corner points of a rectangular
    % region by pointing and clicking the mouse twice
    [x2 x1] = ginput(8);
    % Declare selected points
    mark1pt1=[floor(x1(1)) floor(x2(1))];
```

```
mark1pt2=[ceil(x1(2)) ceil(x2(2))];
[mark1Cx1,mark1Cx2]=calccentroid(img,mark1pt1,mark1pt2)'
mark2pt1=[floor(x1(3)) floor(x2(3))];
mark2pt2=[ceil(x1(4)) ceil(x2(4))];
[mark2Cx1,mark2Cx2]=calccentroid(img,mark2pt1,mark2pt2);
mark3pt1=[floor(x1(5)) floor(x2(5))];
mark3pt2=[ceil(x1(6)) ceil(x2(6))];
[mark3Cx1,mark3Cx2]=calccentroid(img,mark3pt1,mark3pt2);
mark4pt1=[floor(x1(7)) floor(x2(7))];
mark4pt2=[ceil(x1(8)) ceil(x2(8))];
[mark4Cx1,mark4Cx2]=calccentroid(img,mark4pt1,mark4pt2);
cents(1,1)=mark1Cx1;
cents(1,2)=mark1Cx2;
cents(2,1)=mark2Cx1;
cents(2,2)=mark2Cx2;
cents(3,1)=mark3Cx1;
cents(3,2)=mark3Cx2;
cents(4,1)=mark4Cx1;
cents(4,2)=mark4Cx2;
disp(cents)
csvwrite('centroidstemp.csv',cents);
marks(1,1)=floor(x1(1));
marks(1,2)=floor(x2(1));
marks(2,1)=ceil(x1(2));
marks(2,2)=ceil(x2(2));
marks(3,1)=floor(x1(3));
marks(3,2)=floor(x2(3));
marks(4,1)=ceil(x1(4));
marks(4,2)=ceil(x2(4));
marks(5,1)=floor(x1(5));
```

```
        marks(5,2)=floor(x2(5));
        marks(6,1)=ceil(x1(6));
        marks(6,2)=ceil(x2(6));
        marks(7,1)=floor(x1(7));
        marks(7,2)=floor(x2(7));
        marks(8,1)=ceil(x1(8));
        marks(8,2)=ceil(x2(8));
        csvwrite('markstemp.csv',marks);
    end
    % Option 2: Print
    function hPrintMenuitemCallback(hObject, eventdata)
    % Callback function run when the Print menu item is selected
        printdlg(hMainFigure);
    end
    function [marks]=hOpenInstructionsCallback(hObject, eventdata)
        winopen('Instructions.pdf')
    end
    end
```

C.3.2 Strain.m

Below is the MATLAB function for computing optical strain

```
    function [E1,E2,E3,E4,Eavg] = Strain(x,y,u,v,n);
    % Subroutine Strain.m
    %*********************************************************************
    % Program description: Program to calculate Green's Strains
    %*********************************************************************
    % Variables used in this program
    % s = Natural abscissa coordinate
    % t = Natural ordinate coordinate
```

% i = element node (i = 1..4)

% The following variables are used to implement chain rule for expressions

% for the partial derivatives of the displacement components with respect

% to s and t

% dydt(i) = partial derivative of y location of element (i) wrt t

% dyds(i) = partial derivative of y location of element (i) wrt s

% dxdt(i) = partial derivative of x location of element (i) wrt t

% dxds(i) = partial derivative of x location of element (i) wrt s

% dudt(i) = partial derivative of x-displacement of element (i) by t

% duds(i) = partial derivative of x-displacement of element (i) by s

% dvdt(i) = partial derivative of y-displacement of element (i) by t

% dvds(i) = partial derivative of y-displacement of element (i) by s

% J(i) = Jacobian for each element (i)

% Jabs(i) = absolute value of Jacobian

% A = assembled inverse (2x2) matrix of relationships between partial

% derivatives

% cu = assembled 1x2 matrix of partial derivatives of u wrt s, t

% cv = assembled 1x2 matrix of partial derivatives of v wrt s, t

% Cu = solution of matrix cu multipled by matrix A

% Du = variable defined as Cu divided by abs value of Jacobian, Jabs(i)

% dudx = partial derivative of x-displacement of element (i) wrt x

% dudy = partial derivative of x-displacement of element (i) wrt y

% Cv = solution of matrix cv multipled by matrix A

% Dv = variable defined as Cv divided by abs value of Jacobian, Jabs(i)

% dvdx = partial derivative of y-displacement of element (i) wrt x

% dvdy = partial derivative of y-displacement of element (i) wrt y

% Exx(i) = Component of Green's strain in x-direction for element (i)

% Eyy(i) = Component of Green's strain in y-direction for element (i)

% Exy(i) = Component of Green's strain in transverse direction for

% element (i)

```
%*********************************************************************
% Subroutines called in this program
% matrixmult.m = function to multiply two matrices
%*********************************************************************
% Set natural coordinate system variables
s = [-1, 1, 1, -1, 0];
t = [-1, -1, 1, 1, 0];
% From Hoffman and Grigg, eqn 3 gives
% N1 = (1-s)(1-t)/4
% N2 = (1+s)(1-t)/4
% N3 = (1+s)(1+t)/4
% N4 = (1-s)(1+t)/4
for i = 1:n+1;
    % Take the derivative of x with respect to t:
    dxdt(i) = (1/4)*((s(i)-1)*x(1) - (1+s(i))*x(2) + (1+s(i))*x(3) + (1-s(i))*x(4));
    % Take the derivative of x with respect to s:
    dxds(i) = (1/4)*((t(i)-1)*x(1) + (1-t(i))*x(2) + (1+t(i))*x(3) - (1+t(i))*x(4));
    % Take the derivative of y with respect to t:
    dydt(i) = (1/4)*((s(i)-1)*y(1) - (1+s(i))*y(2) + (1+s(i))*y(3) + (1-s(i))*y(4));
    % Take the derivative of y with respect to s:
    dyds(i) = (1/4)*((t(i)-1)*y(1) + (1-t(i))*y(2) + (1+t(i))*y(3) - (1+t(i))*y(4));
    % Take the derivative of u with respect to t:
    dudt(i) = (1/4)*((s(i)-1)*u(1) - (1+s(i))*u(2) + (1+s(i))*u(3) + (1-s(i))*u(4));
    % Take the derivative of u with respect to s:
    duds(i) = (1/4)*((t(i)-1)*u(1) + (1-t(i))*u(2) + (1+t(i))*u(3) - (1+t(i))*u(4));
    % Take the derivative of v with respect to t:
    dvdt(i) = (1/4)*((s(i)-1)*v(1) - (1+s(i))*v(2) + (1+s(i))*v(3) + (1-s(i))*v(4));
    % Take the derivative of v with respect to s:
    dvds(i) = (1/4)*((t(i)-1)*v(1) + (1-t(i))*v(2) + (1+t(i))*v(3) - (1+t(i))*v(4));
    % Calculate the Jacobian matrix from eqn A5 in Hoffman and Grigg
```

```
J(i) = dxds(i)*dydt(i) - dxdt(i)*dyds(i);
if J(i) ¿ 0;
    Jabs(i) = J(i);
else
    Jabs(i) = -1*J(i);
end
% Assemble the matrices given in eqns A3 and A4 in Hoffman and Grigg
A = [dydt(i), -dyds(i); -dxdt(i), dxds(i)];
cu = [duds(i); dudt(i)]; % Equation A1
cv = [dvds(i); dvdt(i)]; % Equation A2
% Evaluate eqn A3
[Cu] = matrixmult(A,cu,length(A(:,1)),length(A(1,:)),length(cu(1,:)));
Du = (1/Jabs(i))*Cu;
dudx(i) = Du(1);
dudy(i) = Du(2);
% Evaluate eqn A4
[Cv] = matrixmult(A,cv,length(A(:,1)),length(A(1,:)),length(cv(1,:)));
Dv = (1/Jabs(i))*Cv;
dvdx(i) = Dv(1);
dvdy(i) = Dv(2);
% Calculate Strain from equation 5
Exx(i) = dudx(i) + 0.5*((dudx(i))**2 + (dvdx(i))**2);
Eyy(i) = dvdy(i) + 0.5*((dvdy(i))**2 + (dudy(i))**2);
Exy(i) = 0.5*(dudy(i) + dvdx(i) + (dudx(i))*(dudy(i)) + (dvdx(i))*(dvdy(i)));
Cu = 0; % Reset C to zero
Cv = 0; % Reset C to zero
Du = 0; % Reset D to zero
Dv = 0; % Reset D to zero
A = 0; % Reset A to zero
cu = 0; % Reset cu to zero
```

```
    cv = 0;% Reset cv to zero
end
% Determine the average interpolated extensional strain at the center node,
% (s,t)=(0,0)
Eavg(1,1)=Exx(5);
Eavg(1,2)=Exy(5);
Eavg(2,1)=Exy(5);
Eavg(2,2)=Eyy(5);
% Place strain values for each marker in an array
E1(1,1) = Exx(1);
E1(1,2) = Exy(1);
E1(2,1) = Exy(1);
E1(2,2) = Eyy(1);
E2(1,1) = Exx(2);
E2(1,2) = Exy(2);
E2(2,1) = Exy(2);
E2(2,2) = Eyy(2);
E3(1,1) = Exx(3);
E3(1,2) = Exy(3);
E3(2,1) = Exy(3);
E3(2,2) = Eyy(3);
E4(1,1) = Exx(4);
E4(1,2) = Exy(4);
E4(2,1) = Exy(4);
E4(2,2) = Eyy(4);
% Calculate Right Cauchy-Green Tensor for each point
I = [1 0; 0 1];
C1 = 2*E1+I;
C2 = 2*E2+I;
C3 = 2*E3+I;
```

```
C4 = 2*E4+I;
% Calculate Right Cauchy-Green Tensor for middle point, (s,t)=(0,0)
Cavg = 2*Eavg+I
```

C.3.3 calccentroid.m

Below is the program used to calculate the x and y co-ordinates of the centroid of an arbitrary marker

```
function [Cx1,Cx2]=calccentroid(pic,pt1,pt2)
% Index into the original image to create the new image
MM = pic(pt1(1):pt2(1), pt1(2):pt2(2),:);
m = length(MM(:,1)); % total length of the rows
n = length(MM(1,:)); % total length of the columns
[cx2,cx1] = aitcentroid(MM); % Find local centroid of marker
Cx1 = (pt1(1)-1) + cx1; % Calculate global x-coordinate of centroid
Cx2 = (pt1(2)-1) + cx2; % Calculate global y-coordinate of centroid
```

C.3.4 aitcentroid.m

Below is the program used to calculate the local centroid of a marker

```
function [meanx,meany] = aitcentroid(pic);
%*****************************************
% Function takes a picture as an argument and returns the x and y
% co-ordinates of its centroid
%*****************************************
[x,y,z] = size(pic);
% Check whether the picture is colored or monochromatic, if colored then converting to gray.
if(z==1);
else
    pic = rgb2gray(pic);
```

```
end
im = pic;
[rows,cols] = size(im);
x = ones(rows,1)*[1:cols]; % Matrix with each pixel set to its x coordinate
y = [1:rows]'*ones(1,cols); % Matrix with each pixel set to its y coordinate
area = sum(sum(im));
meanx = sum(sum(double(im).*x))/area;
meany = sum(sum(double(im).*y))/area;
```

C.3.5 matrixmult.m

Below is a MATLAB function to multiply two matrices

```
function [C] = matrixmult(A,B,n,m,r)
% Function to multiply two matrices
C = 0;
DUM = 0;
for j = 1:r;
    for i = 1:n;
        for k = 1:m;
            DUM = DUM + A(i,k)*B(k,j);
            C(i,j) = DUM;
        end
        DUM = 0;
    end
end
```

APPENDIX D

PARAMETER SENSITIVITY STUDY ON RECRUITMENT FUNCTION

In Chapter 4, collagen fibers were defined to be recruited when the tortuosity decreased below a $\tau_{critical}$ of 1.02 (Section 4.2.2). Here, a parameter sensitivity study was performed to determine the range over which the choice of $\tau_{critical}$ does not significantly change the result (Section D.1 below). Six different values of $\tau_{critical}$ were selected to investigate the sensitivity to its choice.

Furthermore, 25% of the collagen fibers were randomly eliminated from the tortuosity analysis, to determine the effect of number of fibers on the final result (results not shown). For this reduction in fiber number, no significant changes were observed in the parameters listed in Table 3. Note that the results were reported to two significant digits. Lowering the number of fibers by 25% changed the values of the fourth or greater significant digit; thus, we deemed this reduction had an insignificant effect on parameters.

D.1 SENSITIVITY STUDY ON CRITICAL TORTUOSITY

The critical tortuosity value was chosen after analyzing the tortuosity of the 8 specimens tested in Chapter 4. The maximum tortuosity at the highest stretch achieved in each experiment was observed: in several samples this value was very close to 1.02, thus motivating its initial choice. Here, a sensitivity study was performed to determine if this choice of $\tau_{critical}$ was appropriate. Six different values of critical tortuosity ($\tau_{critical}$) were

chosen for Sample 05 in Table 3, including 1.02 used in Section 4.2.2. The fraction of recruited fibers were plotted for each tissue stretch value using each of these choices (Fig 59). The six chosen values were 1.010, 1.020, 1.025, 1.030, 1.040, and 1.050. Also, a critical tortuosity of 1.015 was investigated. Since this choice gave similar results to 1.020, the results were not depicted here.

Following the methods outlined in Section 4.2, the model obtained from using each of these critical tortuosity values was fit to the stress-stretch data obtained from the hUA-MPM system. The cumulative distribution function (eq. 4.3) was fit to the data resulting from each of these selections to obtain the parameters for the recruitment function d_1 with R^2 values (Table 7). Stiffness constants were obtained by fitting Model E for each selection to the data, as described in Section 4.2.4.

The R^2 values for each choice indicated a good fit (Table 7). However, these values may be skewed by the long toe region, and thus may not give an accurate estimation of the goodness-of-fit in the collagen-dominated regime. Visual examination of the curves suggested that, for values above 1.02, the model did not capture the upward bend typical of the mechanical response of arteries. Note the bend in the curve in the figures labeled (iii) through (vi) in Fig. 60, compared to (ii). Therefore, from the results of this parameter sensivity study on Sample 05, we concluded that the choice of $\tau_{critical}$ = 1.02 gave the best results with the highest R^2 values (Table 7 and Fig. 60), thus motivating its selection.

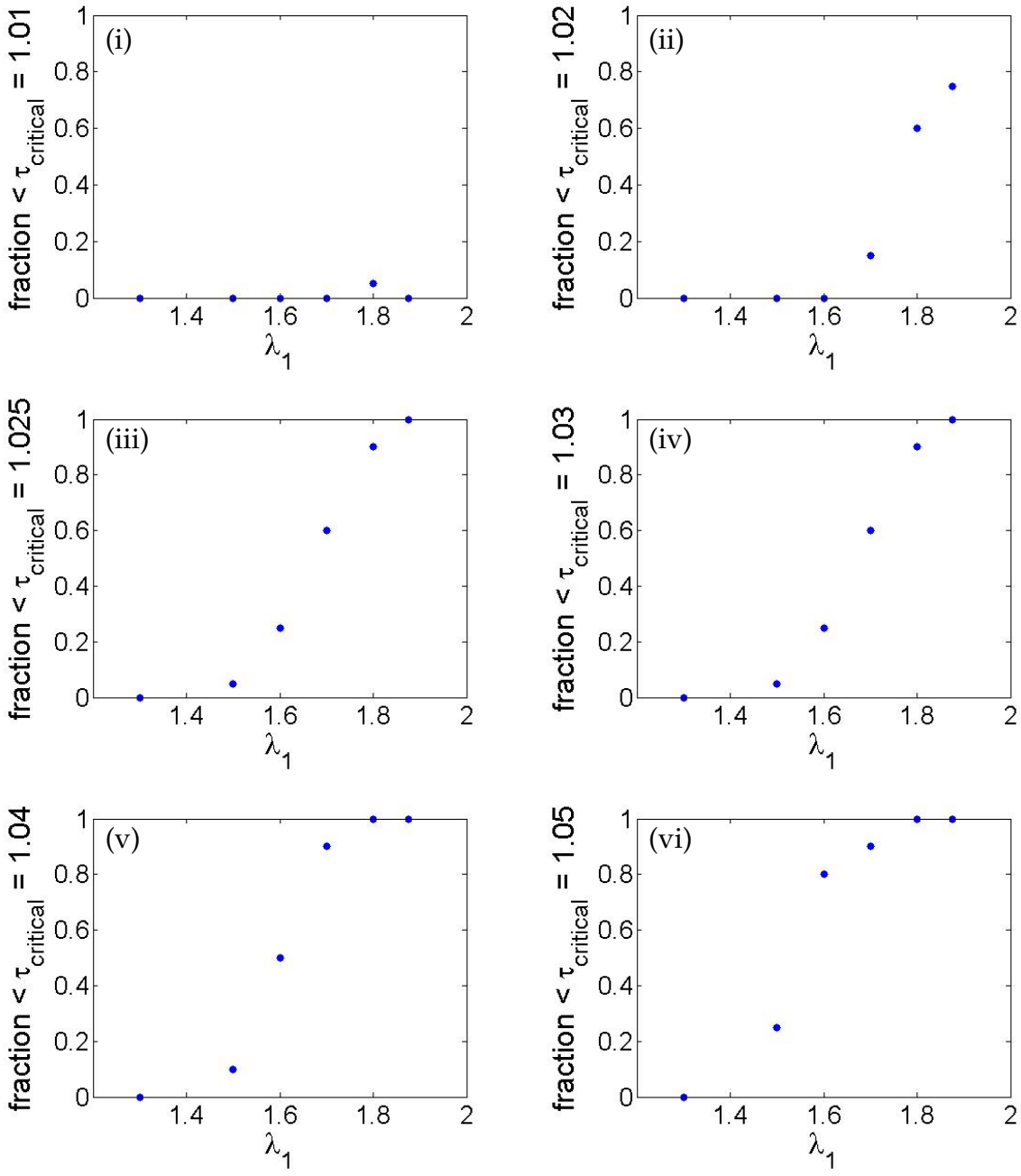

Figure 59: Fraction of fibers recruited by setting $\tau_{critical}$ to (i) 1.010, (ii) 1.020, (iii) 1.025, (iv) 1.030, (v) 1.040, (vi) 1.050. Results taken from Sample 05 in Fig. 31 and Table 3. Data from (ii) was used to evaluate the cumulative distribution function in d_1 for this sample in Chapter 4

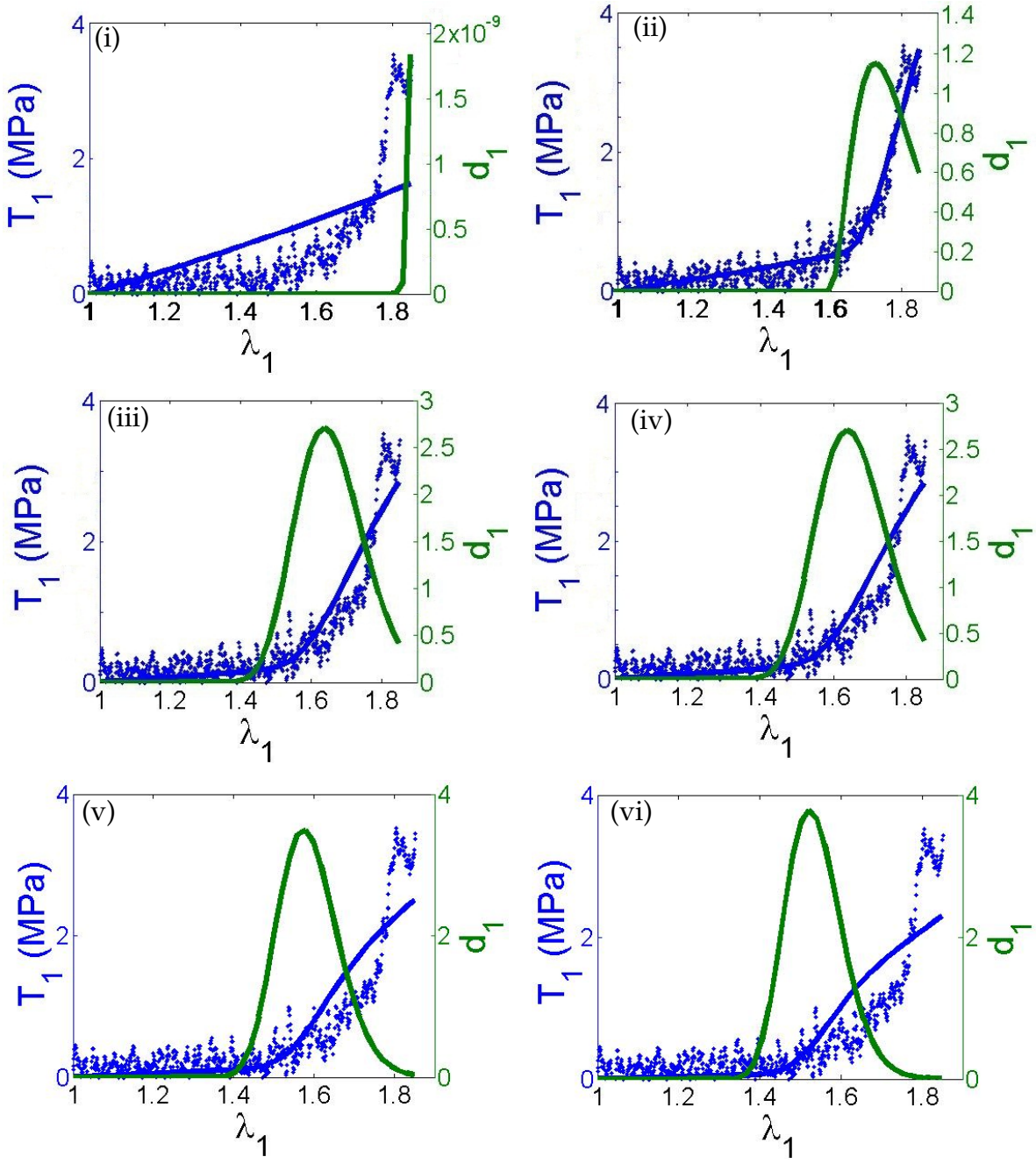

Figure 60: Results from fitting Model E to the stress-stretch data, setting $\tau_{critical}$ to (i) 1.010, (ii) 1.020, (iii) 1.025, (iv) 1.030, (v) 1.040, (vi) 1.050. Results taken from Sample 05 in Table 3. Compare the figure labeled (ii) above to (v) in Fig. 29

Table 7: Parameters (± 95% confidence interval) determined by the least-squares fit to the stress-stretch data acquired from the hUA-MPM system (NaN = Not a Number, infinite values obtained by the numerical technique)

$\tau_{critical}$	λ_{a1}	α	β	R^2	μ(kPa)	η(MPa)	R^2
1.010	1.8	7.2 ± NaN	5.7 ± NaN	0.200	560 ± 220	0.81 ± 23x10^6	0.9753
1.020	1.6	3.3 ± 1.3	22 ± 9.2	0.9957	260 ± 53	47 ± 5.5	0.9969
1.025	1.2	22 ± 7.9	0.032±0.012	0.9972	120 ± 94	9.5± 1.6	0.9943
1.030	1.2	22 ± 7.9	0.032±0.012	0.9972	120 ± 94	9.5± 1.6	0.9943
1.040	1.2	26 ± 5.9	0.022±0.005	0.9993	85 ± 130	7.0± 1.6	0.9910
1.050	1.2	23 ± 15	0.022±0.015	0.9932	48 ± 170	5.9± 1.7	0.9882

APPENDIX E

MATLAB COMPUTER PROGRAMS FOR ANALYZING COLLAGEN

E.1 PROGRAMS FOR ANALYZING FIBER ORIENTATION

E.1.0.1 MultipleImagesCollElas.m Below is a program for superimposing 2D stacks of images.

```
clear all
clear
clc
% Program MultipleImagesCollElas.m
% ————————————————————————————————
% Program description: Opens stacks of multi-photon images and superimposes
% them into a 2D rendering. Only use if have stacks. If images already
% reconstructed by MetaMorph, Imaris, etc., then start with m-file
% SaveForProcessing.m
% When running, please not the number of stacks you are importing, because
% the software will ask you to give it that number. You may select a
% subset of stacks, for example, you could pick image file labeled
% imgz003.tif as your first image and enter "3" for "Number of files."
% In this case, the software would superimpose stack files imgz003.tif,
% imgz004.tif, and imgz005.tif.
```

```
% NOTE: In this program, collagen and elastin stacks are in separate
% folders
% ————————————————————————————————————

% g=input('ENTER: Text file = 2, bmp = 1, tiff = 0 ');
g=0; % Only tiffs!
aimg=0; % Do not invert image
% clrsel=input('ENTER: 1 = collagen (red), 2 = elastin (green) ')
disp('Enter image size in pixels (multi-photon is typically 1024x1024)')
imgsiz=input('ENTER: 512 or 1024 ')
[colfile,colpath]=uigetfile('*.tif','Select collagen image file');
colim=imread([colpath colfile]);
[elfile,elpath]=uigetfile('*.tif','Select elastin image file');
elim=imread([elpath elfile]);
% Give size of image
M=imgsiz;
N=imgsiz;
% Make new black image
rgb=0;
for rgb=1:3;
    newimg(:,:,rgb)=double(zeros(imgsiz,imgsiz));
end
colfilsiz=size(colfile);
elfilsiz=size(elfile);
k=0;
ncol=str2num(colfile(colfilsiz(2)-4))+...
    10*str2num(colfile(colfilsiz(2)-5))+...
    100*str2num(colfile(colfilsiz(2)-6));
nel=str2num(elfile(elfilsiz(2)-4))+...
    10*str2num(elfile(elfilsiz(2)-5))+...
```

```
    100*str2num(elfile(elfilsiz(2)-6));
num=input('ENTER: Number of files ');
for k=1:num;
    %NOTE: RGB, red = 1, green = 2, blue = 0
    % Convert image to double
    colim=double(colim);
    elim=double(elim);
    newimg(:,:,1)=newimg(:,:,1)+colim(:,:,1);
    newimg(:,:,2)=newimg(:,:,2)+elim(:,:,2);
    newimg(:,:,3)=newimg(:,:,3);
    if k > num;
        clear colim elim
        newcolfil=colfile(1:colfilsiz(2)-7);
        newelfil=elfile(1:elfilsiz(2)-7);
        zer=num2str(0);
        if ncol > 10
            colim=imread([colpath newcolfil zer zer num2str(ncol) '.tif']);
            elim=imread([elpath newelfil zer zer num2str(nel) '.tif']);
        else
            if ncol < 100
                colim=imread([colpath newcolfil zer num2str(ncol) '.tif']);
                elim=imread([elpath newelfil zer num2str(nel) '.tif']);
            else
                colim=imread([colpath newcolfil num2str(ncol) '.tif']);
                elim=imread([elpath newelfil num2str(nel) '.tif']);
            end
        end
    end
    ncol=ncol+1;
    nel=nel+1;
```

```
    countdown=num-k
end
maxcol=max(max(newimg(:,:,1)));
newimg(:,:,1)=uint8((newimg(:,:,1)./maxcol)*255);
maxel=max(max(newimg(:,:,2)));
newimg(:,:,2)=uint8((newimg(:,:,2)./maxel)*255);
newimg=uint8(newimg);

figure(1)
imshow(newimg)
elastin(:,:,2)=newimg(:,:,2);
elastin(:,:,1)=double(zeros(imgsiz,imgsiz));
elastin(:,:,3)=double(zeros(imgsiz,imgsiz));
elastin=uint8(elastin);

figure(2)
imshow(elastin)
collagen(:,:,1)=newimg(:,:,1);
collagen(:,:,2)=double(zeros(imgsiz,imgsiz));
collagen(:,:,3)=double(zeros(imgsiz,imgsiz));
collagen=uint8(collagen);

figure(3)
imshow(collagen)
```

E.1.0.2 Courtney.m Below is the program for performing the Courtney algorithm on the superimposed collagen image stacks taken with the multi-photon microscope

```
clear all;
close all
clc
```

```
% Program Courtney.m
% ————————————————————————————————
% Program description: Main program to save multiple data sets for
% accumulation in the AccHisto.m m-file. This program performs the
% Courtney algorithm on the images and saves the results to a data
% file in the sub-directory "dataforAccHisto" which is created one level
% below the directory from which the image files were imported "path."
% Various image file types may be imported into this program.
% ————————————————————————————————
toln=0.0044; % Enter tolerance for angles
% File input
disp('Did you use MATLAB or another program to superimpose stacks?')
sel=input('Enter 0 for MATLAB, 1 for other ');
if sel==0
    [file,path]=uigetfile('*.*','Select image file');
    img=csvread([path file]);
    img=img/255;
else
    disp('Enter the type of image file (typical from multi-photon is tiff) ')
    g=input('ENTER: Text file = 2, bmp = 1, tiff = 0 ');
    imgsiz=input('ENTER: 512 or 1024 ')
    if g==2
        [file,path]=uigetfile('*.txt','Select image file');
        img=load([path file]);
    else
        if g==1
            [file,path]=uigetfile('*.bmp','Select image file');
            img=imread([path file]);
        else
            [file,path]=uigetfile('*.tif','Select image file');
```

```
            img=imread([path file]);
        end
    end
end

img1=img;
disp('Select 3 points on the image to average for background')

figure(1)
imshow(img)
hold on; axis image;
hold off;
% Use ginput to select n points for setting lower threshold level
n=3; % number of points to average for threshold
[x y] = ginput(n); % note y = row, x = column
x=uint32(x);y=uint32(y); % Convert x and y to integers
img=double(img); % convert array values from uint8 to double precision
% Find average of values
% upthsh=0;
lowths=0;
i=0;
for i=1:n

lowths=lowths+img(y(i),x(i));
end
% upthsh=upthsh/3
lowths=lowths/n
% Find size of image
M=length(img(:,1));
N=length(img(1,:));
clear i j
```

```
for i=1:M; % iterate across rows
    for j=1:N; % iterate across columns
        if img(i,j) < = lowths;
            img(i,j)=0;
        end
    end
end
% Edge detection
disp('Enter a value for mask size, 3 works quite well')
s=input('Enter mask size ');
l=2*s+1;
sig=2.0;
clear i j
for i=-s:1:s;
    for j=-s:1:s;
        hy(i+s+1,j+s+1)=(2*i/sig^2)*exp(-(i^2+j^2)/sig^2);
        hx(i+s+1,j+s+1)=(2*j/sig^2)*exp(-(i^2+j^2)/sig^2);
    end
end
clear i j
for i=1:M-l+1; % iterate across rows
    for j=1:N-l+1; % iterate across columns
        gx=0;
        gy=0;
        for p=1:l; % iterate across rows of kernel over current pixel
            for q=1:l; % iterate across cols of kernel over current pixel
                gy=gy+hy(p,q)*img(i-1+p,j-1+q);
                gx=gx+hx(p,q)*img(i-1+p,j-1+q);
            end
        end
```

```
        Gx(i,j)=gx;
        Gy(i,j)=gy;
        G(i,j)=(gx^2+gy^2);
        if (gx ≤0) & & (gy≤0);
            phi(i,j)=2;
        else
            if gx < = 0;
                phi(i,j)=2;
            else
                phi(i,j)=atan(gy/gx);
            end
        end
    end
    countdown1=M+1-l-i
end

% Directional Histogram Construction
disp('Enter a value for accumulator bin size, 4 has worked well')
t=input('Enter accumulator bin size ');
% typically t=12
k=0;
i=0;
j=0;
row=0;
for i=1:t:M-l+1;
    row=row+1;
    col=0;
    for j=1:t:N-l+1;
        col=col+1;
        clear A
```

```
if (M-t-i > =t) & & (N-t-j > =t)
    theta=0;
    k=0;
    index=0;
    for theta=0:1:179
        k=k+1;
        radian=theta*pi()/180;
        p=0;
        q=0;
        a=0;
        sum=0;
        % iterate across subregion
        for p=1:t;
            for q=1:t;
                if phi(i-1+p,j-1+q)==2;
                    a=a+0;
                else
                    a=a+G(i-1+p,j-1+q)*(cos(radian-phi(i-1+p,j-1+q))) 2̂;
                end
            end
        end
        A(k)=a; % accumulator bin sum across subregion
    end
    index=0;
    if max(A) < = 0;
        maxang(row,col)=200;
    else
        [y,index]=max(A);
        maxang(row,col)=index-1;
    end
```

```
        end
    end
    countdown2=M+1-l-i
end

% Save data to files
sfile=[file(1:length(file)-4) '_maxang.dat'];
mkdir([path 'dataforAccHisto']);
csvwrite([path 'dataforAccHistośfile],maxang);
% Normalize G for image
G=(G./max(max(G))).*255;
G=uint8(G);G=double(G);
% Take natural logarithm of G
clear i j
for i=1:length(G(:,1));
    for j=1:length(G(1,:));
        if G(i,j)<=0;
            Glog(i,j)=0;
        else
            Glog(i,j)=log(G(i,j));
        end
        countdown3=length(G(:,1))-i
    end
end

clear x y u v
mag=20;
i=0;
j=0;
n=0;
```

```
row=0;
for i=1:t:M-l+1;
    row=row+1;
    col=0;
    for j=1:t:N-l+1;
        col=col+1;
        if (M-t-i >=t) & & (N-t-j > =t)
            n=n+1;
            x(n)=(j+(t/2)-1)+(s+1);
            y(n)=(i+(t/2)-1)+(s+1);
            if maxang(row,col)==200;
                u(n)=0;
                v(n)=0;
            else
                u(n)=mag*sin(maxang(row,col)*pi()/180);
                v(n)=-mag*cos(maxang(row,col)*pi()/180);
            end
        end
    end
    countdown4=M-l+1-i
end
clear p

n=0;
for p=0:1:179;
    n=n+1;
    abscis(n)=p;
    clear i j
    ord=0;
    for i=1:length(maxang(1,:));
```

```
        for j=1:length(maxang(:,1));
            if maxang(j,i) < 200;
                if abs(p-maxang(j,i)) < toln
                    ord=ord+1;
                end
            end
        end
    end
    ordina(n)=ord;
    countdown4=179-p
end

img=uint8(img);

G=uint8(G);

figure(2)
imshow(G)

figure(3)
imshow(img1);
hold on
quiver(x,y,u,v);

figure(4);
bar(abscis,ordina);
sz=size(img1(:,:));
showcol(:,:,1)=img1(:,:);
showcol(:,:,2)=zeros(sz(1),sz(2));
showcol(:,:,3)=zeros(sz(1),sz(2));

figure(5)
```

```
imshow(showcol);
hold on
quiver(x,y,u,v);
```

E.1.0.3 AccuHisto.m Below is the program for accumulating data from "Courtney.m" into a histogram and for performing a "pull-back" operation for given uniaxial tissue strain.

```
clear all; close all
clc
% Program AccuHisto.m
% ————————————————————————————————
% Program description: This program follows "Courtney.m" and is used to
% accumulate the data into a histogram and perform given pull-back
% operations based on in input uniaxial strain value
% ————————————————————————————————
toln=0.0044; % Enter tolerance for angles
ordina=zeros(1,181);
%NOTE: the filename they enter must have .dat at the end
[filename,pathname]=uigetfile('*.dat','Select data file');
data=csvread([pathname filename]);
clear abscis p
n=0;
for p=0:1:180;
    n=n+1;
    abscis(n)=p;
    clear i j
    ord=0;
    for i=1:length(data(1,:));
        for j=1:length(data(:,1));
```

```
            if data(j,i) < 200;
                if abs(p-data(j,i)) <toln
                    ord=ord+1;
                end
            end
        end
    end
    ordina(n)=ordina(n)+ord;
end

% Place data into larger file
j=0;
k=0;
for j=1:length(data(1,:));
    for k=1:length(data(:,1));
        accum(k,j)=data(k,j);
    end
end
clear data ord

% Convert abscis into radians in ”angle”
angle=abscis;
angle=angle*pi()/180;

% Make ordinate values symmetric
for i =1:uint32(length(ordina)/2)-1;
    ordinasym(i)=(ordina(i)+ordina(uint32(length(ordina))+1-i))/2;
    ordinasym(uint32(length(ordina))+1-i) = ...
      (ordina(i)+ordina(uint32(length(ordina))+1-i))/2;
end
ordinasym(uint32(length(ordina))/2)=ordina(uint32(length(ordina))/2);
```

```
clear ordina
ordina=ordinasym; clear ordinasym

% Normalize ordina to area calculated by integration
sumordina=trap(angle,ordina);
ordina=ordina/sumordina;
disp('to check the area of ordina ')
trap(angle,ordina)
vspace0.5cm
figure;
bar(angle,ordina);
xlabel('theta')
ylabel('rho(theta)')
% Input value for deformation gradient tensor and calculate F-inverse
lam=input('Enter value for stretch b/w L0 and final stretch ')
F=[lam 0 0; 0 1/sqrt(lam) 0; 0 0 1/sqrt(lam)];
Finv = F ^(-1);
C=mmult(F',F);
% Perform a0=F^(-1)a on abscissa values (angle)
clear m m0 angm0 am0chk
clear a j k
for a = 1:length(angle);
    dsdS(a)=sqrt(1/((1/lam^2)*(sin(angle(a)))^2+lam*(cos(angle(a)))^2));
    angm0(a)=asin((dsdS(a))*(1/lam)*sin(angle(a)));
    if a > 91;
       angm0(a)=pi-angm0(a);
    end
    am0chk(a)=acos((dsdS(a))*(sqrt(lam))*cos(angle(a)));
end

% Normalize ordina to new angles angm0
```

```
sumord=trap(angm0,ordina);
ord=ordina/sumord;
A=trap(angm0,ord)

% Input value for deformation gradient tensor and calculate F-inverse
lama1=input('Enter value for stretch b/w La and final stretch ')
Fa1=[lama1 0 0; 0 1/sqrt(lama1) 0; 0 0 1/sqrt(lama1)];
Finva1=Fa1^(-1);
Ca1=mmult(Fa1',Fa1);

% Perform a0=F^(-1)a on abscissa values (angle)
clear m m0 angm0a1 am0chka1 dsdS
clear a j k
for a = 1:length(angle);
    dsdS(a)=sqrt(1/((1/lama1^2)*(sin(angle(a)))^2+lama1*(cos(angle(a)))^2));
    angm0a1(a)=asin((dsdS(a))*(1/lama1)*sin(angle(a)));
    if a > 91;
        angm0a1(a)=pi-angm0a1(a);
    end
    am0chka1(a)=acos((dsdS(a))*(sqrt(lama1))*cos(angle(a)));
end

% Normalize ordina to new angles angm0
sumorda1=trap(angm0a1,ordina);
orda1=ordina/sumorda1;
Aa1=trap(angm0a1,orda1)

figure;bar(angle,ordina,'b');
hold on; bar(angm0,ord,'r');
xlabel('theta')
ylabel('rho(theta)')
```

```
figure;bar(angle-pi/2,ordina,'b');
hold on; bar(angm0a1-pi/2,orda1,'c');
xlabel('theta')
ylabel('rho(theta)')
% ————————————————————————————————————
wr2fil=menu('Write to file?','yes','no');
if wr2fil==1
    csvwrite([pathname 'Rraw_tausym'],ord);
    csvwrite([pathname 'angm_tau_sym'],angm0);
    csvwrite([pathname 'angm0a1_tau_sym'],angm0a1);
end
```

E.2 PROGRAMS FOR ANALYZING FIBER RECRUITMENT

E.2.0.4 TortGamCDF.m Below is the program used to calculate tortuosity from data taken from Imaris.

```
clear all;close all;clc
% Program TortGamCFD.m
% ————————————————————————————————————
% Program description: Main program to fit tortuosity data to cumulative
% Gamma distribution function
% ————————————————————————————————————
global lama1
lama1=input('Input value for lambda_a1 ');
% Bring in data
numbst=input('Enter number of stretches with data ');
dum=0;
for i=1:numbst
    [file,path]=uigetfile('*.dat','Select data file ');
```

```
    filID=fopen([path file],'r');
    data=fscanf(filID, '%g', [1 inf]);
    fclose(filID);
    data=data';
    disp('The array is :')
    disp(data)
    L=str2num(file(1:4));
    Len(i)=L;
    iter=0;
    for j=1:length(data(:))
        dum=dum+1;
        iter=iter+1;
        tort(dum,1)=1/data(iter);
        tort(dum,2)=L;
    end
end
L0=input('Enter L0 in micrometers ');

figure;
plot(tort(:,2)/L0,tort(:,1),'.')
xlabel('lambda');
ylabel('tau');

% Find the maximum in the last (highest stretch) data set
maxnum=0;
for k=1:length(tort(:,1))
    if tort(k,2)>=Len(numbst)
        if (tort(k,1)>maxnum);
            maxnum=tort(k,1)
        end
    end
```

```
end

disp(['Pick another value besides maxnum = ',num2str(maxnum),'? '])
yorn=input('Enter 1 or 0 ');
if yorn==1
    maxnum=input('Enter new value for maxnum ');
end

% Calculate number of fibers active for each length
j=1;
for i=1:numbst
    denom=0; numer=0;
    while(tort(j,2)==Len(i))
        denom=denom+1;
        if(tort(j,1)<=maxnum)
            numer=numer+1;
        end
        j=j+1;
        if(j¿length(tort(:,1)));break;end
    end
    res(i,1)=Len(i);
    res(i,2)=numer;
    res(i,3)=denom;
end

N=sum(res(:,3));
absc=res(:,1)/L0; % absc is x-axis values - here it is stretch
ordina(1)=res(1,2)/res(1,3);
for i=2:numbst;
    ordina(i)=res(i,2)/res(i,3);
end
```

```
% Clear negative numbers
for i=1:numbst
    if ordina(i)¡0;
        ordina(i)=0;
    end
end

figure;
plot(absc,ordina,'.')

% Now fit to the Gamma cumulative distribution function
X0=[2 1];
lb=[0 0];
ub=[1000 1000];
gamord=res(:,2)./res(:,3);
options=optimset('TolFun',1e-20); % Set tolerance
[Xgam, Res, Residual_pwr, Exitflag_pwr,Output,LAMB,Jacobian]=...
lsqcurvefit(@gammafit1,X0,absc,ordina,lb,ub,options);
xplot=linspace(absc(1),absc(length(absc)));
yfit=gammafit1(Xgam,xplot);
figure;plot(absc,ordina,'b.',xplot,yfit,'g-')
% Find 95% confidence intervals
CIjacb=nlparci(Xgam,Residual_pwr,'jacobian',Jacobian);
%Find R2̂ value
R_squared_den = 0.0;
for i = 1:length(gamord);
    R_squared_den = R_squared_den + (gamord(i) - mean(gamord))2̂;
end
R_squared = 1 - (Res/R_squared_den)
clear Res Residual_pwr Exitflag_pwr;
clear lb ub options;
```

```
gmpdf=gammapdf(Xgam,xplot);
figure;plot(xplot,gmpdf,'-')
% Now check that data is normalized to unity sumord=trap(xplot,yfit)
disp(['Alpha value is ',num2str(Xgam(1))])
disp(['with alpha confidence interval ',num2str(Xgam(1)-CIjacb(1,1))])
disp(['Beta value is ',num2str(Xgam(2))])
disp(['with beta confidence interval ',num2str(Xgam(2)-CIjacb(2,1))])
figure;plot(xplot,gmpdf,xplot,yfit)
figure;plot(absc,ordina,'b.',xplot,yfit,'g-',tort(:,2)/L0,tort(:,1),'r.')
figure;
[AX,H1,H2]=plotyy(tort(:,2)/L0,tort(:,1),xplot,yfit);
set(get(AX(1),'Ylabel'),'String','tau')
set(get(AX(2),'Ylabel'),'String','Gammacdf')
set(get(AX(1),'Xlabel'),'String',lambda1')
% set(get(AX(2),'Xlabel'),'String','enter text')
set(AX(1),'fontsize',20)
set(AX(2),'fontsize',20)
set(get(AX(1),'Xlabel'),'fontsize',24)
set(get(AX(1),'Ylabel'),'fontsize',24)
set(get(AX(2),'Ylabel'),'fontsize',24)
set(AX(1),'XLim',[1 max(tort(:,2)/L0)])
set(AX(2),'XLim',[1 max(tort(:,2)/L0)])
```

E.3 PROGRAMS FOR FITTING MODEL TO THE DATA

E.3.0.5 Main.m Below is the program used to compute stress and strain from raw data taken from text files output from LabVIEW

```
clear all
close all
```

```
clc
% Program Main.m
% ————————————————————————————————
% Program description: Main program to calculate stress and strain
% from raw data in text files from LabVIEW program
% ————————————————————————————————
[filename,pathname] = uigetfile('*.txt', 'Select data file');
%NOTE: the filename they enter must have .dat or .txt at the end
filepath1 = [pathname filename];
data=load(filepath1);
%Select the last extension graph for data to fit
p=length(data(:,4));
m=data(p,4); % Number of last cycle
n=m-1; % Cycle of last extension
% Open the geometry file
% NOTE: Length measurements A must be first column and thickness
% measurements H must be second column!
[geometryfile, geopath]=uigetfile('.txt', 'Select geometry file');
geofile=[geopath geometryfile];
geometry=load(geofile);
A=mean(geometry(:,1)); % Units must be in mm
H=mean(geometry(:,2)); % Units must be in mm
clear geometry;
% Get data, for filtering force data
q=0;
num=0;
i=0;
for q=1:p;
    if (data(q,4)<n+1) & & (data(q,4) >n-1)
        num=num+1;
```

```
        f_raw(num)=data(q,3); % Force data
        pos(num)=data(q,2); % Position data
    end
    if((data(q,4)==m) & (i==0));
        num=num+1;
        f_raw(num)=data(q,3);
        pos(num)=data(q,2);
        i=1;
    end
end

% Set up filter
windowSize=7;
f=filter(ones(1,windowSize)/windowSize,1,f_raw);
figure(1);
plot(pos,f)
hold on
[La,y]=ginput(1)
L0=input('Enter value for L0 in mm ');
% Get rid of data under L0
i=0;
booln=0;
num=0;
for i=1:length(pos);
    if (pos(i) >=L0)
        booln=1;
    end
    if booln >0
        num=num+1;
        force(num)=f(i); % Force data
```

```
        position(num)=pos(i); % Position data
    end
end
lam=position./L0;
lama=La/L0;
P=force./(A*H);
Pfil=P;
figure(2)
plot(lam,Pfil,'.b',lam,P,'.g')
xlabel('lambda')
ylabel('P (MPa)')
figure(3)
plot(lam,Pfil)
xlabel('lambda')
ylabel('P (MPa)')
sig=lam.*Pfil; % Cauchy stress
figure(4)
plot(lam,sig)
xlabel('lambda')
ylabel('sigma (MPa)')
mkdir(pathname,'matlab')
dlmwrite([pathname 'matlab/' filename(1:length(filename)-4) 'P.txt'],Pfil);
dlmwrite([pathname 'matlab/' filename(1:length(filename)-4) 'l.txt'],lam);
dlmwrite([pathname 'matlab/' filename(1:length(filename)-4) 'S.txt'],sig);
% Put L0 and La into a matrix and save
a=[L0 La];
dlmwrite([pathname 'matlabfilename(1:length(filename)-4) 'a.txt'],a);
```

E.3.0.6 DataFitFan.m Below is the program used to fit the chosen model to the stress and strain data taken from LabVIEW

```
close all
clear all
clc
format long
%————————————————————————————————————-
% Program description: Main Program to fit data to various models given in
% (Hill MR, Duan X, Gibson GA, Watkins S, Robertson AM, J Biomechanics,
% 2011)
% ————————————————————————————————————
% Custom functions (subroutines) called in this program:
% fan.m = Function to perform a loop to compute Cauchy stress value at
% measured values of stretch
% ————————————————————————————————————
[filename,pathname] = uigetfile('*.*', 'Select data file');
P=dlmread([pathname filename(1:length(filename)-6) 'P.txt']);
l=dlmread([pathname filename(1:length(filename)-6) 'l.txt']);
S=dlmread([pathname filename(1:length(filename)-6) 'S.txt']);
a=dlmread([pathname filename(1:length(filename)-6) 'a.txt']);
% Open fiber dispersion data files
[filen,pathn]=uigetfile('*.*','Select fiber distribution file');
Rtheta=csvread([pathn 'Rrawtausym']);
ang=csvread([pathn 'angm0tausym']); anga1=csvread([pathn 'angm0a1tausym']);
% clear filename pathname fid;
global R angle Gamprm lammax fitchc
fitchc=menu('Pick fiber model','A','B','C','D'); % Pick model
if fitchc == 2 —— fitchc ==3
    Gamprm(1)=input('Enter alpha value for gamma distribution ');
    Gamprm(2)=input('Enter beta value for gamma distribution ');
```

```
end
if fitchc==2
    Gamprm(3)=1;
    angle=ang-pi/2;
else
    Gamprm(3)=input('Enter lambda-a1 for beginning of recruitment ');
    angle=anga1-pi/2;
end
R=Rtheta;
lam=l;lammax=max(lam);
L0=a(1)
% Fit data ————————
% The Cauchy stress is
sig=S; % in N/mm2
% Fit data to stress-stetch relation with SEF given J Biomech article
options=optimset('TolFun',1e-20); % Set tolerance
if fitchc==1 —— fitchc==4
    lb=[0 0 0]; % Set lower bound
    ub=[1e10 1e10 1e10]; % Set upper bound
    X0=[0.115 0.675 1.0]'; % Set first guess of coefficients
else
    lb=[0 0]; % Set lower bound
    ub=[1e10 1e10]; % Set upper bound
    X0=[0.08972 0.808]'; % Set first guess of coefficients
end
% Fit data
[X, Res, Residualpwr, Exitflagpwr,Output,LAMB,Jacobian]=...
lsqcurvefit(@fan,X0,...
lam(1:20:length(lam))',sig(1:20:length(sig)),lb,ub,options);
% Find 95% confidence intervals
```

```
CIjacb=nlparci(X,Residualpwr,'jacobian',Jacobian);
%Find R2 value
Rsquaredden = 0.0;
for i = 1:length(sig);
    Rsquaredden = Rsquaredden + (sig(i) - mean(sig))^2;
end
Rsquared = 1 - (Res/Rsquaredden)
clear Res Residualpwr Exitflagpwr;
clear lb ub options;
% sigfit=fan(X,lam(1:20:length(lam)));
sigfit=fan(X,lam(1:20:length(lam)));
figure;
plot(lam,sig,'b.',lam(1:20:length(lam)),sigfit,'g-')
legend('raw','fitted')
xlabel('lambda')
ylabel('sigma (MPa)')
if fitchc ==2 —— fitchc ==3
    figure;
    [AX,H1,H2]=plotyy(lam(1:20:length(lam)),sigfit,...
    lam(1:20:length(lam)),gammaeval(Gamprm,lam(1:20:length(lam))));
    hold on
    plot(lam,sig,'b.')
end
eta=X(1) % in N/mm2
disp('eta units in N/mm2')
k1=X(2) % in N/mm2
disp('k1 in N/mm2')
% Convert units from N/mm2 to kPa
etaunit=eta*1000 % kPa
disp(['with eta confidence interval ',num2str((X(1)-CIjacb(1,1))*1000)])
```

```
disp('eta in kPa')
k1unit=k1*1000 % kPa
disp(['with k1 confidence interval ',num2str((X(2)-CIjacb(2,1))*1000)])
disp('k1unit in kPa')
if fitchc==1 —— fitchc==4;
    k2=X(3) % unitless
    disp('k2 unitless')
    disp(['with k2 confidence interval ',num2str((X(3)-CIjacb(3,1)))])
end
wr2fil=menu('Write to file?','yes','no');
if wr2fil==1
    csvwrite([filename(1:length(filename)-6) 'sigfit' num2str(fitchc)],sigfit);
end
```

E.3.0.7 fan.m Below is the subroutine used to compute stress from stretch using the chosen model

```
function Sig=fan(X,lam);
% Subroutine fan.m
% Function to perform a loop to compute Cauchy stress value at
% measured values of stretch
% ————————————————————————————————
% Custom functions called in this program:
% Sigfan.m = Function to compute stress, using the different recruitment/orientation
% models
% ————————————————————————————————
% Variables used in this program
% lam = measured stretch values from UA-MPM
% Sig = vector containing components of Cauchy stress tensor in
% circumferential direction, as function of stretch, lam
% X = vector containing material parameters eta0, eta, gamma
```

```
% n = dummy index for iterating thru the vector of stretches, lam
% ——————————————————————————————
n=0;
for n=1:length(lam);
    Sig(n)=Sigfan(X,lam(n));
end
disp('looped')
```

E.3.0.8 Sigfan.m Below is the subroutine used to compute stress from each stretch value using different chosen models

```
function Sig=Sigfan(X,lam);
% Function to compute stress, using the different recruitment/orientation
% models
% ——————————————————————————————
% Custom functions called in this program
% gammaeval.m = Subroutine to calculate the Gamma probability
% distribution function (PDF)
% trap.m = subroutine for performing the trapezoid rule
% ——————————————————————————————
% Variables used in this program
% lam = tissue stretch in direction of fiber
% X = vector containing material parameters eta0, eta, gamma
% eta0 = isotropic material parameter
% eta = anisotropic material parameter (all models)
% gamma = anisotropic material parameter (model A only)
% R = rho(theta), orientation distribution function
% angle = vector of angles from -pi/2 to pi/2
% Gamprm = vector of parameters from fit of crimp data to gamma dist
% function
% fitchc = choice of model in which to fit data: A, B, or C
```

```
% bullet1 = vector containing fiber integral portion of the
% deriviative of anisotropic SEF with i=1
% bullet2 = vector containing fiber integral portion of the
% deriviative of anisotropic SEF with i=2
% lamsqf = square of lam
% dum = dummy variable for counting
% lamvar = vector containing stretch values up to current tissue stretch
% in fiber direction, lam
% infun = vector containing innner function in derivative of anisotropic
% SEF with respect to tissue stretch lambdai (i=1,2,3)
% inint = integral of infun, by trapezoid rule
% Sig = vector containing Cauchy stress tensor components
% Sigiso = isotropic portion of Sig
% Sigan = anisotropic portion of Sig
% ————————————————————————————————————
global R angle Gamprm fitchc
% Get the model parameters in vector X
eta0=X(1);
eta=X(2);
if fitchc==1 —— fitchc==4;
    gamma=X(3);
end
if fitchc==4;
    clear bullet1 bullet2
    dum=0;
    for j=1:0.015:lam
        dum=dum+1;
        lamvar(dum)=j;
        if lam>=Gamprm(3) & & lamvar(dum)>=Gamprm(3);
            infun(dum)=2*(lam/lamvar(dum)^3)*...
```

```
            exp(gamma*(lam/lamvar(dum)^2-1)); % Exponential
        else
            infun(dum)=0;
        end
    end
    clear inint
    inint=trap(lamvar,infun); % here is the inner integral
    clear lamvar infun
    bullet1=inint;
    bullet2=0;
    bullet1=(1/pi)*eta*bullet1;
    Sigan=2*bullet1*(lam^2);
    lam2sq=sqrt(eta0/(lam^2*(eta0+2*bullet2)));
    Sigiso=eta0*(lam^2-1/((lam^2)*(lam2sq)));
    Sig=Sigiso+Sigan;
else
    clear bullet1 bullet2 lamsqf ivar
    for ivar=1:length(angle);
    % Compute lamsqf
    lamsqf(ivar)=lam^2*(cos(angle(ivar)))^2+(1/lam^2)*(sin(angle(ivar)))^2;
    if lamsqf(ivar)>1 %make sure stretches are positive
        dum=0;
        for j=1:0.015:sqrt(lamsqf(ivar))
            dum=dum+1;
            lamvar(dum)=j;
            if fitchc==1
                if sqrt(lamsqf(ivar))¿=Gamprm(3) & & lamvar(dum)>=Gamprm(3);
                    infun(dum)=2*(sqrt(lamsqf(ivar))/lamvar(dum)^3)*...
                    exp(gamma*(lamsqf(ivar)/lamvar(dum)^2-1)); % Exponential
                else
```

```
                infun(dum)=0;
            end
        else
            infun(dum)=gammaeval(Gamprm,lamvar(dum))*...
            (sqrt(lamsqf(ivar))/lamvar(dum)^3); % Neo-Hookean
        end
    end
    clear inint
    inint=trap(lamvar,infun); % here is the inner integral
    clear lamvar infun
    bullet1(ivar)=inint*R(ivar)*(cos(angle(ivar)))^2;
    bullet2(ivar)=inint*R(ivar)*(sin(angle(ivar)))^2;
else
    bullet1(ivar)=0;% Set value to zero if stretch is less than 1
    bullet2(ivar)=0;
end
end
bullet1=(1/pi)*eta*bullet1;
bullet2=(1/pi)*eta*bullet2;
Sigan=2*trap(angle,bullet1)*(lam^2);
lam2sq=sqrt(eta0/(lam^2*(eta0+2*trap(angle,bullet2))));
Sigiso=eta0*(lam^2-1/((lam^2)*(lam2sq)));
Sig=Sigiso+Sigan;
end
```

E.3.0.9 gammaeval.m Below is the subroutine used to calculate the gamma probability distribution function

```
function yval=gammaeval(params,xval);
% Subroutine to calculate the Gamma PDF
% ————————————————————————————————————
```

```
% Custom functions called in this program:
% none
% ————————————————————————————————————-
% Variables used in this program:
% lammax = maximum stretch measured by UA-MPM in given loading curve
% params = vector containing parameters alpha, beta, and lama1
% alpha = first parameter of gamma dist function
% beta = second parameter of gamma dist function
% lama1 = activation stretch for recruitment dist function
% gamfun = vector containing normalized evaluated recruitment dist
% function
% xval = individual data point from
% vector containing stretch values up to current tissue
% stretch in fiber diretion, lam
% ————————————————————————————————————————
global lammax
lama1=params(3);
if xval<lama1;
    yval=0;
else
    gamfun=(xval-lama1)/(lammax-lama1); % Normalize to [0,1]
    yval=gampdf(gamfun,params(1),params(2));
end
```

BIBLIOGRAPHY

[1] H. Zakaria, D. F. Kallmes, R. Kadirvel, Y.H. Ding, D. A. Lewis, and A. M. Robertson. Similar hemodynamic features in elastase-induced rabbit saccular aneurysms compared to those of human aneurysms. In *Proceedings of the 5th World Congress on Biomechanics*, Munich, Germany, 2006.

[2] D. Li and A.M. Robertson. A structural multi-mechanism damage model for cerebral arterial tissue. *American Society of Mechanical Engineers (ASME) Journal of Biomechanical Engineering*, 131(10):101013, 2009.

[3] Z. Zeng, D.F. Kallmes, M.J. Durka, Y. Ding, D. Lewis, R. Kadirvel, and A.M. Robertson. Sensitivity of cfd based hemodynamic results in rabbit aneurysm models to idealizations in surrounding vasculature. *American Society of Mechanical Engineers (ASME) Journal of Biomechanical Engineering*, 132:091009, 2010.

[4] M. R. Hill and A. M. Robertson. Combined histological and mechanical evaluation of isotropic damage to elastin in cerebral arteries. In *Proceedings of the 6th World Congress on Biomechanics*, Singapore, 2010.

[5] M. R. Hill and A. M. Robertson. Abrupt recruitment of medial collagen fibers in the rabbit carotid artery. In *Proceedings of the American Society of Mechanical Engineers (ASME) Summer Bioengineering Conference*, Farmington, PA, June 2011.

[6] M. R. Hill, X. Duan, G. Gibson, S. Watkins, and A.M. Robertson. A theoretical and non-destructive experimental approach for direct inclusion of measured collagen orientation and recruitment into mechanical models of the artery wall. *Journal of Biomechanics*, accepted for publication, 2011.

[7] G.A. Holzapfel and R. W. Ogden. *Mechanics of Biological Tissue*. Springer-Verlag, Berlin, Germany, 2006.

[8] Y. C. Fung. *Biomechanics. Mechanical Properties of Living Tissues*. Springer-Verlag, New York, 1993.

[9] C. Truesdell and W. Noll. *The Non-Linear Field Theories of Mechanics*. Springer-Verlag, Berlin, Germany, 1965.

[10] L. R. G. Treloar. *The Physics of Rubber Elasticity*. Clarendon Press, Oxford, 1958.

[11] A.M. Robertson, M.R. Hill, and D. Li. Structurally motivated damage models for arterial walls- theory and application. In Davide Ambrosi, Alfio Quarteroni, and Gianluigi Rozza, editors, *Modelling of Physiological Flows*, volume 5 of *Modeling, Simulation and Applications*. Springer-Verlag, 2011.

[12] L.A. Taber. *Nonlinear Theory of Elasticity: Applications in Biomechanics*. World Scientific, River Edge, NJ, 2004.

[13] W. W. Nichols, M. F. O'Rourke, and D. A. McDonald. *McDonald's blood flow in arteries: theoretical, experimental, and clinical principles*. Oxford University Press, New York, 2005.

[14] G.A. Holzapfel and T.C. Gasser. A new constitutive framework for arterial wall mechanics and a comparative study of arterial models. *Journal of Elasticity*, 61:1–48, 2000.

[15] M.S. Sacks. Biaxial mechanical evaluation of planar biological materials. *Journal of Elasticity*, 61:199–246, 2000.

[16] M.R. Roach and A.C. Burton. The reason for the shape of the distensibility curves of arteries. *Canadian Journal of Biochemistry and Physiology*, 35:681–690, 1957.

[17] S. Scott, G.G. Ferguson, and M.R. Roach. Comparison of the elastic properties of human intracranial arteries and aneurysms. *Canadian Journal of Physiology and Pharmacology*, 50:328–332, 1972.

[18] R.L. Gleason, L.A. Taber, and J.D. Humphrey. A 2-d model of flow-induced alterations in the geometry, structure, and properties of carotid arteries. *American Society of Mechanical Engineers (ASME) Journal of Biomechanical Engineering*, 126:371–381, 2004.

[19] W. E. Stehbens. Pathology and pathogenesis of intracranial berry aneurysms. *Neurological Resaerch*, 12:29–34, 1990.

[20] W. E. Stehbens. *Pathology of Cerebral Blood Vessels*. C.V. Mosby Co.

[21] W. E. Stehbens. Aneurysms and anatomical variation of cerebral arteries. *Archives of Pathology*, 75:45–64, 1963.

[22] D. Dai, Y. H. Ding, M. A. Danielson, R. Kadirvel, L. W. Hunter, W. Z. Zhan, G. A. Helm, D. A. Lewis, H. J. Cloft, G. C. Sieck, and D. F. Kallmes. Endovascular treatment of experimental aneurysms by use of fibroblast-coated platinum coils: an angiographic and histopathologic study. *Stroke*, 38(1):170–6, 2007.

[23] S. P. Ferns, M. E. Sprengers, W. J. van Rooij, G. J. Rinkel, J. C. van Rijn, S. Bipat, M. Sluzewski, and C. B. Majoie. Coiling of intracranial aneurysms: a systematic

review on initial occlusion and reopening and retreatment rates. *Stroke*, 40(8):e523–9, 2009.

[24] S. Gallas, A. C. Januel, A. Pasco, J. Drouineau, J. Gabrillargues, A. Gaston, C. Cognard, and D. Herbreteau. Long-term follow-up of 1036 cerebral aneurysms treated by bare coils: a multicentric cohort treated between 1998 and 2003. *American Journal of Neuroradiology*, 30(10):1986–92, 2009.

[25] J. Raymond, F. Guilbert, A. Weill, S. A. Georganos, L. Juravsky, A. Lambert, J. Lamoureux, M. Chagnon, and D. Roy. Long-term angiographic recurrences after selective endovascular treatment of aneurysms with detachable coils. *Stroke*, 34(6):1398–403, 2003.

[26] J. Raymond, P. Leblanc, F. Morel, I. Salazkin, G. Gevry, and S. Roorda. Beta radiation and inhibition of recanalization after coil embolization of canine arteries and experimental aneurysms: how should radiation be delivered? *Stroke*, 34(5):1262–8, 2003.

[27] E. Ribourtout, A. C. Desfaits, I. Salazkin, and J. Raymond. Ex vivo gene therapy with adenovirus-mediated transforming growth factor beta1 expression for endovascular treatment of aneurysm: results in a canine bilateral aneurysm model. *Journal of Vascular Surgery*, 38(3):576–83, 2003.

[28] D. O. Wiebers, J. P. Whisnant, 3rd Huston, J., I. Meissner, Jr. Brown, R. D., D. G. Piepgras, G. S. Forbes, K. Thielen, D. Nichols, W. M. O'Fallon, J. Peacock, L. Jaeger, N. F. Kassell, G. L. Kongable-Beckman, and J. C. Torner. Unruptured intracranial aneurysms: natural history, clinical outcome, and risks of surgical and endovascular treatment. *Lancet*, 362(9378):103–10, 2003.

[29] T.J. Inghall and J.P. Whisnant. Subarachnoid hemorrhage. In *Epidemiology of Subarachnoid Haemorrhage*, pages 63–78. Marcel-Dekker, 1998.

[30] L.N. Sekhar and R. C. Heros. Origin, growth, and rupture of saccular aneurysms: a review. *Neurosurgery*, 8:248–260, 1981.

[31] F. T. Merei and F. Gallyas. Role of the structural elements of the arterial wall in the formation and growth of intracranial saccular aneurysms. *Neurological Research*, 2:283–303, 1980.

[32] O. Hassler. Scanning electron microscopy of saccular intracranial aneurysms. *American Journal of Pathology*, 68:511–520, 1972.

[33] C. Kim, H. Kikuchi, N. Hashimoto, M. Kojima, Y. Kang, and F. Hazama. Involvement of internal elastic lamina in development of induced cerebral aneurysms in rats. *Stroke*, 19:507–511, 1988.

[34] G. J. Campbell and M. R. Roach. A physical model for the formation of evaginations: a prospective precursor to the creation of saccular aneurysms. *Stroke*, 15:642–652, 1984.

[35] M.A. Jamous, S. Nagahiro, K.T. Kitazato, T. Tamura, H.A. Aziz, M. Shono, and K. Satoh. Endothelial injury and inflammatory response induced by hemodynamic changes preceding intracranial aneurysm formation: experimental study in rats. *Journal of Neurosurgery*, 107:405–411, 2007.

[36] W. E. Stehbens. *Structure and Function of the Circulation*. Plenum Press.

[37] G. J. Campbell and M. R. Roach. Fenestrations in the internal elastic lamina at bifurcations of human cerebral arteries. *Stroke*, 12:489–496, 1981.

[38] P.B. Canham, H.M. Finlay, J.G. Dixon, and S.E. Ferguson. Layered collagen fabric of cerebral aneurysms quantitatively assessed by the universal stage and polarized light microscopy. *Anatomical Record*, 231:579–592, 1991.

[39] H.M. Finlay, L. McCullough, and P.B. Canham. Three-dimensional collagen organization of human brain arteries at different transmural pressures. *Journal of Vascular Research*, 32:301–312, 1995.

[40] A.C. Burton. Relation of structure to function of the tissues of the wall of blood vessels. *Physiological Reviews*, 34:619–642, 1954.

[41] G. T. Mase and G. E. Mase. *Continuum Mechanics for Engineers*. CRC Press, Boca Raton, FL, 1999.

[42] A.E. Green and W. Zerna. *Theoretical Elasticity*. Oxford University Press, London, 1968.

[43] A.E. Green and J.E. Adkins. *Large Elastic Deformations*. Clarendon Press, Oxford, 1970.

[44] Y. C. Fung. Elasticity of soft tissues in simple elongation. *American Journal of Physiology*, 213:1532–1544, 1967.

[45] Y. C. Fung, K. Fronek, and P. Patitucci. Pseudoelasticity of arteries and the choice of its mathematical expression. *American Journal of Physiology*, 237:H620–H631, 1979.

[46] J.D. Humphrey and F.C. Yin. A new constitutive formulation for characterizing the mechanical behavior of soft tissues. *Biophysical Journal*, 52:563–570, 1987.

[47] R.S. Rivlin and D.W. Saunders. Large elastic deformations of isotropic materials vii. experiments on the deformation of rubber. *Philosophical Transactions of the Royal Society of London A: Mathematical, Physical, and Engineering Sciences*, 243:251–288, 1951.

[48] J. D. Humphrey, R. K. Strumpf, and F. C. Yin. A theoretically-based experimental approach for identifying vascular constitutive relations. *Biorheology*, 26:687–702, 1989.

[49] G.A. Holzapfel and H.W. Weizsacker. Biomechanical behavior of the arterial wall and its numerical characterization. *Computers in Biology and Medicine*, 28:377–392, 1998.

[50] R. Wulandana and A.M. Robertson. Use of a multi-mechanism constitutive model for inflation of cerebral arteries. In *First joint Biomedical Engineering Society (BMES)/ Institute of Electrical and Electronics Engineers (IEEE) Engineering in Medicine and Biology Society (EMBS) Conference*, volume 1, page 235, Atlanta, GA, 1999.

[51] R.J. Atkin and R.E. Craine. Continuum theories of mixtures: basic theory and historical development. *Quarterly Journal of Mechanics and Applied Mathematics*, 29:209–244, 1976.

[52] R.M. Bowen. *Theory of Mixtures. In Continuum Physics, ed. AC Eringen*. Academic Press, New York, 1976.

[53] R.L. Gleason and J.D. Humphrey. A 2d constrained mixture model for arterial adaptations to large changes in flow, pressure and axial stretch. *Mathematical Medicine and Biology*, 22:347–369, 2005.

[54] J.D. Humphrey and K.R. Rajagopal. A constrained mixture model for growth and remodeling of soft tissues. *Mathematical Models and Methods in Applied Sciences (M3AS)*, 12:407–430, 2002.

[55] J.D. Humphrey and K.R. Rajagopal. A constrained mixture model for arterial adaptations to a sustained step change in blood flow. *Biomechanics and Modeling in Mechanobiology*, 2:109–126, 2003.

[56] Y. Lanir. A structural theory for the homogeneous biaxial stress-strain relationships in flat collagenous tissues. *Journal of Biomechanics*, 12:423–436, 1979.

[57] Y. Lanir. Constitutive equations for fibrous connective tissues. *Journal of Biomechanics*, 16:1–12, 1983.

[58] M.S. Sacks, D.B. Smith, and E.D. Hiester. A small angle light scattering device for planar connective tissue microstructural analysis. *Annals of Biomedical Engineering*, 25:678–689, 1997.

[59] M.S. Sacks. Incorporation of experimentally-derived fiber orientation into a structural constitutive model for planar collagenous tissues. *American Society of Mechanical Engineers (ASME) Journal of Biomechanical Engineering*, 125:280–287, 2003.

[60] R. De Vita and W. S. Slaughter. A structural constitutive model for the strain rate-dependent behavior of anterior cruciate ligaments. *International Journal of Solids and Structures*, 43:1561–1570, 2006.

[61] R. Wulandana and A.M. Robertson. An inelastic multi-mechanism constitutive equation for cerebral arterial tissue. *Biomechanics and Modeling in Mechanobiology*, 4(4):235–248, 2005.

[62] K.R. Rajagopal and A.S. Wineman. A constitutive equation for nonlinear solids which undergo deformation induced microstructural changes. *International Journal of Plasticity*, 8:385–395, 1992.

[63] A.S. Wineman and K.R. Rajagopal. On a constitutive theory for materials undergoing microstructural changes. *Archives of Mechanics*, 42:53–75, 1990.

[64] D. Li and A.M. Robertson. A structural multi-mechanism constitutive equation for cerebral arterial tissue. *International Journal of Solids and Structures*, 46:2920–2928, 2009.

[65] S. Roy, C. Boss, R. Rezakhaniha, and N. Stergiopulos. Experimental characterization of the distribution of collagen fiber recruitment. *Journal of Biorheology*, 24(2):84–93, 2010.

[66] C. Miehe. Discontinuous and continuous damage evolution in ogden-type large strain elastic materials. *European Journal of Mechanics, A/Solids*, 14:697–720, 1995.

[67] Y. Lanir. Plausibility of structural constitutive equations for isotropic soft tissues in finite static deformations. *Journal of Applied Mechanics*, 61:695–702, 1994.

[68] Y. Lanir. Plausibility of structural constitutive equations for swelling tissues - implications of the c-n and s-e conditions. *American Society of Mechanical Engineers (ASME) Journal of Biomechanical Engineering*, 118:10–16, 1996.

[69] P.Chadwick. *Continuum Mechanics: Concise Theory and Problems*. Dover, Mineola, NY, 1999.

[70] R.W. Ogden. *Non-linear Elastic Deformations*. Dover, New York, 1997.

[71] A.J.M. Spencer. *Continuum Mechanics*. John Wiley and Sons, Inc., New York, 1980.

[72] G.A. Holzapfel. *Nonlinear Solid Mechanics: A Continuum Approach for Engineering*. Wiley, Chichester, New York, 2000.

[73] A. M. Robertson. Theory of continuous media. Lecture Notes, Department of Mechanical Engineering and Materials Science, University of Pittsburgh, 2010.

[74] A. M. Robertson. Advanced fluid mechanics. Lecture Notes, Department of Mechanical Engineering and Materials Science, University of Pittsburgh, 2007.

[75] M. S. Sacks. Biomechanics of organs, tissues, and cells. Lecture Notes, Department of Bioengineering, University of Pittsburgh, 2007.

[76] M. S. Sacks. Advanced topics in biosolid mechanics. Lecture Notes, Department of Bioengineering, University of Pittsburgh, 2008.

[77] B. D. Coleman and W. Noll. The thermodynamics of elastic materials with heat conduction and viscosity. *Archive for Rational Mechanics and Analysis*, 13(1):167–178, 1963.

[78] C.-C. Wang. On representations for isotropic functions part i. isotropic functions of symmetric tensors and vectors. *Archive for Rational Mechanics and Analysis*, 33:249–267, 1969.

[79] A. Delfino, N. Stergiopulos, J.E. Moore, and J.-J. Meister. Residual strain effects on the stress field in a thick wall finite element model of the human carotid bifurcation. *Journal of Biomechanics*, 30:777–786, 1997.

[80] M.A. Zulliger, P. Fridez, K. Hayashi, and N. Stergiopulos. A strain energy function for arteries accounting for wall composition and structure. *Journal of Biomechanics*, 37:989–1000, 2004.

[81] P.N. Watton, Y. Ventikos, and G.A. Holzapfel. Modelling the mechanical response of elastin for arterial tissue. *Journal of Biomechanics*, 42:1320–1325, 2009.

[82] R.W. Ogden. Large deformation isotropic elasticity - on the correlation of theory and experiment for incompressible rubberlike solids. *Proceedings of the Royal Society of London A*, A326:567–583, 1972.

[83] R.W. Ogden. *Elastic deformations of rubberlike solids, in: H.G. Hopkins, and M.J. Sewell, eds.,* Mechanics of Solids, the Rodney Hill 60th Anniversary Volume. Pergamon Press, Oxford, 1982.

[84] A.J.M Spencer. *Theory of Invariants*, volume 1 of *Continuum Physics*. Academic Press, New York, 1971.

[85] T.C. Gasser, R.W. Ogden, and G.A. Holzapfel. Hyperelastic modelling of arterial layers with distributed collagen fibre orientations. *Journal of the Royal Society Interface*, 3:15–35, 2006.

[86] A.D. Freed, D.R. Einstein, and I. Vesely. Invariant formulation for dispersed transverse isotropy in aortic heart valves: an efficient means for modeling fiber splay. *Biomechanics and Modeling in Mechanobiology*, 4:100–117, 2005.

[87] A.D. Freed. Anisotropy in hypoelastic soft-tissue mechanics. i. theory. *Journal of Mechanics of Materials and Structures*, 3:911–928, 2008.

[88] G.A. Holzapfel and R.W. Ogden. On planar biaxial tests for anisotropic nonlinearly elastic solids. a continuum mechanical framework. *Mathematics and Mechanics of Solids*, 14:474–489, 2009.

[89] A. M. Briones, J. M. Gonzalez, B. Somoza, J. Giraldo, C. J. Daly, E. Vila, M. C. Gonzalez, J. C. McGrath, and S. M. Arribas. Role of elastin in spontaneously hypertensive rat small mesenteric artery remodelling. *Journal of Physiology*, 552(Pt 1):185–95, 2003.

[90] J. M. Gonzalez, A. M. Briones, B. Starcher, M. V. Conde, B. Somoza, C. Daly, E. Vila, I. McGrath, M. C. Gonzalez, and S. M. Arribas. Influence of elastin on rat small artery mechanical properties. *Experimental Physiology*, 90(4):463–8, 2005.

[91] D.M. Gaitan-Leon, D.E. Schmidt, D.W. Chew, D.A. Vorp, and M.S. Sacks. Structural information of cardiovascular tissues using small angle light scattering. In *Proceedings of the American Society of Mechanical Engineers (ASME) Summer Bioengineering Conference*, Lake Tahoe, CA, June 2009.

[92] R.T.A. Megens, S. Reitsma, P.H.M. Schiffers, R.H.P. Hilgers, J.G.R. De Mey, D.W. Slaaf, M.G.A. oude Egbrink, and M.A.M.J. van Zandvoort. Two-photon microscopy of vital murine elastic and muscular arteries. *Journal of Vascular Research*, 44:87–98, 2007.

[93] A. Zoumi, X. Lu, G.S. Kassab, and B.J. Tromberg. Imaging coronary artery microstructure using second-harmonic and two-photon fluorescence microscopy. *Biophysical Journal*, 87:2778–2786, 2004.

[94] D.J. Taatjes and B.T. Mossman, editors. *Cell Imaging Techniques: Methods and Protocols*, Chap. 2, pages 15–35. Humana Press Inc., Totowa, NJ, 2006.

[95] W.R. Zipfel, R.M. Williams, R. Christie, A.Y. Nikitin, B.T. Hyman, and W.W. Webb. Live tissue intrinsic emission microscopy using multiphoton-excited native fluorescence and second harmonic generation. *Proceedings of the National Academy of Sciences (PNAS)*, 100:7075–7080, 2003.

[96] J. J. Martin. *Tension Testing Machines and Extensometers*, volume 8 of *ASM Handbook: Mechanical Testing*. ASM International, Materials Park, Ohio, 2000.

[97] American Society for Testing and Materials (ASTM). *D 412 - 06a: Standard Test Methods for Vulcanized Rubber and Thermoplastic Elastomers - Tension*. ASTM International, West Conshohocken, PA, 2009.

[98] A.H. Hoffman and P. Grigg. A method for measuring strains in soft tissue. *Journal of Biomechanics*, 17(10):795–800, 1984.

[99] J.D. Humphrey, D.L. Vawter, and R.P. Vito. Quantification of strains in biaxially tested soft tissues. *Journal of Biomechanics*, 20(1):59–65, 1987.

[100] American Society for Testing and Materials (ASTM). *E 4 - 08: Standard Practices for Force Verification of Testing Machines*. ASTM International, West Conshohocken, PA, 2009.

[101] B. W. Christ. *Effect of Speciment Preparation, Setup, and Test Procedures on Test Results*, volume 8 of *ASM Handbook: Mechanical Testing*. ASM International, Materials Park, Ohio, 2000.

[102] D.W. Marquardt. An algorithm for least-squares estimation of nonlinear parameters. *Journal of the Society for Industrial and Applied Mathematics (SIAM)*, 11:431–441, 1963.

[103] K. Levenberg. A method for the solution of certain non-linear problems in least squares. *Quarterly of Applied Mathematics*, 2:164–168, 1944.

[104] C. Mimata, M. Kitaoka, S. Nagahiro, K. Iyama, H. Hori, H. Yoshioka, and Y. Ushio. Differential distribution and expressions of collagens in the cerebral aneurysmal wall. *Acta Neuropathologica*, 94:197–206, 1997.

[105] H. Wolinsky and S. Glagov. Structural basis for the static mechanical properties of the aortic media. *Circulation Research*, 14:400–13, 1964.

[106] P. J. Elbischger. *Computer Vision Methods for the Automatic Analysis of Fibrous Structures in Biological Soft Tissues*. PhD Thesis, Graz University of Technology, Graz, Austria, April 2005.

[107] B.B. Chaudhuri, P. Kundu, and N. Sarkar. Detection and gradation of oriented texture. *Pattern Recognition Letters*, 14:147–153, 1993.

[108] W.J. Karlon, J.W. Covell, A.D. McCulloch, J.J. Hunter, and J.H. Owens. Automated measurement of myofiber disarray in transgenic mice with ventricular expression of ras. *Anatomical Record*, 252(4):612–625, 1998.

[109] T. Courtney, M.S. Sacks, J. Stankus, J. Guan, and W.R. Wagner. Design and analysis of tissue engineering scaffolds that mimic soft tissue mechanical anisotropy. *Biomaterials*, 27(19):3631–3638, 2006.

[110] C.A. Wiederhielm. Distensibility characteristics of small blood vessels. *Federation Proceedings*, 24:1075–1084, 1965.

[111] J.G. Barra, R.L. Armentano, J. Levenson, E.I.C. Fischer, R.H. Pichel, and A. Simon. Assessment of smooth muscle contribution to descending thoracic aorta elastic mechanics in conscious dogs. *Circulation Research*, 73:1040–1050, 1993.

[112] E. Meijering, M. Jacob, J.-C.F. Sarria P. Steiner, H. Hirling, and M. Unser. Design and validation of a tool for neurite tracing and analysis in fluorescence microscopy images. *Cytometry*, 58A:167–176, 2004.

[113] F. Cacho, P.J. Elbischger, J.F. Rodriguez, M. Doblare, and G.A. Holzapfel. A constitutive model for fibrous tissues considering collagen fiber crimp. *International Journal of Non-Linear Mechanics*, 42:391–402, 2007.

[114] L. Debelle and A.M. Tamburro. Elastin: molecular description and function. *The International Journal of Biochemistry and Cell Biology*, 31:261–272, 1999.

[115] D. Krex, H. K. Schackert, and G. Schackert. Genesis of cerebral aneurysms–an update. *Acta Neurochirurgica (Wien)*, 143:429–448, 2001.

[116] E.C. Davis. Elastic lamina growth in the developing mouse aorta. *Journal of Histochemistry and Cytochemistry*, 43:1115–1123, 1995.

[117] E.C. Davis. Stability of elastin in the developing mouse aorta: a quantitative radioautographic study. *Histochemistry*, 100:17–26, 1993.

[118] G. M. Hass GM. Elasticity and tensile strength of elastic tissue isolated from the human aorta. *Archives of Pathology*, 34:971–981, 1942.

[119] G. M. Hass. Method for the isolation of elastic tissues. *Archives of Pathology*, 34:807–819, 1942.

[120] G. M. Hass. Relations between structure of the ageing aorta and properties of isolated aortic elastic tissue. *Archives of Pathology*, 35:29–45, 1943.

[121] M. A. Lillie, G. W. Chalmers, and J. M. Gosline. The effects of heating on the mechanical properties of arterial elastin. *Connective Tissue Research*, pages 23–35, 1994.

[122] S. M. Partridge, H. F. Davis, and G. S. Adair. The chemistry of connective tissues. 2. soluble proteins derived from partial hydrolysis of elastin. *Biochemical Journal*, 61:11–21, 1955.

[123] N. Gundiah. *Role of Elastin and Collagen in the Passive Mechanics of the Circulatory System*. PhD Thesis, University of California, Berkeley, Berkeley, CA, 2004.

[124] A. I. Lansing, T. B. Rosenthal, M. Alex, and W. Dempsey. The structure and chemical characterization of elastin fibers as revealed by elastase and by electron microscopy. *Anatomical Record*, 114:555–575, 1952.

[125] K.L. Dorrington and N.C. McCrum. Elastin as a rubber. *Biopolymers*, 16:1201–1222, 1977.

[126] L. Cardamone, A. Valentin, J.F. Eberth, and J. D. Humphrey. Origin of axial prestretch and residual stress in arteries. *Biomechanics and Modeling in Mechanobiology*, 8:431–446, 2009.

[127] A. Valentin, L. Cardamone, S. Baek, and J.D. Humphrey. Complementary vasoactivity and matrix remodelling in arterial adaptations to altered flow and pressure. *Journal of the Royal Society Interface*, 6:293–306, 2009.

[128] A. Valentin and J.D. Humphrey. Parameter sensitivity study of a constrained mixture model of arterial growth and remodeling. *American Society of Mechanical Engineers (ASME) Journal of Biomechanical Engineering*, 131:101006, 2009.

[129] J.D. Humphrey. Remodeling of a collagenous tissue at fixed lengths. *American Society of Mechanical Engineers (ASME) Journal of Biomechanical Engineering*, 121:591–597, 1999.

[130] G. J. Campbell and M. R. Roach. The use of ligament efficiency to model fenestrations in the internal elastic lamina of cerebral arteries. i–modelling scheme. *Journal of Biomechanics*, 16:875–882, 1983.

[131] G. J. Campbell and M. R. Roach. The use of ligament efficiency to model fenestrations in the internal elastic lamina of cerebral arteries. ii–analysis of the spatial geometry. *Journal of Biomechanics*, 16:883–891, 1983.

[132] M.A. Lillie and J.M. Gosline. Limits to the durability of arterial elastic tissue. *Biomaterials*, 28:2021–2031, 2007.

[133] M.A. Lillie and J.M. Gosline. Mechanical properties of elastin along the thoracic aorta in the pig. *Journal of Biomechanics*, 40:2214–2221, 2007.

[134] M.A. Lillie. Corrigendum for lillie ma and gosline jm 'mechanical properties of elastin along the thoracic aorta in the pig' j. biomech. 40 (2007) 2214-2221. *Journal of Biomechanics*, 42:663, 2009.

[135] E. W. Dempsey and A. I. Lansing. Elastic tissue. *International Review of Cytology*, 3:437, 1954.

[136] R. Rezakhaniha, E. Fonck, C. Genoud, and N. Stergiopulos. Role of elastin anisotropy in structural strain energy functions of arterial tissue. *Biomechanics and Modeling in Mechanobiology*, 10(4):599–611, 2011.

[137] A. Shifren and R.P. Mecham. The stumbling block in lung repair of emphysema: elastic fiber assembly. *Proceedings of the American Thoracic Society*, 3:428–433, 2006.

[138] H. S. Oktay. *Continuum damage mechanics of balloon angioplasty*. PhD Thesis, University of Maryland, Baltimore County, Baltimore, Maryland, 1993.

[139] W.I. Schievink and V. Roiter. Epidemiology of cervical artery dissection. *Frontiers of Neurology and Neuroscience*, 20:12–15, 2005.

[140] D. E. Busby and A.C. Burton. The effect of age on the elasticity of the major brain arteries. *Canadian Journal of Physiology and Pharmacology*, 43:185–202, 1965.

[141] L. Hadjinikolaou, K. Kotidis, and M. Galinanes. Relationship between reduced elasticity of extracardiac vessels and left main stem coronary artery disease. *European Heart Journal*, 25:508–513, 2004.

[142] M. F. O'Rourke. Vascular mechanics in the clinic. *Journal of Biomechanics*, 36:623–630, 2003.

[143] T. Weber, J. Auer, B. Eber, and M. F. O'Rourke. Relationship between reduced elasticity of extracardiac vessels and left main stem coronary artery disease. *European Heart Journal*, 25:1966–1967, 2004.

[144] T. Weber, J. Auer, M. F. O'Rourke, E. Kvas, and E. Lassnig. Increased arterial wave reflections predict severe cardiovascular events in patients undergoing percutaneous coronary interventions. *European Heart Journal*, 26:2657–2663, 2005.

[145] C. J. Baker, A. Fiore, E. S. Connolly Jr., K. Z. Baker, and R. A. Solomon. Serum elastase and alpha-1-antitrypsin levels in patients with ruptured and unruptured cerebral aneurysms. *Neurosurgery*, 37:56–61, 1995.

[146] S. Cajander and O. Hassler. Enzymatic destruction of the elastic lamella at the mouth of cerebral berry aneurysm? an ultrastructural study with special regard to the elastic tissu. *Acta Neurologica Scandinavica*, 53:171–181, 1976.

[147] E. S. Connolly Jr., A. J. Fiore, C. J. Winfree, C. J. Prestigiacoma, J. E. Goldman, and R. A. Solomon. Elastin degradation in the superficial temporal arteries of patients with intracranial aneurysms reflects changes in plasma elastase. *Neurosurgery*, 40:903–908, 1997.

[148] P. B. Dobrin, W. H. Baker, and W. C. Gley. Elastolytic and collagenolytic studies of arteries. implications for the mechanical properties of aneurysms. *Archives of Surgery*, 119:405–409, 1984.

[149] P. B. Dobrin and R. Mrkvicka. Failure of elastin or collagen as possible critical connective tissue alterations underlying aneurysmal dilatation. *Cardiovascular Surgery*, 2:484–488, 1994.

[150] T. Hashimoto, H. Meng, and W. L. Young. Intracranial aneurysms: links among inflammation, hemodynamics and vascular remodeling. *Neurological Research*, 28:372–380, 2006.

[151] R. Kadirvel, Y.H. Ding, D. Dai, H. Zakaria, and A. M. Robertson. The influence of hemodynamic forces on biomarkers in the walls of elastase-induced aneurysms in rabbits. *Neuroradiology*, 49:1041–1053, 2007.

[152] H. Meng, Z. Wang, Y. Hoi, L. Gao, and E. Metaxa. Complex hemodynamics at the apex of an arterial bifurcation induces vascular remodeling resembling cerebral aneurysm initiation. *Stroke*, 38:1924–1931, 2007.

[153] N. D. Broom, G. Ramsey, R. Mackie, B. J. Martin, and W. E. Stehbens. A new biomechanical approach to assessing the fragility of the internal elastic lamina of the arterial wall. *Connective Tissue Research*, 30(2):143–55, 1993.

[154] D. Mohan and J. W. Melvin. Failure properties of passive human aortic tissue. i–uniaxial tension tests. *Journal of Biomechanics*, 15(11):887–902, 1982.

[155] M. F. O'Rourke. Arterial aging: pathophysiological principles. *Vascular Medicine*, 12:329–341, 2007.

[156] E. Fonck, G. G. Feigl, J. Fasel, D. Sage, M. Unser, D. A. Rufenacht, and N. Stergiopulos. Effect of aging on elastin functionality in human cerebral arteries. *Stroke*, 40(7):2552–6, 2009.

[157] E. Fonck, G. Prod'hom, S. Roy, L. Augsburger, D. A. Rufenacht, and N. Stergiopulos. Effect of elastin degradation on carotid wall mechanics as assessed by a constituent-based biomechanical model. *American Journal of Physiology, Heart and Circulatory Physiology*, 292(6):H2754–63, 2007.

[158] M. A. Zulliger and N. Stergiopulos. Structural strain energy function applied to the ageing of the human aorta. *Journal of Biomechanics*, 40(14):3061–9, 2007.

[159] C. F. Jiang and A. P. Avolio. Characterisation of structural changes in the arterial elastic matrix by a new fractal feature: directional fractal curve. *Medical and Biological Engineering and Computing*, 35(3):246–52, 1997.

[160] A. Avolio, D. Jones, and M. Tafazzoli-Shadpour. Quantification of alterations in structure and function of elastin in the arterial media. *Hypertension*, 32(1):170–5, 1998.

[161] M. F. O'Rourke. Mechanical principles in arterial disease. *Hypertension*, 26:2–9, 1995.

[162] S. E. Greenwald. Ageing of the conduit arteries. *Journal of Pathology*, 211(2):157–72, 2007.

[163] S. M. Cadwell, R. A. Merrill, Sloman C. M., and F. L. Yost. Dynamic fatigue life of rubber. *Industrial and Engineering Chemistry, Analytical Edition*, 12(1):19–23, 1940.

[164] H. Schechtman and D. L. Bader. In vitro fatigue of human tendons. *Journal of Biomechanics*, 30(8):829–35, 1997.

[165] H. Schechtman and D. L. Bader. Fatigue damage of human tendons. *Journal of Biomechanics*, 35(3):347–53, 2002.

[166] M. L. Raghavan, D. A. Vorp, M. P. Federle, M. S. Makaroun, and W. Webster. Wall stress distribution on three-dimensionally reconstructed models of human abdominal aortic aneurysm. *Journal of Vascular Surgery*, 31:760–769, 2000.

[167] J. N. Reddy. *An Introduction to the Finite Element Method (Second Edition)*. McGraw-Hill, Boston, 1993.